


University Of Jordan
Faculty Of Graduate Studies

٢٧٥
٥

THE WAVELET TRANSFORM, ANALYSES OF FLOW-INDUCED VIBRATION PHENOMENON

By

مكتب كلية الدراسات العليا


Muhammed S. Abu-Samak

SUPERVISOR

Dr. M. Nader Hamdan

Submitted in Partial Fulfillment of the Requirements For the Degree of
Master of Science in Mechanical Engineering.

Faculty of Graduate Studies, University of Jordan.

Amman , Jordan

May, 1994

٥/٢/٩٤

This thesis was defended successfully on May 30, 1994

COMMITTEE MEMBERS

SIGNATURE

Dr. M. Nader Hamdan

Mechanical Engineering Department

University of Jordan

Chairman of Committee

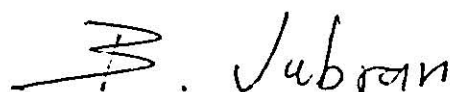


Dr. Bassam Ali Jubran

Mechanical Engineering Department

University of Jordan

Member of Committee

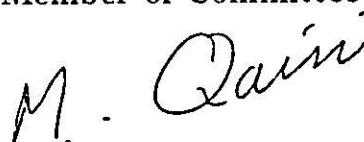


Dr. Mazen al-Qisi

Mechanical Engineering Department

University of Jordan

Member of Committee



ACKNOWLEDGEMENTS

It is with deep pleasure I express my thanks to all who helped me during the preparation and completion of this work. Special thanks are indebted to my supervisor, Dr. M.Nader Hamdan, and to Dr. Bassam Jubran whom without their support, encouragement, and advice, my work could have been more difficult. My thanks to the staff of the mechanical engineering laboratories, especially to Mr. Aref Shaheen. Also I highly appreciate the patient and support of my family during my long preoccupation with this research, I should not forget the support given to me throughout this work by all my friends, especially; Mohammed, Nader, Nasha't, Husam, Baha'a, Tayser, and Ehab.

Contents

COMMITTEE MEMBERS	ii
Acknowledgements	iii
List of Figures	vii
Nomenclature	xv
Abstract	xviii
1 INTRODUCTION	1
1.1 Introduction	1
1.2 Spectral Analysis	2
1.3 The Importance of Spectral Density	3
1.4 Other Signal Processing Techniques	4
1.4.1 Short Time Fourier Transform (STFT)	5
1.4.2 Gabor Expansion (GE)	6
1.5 Layout of the Thesis	7
2 FLOW - INDUCED VIBRATION PHENOMENON	9
2.1 Introduction	9
2.2 The Flow-Induced Vibration Phenomena	10
2.2.1 General Description of The flow-induced vibration Phenomena	10
2.3 Forms of Flow Induced Vibration	12

- 2.3.1 Vortex shedding 12
- 2.3.2 Fluid-Elastic Excitation (Galloping) 13
- 2.3.3 Flutter 14
- 2.4 Literature Survey 15
- 3 THE WAVELET TRANSFORMS 27**
- 3.1 Introduction: 27
- 3.2 Classification of Signals: 27
 - 3.2.1 Correlation Methods : 29
 - 3.2.2 The power Spectrum : 32
- 3.3 Wavelets and the Wavelet Transform (WT): 33
 - 3.3.1 Wavelets: 33
 - 3.3.2 Grossmann-Morlet Time-Scale Wavelets : 35
 - 3.3.3 Time Frequency Wavelets : 37
 - 3.3.4 The Wavelet Transforms : 39
- 3.4 Literature Review 46
- 4 APPARATUS AND INSTRUMENTATION 51**
- 4.1 Introduction 51
- 4.2 The Test Model : 52
- 4.3 Instrumentation :- 53
 - 4.3.1 Velocity Measurement (Hot Wire Anemometer.) : 53
- 4.4 Vibration Measurements : 54
- 4.5 Experimental procedure : 55
- 4.6 Repeatability of Measurements : 57

5	DISCUSSION OF RESULTS	58
5.1	Introduction :	58
5.2	Frequency Distribution :	59
5.3	Time Series :	61
5.4	Correlation Functions Analysis of The Flow Induced Vi- bration Signals	62
5.5	Power Spectrum	64
5.6	Wavelet Transform Analysis of the Flow-Induced Vibra- tion Process:	67
6	CONCLUSIUONS AND RECOMMENDATIONS	74
6.1	Introduction:	74
6.2	Conclusions	74
6.2.1	Experimental and classical representations	74
6.2.2	The wavelet representations:	77
6.3	Recommendations:	78
	REFERENCES	175
	APPENDICES	187
	APPINDIX A	188
	APPINDIX B	198
	APPINDIX C	201
	APPINDIX D	203
	APPINDIX E	214

List of Figures

Figure 2.1 : A classification of flow- induced vibrations, Blevins [9]	80
Figure 2.2: Sketch of alternate vortex shedding process behind a circular cylinder. A sequence of events begins at (1) and continues to (8), [30]	81
Figure 2.3 : A typical power spectrum of the flow velocity, at Re=200 for the location ($x=2d$, $y=2d$). Only the locked- on shedding frequency, $f=1.1 f_n$ the spectrum frequency, $f=2.2 f_n$ and their harmonics are dominant in the spectrum [16]	82
Figure 2.4 : A typical frequency response curve showing the normalized velocity response amplitude as a function of the forcing frequency for Re= 920, the vibration parameter ω_1 $= 0.14$, and $d= 1.27$ cm; [7]	83
Figure 2.5 a and b: Record of cylinder oscillation above the lock-in region; Re= 135, $\zeta = 0.00120$ [10]	84
Figure 2.6 : Effect of blocking plates on velocity spectrum for a fixed cylinder ($d= 32.6$ mm, $U= 16.0$ m/s [32]	85
Figure 2.7: Translation-mode oscillation of cylinders without blocking plates. [32]	86

Figure 2.8: Translation-mode oscillation of cylinders with blocking plates [32]	87
Figure 2.9 : Fluctuating flow velocity spectrum, peak frequency of velocity spectrum and oscillation frequency for single cylinder oscillation as functions of U ; (probe : $x/d = 2$, $y/d = 1.5$, $z/d = 1$). (a) Karmman vortex excitation for $s/d = \infty$ (single cylinder); (b) excitation induced by the downstream cylinder for $s/d = 0.0625$. [33]	88
Figure 2.10 : Change of velocity spectrum along the upstream cylinder of the fixed system ($s/d = 0.25$, $U=4.28$ m/s; probe position : $x/d = 2.0$, $y/d = 1.5$ to 3.5 , $z/d = 1.0$. [33]	89
Figure 2.11 : Time history of response of an array of tubes (7 By 6) in water subjected to a gap cross-flow for different locations of the hot wire. [34]	90
Figure 2.12 : Effect of gap width h on acceleration frequency spectrum of tubes (7 By 6 tube array), [34]	91
Figure 2.13 : Power spectral density, $\alpha = 15$ deg [36]	92
Figure 2.14 : Time history of cylinder displacement.	93
Figure 2.15 : Velocity traces taken in near- wake at spanwise locations to off-midplane a and b for basic states of response.	94
Figure 2.16 : Power spectral density of velocity fluctuation on wake for basic states of response	95
Figure 3.1 : correlation and power spectral density estimations Flow Chart	96
Figure 3.2 : Processing the power spectrum	97

Figure 3.3 : computation of FFT	98
Figure 3.4 : FFT Flow Chart	99
Figure 3.5 : Different views of a wavelet	100
Figure 3.6 : WT Flow Chart	101
Figure 3.7 (a) : Wavelet filter bank structure. The down-arrow decimation. The output of the transform is the family of signals w^i , forming the two parameter transform w_j^i in the scale-time plane. Following terminology to be introduced. w^i is the (decimated) discrete wavelet transform. (b) : Diagram of an implementation of the undecimated DWT . [56]	102
Figure 3.8 : A trous structure as derived by Holshneider et. al [71], (b) Basic computational cell for computing CWT coefficients octave and octave. (c) Connection of the cells used in Rioul's work and corresponding location of the wavelet coefficients in the time- scale plane. [73]	103
Figure 3.9 : Some examples of orthonormal wavelet bases with compact support constructed by Daubechies [53]. . The number of nonvanishing moment is, respectively, 4, 12, and 20, corresponding to support widths of, respectively, 3, 11, and 19. [65]	104

Figure 3.10 (a) : Basis functions and time- frequency resolution of the wavelet transform (WT). (i) Basis functions. (ii) Coverage of time-frequency plane. (b) : Basis functions and time frequency resolution of the short-time Fourier transform (STFT). (i) Bais functions. (ii) Coverage of time-frequency plane. [74] 105

Figure 3.11 (a) : The process of obtaining two-dimensional linear phase set from the one-dimensional one. (b) Comparison of the discrete wavelet transform using a filter bank. [75] 106

Figure 4.1:Schematic diagram of the wind tunnel and the test section.[82] 107

Figure 4.2 : End plates details. [84] 108

Figure 4.3 : Overall Scene of the instrumentation 109

Figure 4.4 : Hot Wire Calibration curve, Probe 55p14. 110

Figure 4.5 : Simplified diagram of the constant-temperature anemometer [83] 111

Figure 5.1 : Frequency distribution at U=5.0 m/s and U=5.85 m/s 111

Figure 5.2 : Frequency distribution at U=6.78 m/s and U=7.81 m/s 112

Figure 5.3 : Frequency distribution at U=8.93 m/s and U=10.15 m/s 113

Figure 5.4 : Frequency distribution at U=11.47 m/s and U=12.9 m/s 114

Figure 5.5 : Frequency distribution at $U=14.46$ m/s and $U=16.11$ m/s	115
Figure 5.6 : Frequency distribution at $U=17.89$ m/s and $U=19.87$ m/s	116
Figure 5.7 : Frequency distribution at $U=21.84$ m/s and $U=22.9$ m/s	117
Figure 5.8 : Frequency distribution at $U=24.01$ m/s and $U=26.33$ m/s	118
Figure 5.9 : Frequency distribution at $U=28.79$ m/s and $U=31.41$ m/s	119
Figure 5.10 : The 1st time-series at $U=28.79$ m/s	120
Figure 5.11 : The 2nd time-series at $U=28.79$ m/s	121
Figure 5.12 : The 3rd time-series at $U=22$ m/s	122
Figure 5.13 : The 4th time-series at $U=19.79$ m/s	123
Figure 5.14 : The 5th time-series at $U=19.79$ m/s	124
Figure 5.15 : The 6th time-series at $U=17.9$ m/s	125
Figure 5.16 : The 7th time-series at $U=24.01$ m/s	126
Figure 5.17 : The 8th time-series at $U=22.9$ m/s	127
Figure 5.18 : The autocorrelation function of the 1st time-series	128
Figure 5.19 : The autocorrelation function of the 2nd time-series	129
Figure 5.20 : The autocorrelation function of the 3rd time-series	130
Figure 5.21 : The autocorrelation function of the 4th time-series	131
Figure 5.22 : The autocorrelation function of the 5th time-series	132
Figure 5.23 : The autocorrelation function of the 8th time-series	133
Figure 5.24 : The autocovariance function of the 1st time-series	134

Figure 5.25 : The autocovariance function of the 2nd time-series	135
Figure 5.26 : The autocovariance function of the 3rd time-series	136
Figure 5.27 : The autocovariance function of the 4th time-series	137
Figure 5.28 : The autocovariance function of the 5th time-series	138
Figure 5.29 : The autocovariance function of the 8th time-series	139
Figure 5.30 : The crosscorrelation function of the 1st and 2nd time-series	140
Figure 5.31 : The crosscorrelation function of the 4th and 5th time-series	141
Figure 5.32 : The crosscovariance function of the 1st and 2nd time-series	142
Figure 5.33 : The crosscovariance function of the 4th and 5th time-series	143
Figure 5.34 : The power spectrum of the autocorrelation func- tion of the 1st time-series	144
Figure 5.35 : The power spectrum of the autocorrelation func- tion of the 2nd time-series	145
Figure 5.36 : The power spectrum of the autocorrelation func- tion of the 3rd time-series	146
Figure 5.37 : The power spectrum of the autocorrelation func- tion of the 4th time-series	147
Figure 5.38 : The power spectrum of the autocorrelation func- tion of the 5th time-series	148
Figure 5.39 : The power spectrum of the autocorrelation func- tion of the 6th time-series	149

Figure 5.40 : The power spectrum of the autocorrelation function of the 7th time-series	150
Figure 5.41 : The power spectrum of the autocorrelation function of the 8th time-series	151
Figure 5.42 :The wavelet transform of the frequency distribution at U=5.0 m/s using Mallat wavelet	152
Figure 5.43 :The wavelet transform of the frequency distribution at U=5.0 m/s using Daubichies' wavelet	153
Figure 5.44 :The wavelet transform of the frequency distribution at U=5.0 m/s using Modulated Gaussian wavelet	154
Figure 5.45 :The wavelet transform of the frequency distribution at U=5.0 m/s using 8th derivative of Gaussian wavelet	155
Figure 5.46 :The wavelet transform of the frequency distribution at U=5.0 m/s using (One cycle of sine) wavelet	156
Figure 5.47 :The wavelet transform of the frequency distribution at U=5.0 m/s using Mexican hat wavelet	157
Figure 5.48 :The wavelet transform of the frequency distribution at U=5.85 m/s using Modulated Gaussian wavelet	158
Figure 5.49 :The wavelet transform of the frequency distribution at U=6.79 m/s using Modulated Gaussian wavelet	159
Figure 5.50 :The wavelet transform of the frequency distribution at U=7.81 m/s using Modulated Gaussian wavelet	160
Figure 5.51 :The wavelet transform of the frequency distribution at U=19.79 m/s using Modulated Gaussian wavelet	161

Figure 5.52 :The wavelet transform of the frequency distribution at U=26.33 m/s using Modulated Gaussian wavelet . . .	162
Figure 5.53 :The wavelet transform of the frequency distribution at U=28.79 m/s using Modulated Gaussian wavelet . . .	163
Figure 5.54 :The wavelet transform of the frequency distribution at U=31.41 m/s using Modulated Gaussian wavelet . . .	164
Figure 5.55 :The wavelet transform of the 1st time-series using 8th Derivative of the Gaussian wavelet	165
Figure 5.56 :The wavelet transform of the 1st time-series using Modulated Gaussian wavelet	166
Figure 5.57 :The wavelet transform of the 1st time-series using Mexican Hat wavelet	167
Figure 5.58 :The wavelet transform of the 2nd time-series using Modulated Gaussian wavelet	168
Figure 5.59 :The wavelet transform of the 3rd time-series using Modulated Gaussian wavelet	169
Figure 5.60 :The wavelet transform of the 4th time-series using Modulated Gaussian wavelet	170
Figure 5.61 :The wavelet transform of the 6th time-series using Modulated Gaussian wavelet	171
Figure 5.62 :The wavelet transform of the 7th time-series using Modulated Gaussian wavelet	172
Figure 5.63 :The wavelet transform of the 8th time-series using Modulated Gaussian wavelet	173

NOMENCLATURE

\vec{a} :	Accelaration
a :	Frequency scale in the wavelet transform
b :	Time translation in the wavelet transform
C_d :	Drag coefficient
D :	Diameter of oscillating cylinder
d :	Bandwidth of the Gabor window
E :	The expectation operator
f :	Frequency
f_n :	Natural frequency of the test system
f_0 :	Centerd frequency of a wavelet
f_s :	Shedding frequency
f_{nz} :	Frequency due to the translation mode
$f_{n\theta}$:	Frequency due to the rotational mode
GE :	Gabor expansion
$g(t)$:	Analysis window in the Gabor expansion
$h(t)$:	A wavelet in time domain
$H(\omega)$:	A wavelet in frequency domain
I :	The electrical current

- i : logarithmic grid related to the frequency scale
 K : Spring constant
 l : Length of the oscillating cylinder
 l/D : The aspect ratio
 $L^2(\tilde{R})$: Space of the square integrable functions
 m : Dilation parameter to construct a family of wavelets
 n : Translation parameter to construct a family of wavelets
 Nu : Nusslet number
 Re : Reynold number
 RMS : Root mean square
 $R_{xx}(t)$: Autocorrelation function
 $R_{xy}(t)$: Crosscorrelation function
 \tilde{R}^n : Space of n integrable functions
 S : Strouhal Number
 $STFT$: Short time Fourier transform
 s : Gap spacing
 s/d : Relative gap spacing
 T : Sampling rate

T_a :	The ambient temperature
T_w :	The temperature of the hot wire
t :	Time
U :	Free stream velocity
U/fD :	Reduced velocity
W_m :	Analysis window in power spectral density
WT :	The wavelet transform
$x(t)$:	Flow-induced vibration time signal
\bar{X}, \bar{Y} :	Estimated mean of a time signal
α :	Angle of incidence
$\gamma(t)$:	Analysis window in STFT
$\gamma_{xx}(t)$:	Autocovariance function
$\gamma_{xy}(t)$:	Crosscovariance function
δ :	Displacement thickness
$\zeta(t)$:	Damping ratio
ρ :	Density of air
τ :	The time delay

ABSTRACT

Title : " THE WAVELET TRANSFORM ANALYSES OF
FLOW-INDUCED VIBRATION PHENOMENON "

prepared by : Muhammed S. Abu-Samak

suprvised by : Dr. M. Nader Hamdan :

Flow-induced vibration of a single cylinder subjected to a uniform cross flow is investigated experimentally using both traditional methods and the newly techniques of wavelet transforms. The results of using wavelet transforms are compared with those obtained by classical methods, such as, autocorrelation functions, autocovariance functions, crosscorrelation functions, crosscovariance functions, and power spectral density. Several types of wavelets were used in the analysis of the non-stationary signals of flow-induced vibration process.

It is found that the modulated Gaussian wavelet was the most suitable one, in terms of computational effort and efficient representation, for the analyze of the flow-induced vibration signals. The results obtained show that the wavelet transform reveals many important information regarding

the transient boundaries and chaotic behaviour which are not revealed in other techniques. Also a computational saving was obtained by using fast convolution techniques, such as fast Fourier transform, in a suitable manner.

Recommendations are also given for future work concerning the usage of wavelet transforms in studying some relevant topics, especially, turbulent flow, vortex-shedding phenomena, where results of these studies can be used in the analysis of the flow-induced vibration process.

Chapter 1

INTRODUCTION

1.1 Introduction

The widespread use of computers in the past decades and the corresponding ability to perform high-speed calculation on incoming data samples in real time have produced a virtual revolution in the field of signal processing. This use of the high-speed computers made the field of signal processing invades many divers disciplines ; Mechanical engineers are one of those concerned with signal-processing techniques.

One common technique of processing the time-varying signals is to transform it into its equivalent form in the frequency domain. This corresponds to finding its Fourier transform representation which has been widely used for data-reduction purposes; in many cases the frequency domain version of the signal is easier to interpret and characterize. This representation can explain the modifications made in signals as they progress through linear systems. Moreover, random signals, in particular, are more suitably characterized by the frequency domain approach which is called the spectral analysis of random signals and has found a widespread applications in many areas of science, engineering economic, social science, etc. The following is a brief outline of the various methods

used to analysis random signals.

1.2 Spectral Analysis

Spectral Analysis of functions is used for studying the time-series in another plan from another point of view. It is obtained from an invertible transformation from time domain description of a function, $x(t)$, to a frequency domain description, $X(\omega)$, or more generally for a joint time and frequency-domain description(see appendix - A).

Spectral analysis applies to both continuous time functions, called waveforms, and discrete time functions, called sampled - data.[1] The main purpose of spectral analysis is to represent a function by a sum of weighted sinusoidal functions called spectral components; that is, to analyze or to decompose a function into these spectral components. The weighting function in this decomposition is a density of spectral components. This spectral density or simply the spectrum can be efficiently convenient, and often reveals the description of the function.

The spectral representation of a signal in a noisy medium may result in attenuation of the noise in that medium while leaving the signal intact. This spectral filtering is an example of the advantage of using the spectral representation. In many cases one can also use the spectral representation of a time signal in such a way as to code it, i.e, to compress the amount of data used to represent information extent of the signal for the purpose of efficient storage or transmission.

1.3 The Importance of Spectral Density

There are three principal reasons for using the spectral analysis, namely, to provide useful descriptive statistics, as a diagnostic tool to indicate which further analyses might be relevant, and to check postulated theoretical models. However, the success experienced with this technique seems to vary with the length of series available to analysis.

In the case of random signals there are some advantages for the use of spectral analysis which can be summarized as follows :

1. Signal spectra are often much simpler representation of the original time signal.
2. It plays a simplifying role in explaining the effects of linear processing or filtering the random signals.
3. The representation of random signals in terms of sinusoidal-waves which is inherent in spectral analysis is often physically satisfactory.[2]

A random signal is considered to be a member of an ensemble of discrete - time signals which are characterized by a set of probability density functions , i.e, for a specific signal of a particular time, the amplitude of the signal samples at that time is assumed to have been determined by an underlying scheme of probabilities.

Random signals may be classified into stationary signals and nonstationary ones. In this work, more emphasize will be placed on the nonstationary type which is more representative of the flow-induced vibration

signals.

The key to the mathematical representation of random signals, in general, lies in their description in terms of averages. Random signals are not absolutely summable or square summable and consequently do not directly have Fourier transforms which make the spectral analysis more difficult. However, in the case of stationary random signals, one can use the power spectral density of the autocorrelation or autocovariance functions where many (but not all) of the properties of the analyzed signals can be summarized and the Fourier transform of these functions often exists.[3]

On the other hand, the nonstationary signals depends on the reference time chosen. Thus the autocorrelation function and power-spectral density will be poor tools in the analyses of these signals. Furthermore, the distribution of energy over the frequency cannot be attained by the use of spectral analysis [4].

To overcome the problems associated with the spectral representation of random signals, other techniques have been developed and will be the subject of the next section.

1.4 Other Signal Processing Techniques

The need to represent a signal in both the time and the frequency domain has resulted in an enormous increase in the volume of research in the field of "time - frequency representations" (TFR). Some examples are given below.

1.4.1 Short Time Fourier Transform (STFT)

One of the most important signal representation is the short time Fourier transform (STFT) or the windowed Fourier transform which is obtained by suitably pre-windowing the analyzed signal. Mathematically it is expressed as follows:

$$STFT(t, f) = \int_{t'} x(t') g^*(t' - t) e^{-j2\pi f t'} dt' \quad (1.1)$$

Thus, the STFT at time t is the Fourier Transform (FT) of the signal, $x(t')$, multiplied by a shifted window defined by $g^*(t' - t)$ centered around t where the $*$ stands for the conjugate function. Windowing the signal leads to a tradeoff in time resolution versus frequency resolution. Good time resolution requires short duration windows, whereas good frequency resolution requires long duration windows. The window has a negligible energy outside the interval centered around t . The desired time and frequency resolution dictates the exact size of this interval [5]. The multiplication by relatively short window effectively suppresses the signal outside a neighborhood around the analysis time point $t' = t$. The STFT is simply a "local spectral" of the signal $x(t)$ around the analysis time t . It is evidently a linear Time-Frequency representation (TFR) (see Appendix B) , complex valued, in general , and it is significantly influenced by the choice of the analysis window, $g(t)$. In the case of a fast changeable signal it is difficult to choose a suitable short-time window and this restrict the use of STFT.[5]

some signal components then the TFR of $x(t)$ is the same linear combination of the TFRs of each of the signal components. This is given by

$$x(t) = c_1 x_1(t) + c_2 x_2(t) \quad (1.5)$$

$$TFR_x(t, f) = c_1 TFR_{x_1}(t, f) + c_2 TFR_{x_2}(t, f) \quad (1.6)$$

For a complete view of the TFRs one must mention that although the linearity of a TFR is a desirable property, the quadratic structure of a TFR is an intuitively reasonable assumption when we want to interpret a TFR as a time-frequency energy distribution or instantaneous power spectrum [1]. In Appendix C, there is a list of some important TFRs. Finally, the wavelet transforms are considered to be a powerful tool in analyzing the nonstationary signals as they can overcome the disadvantages of the other representations which have already been highlighted.

1.5 Layout of the Thesis

The thesis is divided into six chapters, of which this introduction is the first. Chapter 2 outlines the flow - induced vibration phenomenon together with the previous works that might be related to the present investigation.

A formal and indepth discussion of the mathematical principles of wavelet transforms and comparisons with other processing methods are the subject of Chapter 3. Chapter 4 describes the experimental set up used to provide the data used for the wavelet transform analysis. Chapter 5 presents and discusses the experimental results together with their analysis using different techniques.

Finally, Chapter 6 reports the concluding remarks gained from the present investigation, together with the recommendations for further work.

Chapter 2

FLOW - INDUCED VIBRATION PHENOMENON

2.1 Introduction

The viscous flow past a two-dimensional bluff body and the resulting recirculation region behind the bluff body have been the subject of numerous investigations [7-11]. These studies have been motivated by the desire to understand the fundamental physics of such flows, vortex street formation and near-wake flow.

The theory of vortex shedding is very complex, and exact solution to the fluid-elastic problem has not, yet, been found. More recently a number of promised studies which examined oscillating flow problems have begun to relate the motion of the vortices to the forces acting on the cylinder. In addition, the vortex motions are explained in terms of the relevant dimensionless parameters.

Furthermore, recent experiments [7, 8] ensure that a bluff body in a perturbed incident flow consisting of a mean flow with a periodic component superimposed upon it is identical, under suitable conditions, to the vortex resonance of a cylinder oscillating in line with an incident uniform flow.

In general, large-amplitude vibrations due to vorticity shedding are observed when the flow reaches a critical value. These vibrations have a destructive effect on bridges, cables, and other structures, which make the study of the flow induced vibration of a practical importance especially with the modern industry applications of these systems. In this Chapter, some of the investigations that have been reported are summarized so as to give account of recent contributions to the literature on the flow-induced vibrations and related aspects.

2.2 The Flow-Induced Vibration Phenomenon

2.2.1 General Description of The flow-induced vibration Phenomenon

If a cylinder is set normal to a uniform flow direction, the fluid-structure dynamic interaction will induce a lateral oscillation of the cylinder. This self-excited motion is caused by the fluctuating fluid pressure forces on the cylinder surface which are generated by vortices shed alternately from each side of the cylinder. The knowledge of the behavior of the forces resulting from this interaction is essential for the adequate design of this problem.

It has been observed that when one of the natural frequencies of the immersed body is near the vortex-shedding frequency and the damping of the system is low, self excited vibrations of the body can be induced. These resonant oscillations are accompanied by a "lock-on" or capture of the vortex-shedding frequency by the vibration frequency. The vortex-shedding frequency, f_s , is expressed as a non-dimensional Strouhal number,

S, where $S = \frac{f_v d}{U}$, here U is the free stream velocity and, d is the diameter of the body [9]. Furthermore, the fluid-dynamic forces (the periodic lift and the drag forces) on the body can be amplified through a nonlinear interactive process resulting in an increase in the vibration of the body with changes in the flow field in the near wake of the body [10].

The "lock-on" or synchronization effect between the vortex and vibration frequencies will cause a deviation between the theoretical frequency, obtained from the Strouhal, and the experimental vortex-shedding frequency, which is equal to the cylinder natural frequency, when the amplitude of cylinder oscillation passes a critical threshold. Also, the "lock-on" effect is observed when a cylinder is forced to oscillate sinusoidally in a uniform stream. One could conclude from this that the body-wake system behaves as a nonlinear, self-excited oscillator.

Blevins [9] put a general classification of the flow-induced vibrations based on the nature of the flow and the characteristics of the structure as shown in Fig. (2.1) . Blevins [9] was one of those who tried to develop an approximate theoretical model for the fluid-structure interaction problem with some success.

The main An essential reason for the difficulty of developing a successful model is due to the relatively large number of parameters affecting the amplitude of the vibrating body. These parameters include;the reduced velocity,mass Ratio,Reynolds number and the damping factor.

2.3 Forms of Flow Induced Vibration

There are three forms of flow-induced vibration; vortex shedding, fluid elastic or galloping and flutter. Following is a brief description of each of these forms.

2.3.1 Vortex shedding

Vortex shedding has been the most common form of fluid dynamic excitation for a single cylinder. Blevins [9] described the mechanism of separation and vortex shedding. He claimed that when the fluid flows toward the leading edge of a bluff body the fluid pressure rises from the free stream pressure to the stagnation pressure. This will develop boundary layers on both sides of the cylinder. These boundary layers separate from each side of the cylinder surface near the widest section and form two free shear layers which bound the wake. Since the innermost portion of the free shear layers moves much more slowly than the outermost portion of the layers which are in contact with the free stream, the free shear layers tend to roll up into descending, swirling vortices. This mechanism is shown in Fig(2.2). The shedding of the formed vortices alters the pressure distribution, and the cylinder experiences a time-varying force at the frequency of vortex shedding.

Lock-on phenomenon is an important feature of vortex-shedding excitation. If the frequency of the vortex-shedding is in resonance with the natural frequency of the member that produces it, large amplitude oscillations with consequent large stresses can develop.

These oscillations begin when the velocity increases or decreases so

that the shedding frequency approaches the natural frequency of the structure. Lock-on occurs over a certain range of velocities depending on the structural and flow properties. This is the difference between the lock-on and the usual case of resonance which exhibits a single resonance point.

As the lock-on phenomenon begins and the motion of the vortex shedding locks into the structural frequency, a feed path is completed so that the motion of the structure controls the vortex shedding. Lock-on phenomenon disappears beyond a critical condition due to the limited capacity of the oscillating structure to alter the frequency of vortex shedding.

2.3.2 Fluid-Elastic Excitation (Galloping)

The flow-induced vibration of bluff structure is commonly referred to as stall flutter or galloping. Galloping can arise in any lightweight, flexible, structure exposed to a flow. A wide variety of cross sections, including square, rectangular, right angle, and stalled aerofoil are potentially unstable owing to aerodynamic galloping.

The main assumption of galloping analysis is that the fluid force on the structure is determined solely by the instantaneous relative velocity and the angle of attack of the flow to the structure. This implies that the information about the fluid force can be measured by wind tunnel test on stationary model held at various angles

The most fascinating feature of the interference galloping is that both the mean position of the motion and the body's oscillation frequency may vary appreciably with increasing flow velocity. Another notable feature is

that the vibration amplitude always approach asymptotically a constant value. The instability is either in the form of the a vortex-resonance or a galloping. The cylinder never exhibits a combined vortex-resonance and a galloping or a vortex-resonance followed by a galloping [11].

Galloping vibration can be prevented by increasing the internal damping of the structure, reducing the flow velocity, stiffening the structure and increasing the mass of the structure without lowering its natural frequency or damping.

2.3.3 Flutter

Flutter has been defined as the dynamic instability of an elastic body in an airstream and is produced by aerodynamic force which result from the deflection of the elastic body from its undeformed state [12].

Flutter can occur in any engineering application of more than two degrees of freedom, such as long-span suspension bridges and turbine blades. The main reason of flutter is due to coupling interaction of bending and torsion modes.

The aerodynamic forces of aircraft flutter are, often, sufficiently large, to produce large shifts of the natural frequency, while in galloping vibration they are usually small to produce significant shifts of the natural frequencies. Also, aerodynamic flutter is produced by more than one mode, but galloping vibrations affects a single mode.

2.4 Literature Survey

The fluid flow and the structure are interactive systems, and their interaction is dynamic [9]. The understanding of the nature of this interaction and forces development are necessary steps to get a sufficient picture about the system. Fluid forces cause the structure to deform, and thus the structure orientation to the flow may change in the direction of the fluid forces. This change will produce a new pressure distribution around the cylinder as well as affecting the body stiffness and its natural frequency. A summary of some important studies will be presented below.

Griffin and Hall [13-16] reported the results of recent experiments about the vortex shedding and the flow control in bluff body wakes. They claimed that both symmetric and asymmetric vortex patterns were observed over a wide range of oscillation conditions. For the in-line oscillations, vortex lock-on was observed at $f = 2, 3$, and $4 f_n$, with an asymmetric street formed at twice the basic Strouhal frequency and a symmetric street formed at three times the Strouhal frequency. The asymmetric pattern was complex in that one row consisted of a line of single vortices, whereas the other row consisted of a line of oppositely rotating vortex pairs. The vortex lock-on at three times the Strouhal frequency resulted in the formation of a symmetric street of vortices. In these cases the basic patterns persist downstream over a large number of oscillation cycles. When the oscillation frequency is four times the Strouhal frequency, a symmetric pattern is formed but rapidly loses its

coherence in the early wake.

After an initial period of time corresponding to the quasi-steady stage in the forced perturbed flow calculation, the resulting streamwise velocity history at a point in the near wake is periodic. The corresponding power spectrum in Fig.(2.3) contains primary peaks at $f = 1.1$ and $2.2 f_n$ as expected, and secondary peaks at superharmonics of these values. No additional peaks appear in the spectrum, where the power spectrum gives evidence of lock-on in the fully developed flow. A more extensive discussion of the spectral element computations of the perturbed flow cylinder lock-on is given by Hall and Griffin [14].

Filler et. al.,[7], investigated the response of the shear layers separating from circular cylinder to small amplitude rotational oscillations. A plot of the velocity (u'/U) in the wake form as a function of the oscillation Strouhal number S_t is shown in Fig.(2.4). Here the oscillation parameter $\Omega_1 = \omega_1 \frac{d}{2U}$ where ω_1 is the frequency of the rotational oscillations. At the lower frequencies near the usual Karmman shedding frequency, a large resonant peak is seen when the oscillation is in that range. However, at the higher imposed frequencies there is a secondary broad peak in the range of the shear layer instability frequencies. In the Karmman frequency range of vortex shedding the wake behaves like a nonlinear oscillator near resonance. This behavior is well known [17-20] and has been explored by numerous investigators for the cases of cross-flow and in-line oscillations. An important finding by Tokumaru and Dimotakis [8] is that active control of the near-wake vortex formation and flow physics by rotational oscillations of the cylinder can reduce the

drag on the cylinder by as much as a factor of six. This increase in C_D is accompanied by a comparable decrease in the wake displacement thickness δ_* (by a factor of five) as defined by an integral of the cross-stream wake velocity distribution over the height of the channel.

The introduction of the absolute/convective theory of fluid dynamic stability has led to a promising new approach and a new theoretical framework for understanding the physics of vortex formation and near-wake flow development.[21-27].

Recent stability calculations based upon computed and measured mean velocities in the wakes of stationary circular cylinders suggest that the vortex formation region is absolutely unstable while the fully-formed vortex street is convectively unstable. The vortex formation region is thought to be a complex global region that is characterized by the interaction between the model and the flow upstream and downstream propagating vorticity waves, [28-30].

Karniadakis and Triantafyllou [21] conducted a linear stability analysis of the time-averaged flow in the near-wake which was derived from their direct numerical simulation of the cylinder wake at $Re=100$. Further research based upon these new analytical and computational approaches described herein is likely to lead to a new and more complete fundamental understanding of the near-wake vortex dynamics and vortex lock-on which until now have been studied mostly by using the more traditional modeling approaches combined with experiments. These investigations suggest that modification and control of the basic instability or formation mechanisms of the wake by imposed oscillations, i.e., cross-flow, in

line and rotational, incident flow perturbations, and an imposed sound field provide a means for making substantial alterations to the near-wake vortex pattern, and possibly to the middle-and far-wake flow patterns as well which exist relatively far downstream from the wake-generating body.

Anagnostopoulos et al. [10] conducted an experimental investigation at low Reynolds numbers to study the response characteristics of a vortex-excited oscillations of a circular cylinder mounted elastically in a water channel and record the time histories of the cylinder oscillation Figs. (2.5a) and (2.5b). They claimed that the maximum oscillation amplitude occurs near the lower limit of the "lock-on" region unlike the results of [15,26,31], where the maximum amplitude observed was near the middle of the "lock-on" region. These study focus on the Reynolds number between (90-150), where the vortex-street wake behind the cylinder is fully laminar.

Moreover, Shirakashi et al.[32] observed an unexpected subharmonic-like resonance at $\frac{f_v}{f_n} = 3$ in addition to the normal one at $\frac{f_v}{f_n} = 1$, where f_v is the Karman vortex shedding frequency and f_n is the natural frequency for the cylinder oscillation. They explained the presence of these peaks by the fact that the oscillating behavior of an elastically supported cylinder whose natural frequency $f_{n\theta}$ for the rotation-mode oscillation is several times higher than that for the translation mode f_{nz} as follow when the free flow velocity U is low, a translation-mode oscillation occurs at a frequency $f = f_{nz}$. With increasing U , its amplitude attains a maximum peak when the vortex shedding frequency f_v is equal to f_{nz} . Further increase in U

results in a second maximum amplitude which occurs when the ratio $\frac{f_v}{f_{nz}}$ is around three, with the motion remaining purely translational. As U becomes even higher, a rotation-mode dominates the flow process which gives a third maximum amplitude peak in the displacement at the end of the cylinder when $\frac{f_v}{f_{nz}}$ is around three.

It is worth noting here that in the case of a cylinder without end plates an additional peak was found in the spectrum S_u at a frequency nearly one-third of the usual Karmman vortex-shedding frequency, when the probe was located on the wall of the test cylinder at a point near to the side wall [32]. The effects of open slots on the vortex-shedding were also observed for a fixed cylinder as shown in Fig. (2.6)(b), which confirmed that the additional peak of S_u at $f = \frac{f_v}{3}$ was not induced by the cylinder oscillation. When the blocking plates were attached to the cylinder, all foregoing effects of the slots were completely erased as shown in Fig. (2.6) (a) ,both for fixed cylinders and oscillating cylinders.

The effects of the blocking plates on the oscillating behavior of a cylinder are clearly revealed from Figs. (2.7) and (2.8) [32]. In Fig. (2.7) the translation-mode oscillation of a cylinder without blocking plates has two resonant amplitude peaks at $\frac{f_v}{f_{nz}} = 1$ and $\frac{f_v}{f_{nz}} = 3$, and the latter of these two peaks is considered to be caused by the Additional peak of S_u at $f = \frac{f_v}{3}$ near the side walls. By attaching the blocking plates, the higher velocity peaks in Fig. (2.7) were completely removed and the lower velocity peaks became more sharps as seen in Fig. (2.8).

Later on, Shirakashi et. al. [33] investigated the Karmman vortex excitation of an elastically supported cylinder in cross-flow for circular

cylinder and their results can be summarized as follows:

1. The spectrum peak frequency in Figure (2.9)(a) gives a Strouhal number $S = \frac{f_v}{UD}$ around 0.2 and the oscillation is significant only when $f_v = f_{nz}$. Hence, the peak of the velocity spectrum for a single cylinder corresponds to Karmman vortex-shedding. In contrast, in Figure (2.9)(b), the peak due to Karmman vortex-shedding vanishes and two peaks appear in the spectra at lower frequencies. The higher frequency for the blunt peak is just twice the lower frequency for the higher sharp peak. In Figure (2.9)(b), this lower frequency is denoted by f_v to distinguish it from that by Karmman vortex-shedding. As clearly seen in Figure (2.9)(b), the upstream cylinder in this case always oscillates at its natural frequency f_{nz} and the maximum amplitude of this new excitation is attained when $f_v = f_{nz}$. The displacement at the maximum excitation are almost sinusoidal, with a slight modulation; i.e. the spectra of the displacements are concentrated at a frequency $f = f_{nz}$. Since f_{nz} is the natural frequency determined from free damped oscillation in still air, it is inferred that the effective mass is equal to the mass in still air and the damping factor is as small as in the free damped oscillation.
2. When a hot-wire probe is moved along the upstream cylinder, the velocity spectrum changes as shown in Fig (2.10). The transition point at $\frac{y}{d} = 2.25$ represents the spanwise position beyond which the peak corresponding to longitudinal vortex-shedding disappears from the spectrum. The sharp peak which appears in the region of $\frac{y}{d}$

respect to time.

Eckerle [35] presents some concluded remarks in his study on the effects of velocity on the three-dimensional separated flow region in front of a cylinder. He found that the separation in front of cylinder depends on the momentum and is related to the approaching free stream velocity and boundary-layer thickness. At relatively low incoming free stream velocities, the reverse flow did roll up into vortex in the plane of symmetry.

Ota et.al.[36] investigated the dynamic response of an elliptic cylinder. Typical examples of their results of the power spectral density of the velocity fluctuation for an angle of incidence, $\alpha = 15$ deg and at the subcritical Reynolds number, $Re = 35,800$, are shown in figures 2.13 which shows a high peak at the vortex-shedding frequency. However, in the critical Reynolds number region, $Re = 80,100$, two spectra were observed at different times. One of them shows a narrow peak at 220 Hz as found in Fig. (2.13)(b) and another shows a weak vortex-shedding at 580 Hz in Fig. (2.13)(c). The flow around the cylinder is observed to fluctuate intermittently with time from the former to the latter. That is, the flow is very unstable and exhibits the subcritical one at one moment but changes into the critical one at other time. Such a fluctuation of the flow may be originated from the formation of the separation bubble and its burst. At $Re = 101,400$ beyond the critical Reynolds number, $Re = 80,100$, the flow around the cylinder becomes relatively stable, though the peak frequency of the spectrum fluctuates from 700 Hz to 800 Hz, and the power spectral density extends in a very wide range of frequency, as shown in Fig. (2.13)(d).

More recently Marn et. al. [37] have used a good technique to study the cross flow induced vibration. In his work a vorticity formulation of the instability problem has been used to establish the onset of fluid elastic instability. Perturbation equation were developed and solved numerically . The fluid forces were obtained by integrating the pressure along the surface of the cylinder motion to predict the threshold of the dynamic instability. Criteria for the occurrence of instability were explained and a simple optimization and parametric study was implemented by varying the disturbance patterns, the Reynold number, the geometry, and the pitch to diameter ratios.

Obasaju et. al. [38] conducted an experimental study of rectangular and cut-out square cylinders. Fig. (2.14) shows eight samples traces of the displacement of the vibration cylinders of approximately 2 minutes each. For the cut-out square, the recording was made at $\frac{U}{ND} = 3.55$ ($A_{RMS}/d = 0.0176$) where the peak of the response of the cylinder occurred. Trace (a) shows that the vibration amplitude remained at one level for a long time before drifting to another level. The drift may have been caused by a minute change in the tunnel wind speed.

Traces (b) to (f) shown in figure 2.14 characterize the displacement of the rectangular cylinders when, height to diameter ratio(H/D) = 4 , 5 and 50 and the angle of incidence, α , is in the range $30 < \alpha < 70$. Traces (b) to (d) in Fig 2.14 show that when $\frac{U}{ND} = \frac{1}{S}$, where S is the Strouhal number, the vibration amplitude was irregular and there were periods when there was little or no vibration. Near $\frac{U}{ND} = \frac{1}{2S}$, there was a burst-type response with rather long intervals between burst, see

trace (e) in Fig.(2.14). When $\frac{U}{ND}$ was significantly higher than $\frac{1}{5}$ the amplitude was irregular and has a low frequency modulation, see trace (f). Traces (g) and (h) in Fig.(2.14) characterize the displacement of the rectangular cylinder when height to diameter ratio ,H/D = 4 and 5 and the angle of incidence is in the range $10 < \alpha < 30$. When $\frac{U}{ND} = \frac{1}{5}$, the vibration amplitude was fairly regular, see trace (g). Taking $\frac{U}{ND}$ slightly away $\frac{1}{5}$ gave the "beating" type of vibration shown in trace (h).

Moreover, Nuzzi et al [30] studied the three dimensional vortex formation from an oscillating non-uniform cylinder. From their contribution the period-doubled response of the wake is presented by the lower velocity trace in the middle column of figure (2.15). The upper trace indicates that the vortex formation in that portion of the wake is still highly periodic with insignificant modulation, and thereby locked-on. The drastic differences between these traces in the middle column of figure (2.15) emphasizes the fact that the period-doubled wake instability from the three-dimensional portion of the cylinder is indeed a localized phenomenon.

Also spectra of the near-wake velocity fluctuations characteristic of the lock-in state are illustrated in figure (2.16). The predominant peak of the near-wake instability, i.e. the vortex formation, occurs at the same frequency for the midplane b, which corresponds to midplane of three-dimensional portion of a cylinder having gradual spanwise portion in diameter, and off-midplane a, which represents location within region of two-dimensional vortex formation from cylinder, locations, emphasizing the occurrence of the global lock-in along the entire span of the cylinder.

The spectrum at the top of the left-hand column of figure 2.16 shows

the case of lock-on response of the wake at the off-midplane allocation. Correspondingly, at the midplane b location, there appears to be the period-doubled component $\frac{1}{2f_0}$ and the high components at f_0 , $f_0+1/2f_0$, and so on.

Increased irregularity of the spectrum at the midplane b location is evident in the bottom spectrum in the right-hand column of figure 2.16, corresponding to the regime of complex modulation fascinated in figure 2.16. It is characterized by a number of discrete, nonlinearity interacted spectral components. Correspondingly, at the off-plane a location, there exist the fundamental frequency f_0 , subharmonic frequency $\frac{f_0}{2}$ and higher-order components due to the nonlinear interaction.

Finally, Baker et. al. [40] present some comments about the transition process as a whole within horseshoe vortices. They show that it would seem quite possible to discuss horseshoe vortices processes using the language of nonlinear dynamics i.e., chaos theory. They found that as the Reynolds number increases the number of horseshoe vortices increases from 2 to 4 to 6. Two distinct sorts of oscillation then occur (examples of period doubling), before a final breakdown to turbulence (or chaos). If the above speculations are correct then it is also possible that a similar process occurs in turbulent vortex systems at even higher Reynold numbers. Such a description is an attractive one, but in essence is no more than an analogy. If the "route to chaos" offered by horseshoe vortex systems is to be fully described, a great deal more experimental work is required to describe the process fully. If this is done, however, it perhaps offers a way in which an "engineering scale" transition problem

can be analyzed by using the powerful techniques of nonlinear dynamics.

In most of the aforementioned investigations the authors presented measurement of the RMS acceleration of the structures vibration versus free stream velocity, for the time signal analysis, while for the frequency analysis they presented the power spectral density assuming the process to be stationary.

In the present work a more general approach to signal analysis, mainly , the wavelet transform will be adopted. Based on knowledge gained so far in other similar applications it is hoped that the wavelet transform can reveal several aspects of the flow-induced vibration process which are difficult to show using the classical methods of signal processing.

Chapter 3

THE WAVELET TRANSFORMS

3.1 Introduction:

Wavelets are rapidly finding applications as tools for the analysis of non-stationary signals. The main objective of this Chapter is to explain what is meant by the terms "wavelets" and "the wavelet transforms" and the relationship between the two terms. In section 3.2, classification of the signals, often encountered in practice, will first be introduced. Then the most well known traditional methods of signal processing, such as correlation functions and power spectrum density are hopefully discussed in the rest of section 3.2. Section 3.3 presents the wavelet transforms where their main characteristics are also discussed. Finally the literature review conducted, concerning the wavelet transforms, (WT), in this study will be presented in section 3.4, together with the application of WT to different engineering problems

3.2 Classification of Signals:

Signal processing is concerned with two broad classes of waveforms: deterministic and random (Stochastic) signals. The deterministic waveform is one which can be completely specified as a function of time while a ran-

dom waveform cannot be completely specified as a function of time so it is modeled by means of its statistical properties.

A random process is an indexed family of random variables X_j . The family of random variables is characterized by a set of probability distribution functions that in general may be a function of the index j . In using the concept of random process as a model for discrete-time signals, the index j is associated with the time index [1].

A random signal is stationary if its properties are statistically invariant over time. A well-known stationary signal is the white noise, which, in its sampled form, appears as a series of independent drawings. A stationary signal can exhibit unexpected events, such as, pulses, but we know in advance the probabilities of these events, i.e, they are statistically predicatable known.

The ideal tool for studying stationary signals is the Fourier transform. In other words, stationary signals decompose canonically into linear combinations of waves (sines and cosine). In the same way, signals that are not stationary decomposes into linear combinations of wavelets [41].

The study of nonstationary signals, where transient events may appear cannot be predicted even statistically with knowledge of the past, and this necessitates techniques that are different from Fourier transform. These techniques, in addition to those discussed in Chapter one, include wavelets of the time-frequency type most suitable to the analysis of quasi-stationary signals, and time-scale wavelets which are adapted to nonstationary signals.

In the following , the classical techniques, such as , spectral analy-

of the fact that the calculation of the coefficients of DFT can be carried out iteratively, which results in a considerable saving of computation time. Specifically, if the time series consist of $N=2^n$ samples, then about $2nN = 2N \log_2 N$ arithmetic operations are required to evaluate all N associated of the DFT coefficients. The number of operations required for the calculation of the DFT coefficients with straightforward procedures is (N^2) [44].

3.3 Wavelets and the Wavelet Transform (WT):

A wavelet transform, $WT(a,b)$, is a function of two adjustable parameters (a) and (b) , where (b) is a translation in time and (a) is a parameter that governs the frequency distribution.

By controlling these parameters, one obtains a signal representation that is well localized in both time and frequency. Following are the various definition of wavelets and then the wavelet transform.

3.3.1 Wavelets :

The first definition of a wavelet due to Grossmann and Morlet [45] is as follows: A wavelet is a function $h(t)$ in $L^2(\tilde{R})$ whose Fourier transform $H(\zeta)$ satisfies the condition

$$\int_0^{\infty} |H(t\zeta)|^2 \frac{dt}{t} = 1 \quad (3.11)$$

almost every where. $L^2(\tilde{R})$ is the space of the squared integrable functions and ζ is a dummy variable.

The second definition of a wavelet is due to the Littlewood-Paley-Stein theory [41] where a wavelet is defined as a function $h(t)$ in $L^2(\tilde{R})$

whose Fourier transform $H(\zeta)$ satisfies the condition

$$\sum_{-\infty}^{\infty} |H(2^{-j}\zeta)|^2 \frac{dt}{t} = 1 \quad (3.12)$$

almost everywhere. If $h(t)$ is a wavelet in this sense, then $(\log 2)^{-5} \cdot h(t)$ satisfies the Grossmann-Morlet condition.

The third definition refers to the work of Franklin and Stromberg [41]. A wavelet is a function $h(t)$ in $L^2(\tilde{R})$ such that $2^{\frac{j}{2}}h(2^jx - k)$ for each $j, k \in \tilde{r}$ is an orthonormal basis for $L^2(\tilde{R})$. Such a wavelet $h(t)$ necessarily verifies the second condition.

From above it can be seen that in going from the first to the third definition we are adding more conditions and thus narrowing the scope of the "wavelet." The same is true for the wavelet analysis of a function. In the general Grossmann-Morlet theory, the wavelet analysis of a function, say $f(t)$, yields a function $W(a,b)$ of $n+1$ variables, where $a > 0, b \in \tilde{R}^n$.

It should be shown that not every function can be a wavelet. Grossmann and Morlet [45] give the following conditions, based on group theory, for a function $h(t)$ to be a wavelet :

1. Square integrability condition:

$$\int |h(t)|^2 < \infty \quad (3.13)$$

2.

$$H(\omega) = 0 \quad \omega \leq 0 \quad (3.14)$$

where $H(\omega)$ is the Fourier transform of $h(t)$. These two conditions ensure that the transformation is a bounded invertible operator in

the appropriate space.

3. The third condition, which is called the "admissibility condition", is :

$$\int du \exp^u \int |H(\omega)(\exp^u \omega|^2 d\omega < \infty$$

If these conditions are satisfied then the corresponding WT(a,b) is a defined transform.

The WT can be considered as time-frequency representations or time-scale ones according to the parameters (a)and(b). In the following a more detail picture of these types with emphasize on the time-scale transforms which are more suitable to the analysis of nonstationary signals will be presented

3.3.2 Grossmann-Morlet Time-Scale Wavelets :

"Time-scale" analysis (also called "space-scale" in the image case , or "multiresolution analysis") involves using a vast range of scales for signal analysis. This notion of scale, which refers to cartography, implies that the signal (or image) is replaced, at a given scale, by the best possible approximation that can be drawn at that scale. By "traveling" from the large scales toward the fine scales, one "zooms on" and arrive at more and more exact representation of the given signal.

The analysis is then done by calculating the change from one scale to the next. These are the details that allow one, by correcting a rather crude approximation, to move toward a better quality representation. This algorithmic scheme is called "multiresolution analysis" and is devel-

oped by Mallat [47]. For more insight on the multiresolution theory see Appendix D.

The wavelets are defined by starting with a function of the real variable t . This function is called a "mother wavelet" provided it is well localized and oscillating. (By oscillating it resembles a wave, but by being localized it is a wavelet.). The localization condition is expressed in the usual way as it decreases rapidly to zero when t tends to infinity. The second condition suggests that it vibrates like the wave [48]. This requires that the integral of $h(t)$ to be zero, and that the same hold true for the first m moments of $h(t)$. This is expressed as

$$\begin{aligned} \int_{-\infty}^{\infty} h(t)dt &= \int_{-\infty}^{\infty} t^{m-1}h(t)dt \\ &= 0 \end{aligned} \tag{3.15}$$

The "mother wavelet", $h(t)$, generates the other wavelets of the family. This is done by changing the scale a , i.e , the scale of $h(t)$ is conventionally 1, while $h_{(a,b)}(t)$ has a scale of (a) , $a > 0$ and by translation in time by (b) , i.e , (the function $h(t)$ is conventionally centered around 0, and $h_{(a,b)}(t)$ is then centered around (b)). Thus we have :

$$h_{(a,b)}(t) = \frac{1}{a^{-s}} h\left(\frac{t-b}{a}\right), \quad b \in \tilde{\mathbb{R}} \tag{3.16}$$

Alex Grossmann and Jean Morlet [40] have shown that, if $h(t)$ is real-valued, this family of wavelets can be used as if it were an orthonormal basis. This means that any signal of finite energy can be represented as a linear combination of wavelets set and that the coefficients of this combination are, up to a normalizing factor, measure , in a certain sense,

the fluctuations of the signal , $x(t)$, around the point (b) , at the scale given by $(a) > 0$.

Thus, by selecting an appropriate "mother wavelet", $h(t)$, and generating a set of wavelets, $h_{a,b}(t)$, one is able to represent a dynamic signal in another mixed plane of the shifted time and the corresponding frequency content at a scale a , in which the analysis can see more than one view of this signal. By changing the scale (a) one moves to a more detailed picture of the frequency content of the original signal [47]. For example, at a coarse scale of (a) one can look at the global scene of the analysed signal and at more finer (a) 's one move to another detailed frequency analysis of the signal. These characteristics make the time-scale transforms appropriate for the analysis of nonstationary signals .

3.3.3 Time Frequency Wavelets :

The WT representation was originally introduced as a time-scale representation. Although this representation is based on well defined abstract mathematical concepts ,their physical meaning, however, are not easily grasped by the practicing engineer.

This motivated signal-processing experts to find a more physically interpreting version of WT transform which led to the development of Malvar wavelets in 1987,[49],and wavelets packets in 1990 [50]. With the Malvar wavelets the signal is segmented adaptively and optimally, and then the segments are analysed using classical Fourier analysis. The wavelets packets reverse this order, i.e, first the signal is filtered and then analyzed in the time variable. These two techniques were described by

ville in 1947 [41]. He wrote, "we can either, first cut the signal into slices (in time) with a switch; then pass these different slices through a system of filters to analyze them. Or we can, first filter different frequency bands ; then cut these bands into slices (in time) to study their energy variations". The first approach leads to Malvar wavelets and the second to the wavelets packets. The time-frequency wavelets, however, are more suitable to study the quasi-stationary signals and there are many restrictions that complicate their direct application, for example, the Malvar structure which is a family of orthonormal bases $u_{k,l}$, are defined as :

$$\begin{aligned}
 u_{k,l}(t) = & \\
 & 2w(t - 2l\pi) \cos\left(\frac{kt}{2}\right) \quad l \in \tilde{2z}, k = 1, 2, 3, \dots \\
 & w(t - 2l\pi) \quad l \in \tilde{2z}, k = 0 \\
 & 2w(t - 2l\pi) \sin\left(\frac{kt}{2}\right) \quad l \in \tilde{2z} \cup \{k = 1, 2, 3, \dots\}
 \end{aligned}
 \tag{3.17}$$

where $w(t)$ is a variable length window having the property that both $w(t)$ and its Fourier transform decay exponentially and obey the following restrictions:

$$\begin{aligned}
 w(t) = 0 & \quad \text{if} \quad t \leq -\pi \quad \text{or} \quad t \geq 3\pi \\
 w(t) = w(2\pi - t) & \quad \text{if} \quad 0 \leq w(t) \leq 1 \\
 w^2(t) + w^2(-t) = 1 & \quad \text{if} \quad -\pi \leq t \leq \pi
 \end{aligned}
 \tag{3.18}$$

In addition, the above constructions may suffer from some irregularity [49], and other conditions as , for example, those imposed by Meyer and Coifman [41,51]. The problem gets even more complex, when we consider

the application of wavelet packets [50].

Based on the above discussion, in this work, the time-scale wavelets and the time-scale transforms will be adopted for the analysis of the flow-induced vibration signals. In making this choice the following factors were taken into consideration :

1. The time-scale wavelets are more suitable for the analysis of non-stationary processes, such as, the flow-induced vibration process.
2. They are easier to formulate mathematically and to be computed efficiently.

3.3.4 The Wavelet Transforms :

The wavelet transforms (WT) was first given by Morlet and Grossmann [40] for the analysis of seismic data and it is defined as :

$$WT(a, b) = \frac{1}{a^{-0.5}} \int_{-\infty}^{\infty} x(t)h\left(\frac{t-b}{a}\right)dt \quad (3.19)$$

where the wavelet function $h(t)$ is an appropriate window like the modulated Gaussian . The WT is the convolution of a signal $x(t)$ with an analysis window $h(t)$ shifted in time by (b) and dilated by a scale parameter (a) . The scale parameter (a) can be chosen such that it is inversely proportional to frequency. The factor $|a|^{-0.5}$ is used to ensure energy preservation [52] and there are various ways of discretizing time-scale parameters, (a) and (b) , each one yields a different type of wavelet transform. The purpose of WT is to extract the localized conditions of the signal labeled by these scale parameters (a) and (b) and then the signal can be computed by expanding it into a family of functions , i.e., into

a set of frequency channels of equal bandwidth on a logarithmic scale [52,53].

At this point in time , the clear and complete picture of what wavelets have added to our understanding of the multiresolution technique, is far from being fully understood. However there is some promising advantages of WT like:-

1. The isolation of events in time (or space) and frequency.
2. Since one can choose the scale parameter such that it is inversely proportional to frequency, the WT provides high spectral resolution and poor temporal resolution for low frequency. Conversely, for high frequency it provides high temporal resolution, enabling the WT to "zoom on " the singularities [54,55].

The significance of WT is probably best grasped by comparing it to the short time Fourier transform "STFT", where

$$STFT(\omega, b) = \int h(t - b) \exp^{j\omega t} x(t) dt \quad (3.20)$$

where ω and b are the frequency and the centered time of the analyzed signal respectively.

Thus, to obtain $STFT(\omega, b)$, one multiplies the signal by an appropriate window $h(t-b)$ like Gaussian centered at time b (sliding analysis windows) and then takes the Fourier transform. The mathematical terms is an expansion of the signal in terms of a family of function $h(t-b)e^{j\omega t}$, which are generated from a signal function $h(t)$ through translation (b) in time and translation ω in frequency. In contrast, the WT is an expansion of

functions $h(\frac{t-b}{a})$ generated by translation (b) in time and dilation (a) in time (concentration in frequency).

The continuous WT resembles a continuous bank of STFT with a different window for each frequency. The significance of this is that, while the STFT window have the same time and frequency resolution, the WT have time resolution decreases with a and frequency resolution increases with a. This property can be of a great advantage in signal processing since high frequency characteristics are generally highly localized in time whereas slowly varying signals require good low frequency resolution [55]. As originally proposed by Morlet et.al. [45], $h(t)$ was a modulated Gaussian which is defined as :

$$h(t) = e^{j\omega_0 t} \exp \frac{t^2}{2} \quad (3.21)$$

This function is still the prototypical analyzing wavelet for signal processing application [56]. The above wavelet only satisfies the admissibility condition approximately and so cannot be an admissible analyzing wavelet. However at $\omega_0 \gg 0$ the Gaussian will be very close to an admissible analyzing wavelet.

In Chapter Five other possibilities of analyzing wavelets will be studied. Here, our exclusive concern will be the discrete values for (a) and (b). In particular, the parameter a is chosen to be equal to 2^i where i is termed the octave of the transform [56-59] , i.e , $WT(a,b)$ will be:

$$WT(2^i, b) = \frac{1}{\sqrt{2^i}} \int h(\frac{t-b}{2^i})x(t)dt \quad (3.22)$$

Moreover, b is taken to be a multiple of a, i.e, $b = n.2^i$ and this leads to:

$$WT(2^i, 2^i n) = \frac{1}{\sqrt{2^i}} \int h(\frac{t}{2^i} - n)x(t)dt \quad (3.23)$$

A logical step in applying the WT to discrete signals is to discretize the above integral, this leads to define the discrete wavelet transform, DWT, as follows;

$$WT(2^i, 2^i n) = \frac{1}{\sqrt{2^i}} \sum_k h\left(\frac{t}{2^i} - n\right) x(t) \quad (3.24)$$

Each equation provides a multiresolution analysis of $x(t)$ specifically, the coefficients $W(2^i, 2^i n)$ carry information about $x(t)$ near the frequency 2^i and near the time instant $2^{-i}k$ and the above sum provides an approximation to $x(t)$ up to scale 2^i , i. e, it provides a low pass filtered version of $x(t)$ with less details. This is one of the aspects which make WT decomposition is a powerful tool in studying the scaling properties of the signal [60-63].

In studying the flow-induced vibration signals which are a nonstationary type, the Daubichies' approach [64] is adopted. The scale and translation parameters (a) and (b) where chosen such that they constitute discrete lattices of wavelets. This leads to :

$$\begin{aligned} h(t) &= h_{a_0^m, nb_0 a_0^m}(t) \\ &= a_0^{-\frac{m}{2}} h(a_0 t^{-m} - nb_0) \end{aligned} \quad (3.25)$$

in this study a_0 and b_0 are chosen to be 2.0 and 1.0 respectively.

However, these functions $h(t)$ are of very particular type. Typically their Fourier transform $H(\omega)$ has a compact support (Eq. 3.10). Moreover, for practical purposes, it is desirable to use functions $h(t)$, that are very concentrated. It is quite true that the choice of this wavelet will play an important role in identifying the properties of the analysed signal.

The problem of choosing a suitable wavelet is thoroughly discussed in [61-63]. They presented many conditions based on the optimization techniques, quadrature mirror filter theory and difference equations for the optimal choice. In the present study the well known wavelets are selected in order to study the flow induced vibration signals. These wavelets, in Fourier transform version, will be compared in order to choose the most suitable wavelet for the analysis of flow-induced vibration signals.

In what follows the mathematical definition of these wavelets are presented.

1. Mallat [47], used a multiresolution signal decomposition theory and quadrature mirror filters to compute an orthonormal wavelet and used it in a computer vision applications. This wavelet is defined as :

$$H(\omega) = \frac{e^{-j(\frac{\omega}{2})}}{\omega^4} \cdot \left(\frac{F(\frac{\omega}{2}) \cdot T}{F(\omega)F(\frac{\omega}{2})} \right) \quad (3.26)$$

where T is a delay factor, and

$$F(\omega) = \frac{N_1(\omega) + N_2(\omega)}{105(\sin \frac{\omega}{2})} \quad (3.27)$$

$$N_1(\omega) = 5 + 30(\cos(\frac{\omega}{2})^2) + 30(\cos(\frac{\omega}{2})^2)(\sin(\frac{\omega}{2})^2) \quad (3.28)$$

$$N_2(\omega) = 2(\cos(\frac{\omega}{2})^2)(\sin(\frac{\omega}{2})^4) + 70(\cos(\frac{\omega}{2})^4) + \frac{2}{3}(\sin(\frac{\omega}{2})^6) \quad (3.29)$$

2. Daubichies construct a tight frame wavelet [64,65] with no restriction on the choice of the parameters a_0, b_0 other than $a_0 > 1$ and $b_0 \neq 0$

:-

$$H(\omega) = (\log a_0)^{-1/2} \begin{cases} 0 & \omega \leq l \\ \sin\left[\frac{\pi}{2} v\left(\frac{\omega-l}{l(a_0-1)}\right)\right] & l \leq \omega \leq a_0 l \\ \cos\left[\frac{\pi}{2} v\left(\frac{\omega-a_0 l}{l(a_0-1)}\right)\right] & a_0 l \leq \omega \leq a_0^2 l \\ 0 & \omega \geq a_0^2 l \end{cases} \quad (3.30)$$

where :

$$l = \frac{2\pi}{b_0 a_0^2 - 1} \quad (3.31)$$

and :

$$\begin{aligned} v(x) &= 0 \quad x \leq 0 \\ &= x \quad 0 < x < 1 \\ &= 1 \quad x \geq 1 \end{aligned} \quad (3.32)$$

3. Meyer [41] used Daubichies' wavelet and constructed another one which reflects a deep understanding of the concept of multiscale analysis, this wavelet is defined as :

$$H_1(\omega) = \frac{1}{\sqrt{2\pi}} \exp^{j\omega/2} (H(\omega) + H(-\omega)) \quad (3.33)$$

where, $H(\omega)$ is "Daubichies' wavelet"

4. The Mexican hat, which is the second derivatives of the Gaussian, and defined as [64]:

$$H(\omega) = \frac{2}{\sqrt{3}} \pi^{-1/4} \omega^2 \exp^{-\omega^2/2} \quad (3.34)$$

5. The 8th derivative of the Gaussian is [64] :

$$H(\omega) = \frac{2^{15} 7}{15} \pi^{-1/4} \omega^8 \exp^{-\omega^2/2} \quad (3.35)$$

6. One cycle of the sine function is given by ;

$$h(\omega) = \frac{\sqrt{2}}{\pi} \frac{\sin \pi \omega}{1 - \omega^2} \quad (3.36)$$

This function was constructed mathematically [64] and not used for practical applications.

7. The modulated Gaussian, that was used by Morlet [46] in analysing seismic data,

$$h(\omega) = \pi^{-1/4} \left(\exp \frac{(\omega - \omega_0)^2}{2} - \exp \frac{-\omega^2}{2} \exp \frac{-\omega_0^2}{2} \right) \quad (3.37)$$

Kadamba and Boudreaux [66,67] used this wavelet with $\omega_0 = \pi \left(\frac{2}{\log 2} \right)^{1/2}$.

These wavelet were used in the following discrete implementation of the wavelet transform, which were used in the analysis of the nonstationary signals obtained from the flow-induced vibration process.

$$WT(m, n) = \sum_{m, n \in \mathbb{Z}} a_0^m \int \exp^{im b_0 a_0^m \omega} h(a_0^m \omega) f(\omega) d\omega \quad (3.38)$$

where f , h are the Fourier representations of the analyzed signal and the chosen wavelet, respectively.

Figure 3.6 shows the flow chart that has been used in the present investigation to compute the wavelet transform of an appropriate signal where the computer program is listed in Appendix E.

3.4 Literature Review

As mentioned in previous sections the wavelet transform was developed recently by Grossmann and Morlet [45,46], in 1984, and was done by the decomposition of square integrable wavelets. These wavelets were then obtained by shift and dilation from any one of them.

The shift and dilation provide a chance to look at the signals at different scales and that will clarify discontinuities and transient boundaries of these signals. These advantages make WT a very suitable tool in dealing with signal processing and this was the first usage of WT ; to study a seismic signal[45,68]. Later on Kronaland-Martient [67] used WT to study the sound patterns. Also Flandrin [69-70] made a remarkable contribution by applying WT to the nonstationary signals. At the same time Holschneider [71] developed a real time algorithm for signal processing using WT.

More recently , Shensa [56] tried to clarify the relationship between discrete WT (DWT) and continuous WT (CWT) by a through treatment of the algorithm a' trous' [72], which used a CWT, and the multiresolution approach [47], which used DWT. Shensa [56] brought these two algorithms together in a generalized one and then provided a systematic framework (Fig. 3.7) for DWT and derived the conditions under which DWT computes CWT exactly.

Rioul and Duhamel [73] applied fast convolution techniques to achieve fast algorithms for DWT and CWT. Their effort reduced the computational complexity from L to $\log L$ for large filter lengths where L is the

filter length. They compared several methods for implementing various kinds of WT efficiently. Each of these methods uses the DWT by pre-filtering the analysed signal (see Fig. 3.8). Also this prefilter design is discussed .

The WT analysis is performed using a signal prototype function called a wavelet which can be thought of as a bandpass filter. Based on iterations of discrete filters Daubechies [52,53] constructed compactly supported orthonormal wavelets (see Fig. 3.9) ,and a detailed treatment of their solutions are presented in [64].

Vetterli in successive papers [54,55,74] discussed the relationships of wavelets,filter banks and multiresolution systems, and compared the WT with STFT (see Fig. 3.10). Furthermore, Kovacevic and Vetterli [75] presented new results on multidimensional filter banks and their connection to multidimensional non separable wavelets (Fig. 3.11). They showed the difficulty of designing regular wavelets in multiple dimensions. However, they presented some initial results indicating a direction for future work.

One of the important fields corresponding to WT is the comparison of this technique with older ones such as Gabor analysis, STFT and Wigner distribution (WD).

Delpratn et.al.[76] compared the WT with Gabor analysis and they claim that there absolutely no difference between them in procedures and concluded that the only difference lies in the behaviour of the squared modulus of their representations,i.e, the time-frequency energy density. In their investigation they emphasized on the precise estimation for frequency and amplitude modulation laws but not for the case of multicom-

which may be insufficient for a complete representation.

Another word about the measurements. Farge [86,41] indicated that the experimentation in fluid dynamics was to a considerable extent a somewhat recondite form of computation which provide, and is still providing, the decisive mathematical ideas in the field of fluid dynamics. Farge believes that it is now the time to concentrate on effecting the transition to digital devices rather analogy type such as wind tunnels, and that will increase the power of our approaches to an unrepresented extent.

A more detailed survey of the relevant literature may be found in [41,47,60].

Chapter 4

APPARATUS AND INSTRUMENTATION

4.1 Introduction

The purpose of the experimental work in this thesis is to study the time-history of the acceleration amplitude of the vibration of the circular cylinder subjected to cross flow. Following is a description of the apparatus and the instruments used in this study are presented. Also, the measurements techniques used are discussed.

It is noted that the experimental set-up and experimental procedure used in this work has been used by other graduate students at the University of Jordan ,mechanical engineering laboratories[87,88].

4.2 Apparatus

An outline of the apparatus and coordinate system used in this study are shown in figure (4.1). The wind tunnel was an open circuit suction type with a nozzle having a length of 0.9m and an area reduction factor of 1/9. It is covered by a screen which works as a protective system. The maximum flow velocity was 36 m/s and the turbulent intensity of the free stream at the working section was 0.35%.

The test section channel was a straight duct made of 1 Cm thickness perspex and has a cross section of 30 cm by 30cm and is 2 m in length.

The maximum flow rate used was $3.24 \text{ m}^3/\text{s}$. The flow rate was controlled by double butter fly valve, and was generated from a fan driven by a 5.6 Kw, 3 phase motor which rotates at 2900 rpm.

4.3 The Test Model :

The test model used in this experiment was a circular cylinder of a 21.5 mm in diameter. It is an aluminum tube which has a wall thickness of 1 mm and length of 440 mm. As shown in fig. (4.1) the test cylinder was set horizontally in the central plane of the measuring channel. It passed through the slots on the side walls of the measuring section and was supported by two identical plate springs outside the side walls . This setup allowed the displacement of the cylinder only in the vertical direction. In order to eliminate the influence of the flow through the slots blocking plates were attached to the cylinder at both ends. These end plates should be employed to ensure that the flow conditions associated with an infinitely long, or 'two-dimensional', cylinder occur around models confined within the working section of a wind tunnel. Indeed, this technique which relies upon the isolation of interference effects that arise as a result of the interaction of the tunnel wall boundary layer with the model, has been utilized in numerous studies [89-91]. These results showed that the rectangular plates should have an upstream dimension (distance of leading edge from the cylinder's axis) sufficiently large to isolate the horseshoe vortex generated at the wall-model intersection, but

small enough to avoid substantial boundary layer growth on the plate itself, and tail dimensions adequate to prevent any wake interferences. In this respect a plate of the dimensions shown in fig.(4.2) was recommended as the most appropriate for similar test conditions [89].

Hot - wire props were used to detect the free flow velocity. The acceleration amplitude at one end of the upstream cylinder was measured using an accelerometer since the acceleration amplitude of the both ends were almost the same under all experimental conditions [33]. Vibration acceleration of the cylinder in the vertical direction was monitored simultaneously on the vibration meter and the digitizing oscilloscope as shown in Fig 4.3 .

4.4 Instrumentation :-

4.4.1 Velocity Measurement (Hot Wire Anemometer.) :

When an electrically heated wire is placed in a flowing stream heat will be transferred between the two, depending on a number of factors. These factors are governed by the three dimensionless quantities, the Nusselt (N_u), Reynold (R_e), and Prandtl numbers (P_r).

The heat supplied to the sensor is equal to the heat lost Q and is given by,

$$Q = P = I^2 R \quad (4.1)$$

King [85] obtained the following expression for the heat transfer coefficient.

$$N_u = C + DU^n \quad (4.2)$$

From equations (4.1 and 4.2) it can be shown that :

$$V^2 = A + BU^n \quad (4.3)$$

Where A, B, C, and D, are constants which are determined by calibration. The value of n is usually 0.4-0.5 for $0.1 < Re < 10^5$. The above relation (Fig. 4.4) usually yields straight line when V^2 is plotted against $U^{1/2}$ [87].

A DISA constant-temperature hot wire anemometer with a transverse mechanism, as shown in fig. (4.5), was used in the experiments. It consists of a wheatstone bridge and servo amplifier. The hot wire was connected with a probe type 55P14 by a straight probe support, the overall length of the cable which connected from the hot wire to the constant temperature anemometer was 5m. The output D.C voltage and the RMS voltage were measured using 55D30 D.C voltmeter and the 55D35 RMS voltmeter, respectively.

4.5 Vibration Measurements :

The acceleration amplitude of the vibration in the vertical direction was measured by an accelerometer type (B & K 4370) attached to the left end of the test cylinder as shown in fig. (4.1). The output signal of the accelerometer was simultaneously fed to the vibration meter type (B& K 2511) and a digitizing oscilloscope type (II p 54501 A). A tunable pass band filter (B &K 1021) was connected to the vibration meter to measure the acceleration amplitude at a desired frequency.

From equations (4.1 and 4.2) it can be shown that :

$$V^2 = A + BU^n \quad (4.3)$$

Where A, B, C, and D, are constants which are determined by calibration. The value of n is usually 0.4-0.5 for $0.1 < Re < 10^5$. The above relation (Fig. 4.4) usually yields straight line when V^2 is plotted against $U^{1/2}$ [87].

A DISA constant-temperature hot wire anemometer with a transverse mechanism, as shown in fig. (4.5), was used in the experiments. It consists of a wheatstone bridge and servo amplifier. The hot wire was connected with a probe type 55P14 by a straight probe support, the overall length of the cable which connected from the hot wire to the constant temperature anemometer was 5m. The output D.C voltage and the RMS voltage were measured using 55D30 D.C voltmeter and the 55D35 RMS voltmeter, respectively.

4.5 Vibration Measurements :

The acceleration amplitude of the vibration in the vertical direction was measured by an accelerometer type (B & K 4370) attached to the left end of the test cylinder as shown in fig. (4.1). The output signal of the accelerometer was simultaneously fed to the vibration meter type (B& K 2511) and a digitizing oscilloscope type (H p 54501 A). A tunable pass band filter (B &K 1021) was connected to the vibration meter to measure the acceleration amplitude at a desired frequency.

4.6 Experimental Procedure :

It is to be noted that a detailed description of the experimental setup and procedure adopted in this work is given by [87, 88]. They used these measurements procedure to study flow induced vibration of a single cylinder subjected to a cross flow. The following steps were taken through the course of the experimental work.

1. The hot wire was calibrated as described in [88]. then it was placed in its position which is in the fully developed flow region.
2. The vibration meter was calibrated to ensure that it works properly.
3. The accelerometer was fixed at the left end of the cylinder and connected to the vibration meter.
4. The digitizing oscilloscope was switched on and the parameters which govern its operation are adjusted.
5. The vibration meter was connected to the digitizing oscilloscope and necessary steps were taken to ensure that this connection is done in a suitable way.
6. The tunable pass band filter was connected to the vibration meter when the reading at a desired frequency is recorded, then this filter was removed, using a linear bypass switch, when the time history at certain velocity is required.
7. The fan was switched on and the flow was varied in the range (5-36) m/s. Each time the flow was varied, five minutes were given to

obtain a steady flow condition.

8. The vibration signal was averaged for five readings, monitored on the digitizing oscilloscope.
9. A time-series was chosen and digitized and then taken as a sample to be studied. This was repeated at certain conditions. The digitization (discretization) of these time-series was carried out at a sampling rate that obeys the Nyquist formula, that is, the sampling frequency must be at least double of the Nyquist frequency. Mathematically, this condition is expressed as,

$$\omega_s = \frac{2\pi}{t_s} \geq 2\omega_n \quad (4.4)$$

where ω_s is the sampling frequency, and t_s is the sampling rate. This leads to

$$f_n \leq 0.5 \text{ per time sampling} \quad (4.5)$$

In other words, noting that the natural frequency of the test model is 120 HZ, a time sampling at a rate of 2 ms will be satisfactory to contain all the frequency content of the process. Also this sampling rate leads to a Nyquist frequency of about 500 Hz.

10. Steps 5-6 were repeated and the acceleration amplitude was measured.

From time to time, the hot wire was recalibrated, and the calibration of the vibration meter and the tunable pass filter were tested.

Chapter 5

DISCUSSION OF RESULTS

5.1 Introduction :

In order to see what sort of informations about the dynamic characteristics of the flow-induced vibration can be revealed using wavelet transform and are not obtained using classical methods, such as, correlation functions and power spectrum, the flow velocity was varied gradually in the range of free stream velocities (5-31.4) m/s. The variation of the RMS of the amplitude of the acceleration (\bar{a}) with frequency was measured in the above specified velocity range. Also a number of time series for various conditions were recorded as described in Chapter 4.

In the following sections, the measured frequency distribution will be first discussed. Next the experimental time series are studied in section 5.3. These time series will be analyzed using the two classical techniques which are correlations functions and power spectrum distribution. Finally, the advantages and disadvantages of using the new technique of signal processing, the wavelet transform (WT), in the analysis of the dynamic processes of concern to mechanical engineers, such as, the flow-induced vibration process, are discussed in section 5.6 .

5.2 Frequency Distribution :

The test cylinder was mounted under the condition described in chapter 4 . The natural frequency f_n of that system was determined through a simple impulse test which was found to be $f_n = 120$ Hz.

The measured acceleration (\vec{a}) with frequency shows two resonance hills one at the natural frequency and the second at frequency around three natural frequencies as shown in Figures(5.1 - 5.9). From these figures it can be seen that, in general, the second peak was wider in shape and greater in magnitude than the peak at $f=f_n$. This behaviour is not observed in (Fig. 5.1) which corresponds to $U= 5.00$ and 5.8 m/s, where the two peaks approximately equal. The most accepted explanation here is that the two modes, translation and rotational modes described in Chapter two, which are responsible for the presence of these two peaks are strongly coupled.

Moreover, another reduced peak for all conditions of this work was observed at about $f=1/3f_n$ as seen in Figures(5.1-5.9). It is assumed by Shirakashi[32] that this peak will not appear in the presence of the end plates, but in our experiment, in which the end plants were used, this peak did not vanish completely but it was reduced to a small value. Throughout this experiment the acceleration was observed in the attain a constant value at velocity range of (5-11) m/s in the frequency range (100-120)Hz .

Figure 5.2 shows a decrease of the first peak magnitude, (\vec{a}_{nz}), whereas the second ($\vec{a}_{n\theta}$) still constant at about (0.3 m/sec²).In this case the two

peaks are sharper than these in Figures(5.3-5.9). As in the previous case (Fig. 5.1), the acceleration amplitude remains constant $\bar{a} = 0.07\text{mm/s}^2$ in the frequency range (160-320) Hz.

For a stream velocity (U) of 8.93 m/s (reduced velocity=3.5), the acceleration magnitude increased to about 0.24 mm/s^2 at $f=f_n$. In this case, acceleration amplitude in the frequency range (160-320) no longer remains constant and begins to show rapid fluctuations with increasing velocity. The lock-on region starts at this value $U=8.93$. It also observed the \bar{a} has a higher value compared to that obtained in the range (5-11.47)m/s as shown in Fig's (5.1-5.5), i.e, there is a local maxima at this value($U=8.93\text{ m/s}$)

Also, for U greater than 8.93 m/s the second peak was observed to start increasing at a faster rate than the first peak.

From figure 5.4, one can see that the value of \bar{a} decreases from 0.24 mm/s^2 at $U=10.15\text{ m/s}$ to 0.22 mm/s^2 at 11.47 m/s and at $U=24.9\text{ m/s}$, $\bar{a}= 0.5\text{ mm/s}^2$. An important note here is that a second local maxima in the amplitude acceleration is observed. In this region the rotation mode trends to dominant as can be seen from Figures(5.5-5.9), where the ratio of $\left(\frac{\bar{a}_{n\ell}}{\bar{a}_{nz}} = 1.5\right)$ at $(U=11.47 - U=10)\text{ m/s}$. This ratio increases to about $\left(\frac{\bar{a}_{n\ell}}{\bar{a}_{nz}} = 1.5\right)$ at $U=17.89\text{ m/s}$, see Fig. (5.6).

In the Fluid-elastic region, the acceleration decreases to about $\bar{a} = 0.3\text{mm/s}^2$, then increases to about $\bar{a} = 0.55\text{mm/s}^2$ at $U=28.70\text{ m/s}$, after that it continues to increase, such that, at $U= 31.4\text{ m/s}$ $\bar{a} = 0.6\text{mm/s}^2$

The large variations in \bar{a} at $f = 3f_n$ is a characteristic feature of the Fluid-elastic region, where as shown in Fig.5.9 a successive peaks appear

at (260-300) Hz with large values of \vec{a} , for example, $\vec{a} = 4.0\text{mm/s}^2$ at $U=31.41$ m/s when $f=320$ Hz and $f=340$ Hz.

5.3 Time Series :

As mentioned in chapter (4), the sampling rate were chosen to be 2 ms and according to this criteria, different time-series were taken at different situations as described below.

The first time-series was taken at free velocity ($U= 28.794$) and the measurements of vibration acceleration \vec{a} were taken. Figure (5.10) shows this time series and the first impression about this signal is that one deals with a random signal. However, the certainty of this claim will be verified by using test techniques of randomness in the next section. Another time series (Figure 5.11) for about 0.04 sec is taken at the same velocity after five minutes period to study similarity between these two signals. However, these two signals show a big differences in shape and magnitude.

Figure (5.12) shows the third time series which was taken at a free stream velocity of 22 m/sec., i.e., in the lock -on region. The irregular behaviour of this time-series continues to appear. This time-series was filtered at $f = f_n$, i.e., this signal represents the acceleration distribution with the tunable band pass filter was tuned to the cylinder natural frequency f_n . This waveform shows a beating like behaviour of variable strength which may be due to the nonlinearity of the process.

Other two time-series at $U=19.79$ were taken with the same sampling rate but for different periods. The first was taken for about 0.04 sec and

the second for 0.32 sec . These two signals are shown in figures (5.13 and 5.14) respectively. Figure (5.15) shows the sixth time-series. This series represented the waveform of the vibration acceleration \bar{a} at $U=17.9$. The last two signals were taken at a lower sampling rate , i.e, 0.4 ms and 1.5 ms respectively. The first of them was taken at $U= 25$ m/s, while the other at $U=22.9$ m/sec. These two signals are shown in figures (5.16 and 5. 17) .

The above discrete-time signals show a big difference and shape which indicate the random characteristics of this process. The information carried by these signals using the above representations can not be reconstructed or implemented and this necessitates other representations of these signals. This is done in the following sections.

5.4 Correlation Functions Analysis of The Flow Induced Vibration Signals

In studying the flow induced vibration signals, different correlation functions are used in order to examine their roles in identifying the randomness of the process and try to make use of these correlation properties in studying the experimental signals.

The autocorrelation function of the first time-series is shown in figure (5.18). The same feature of fluctuation that was observed for the time-series were also observed for the autocorrelation functions. This ringing without any systematic pattern of the autocorrelation function is an indication of the signal randomness. The trend of the autocorrelation function to the negative values is an indication for the nonstationarity of

the time-series, that is , the negative value of the autocorrelation means that the signal, more likely, varies rapidly and this is the case in autocorrelation representation of the other time series. See figures (5.18 and 5.23).

The autocorrelation functions of two different signals which taken at the same velocity, $U = 28.70$ m/s are shown in figures (5.18 and 5.19). These figures show a big difference in the behaviour of these signals which is another evidence of a nonstationarity behaviour of the signals that resulted from the flow-induced vibration phenomenon.

The third time-series filtered at a particular frequency ($f = f_n$) shows a beating pattern which may indicate a strong nonlinear dynamic behaviour of this process.

The next figures (5.24-5.29) which show the autocovariance of the vibration time signals represent another evidence of the nonstationarity of these signals. According to the criteria represented in chapter 3 the autocovariance values are to decrease rapidly with increasing time. If this is violated at one point the process is no longer a stationary one. For most of the studied signals a rapidly increasing values of \bar{a} were obtained which indicate not only the nonstationarity of the process, but also the possibility of the chaotic motion especially in the lock-on region. This can be seen by comparing figures (5.24 and 5.27) from one side and figures (5.28 and 5.29) from the other.

Moreover, studying the flow-induced vibration process through the crosscorrelation and crosscovariance function is examined using figures (5.30-5.34). These figures show clearly the uncorrelated relationship be-

tween two different signals taken at the same velocity at different periods.

Although these techniques give an answer about the stationarity of the flow-induced vibration and may check the presence of chaotic motion, they do not give suitable informations about the energy distribution of the system or on how to control this rapidly varying process which limits the validity of such techniques in studying the nonstationary processes and necessitates other signal processing techniques. In the next section, the power spectrum representation of these signals will be presented and discussed. Each of these two techniques, correlation methods and power spectrum, study a certain signal in different space, the first in time domain while the other in frequency domain, i.e., they are of a complementary nature.

5.5 Power Spectrum

As pointed out earlier in chapter 3, the power spectrum of a signal measures the average rates of fluctuation of the signal. Also it represents the distribution of power with respect to frequency.

Figure(5.34) shows the power spectral density of the first time-series shown in figure (5.10). The power spectrum in this figure was calculated using the fast Fourier transform algorithm of the autocorrelation functions. This power spectrum is seen to be a rather irregular function of frequency. This irregularity is also apparent in the next figures (5.34 and 5.41) which are the power spectrum representation of the other flow-induced vibration time-series shown in figures (5.10-5.17) respectively. From these figures the following remarks may be observed regarding the

flow-induced vibration process considered :

1. In some of these figures, two maximum peaks are shown, one at $f=f_n$ and the other at around $f=3f_n$. These peaks, however, do not show the clear distinguished shape as they appear in the measured frequency distribution shown in figures (5.1-5.9).
2. The power spectrum representations are easier to interpret physically than the representation of the correlation functions or the original time signal and this is one of its advantages.
3. The power spectrum corresponding to different flow velocities as well as that for the same velocity and different instants was observed to vary for different time signals, i.e, for each flow velocity one obtains a different power spectrum. This indicates the nonstationarity of the signal.
4. The continuity and broadness of the power spectrum representations and the rapid fluctuations are indications that the flow induced vibration process as occurs in Figures 5.39 and 5.40 is possibly chaotic under these conditions.
5. Some figures, such as 5.31 shows a rather an unexpected representation of the signal which may be the result of experimental error or sampling representations.
6. The variations of power spectrum from positive values, in dB, in some figures (5.33-5.36) to negative values, in dB, in others (5.37,5.38)

ensure that this technique is not suitable for the representation of the nonstationary signals.

7. As it is well known, the power spectrum representation can not give a suitable information about the acceleration distribution in the time domain since it is a function of frequency only. This is one of the disadvantages of this representation.
8. The rapid variation of the power spectrum representation makes the control of this process in frequency domain highly difficult, this is due to rapid fluctuations of the power spectrum. This is another motivation for using other more efficient techniques such as the wavelet transform which will be used in the next section to study the flow-induced vibration signals.

5.6 Wavelet Transform Analysis of the Flow-Induced Vibration Process:

Wavelet transform, WT, is a technique for decomposing a signal into components that have good localization both in time and frequency. Because of these time and frequency localization properties, WT can provide local information on a signal that can not be obtained using the previously discussed traditional techniques. In this study, various types of wavelets were used to analyze the flow-induced vibration signal, namely, Mallat , Daubichies, Meyer, Eighth derivative of Gaussian, Mexican hat, One cycle of sine, and Modulated Gaussian. These wavelets are compared and the most suitable one for the representation of the flow induced vibration signal is selected. The time-scale version of the wavelet transform was chosen for the reasons mentioned in Chapter 3.

The time-scale version used here replaced the time series or frequency distribution with a scale parameter related to time and frequency but not equal to them. The frequency scale obeys the Nyquist frequency i.e. $1 < a^m < f_s$, where $2f_s T \leq 1$ and the value at the frequency scale is related to the frequency by:

$$a^m = \sqrt{\frac{f_0}{f}} \quad (5.1)$$

where f_0 is an arbitrary value that related to the distribution of the wavelet itself and called the central frequency.

The wavelet transform representation of the flow-induced vibration signals are shown in Figures (5.42-5.03). The following remarks can be observed from these figures.

1. Processing the measured frequency distribution, at $U = 5.0$ m/s, as the first signal by the different types of wavelets show the following

:

(a) The Mallat wavelet, which is usually used in the image coding in computer vision, does not give a suitable representation of this signal. In the frequency range (40-800) Hz, in which the flow-induced vibration signal, under our experimental conditions, is active, the wavelet transform, using Mallat wavelet, behaves as a high pass filter, i.e, the signal, is filtered here as a noise and is not processed, see Fig. (5.42). This behaviour is due to the fact that, in image coding, one often deals with high range of frequencies while the present flow-induced vibration process is, basically, a low frequency process.

(b) The Daubichies' tight frame wavelet shows a good representation of the analyzed signal, Fig. (5.43). The signal was filtered efficiently and the overall scene of the signal was very clear. However, in using this wavelet a finer scale is needed in order to have a more satisfactory representation.

(c) The Meyer's wavelet, which is a special type of Daubichies' tight frame wavelet, did not detect the signal at the scale used in this investigation. The efficient usage of this wavelet requires a large computer storage capability which was not available in the present work; for example, the grid used in the presentation was relatively high ($m=1$), for a finer resolution a grid of logarithmic scale (say

0.1) should be used which requires increasing the storage memory needed by a factor of 1000.

(d) The results of last four wavelets; Mexican hat, One cycle of sine, Eighth derivative of Gaussian, and Modulated Gaussian, as shown in Figures (5.44-5.47) show a good representations of the flow-induced vibration signal. They act like band pass filters that is, the irregularities in these signals were attenuated then these signals were properly distributed over the time and the frequency. However, the modulated Gaussian wavelet is considered to be the more reliable one for processing the flow-induced vibration signals as it has a low centered frequency ($f_0 = 5.3$) with relatively small band width. This enable this wavelet to detect then analyze these signals properly. Also the modulated Gaussian can be computed efficiently as it does not require large computer memory in comparison to Daubechies's and Meyer's wavelets.

2. Wavelet transform, considered as time-frequency analyses method, enables one to see the signal in both time and frequency domains as can be seen in Figures (5.42-5.63). For example, the WT describes the flow-induced vibration signals as temporal multiresolution decomposition as shown by the time-scale; that is, at a fixed resolution of frequency scale the flow-induced vibration signals can be viewed with progress in time. Also, the WT describes the flow-induced vibration signals as a subband frequency decomposition as shown by

0.1) should be used which requires increasing the storage memory needed by a factor of 1000.

(d) The results of last four wavelets; Mexican hat, One cycle of sine, Eighth derivative of Gaussian, and Modulated Gaussian, as shown in Figures (5.44-5.47) show a good representations of the flow-induced vibration signal. They act like band pass filters that is, the irregularities in these signals were attenuated then these signals were properly distributed over the time and the frequency. However, the modulated Gaussian wavelet is considered to be the more reliable one for processing the flow-induced vibration signals as it has a low centered frequency ($f_0 = 5.3$) with relatively small band width. This enable this wavelet to detect then analyze these signals properly. Also the modulated Gaussian can be computed efficiently as it does not require large computer memory in comparison to Daubiechie's and Meyer's wavelets.

2. Wavelet transform, considered as time-frequency analyses method, enables one to see the signal in both time and frequency domains as can be seen in Figures (5.42-5.63). For example, the WT describes the flow-induced vibration signals as temporal multiresolution decomposition as shown by the time-scale; that is, at a fixed resolution of frequency scale the flow-induced vibration signals can be viewed with progress in time. Also, the WT describes the flow-induced vibration signals as a subband frequency decomposition as shown by

the frequency scale; that is, at a fixed resolution of time, i.e., a distinct time instant, the flow-induced vibration signals can be viewed at different subband of frequencies.

3. Most of the significant frequency and time properties of the analyzed signal presented in the above figures can be seen in a coarser view than in the original signal. These figures show clearly the regions of intensive energy distribution, at a frequency scale of (-2) to (-3), the moderate region, (-1.2) to (-2) and (-3) to (-3.2), and low energy region outside these intervals, where (0), (-1.2), (-2), (-3), and (-3.2) frequency scale corresponds to (5), (28), (85), (339), and (448) Hz respectively as estimated from equation (5.1). These results are in full agreement of these obtained from the measured frequency distribution Figures (5.1-5.9). Moreover, according to time-scale, in most of these figures the peak at $f = f_n$ appears firstly, then the combination of this peak and that at $f = 3f_n$ appear after an initial period of time. These results were not observed by using any of aforementioned classical techniques.
4. By comparing Figures (5.18-5.41) which show the flow-induced vibration time series analysis using classical techniques, with those corresponding to the wavelet transform representation of these signals, Figures (5.56-5.63), the wavelet representations of these signal were more simplified than those obtained using classical techniques. Despite this simplicity, the main characteristics of these signals are not ignored but they are, somehow, amplified. For example, WT

representation show clearly the energy distribution at each single point of time instant and frequency band; that is, the zones of energy are clarified, also the dominant peaks are amplified.

5. As shown in Figures (5.47-5.54) the wavelet transform code the signal efficiently in such a way that the data needed to represent the whole signal, in the case of the wavelet transform, is fewer than the original signal. That is, any software realization of the wavelet representations, figures (5.45-5.63), only implement a finite numbers of octaves from (4) to (-4) frequency scale. As the wavelets (filters) used, as a principle, are derived from the "mother wavelet", see section 3.3, one can code the the flow-induced vibration signal at a specific scale, say (-1) frequency scale, and then construct the other representations at other octaves from this specified scale.

6. As it is well known that the most popular approach to identify a non-stationary system, i.e, time-varying system, is to employ an adaptive algorithm and try to track the system's trajectory. Despite the wide use of this approach, it can not handle rapidly varying systems, such as the flow-induced vibration process. If the coefficients change fast enough, compared to the algorithm's convergence time, the adaptive algorithm will not be able to track the system's time evolution.

To overcome this problem, more explicit modeling of the coefficients' evolution is required. One approach is to impose the probabilities structure on the coefficients' trajectories and regard them as stochastic processes. Then, the coefficients are estimated with the

use of Kalman filtering [94].

From a general look to the wavelet representation of the different signals one may consider that the randomness of these signals no longer exists, and this is why WT is used extensively to study non-stationary signals. These properties make the estimation of the system parameters (coefficients) related to the dynamic response of the system much effective in identifying the stability boundaries and then to control the process effectively. This may be done by expanding each time-varying coefficient onto a set of basis sequences. If each coefficient's time-evolution can be well approximated by a combination of a small number of basis sequences, then the identification task is equivalent to the estimation of parameters in this expansion [94].

7. The employment of the multiresolution ideas to address the approximation of the aforementioned time-varying coefficients and propose a wavelet basis for the coefficient expansion will better model the local as well as global characteristics of the system's trajectory, and, hopefully, will provide guidelines in choosing the optimal wavelet basis for the given problem [94]. From the wavelet transform results Fig's [5.47-5.54], there was one major dominant frequency. Hence, by using WT to determine the local dominant frequencies, a more accurate way of estimating the system parameters may results. Also, since the information concerning the frequency content obtained from WT may describe the dynamic behaviour of the sys-

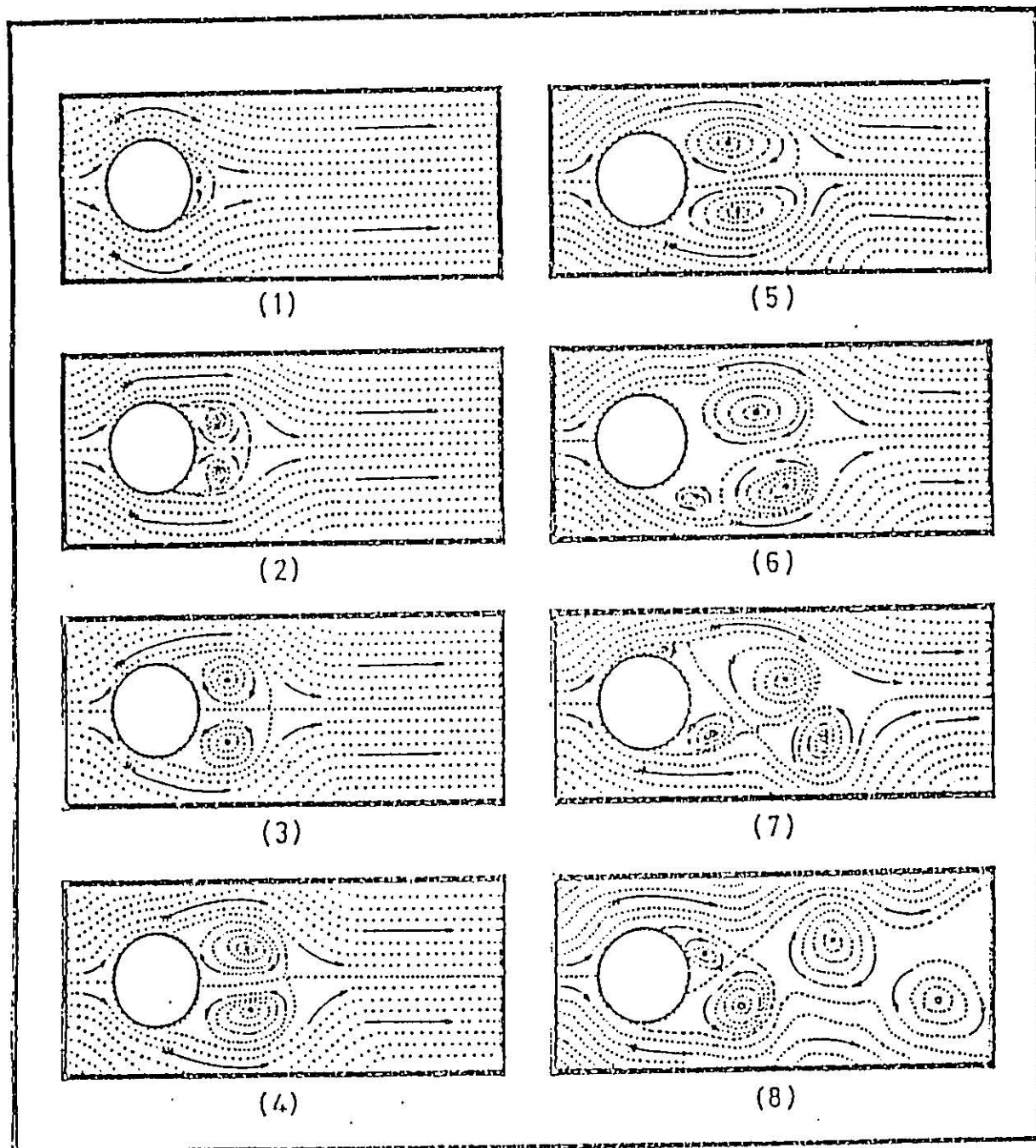


Figure 2.2: Sketch of alternate vortex shedding process behind a circular cylinder A sequence of vents begins at (1) and continues to (8), [30]

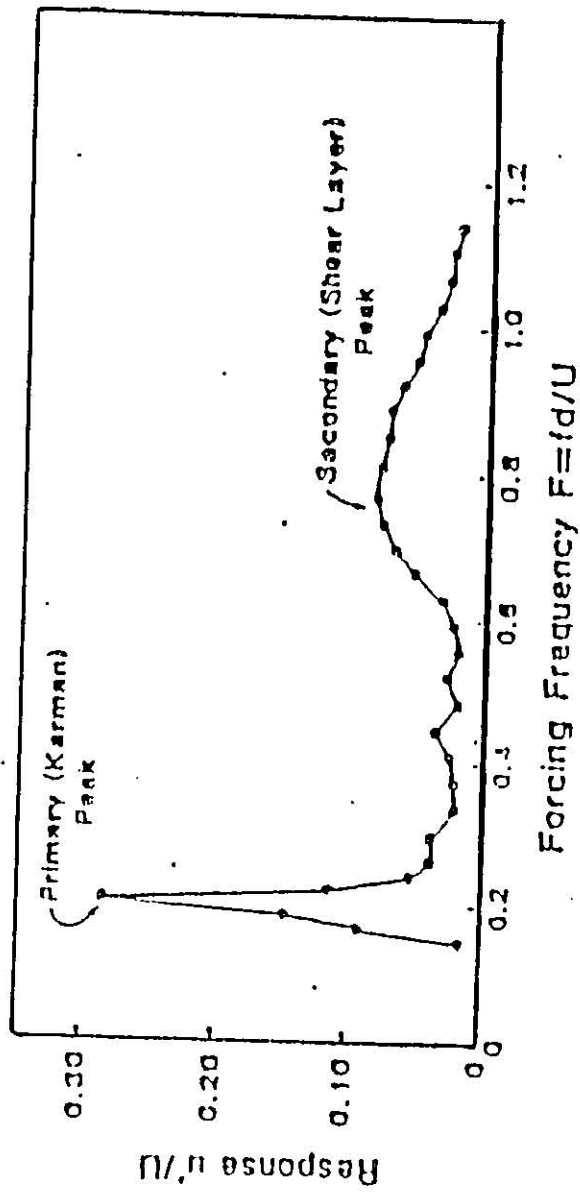


Figure 2.4: A typical frequency response curve showing the normalized velocity response amplitude as a function of the forcing frequency for $Re=920$, the vibration parameter $\omega l=0.14$, and $d=1.27$ cm; [7]

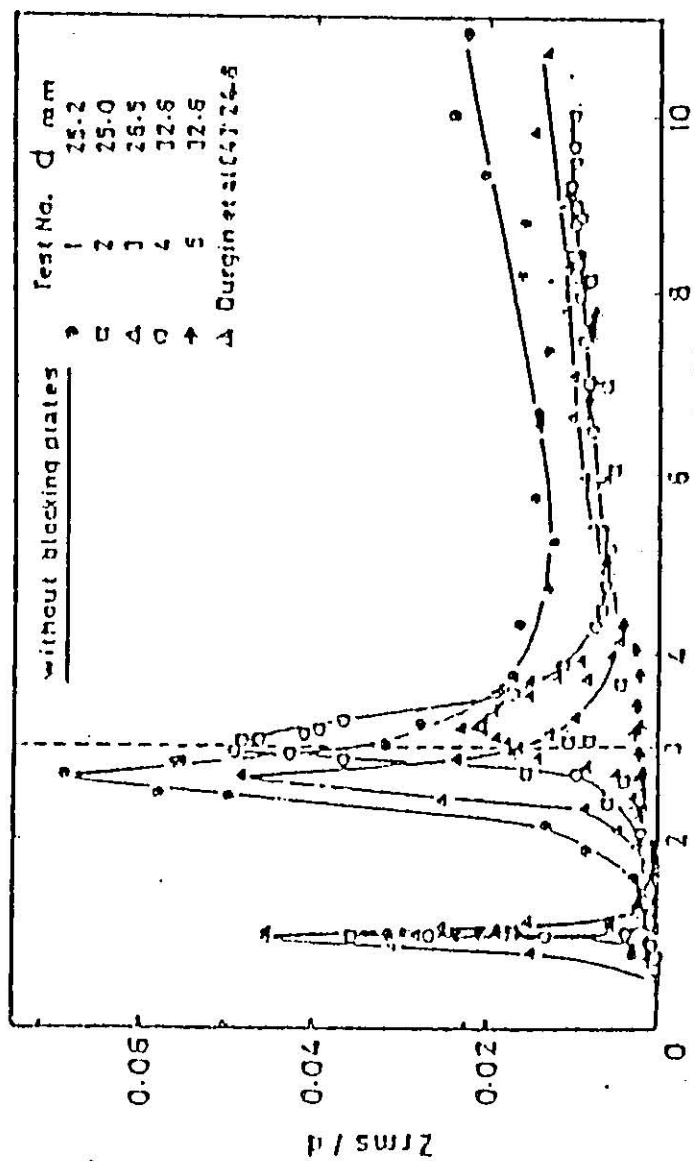


Figure 2.7: Translation-mode oscillation of cylinders without blocking plates [32]

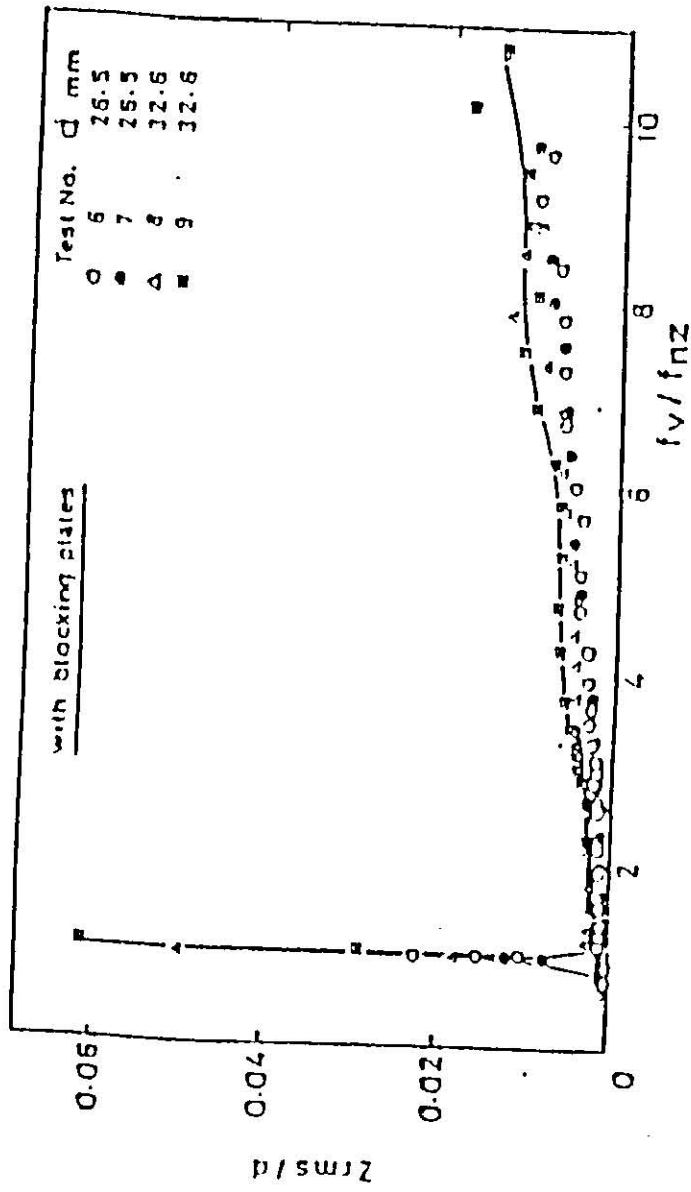


Figure 2.8: Translation-mode oscillation of cylinders with blocking plates [32]

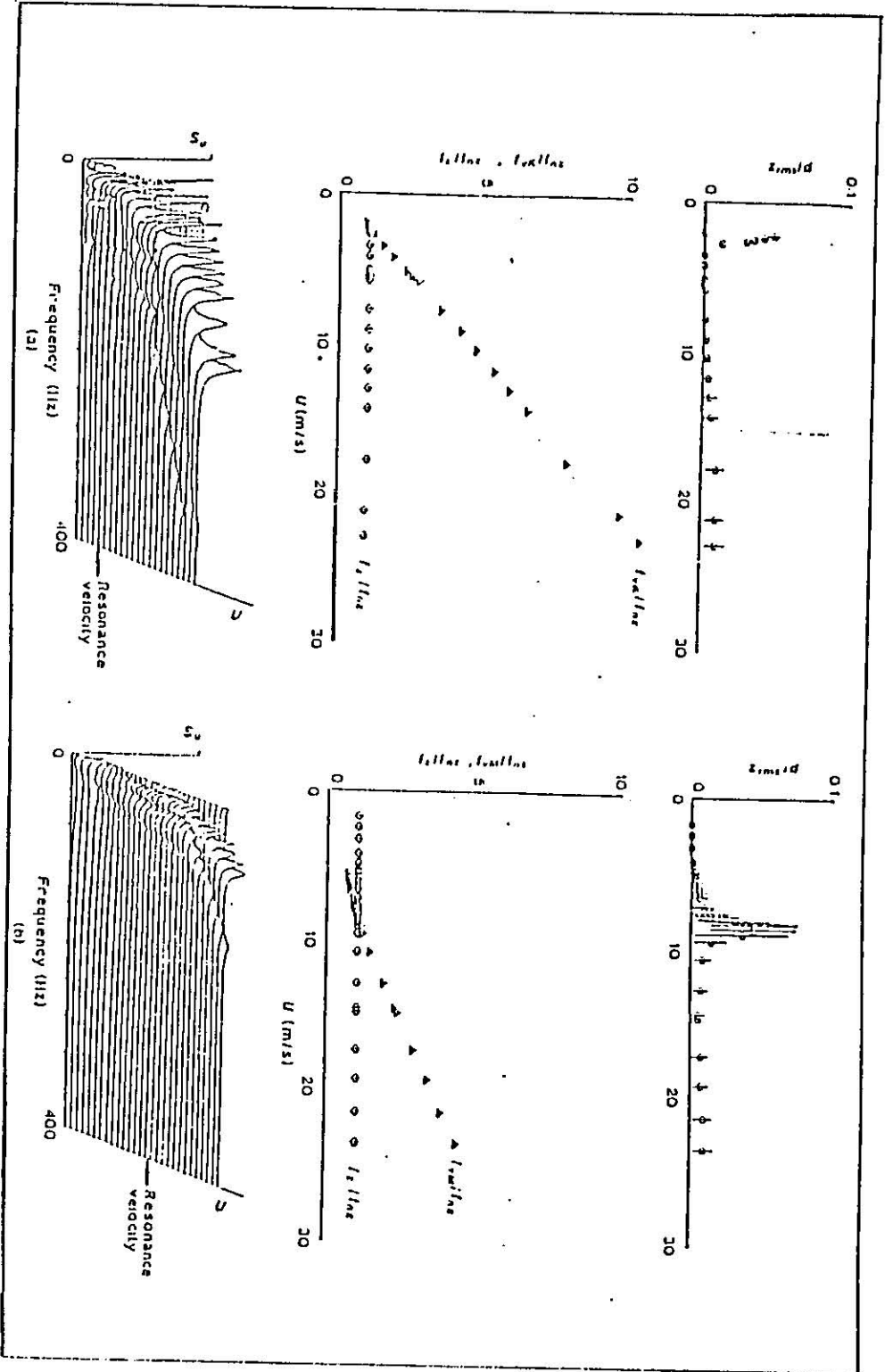


Figure 2.9 : Fluctuating flow velocity spectrum, peak frequency of velocity spectrum and oscillation frequency for single cylinder oscillation as functions of U ; (probe : $x/d = 2$, $y/d = 1.5$, $z/d = 1$) (a) Karmman vortex excitation for $s/d = \infty$ (single cylinder); (b) excitation induced by the downstream cylinder for $s/d = 0.0625$. [33]

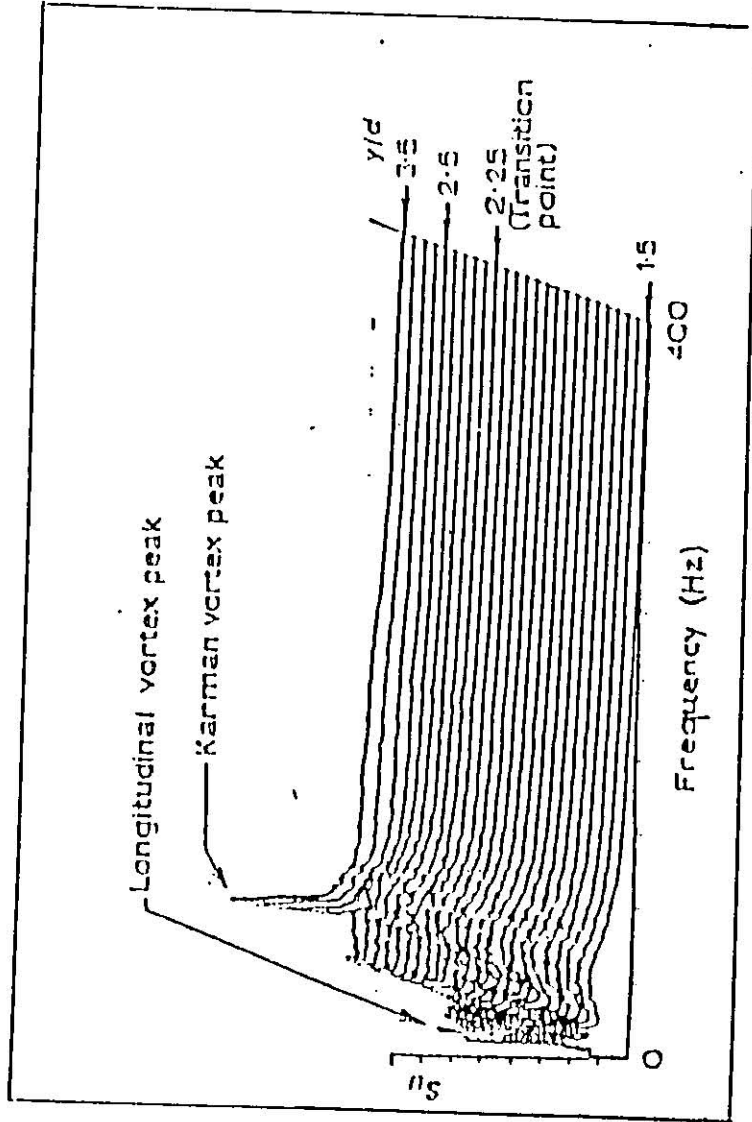


Figure 2.10 : Change of velocity spectrum along the upstream cylinder of the fixed system ($s/d = 0.25$, $U=4.28$ m/s; probe position : $x/d = 2.0$, $y/d = 1.5$ to 3.5 , $z/d = 1.0$) [33]

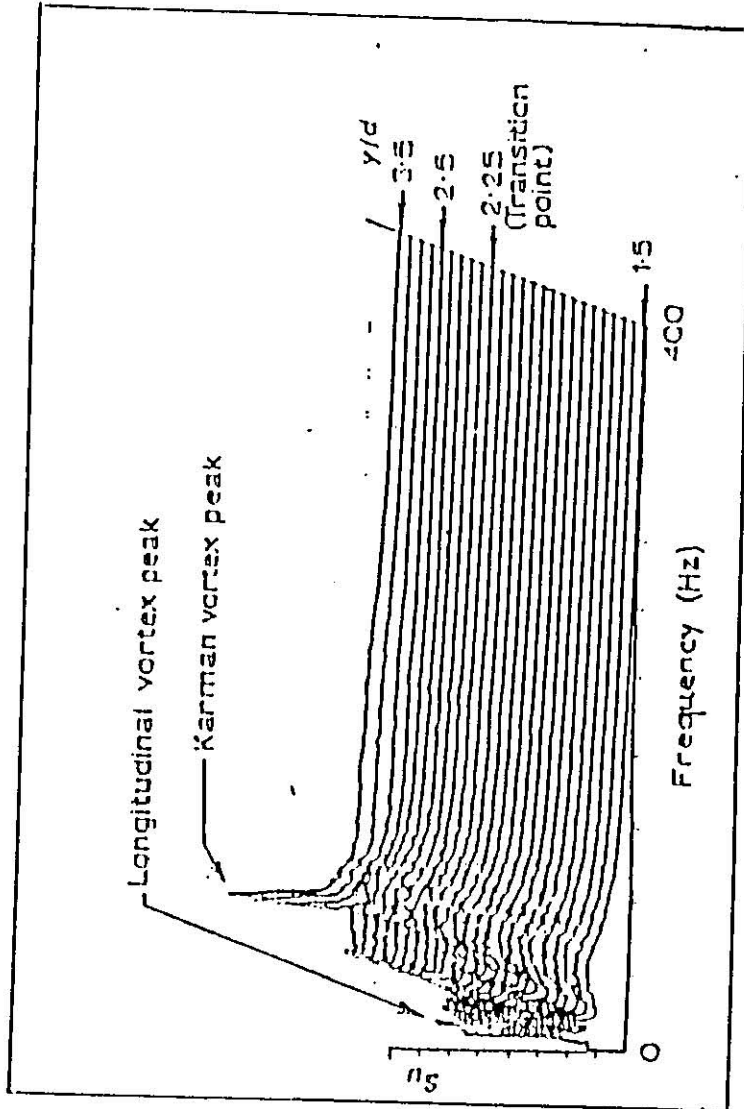
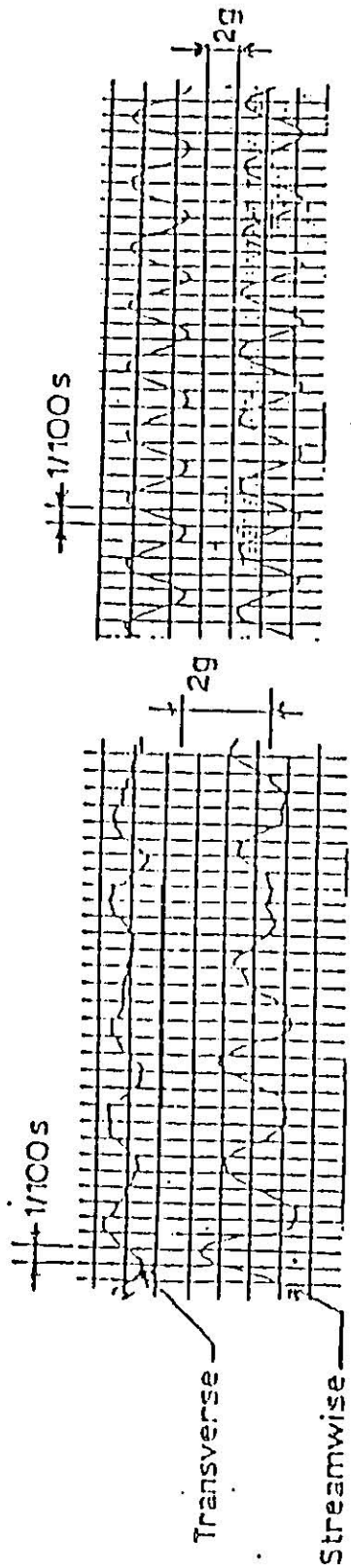
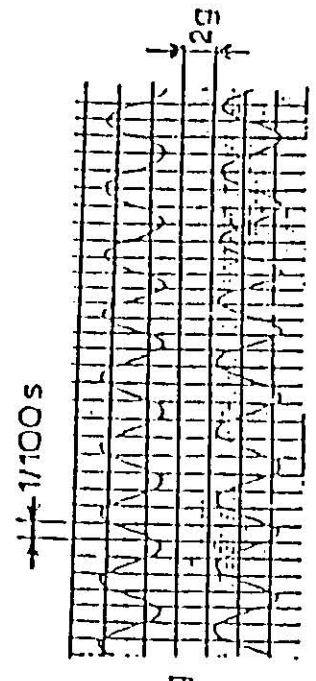


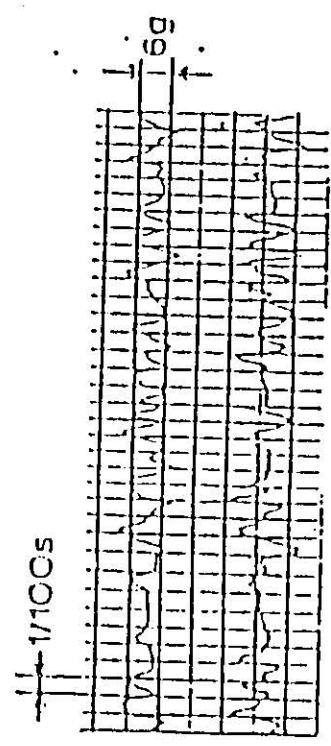
Figure 2.10 : Change of velocity spectrum along the upstream cylinder of the fixed system ($s/d = 0.25$, $U = 4.28$ m/s; probe position : $x/d = 2.0$, $y/d = 1.5$ to 3.5 , $z/d = 1.0$) [33]



(a) $\xi = 0\text{mm}$ (point D); $V_j = 5.8\text{ m/s}$



(b) $\xi = 10.6\text{mm}$ (point E); $V_j = 3.0\text{ m/s}$



(c) $\xi = 10.6\text{mm}$ (point F); $V_j = 8.5\text{ m/s}$

Figure 2.11 : Time history of response of an array of tubes (7 X 6) in water subjected to a gap cross-flow for different locations of the hot wire [34].

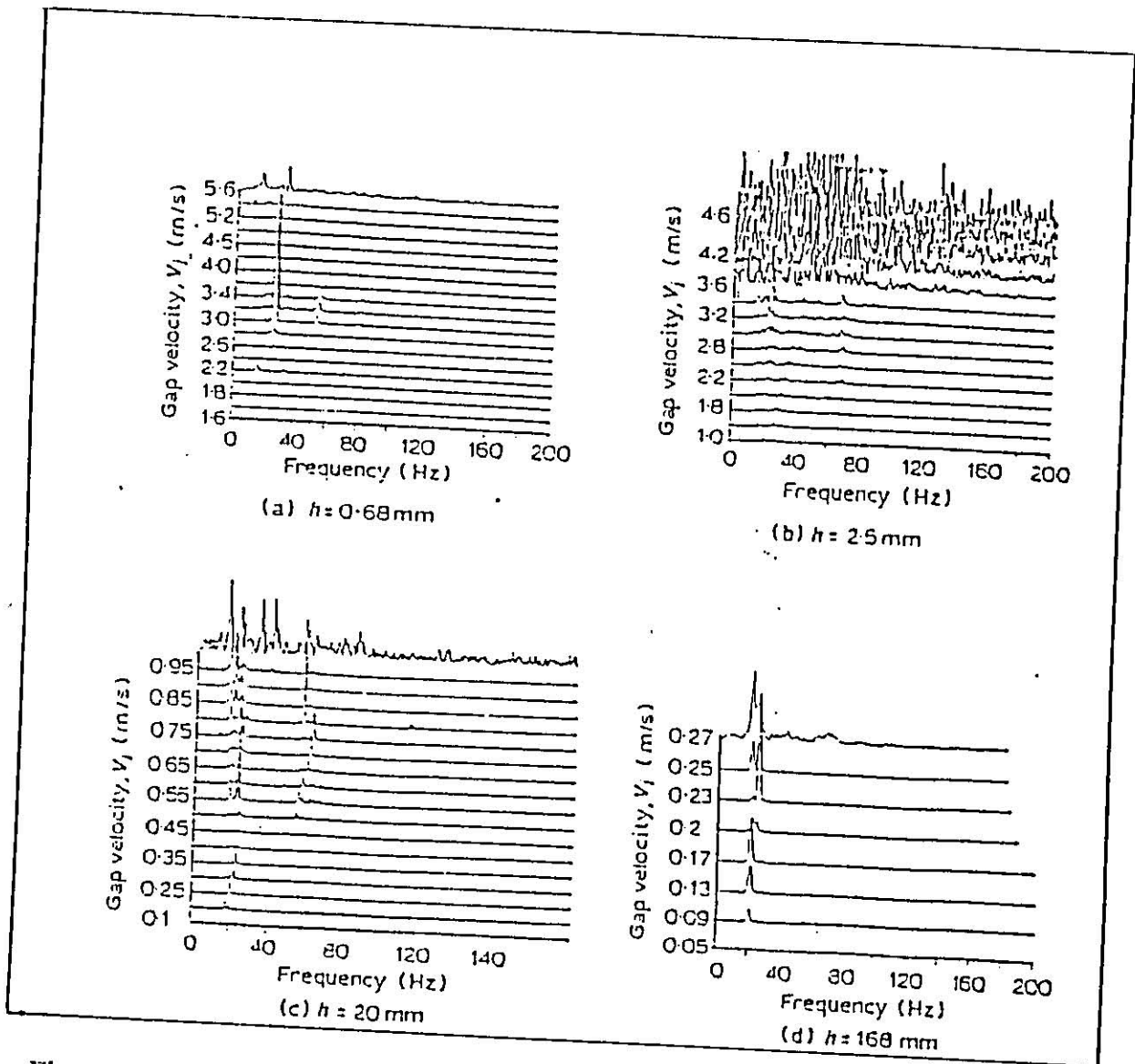


Figure 2.12.: Effect of gap width h on acceleration frequency spectrum of tubes (7x6 tube array), [34]

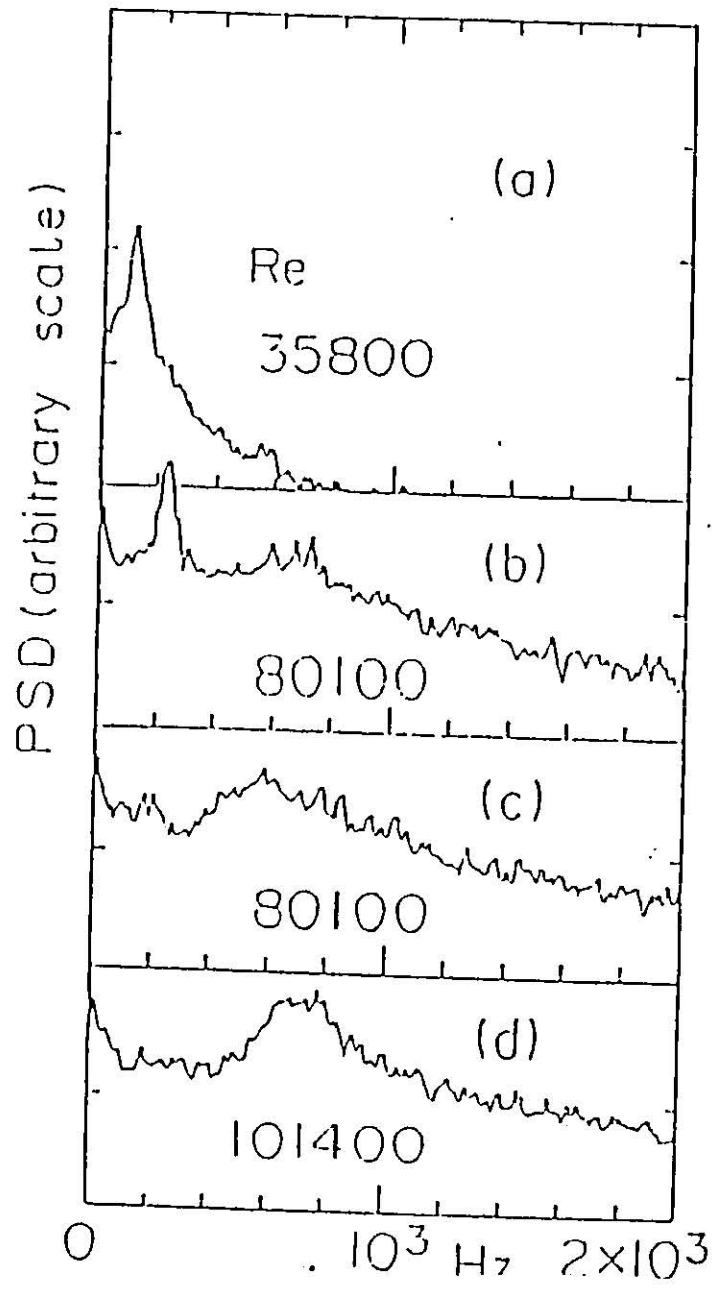


Figure 2.13.: Power spectral density, $\alpha = 15.\text{deg}$ [36]

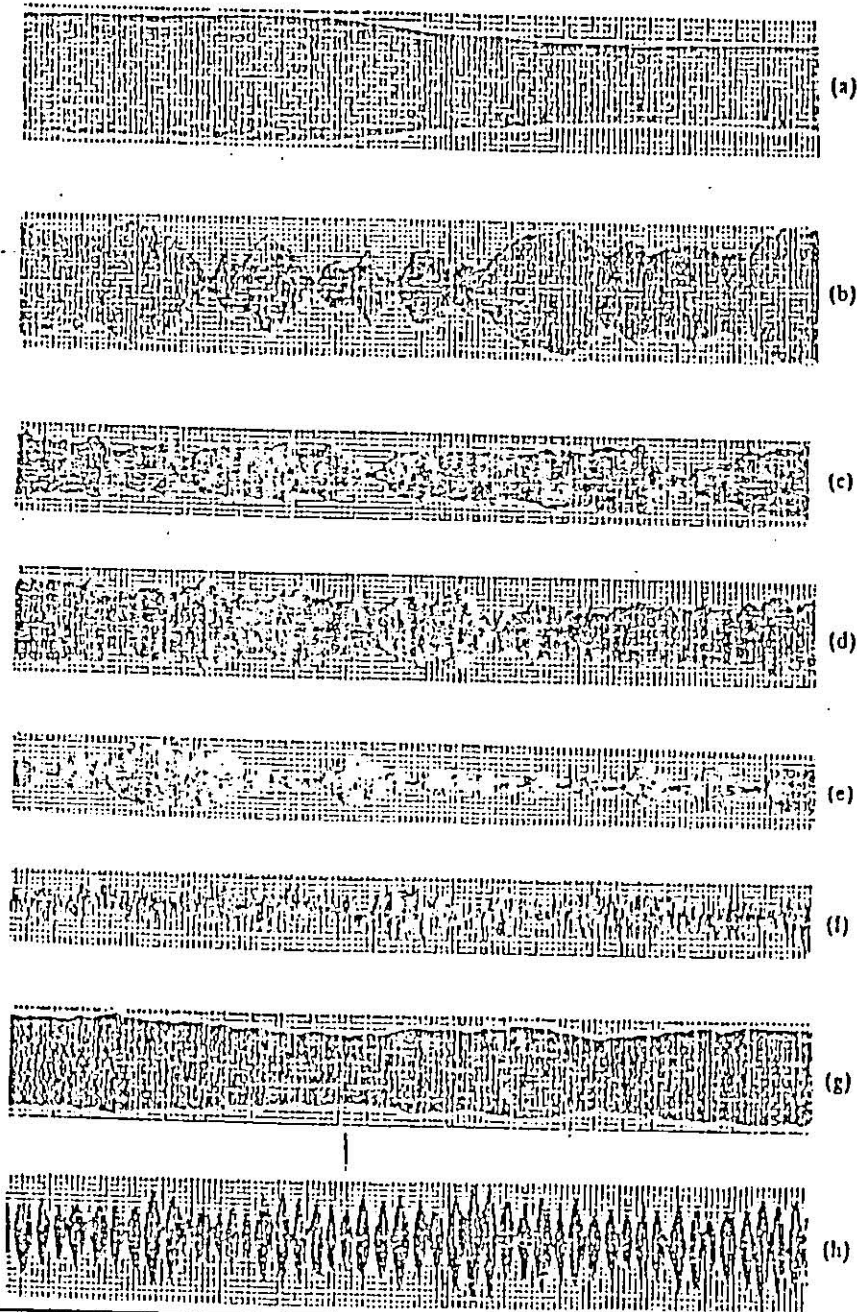


Figure 2.14.: Time history of cylinder displacement (a) Cut-out square, $e/D = 0.214$, $U/ND = 3.55$; (b) plate, $H/D = 50$, $\alpha = 40(\text{degree})$, $U/ND = 5.67$; (c) rectangular cylinder, $H/D = 5$, $\alpha = 40(\text{degree})$, $U/ND = 5.54$; (d) rectangular cylinder, $H/D = 5$, $\alpha = 60(\text{degree})$, $U/ND = 6.08$; (e) rectangular cylinder, $H/D = 5$, $\alpha = 60(\text{degree})$, $U/ND = 3.29$; (f) rectangular cylinder, $H/D = 5$, $\alpha = 60 \text{ degree}$, $U/ND = 8.48$; (g) rectangular cylinder, $H/D = 5$, $\alpha = 30 \text{ degree}$, $U/ND = 5.55$; (h) rectangular cylinder, $H/D = 5$, $\alpha = 30 \text{ degree}$, $U/ND = 5.05$. [38]

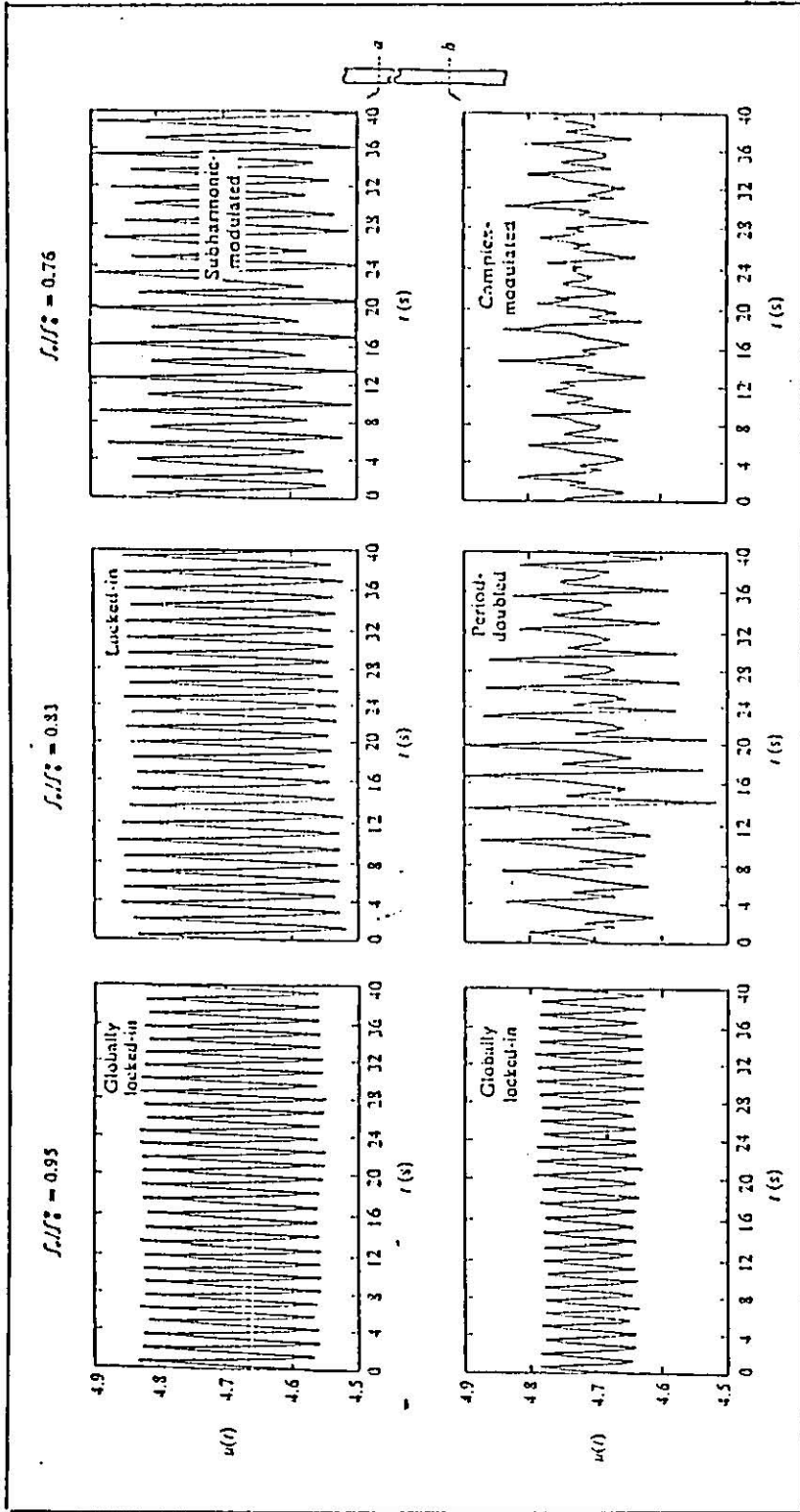


Figure 2.15: Velocity traces taken in near-wake at spanwise locations to off-midplane a and b for basic states of response: (a) global lock-in along entire span of cylinder at $f_c/f_o = 0.95$; (b) localized period-doubling from three-dimensional region of cylinder embedded within locked-in vortex formation at $f_c/f_o = 0.83$, and (c) complex modulation of three-dimensional vortex formation embedded within subharmonic-modulated vortex formation at $f_c/f_o = 0.76$ [39]

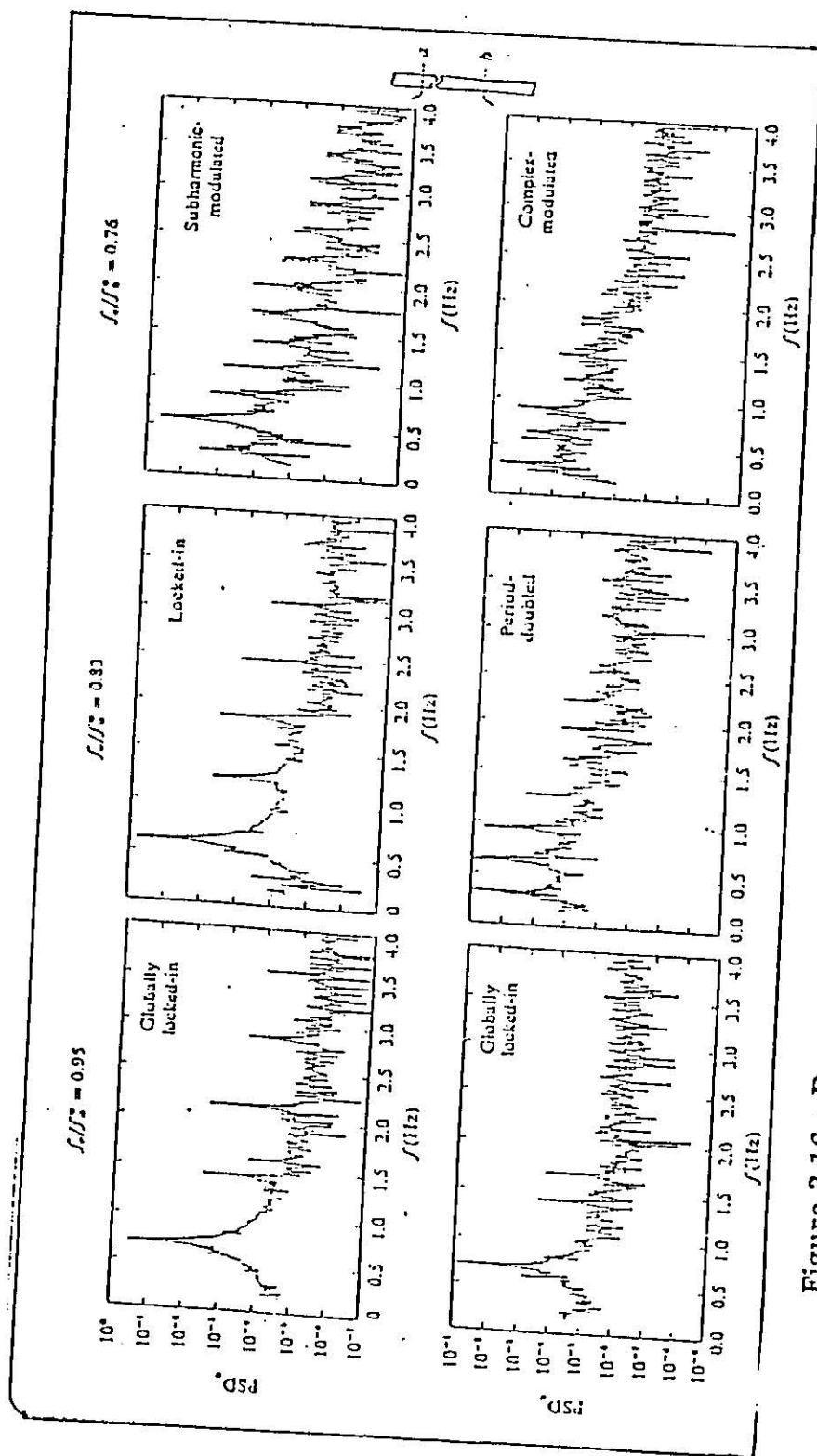


Figure 2.16 : Power spectral density of velocity fluctuation on wake for basic states of response (a) global lock-in along entire span of cylinder at $f_e/f_o = 0.95$; (b) period doubled three-dimensional vortex formation embedded within two-dimensional vortex formation at $f_e/f_o = 0.83$; and (c) complex modulation embedded within subharmonic modulated vortex formation at $f_e/f_o = 0.76$ [39]

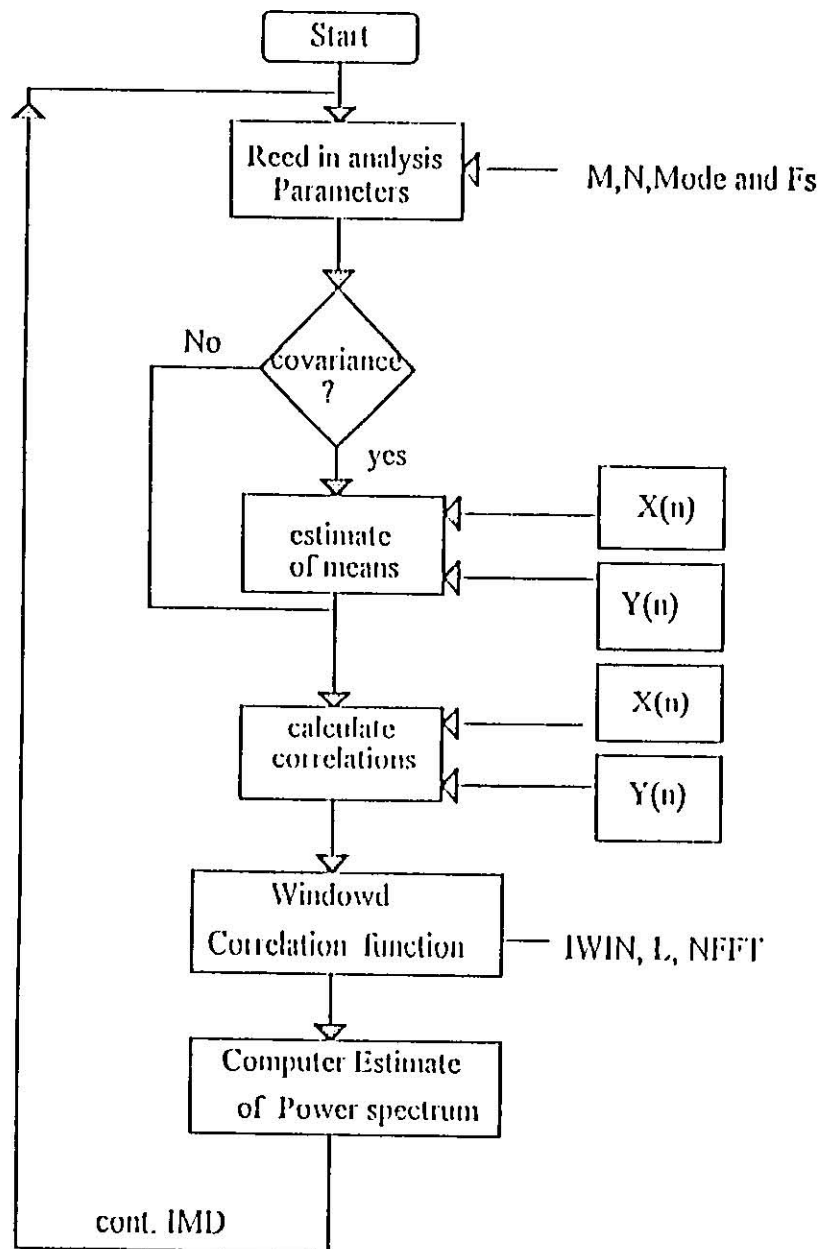


Figure 3.1 : correlation and power spectral density estimations Flow Chart

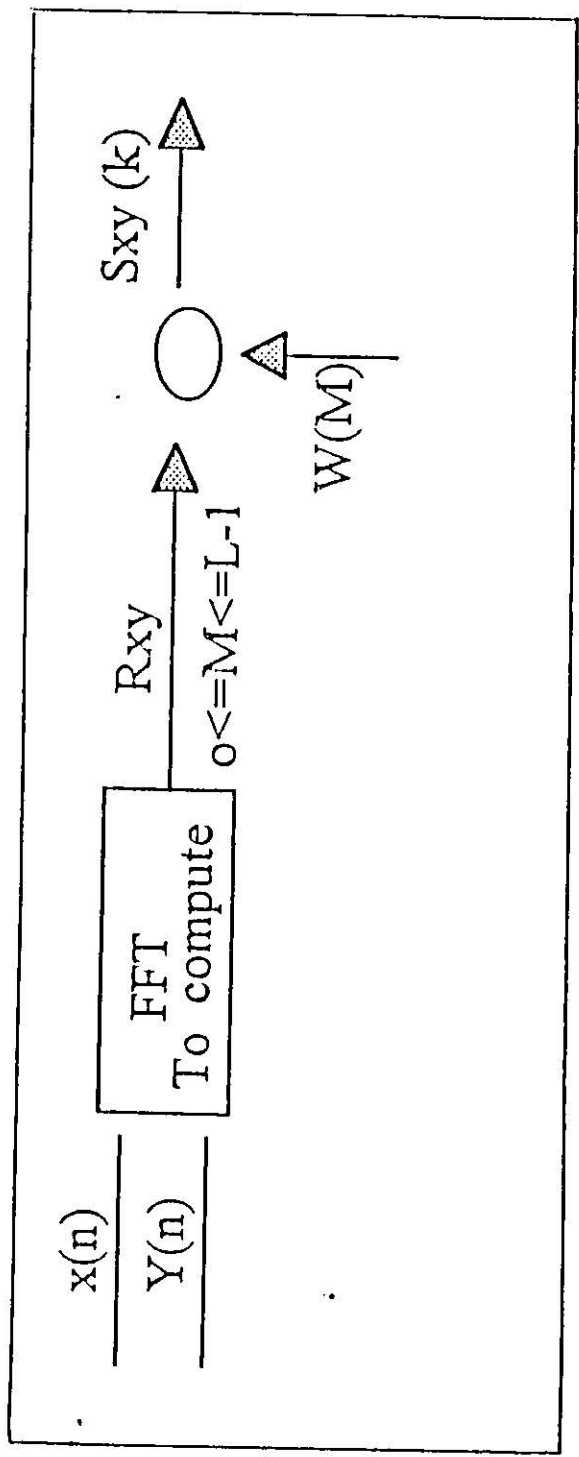


Figure 3.2: Processing the power spectrum

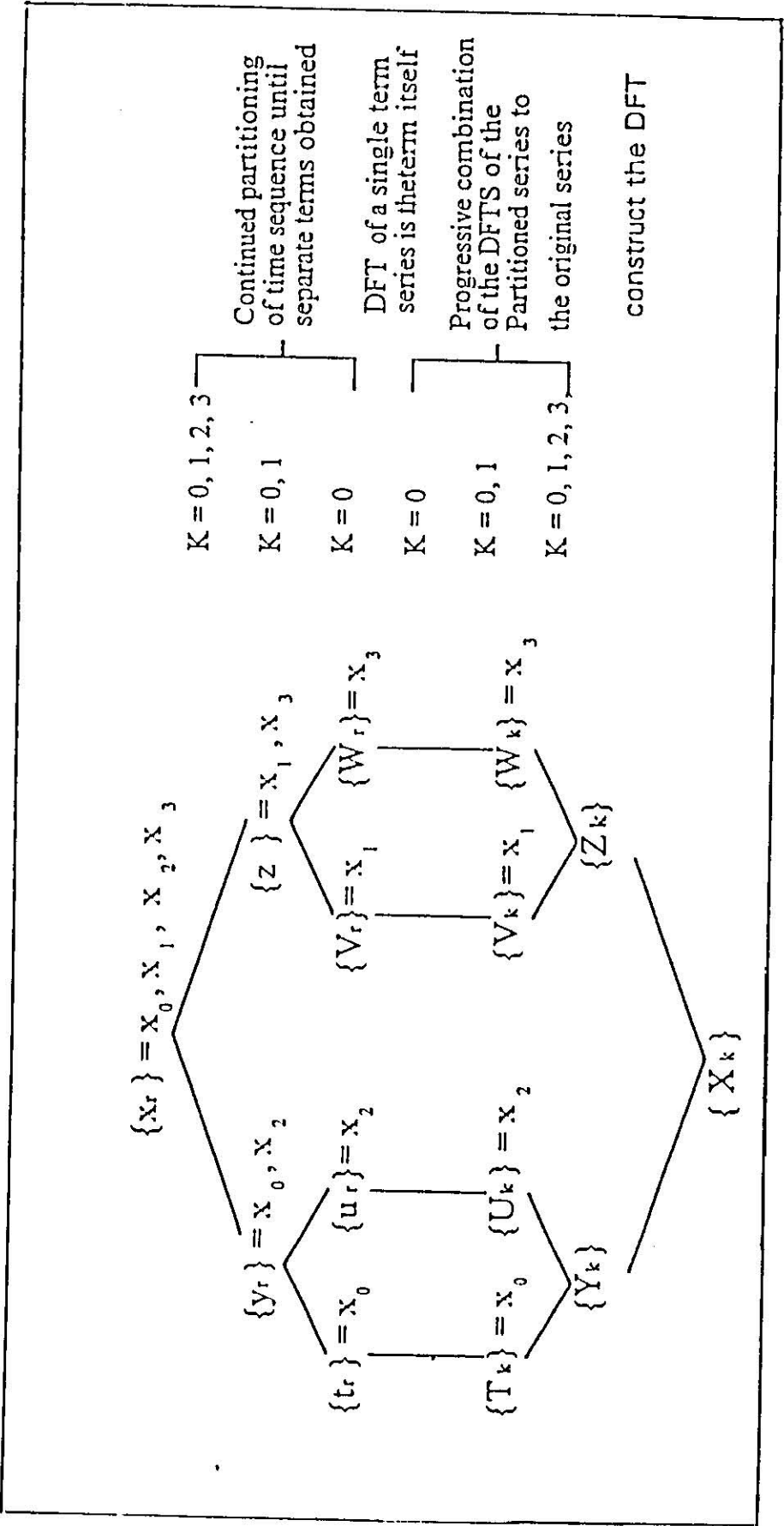
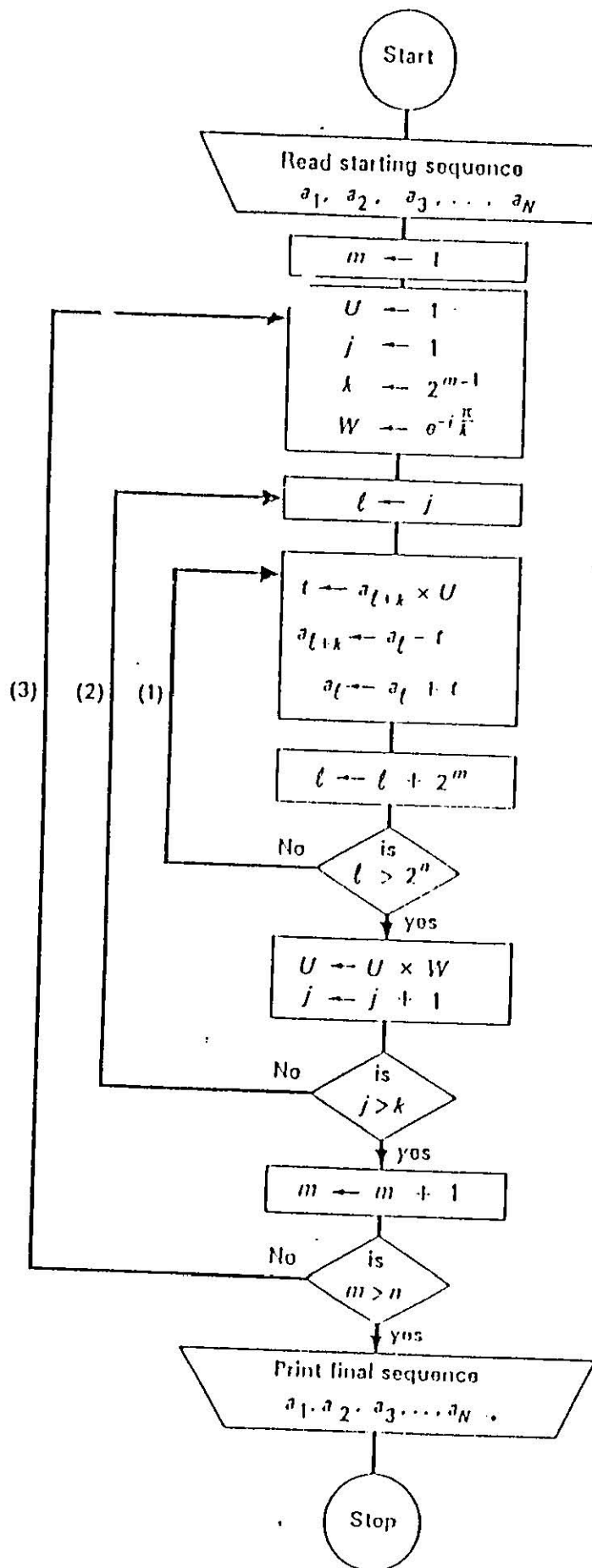


Figure 3.3 : computation of FFT



Notes

Sequence entered in bit-reversed order after dividing each term by N

Sequence length $N = 2^n$
Calculation proceeds in n steps

For step m butterflies are $k = 2^{m-1}$ wide and data is organised in blocks 2^m wide

Loop (1) takes the calculation from block to block on the same butterfly

Loop (2) takes the calculation from one butterfly to the next (in each block)

Loop (3) takes the calculation from one row of butterflies to the next row

Figure 3.4 : FFT Flow Chart

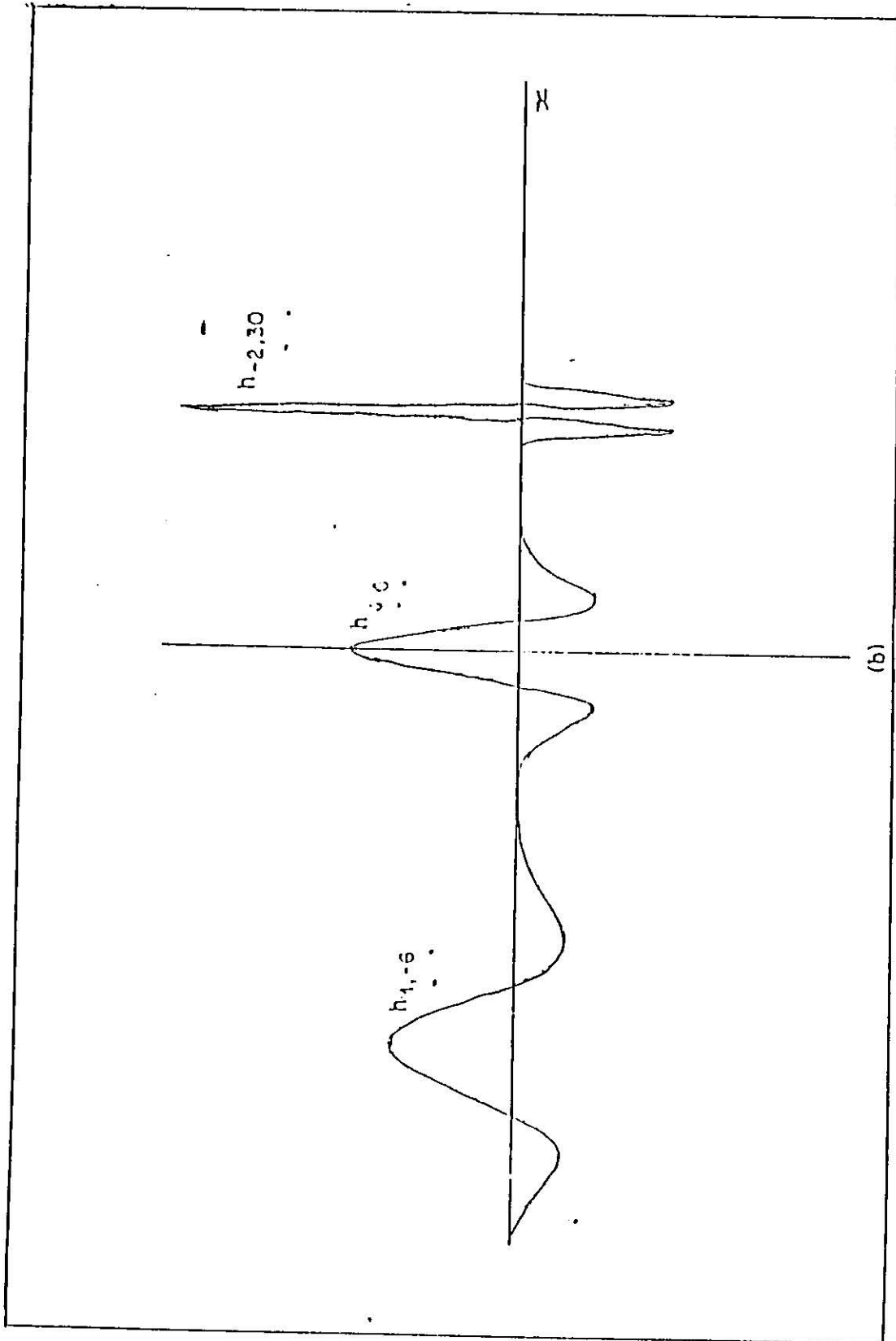


Figure 3.5 : Different views of a wavelet

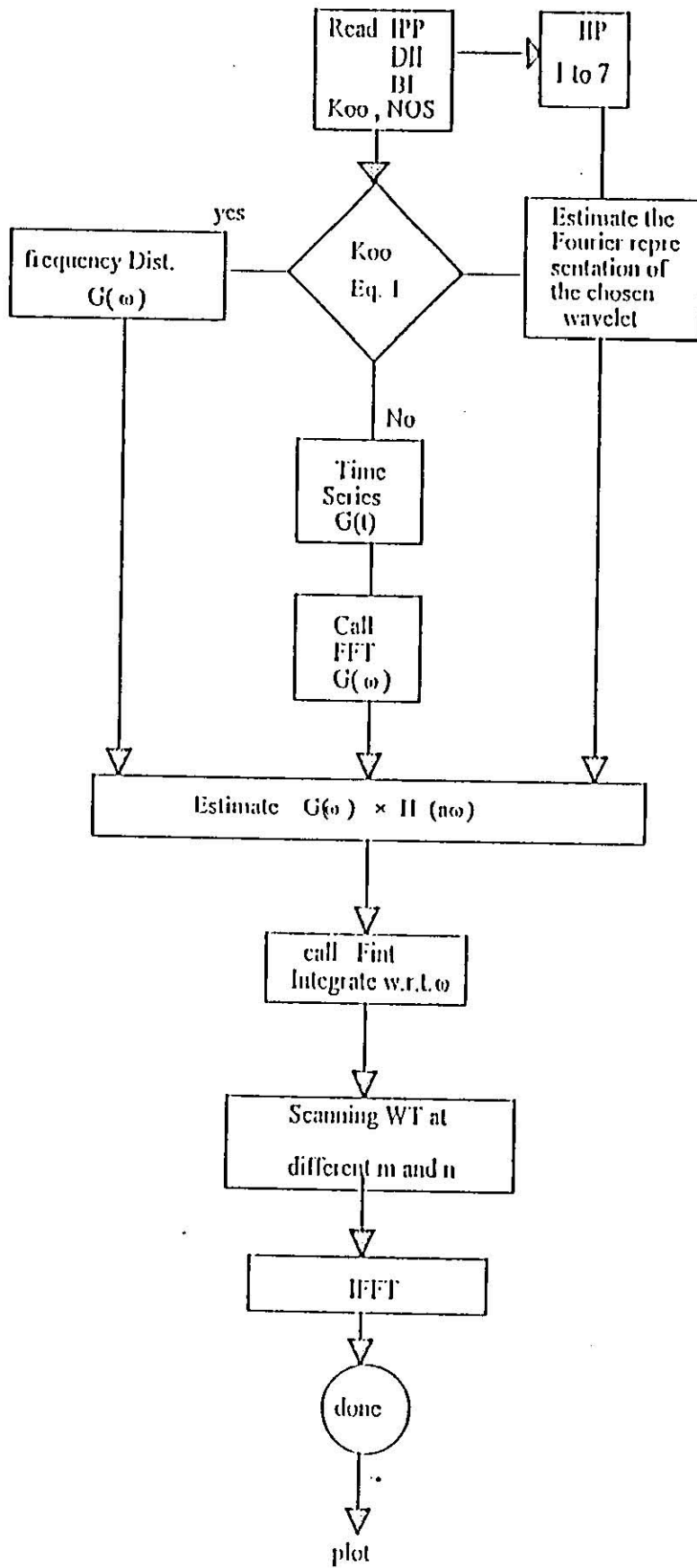


Figure 3.6 : WT Flow Chart

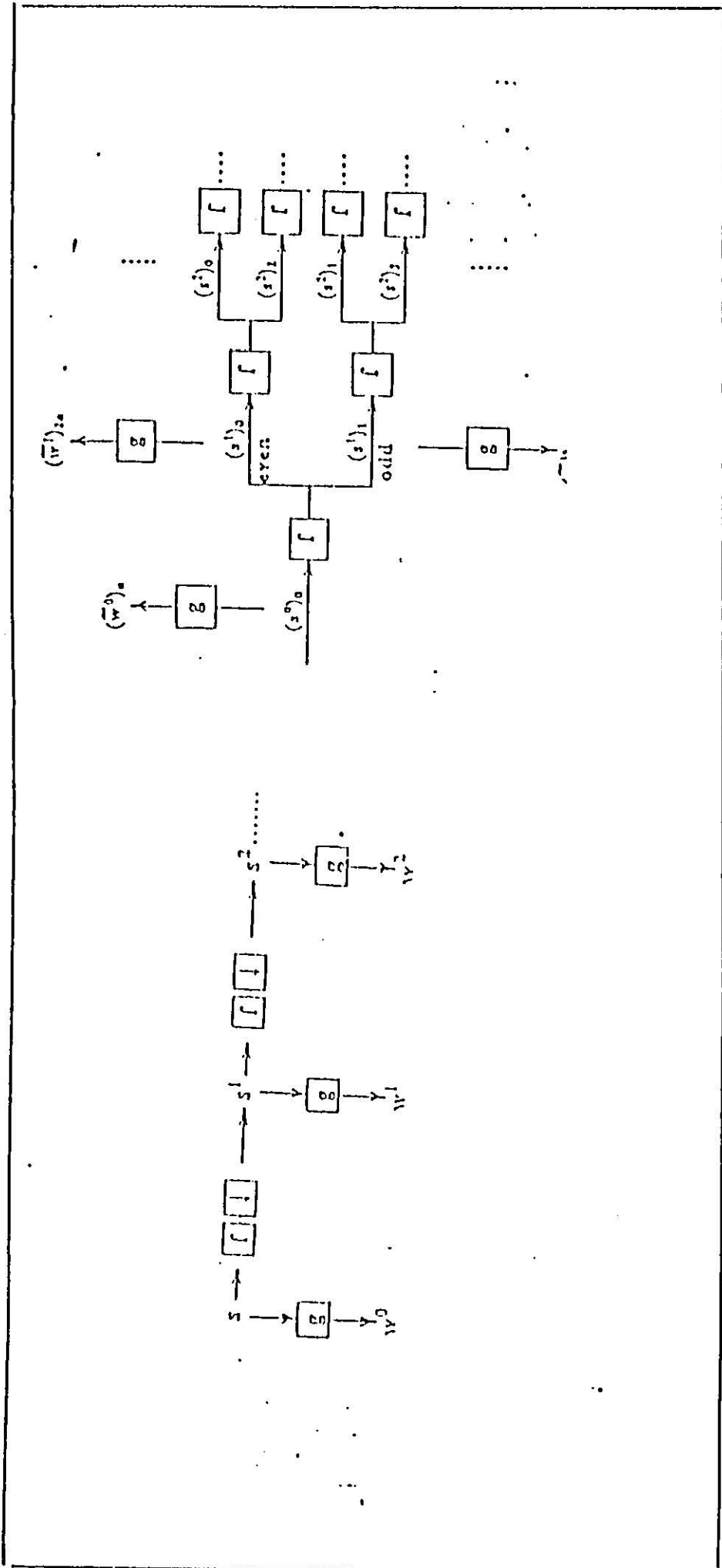


Figure 3.7 (a) : Wavelet filter bank structure The down-arrow decimation The output of the transform is the family of signals w^i , forming the two parameter transform w^j in the scale-time plane Following terminology to be introduced w^i is the (decimated) discrete wavelet transform (b) : Diagram of an implementation of the undecimated DWT [56]

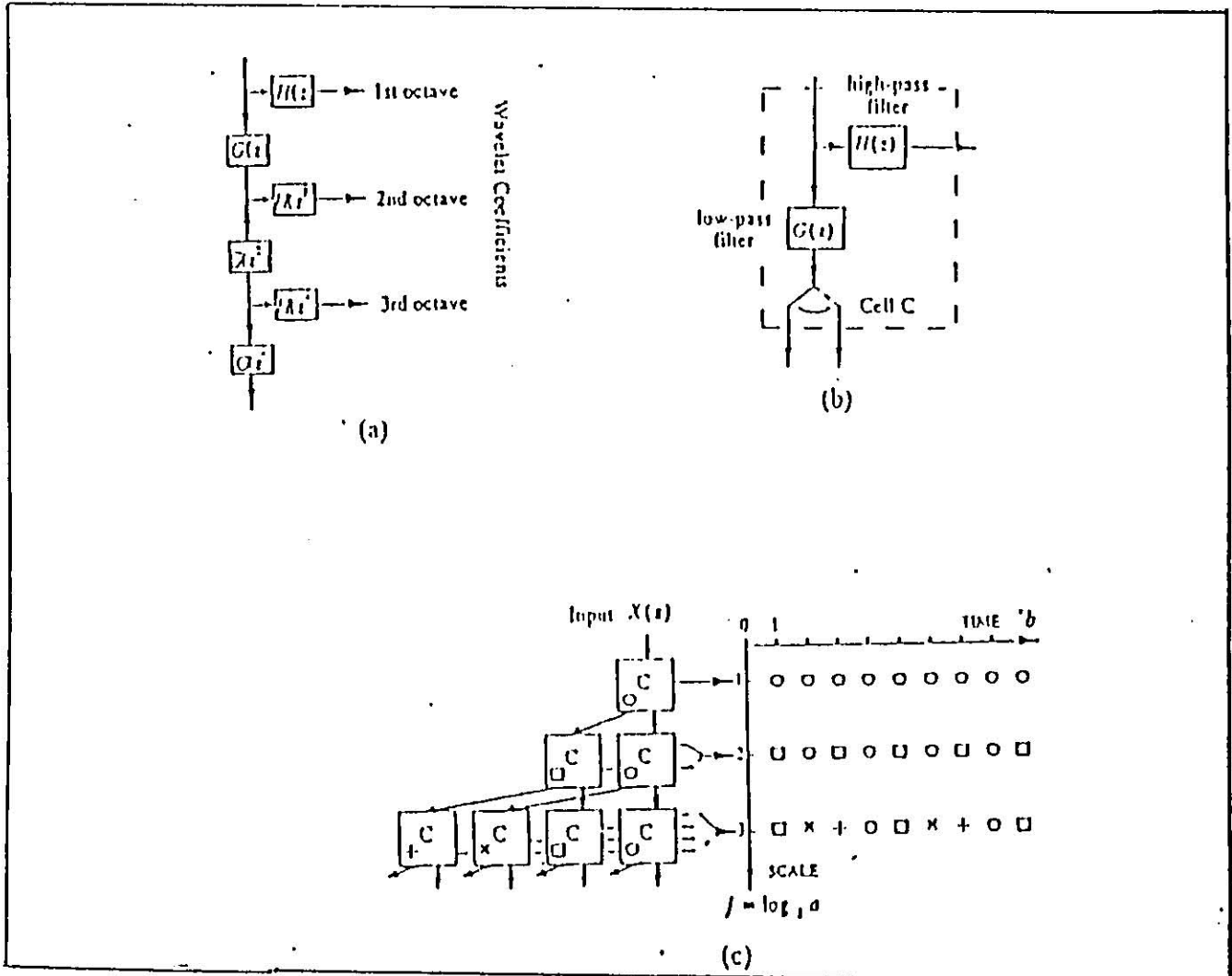


Figure 3.8 : (a) A trous structure as derived by Holshneider et. al [71], (b) Basic computational cell for computing CWT coefficients octave and octave (c) Connection of the cells used in this paper and corresponding location of the wavelet coefficients in the time-scale plane [73]

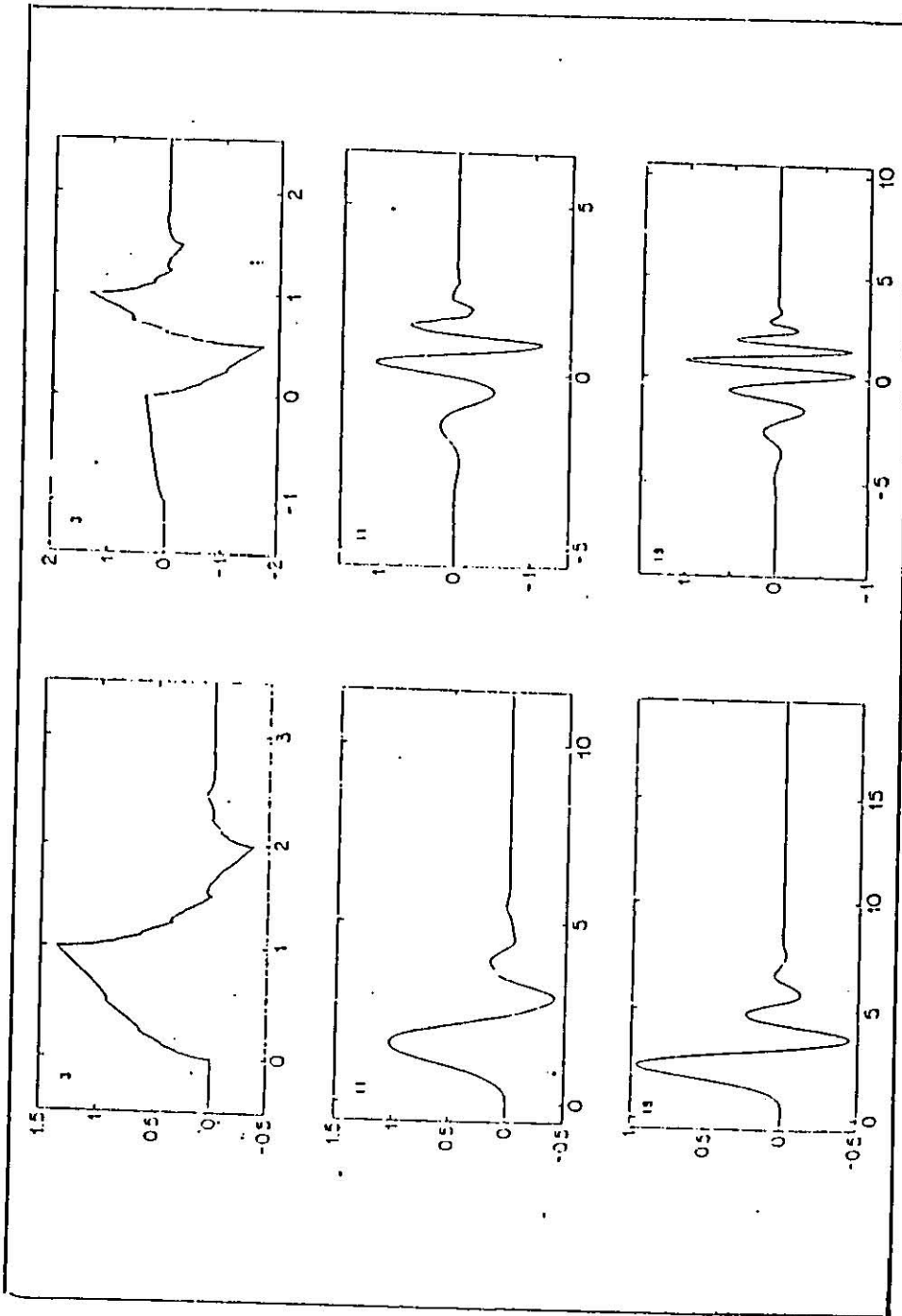


Figure 3.9 : Some examples of orthogonal wavelet bases with compact support constructed in Daubechies [53] The number of nonvanishing moment is, respectively, 4, 12, and 20, corresponding to support widths of, respectively, 3, 11, and 19 [65]

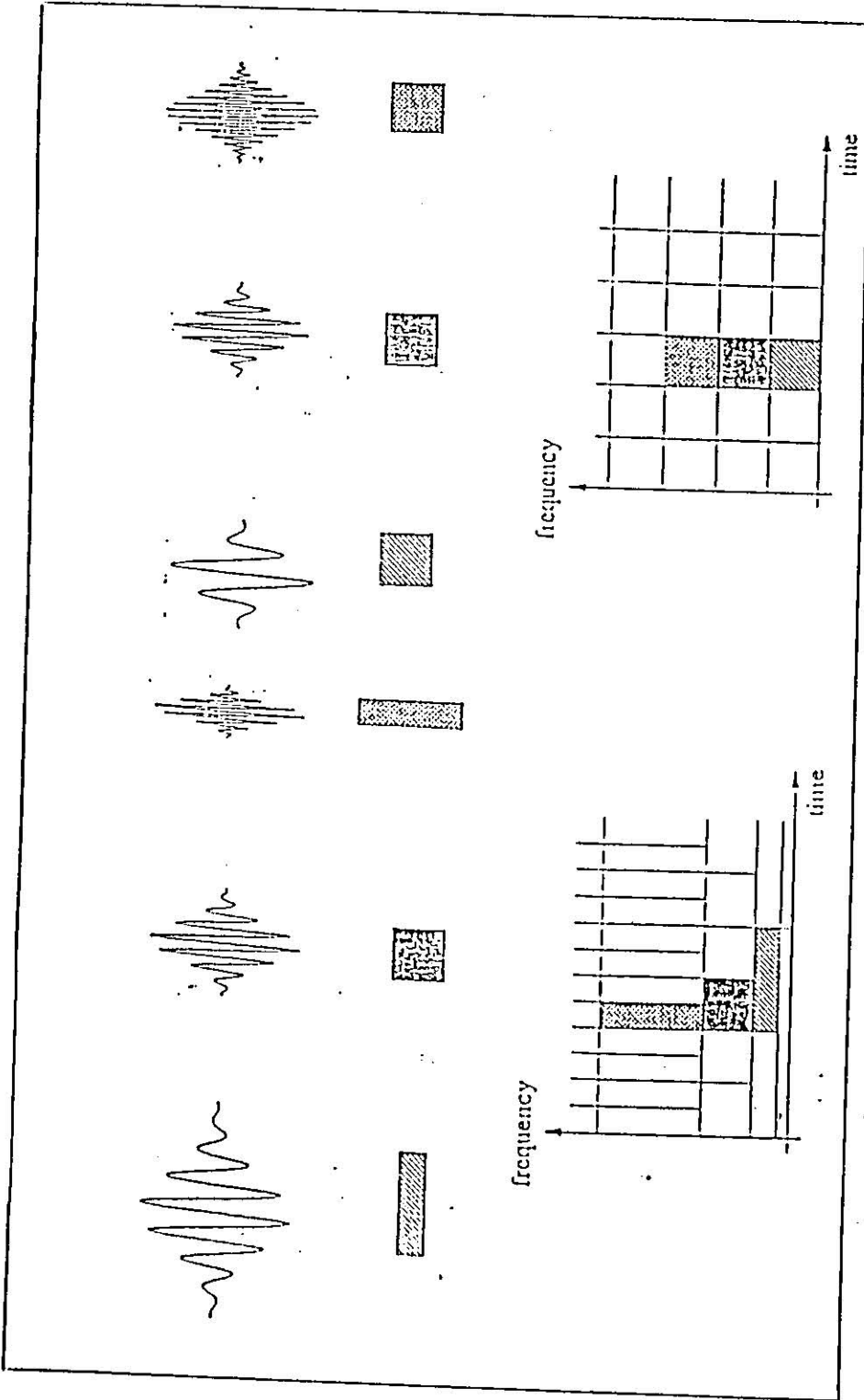


Figure 3.10 (a) : Basis functions and time- frequency resolution of the wavelet transform (WT) (i) Basis functions (ii) Coverage of time-frequency plane (b) : Basis functions and time frequency resolution of the short-time Fourier transform (STFT) (i) Basis functions (ii) Coverage of time-frequency plane [74]

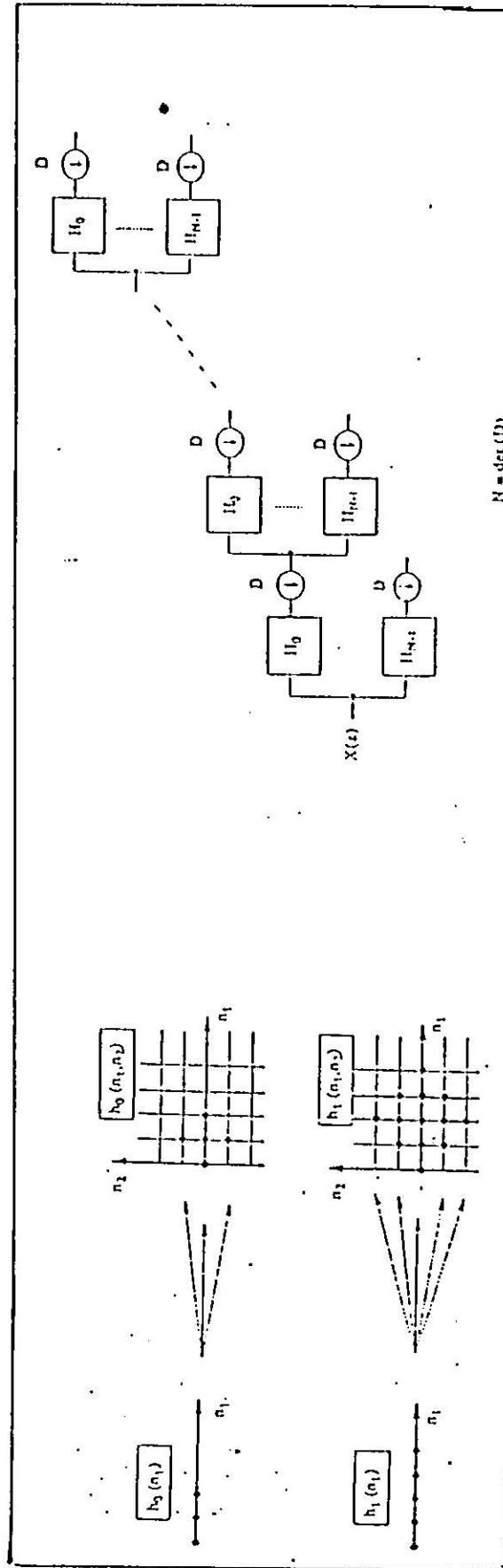


Figure 3.11 (a) : The process of obtaining two-dimensional linear phase set from the one-dimensional one (b) Comparison of the discrete wavelet transform using a filter bank [75]

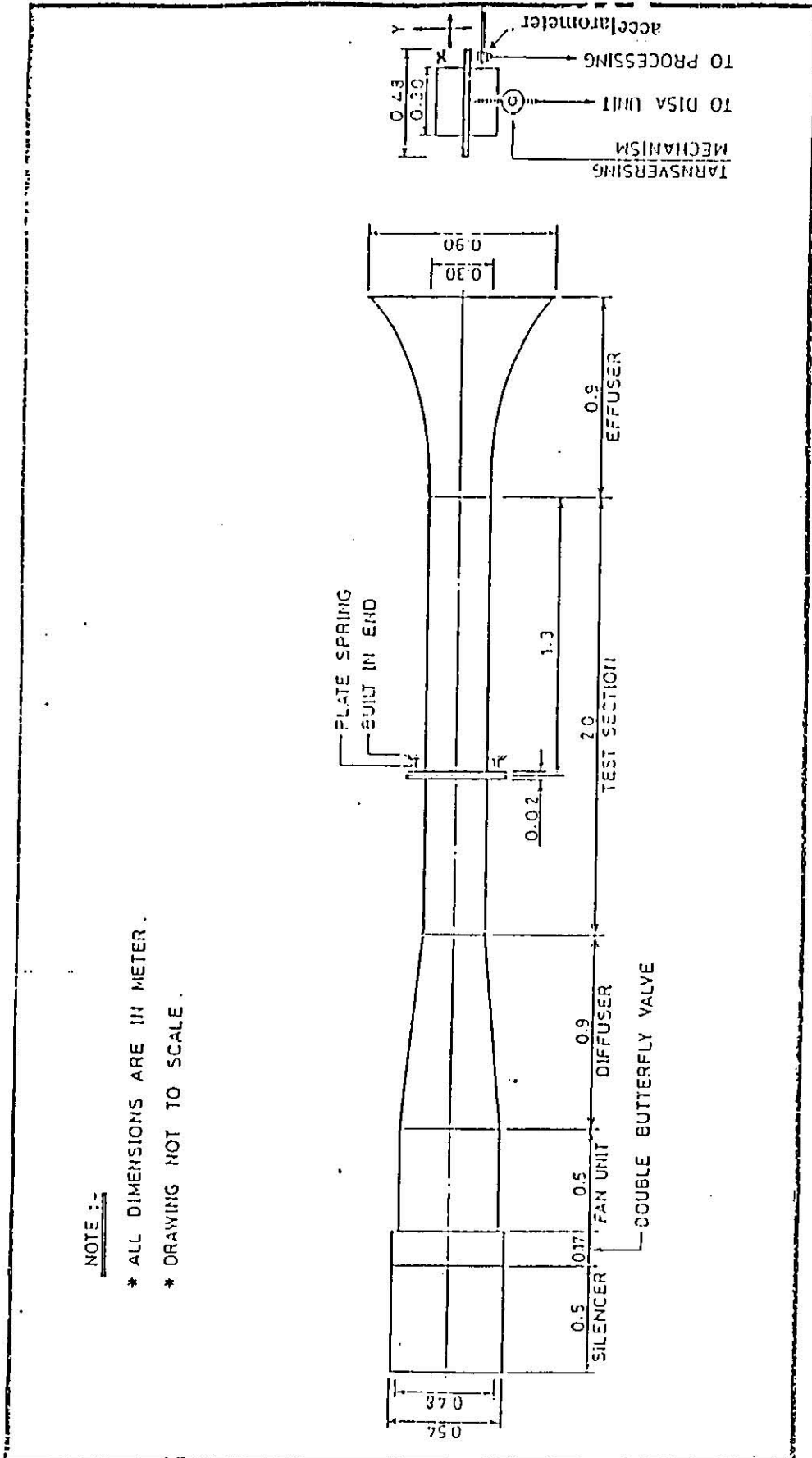


Figure 4.1: Schematic diagram of the wind tunnel and the test section [82]

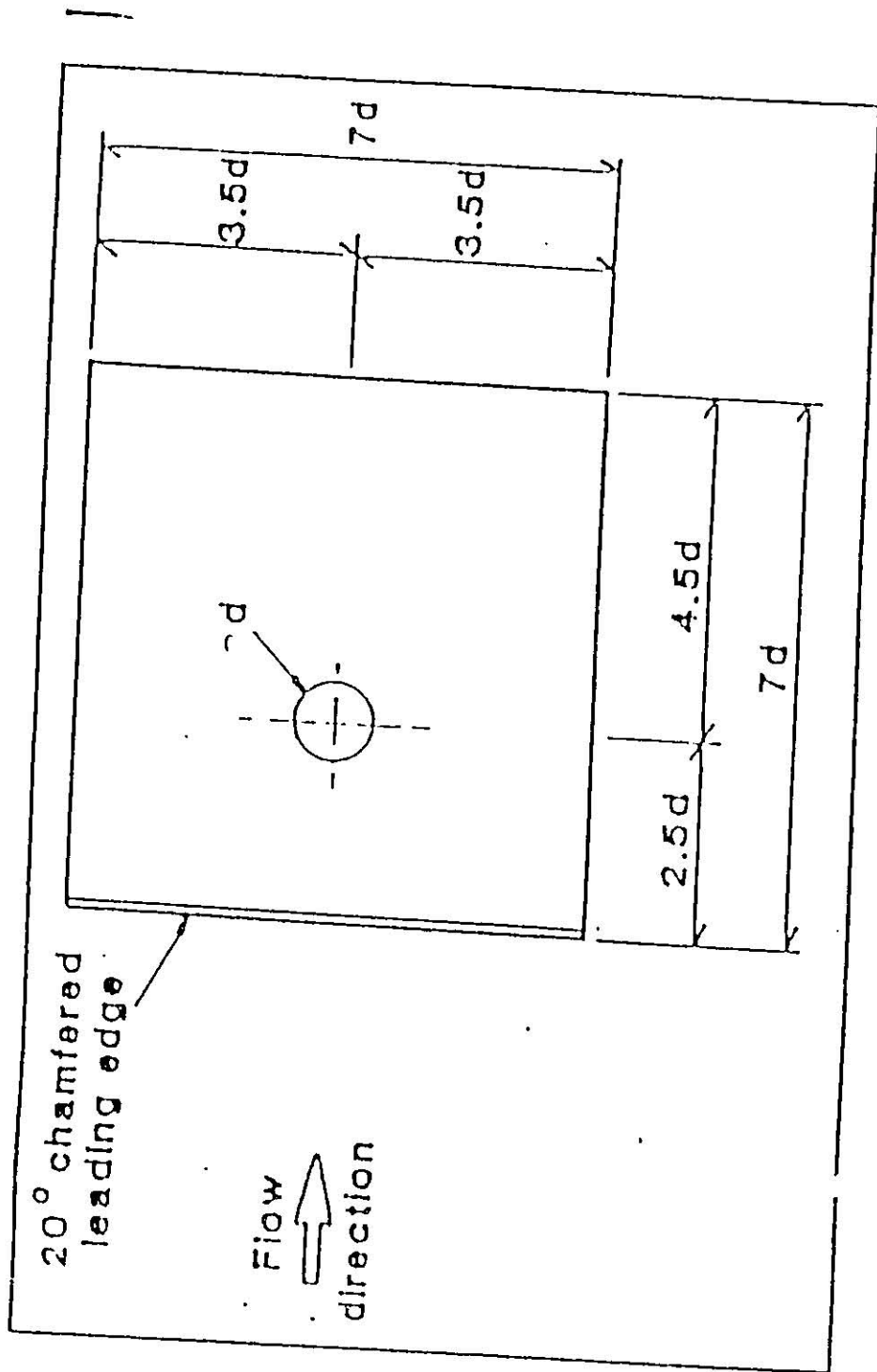


Figure 4.2 : End plates detail [84]

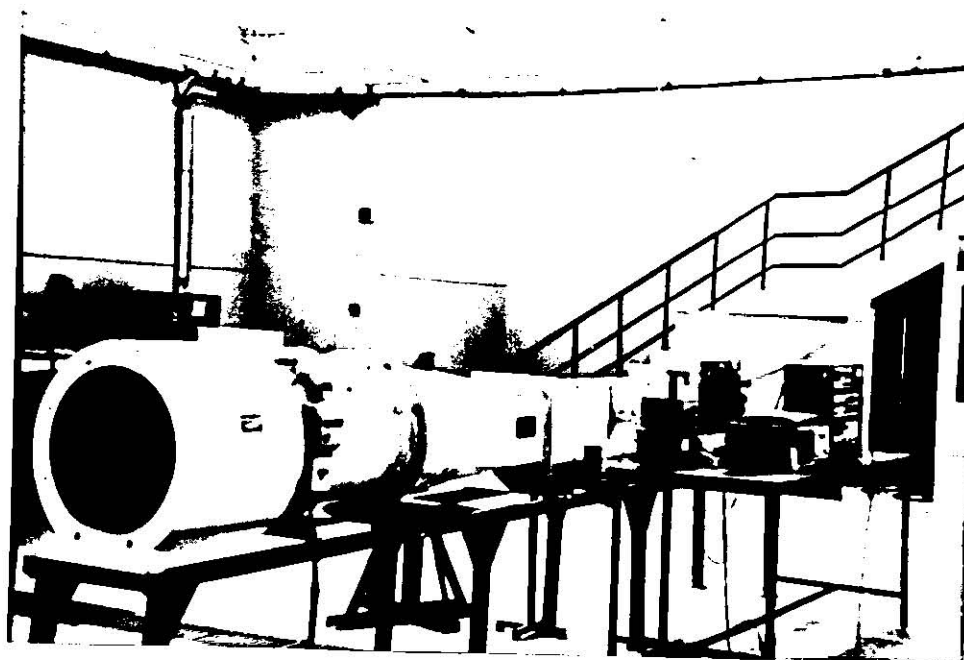
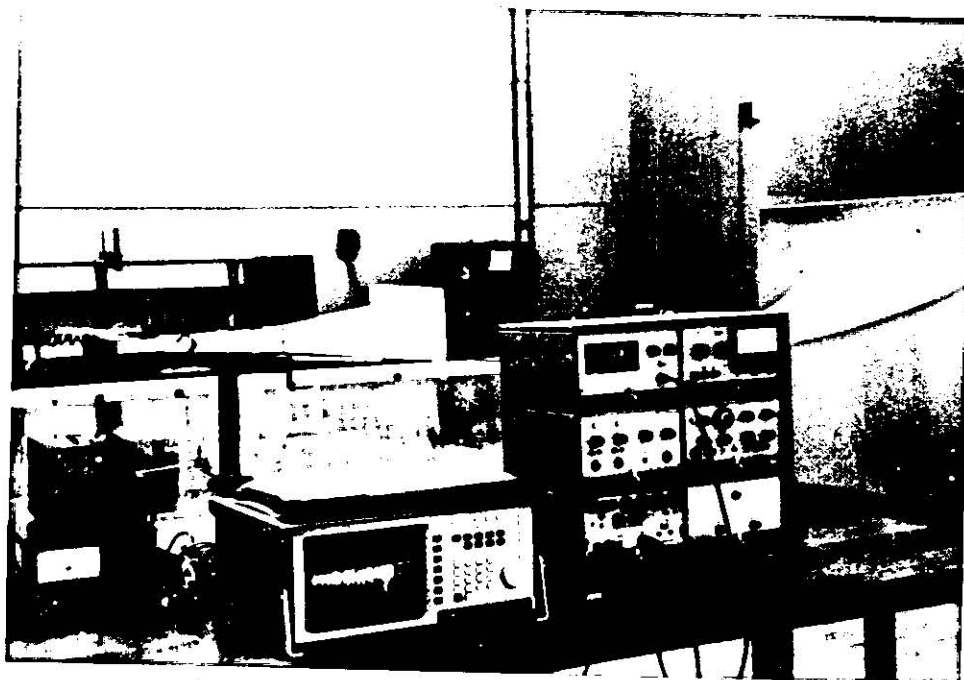


Figure 4.3 : Overall Scene of the instrumentation

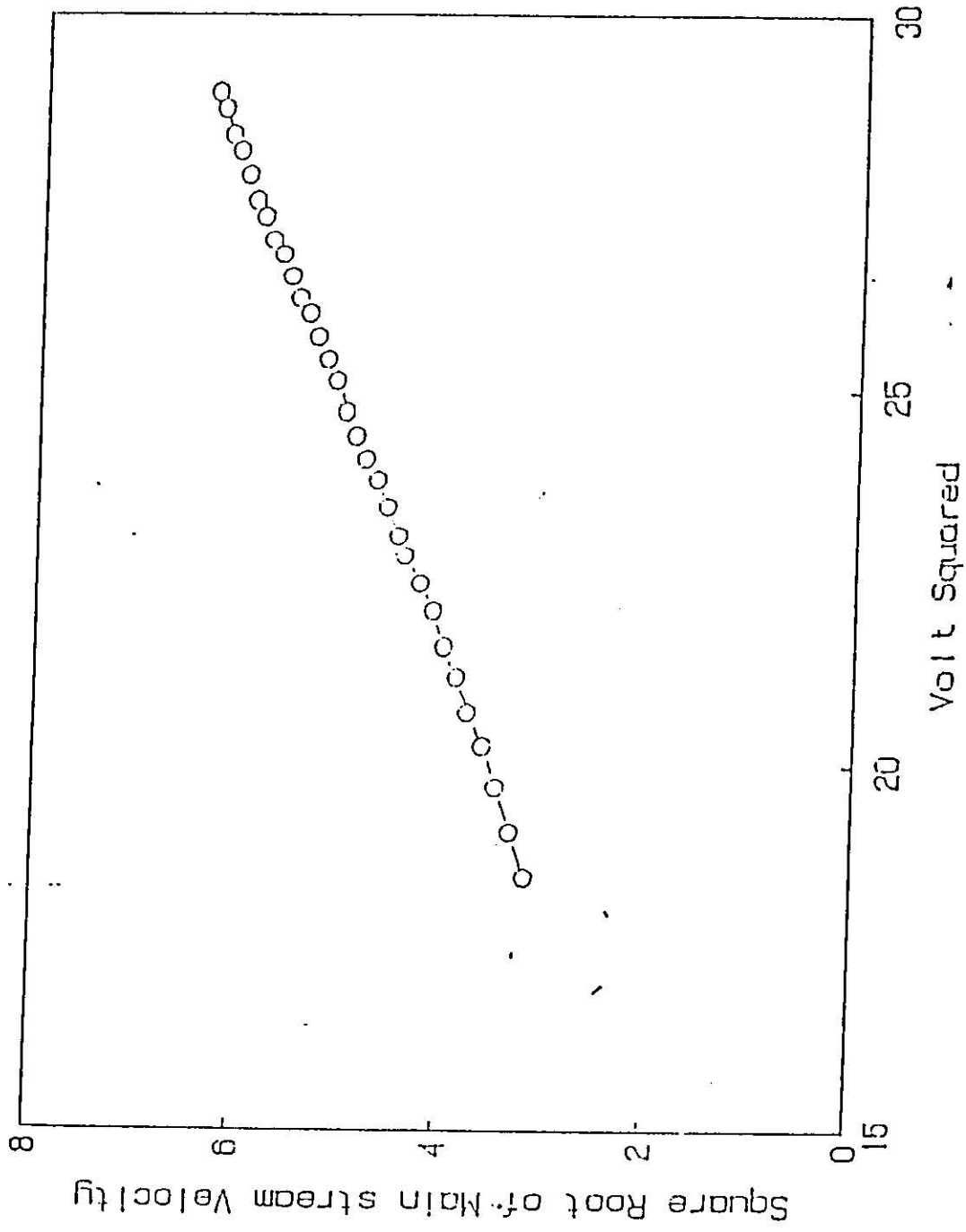


Figure 4.4 : Hot Wire Calibration curve, Probe 55p14.

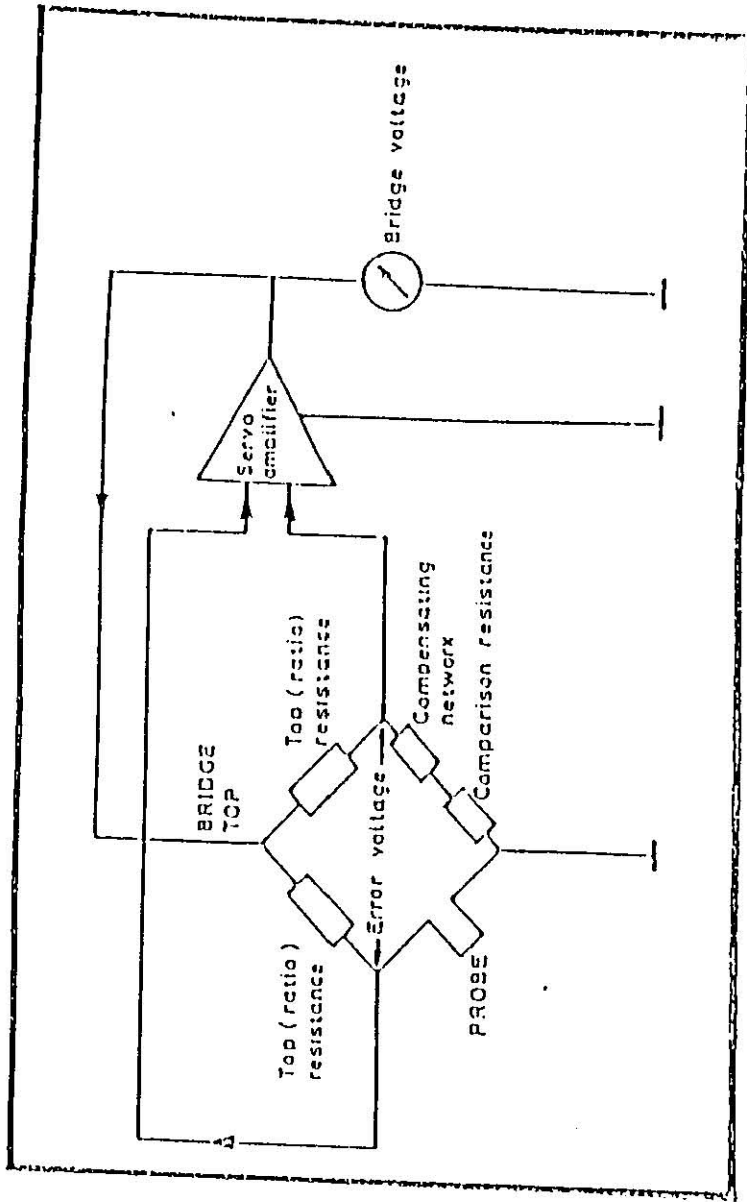


Figure 4.5 : Simplified diagram of the constant-temperature anemometer [83]

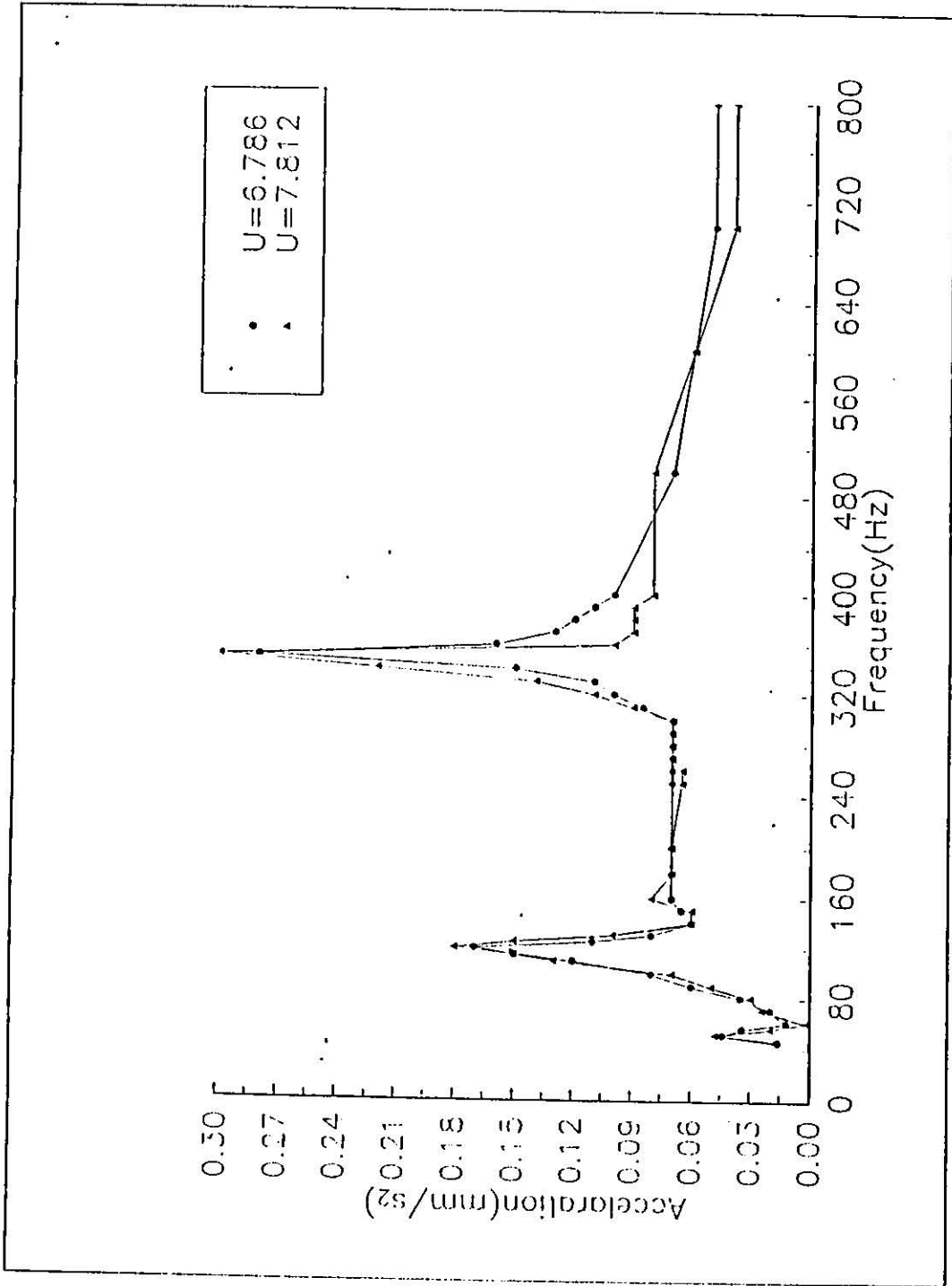


Figure 5.2 : Frequency distribution at U=6 78 m/s and U=7.81 m/s

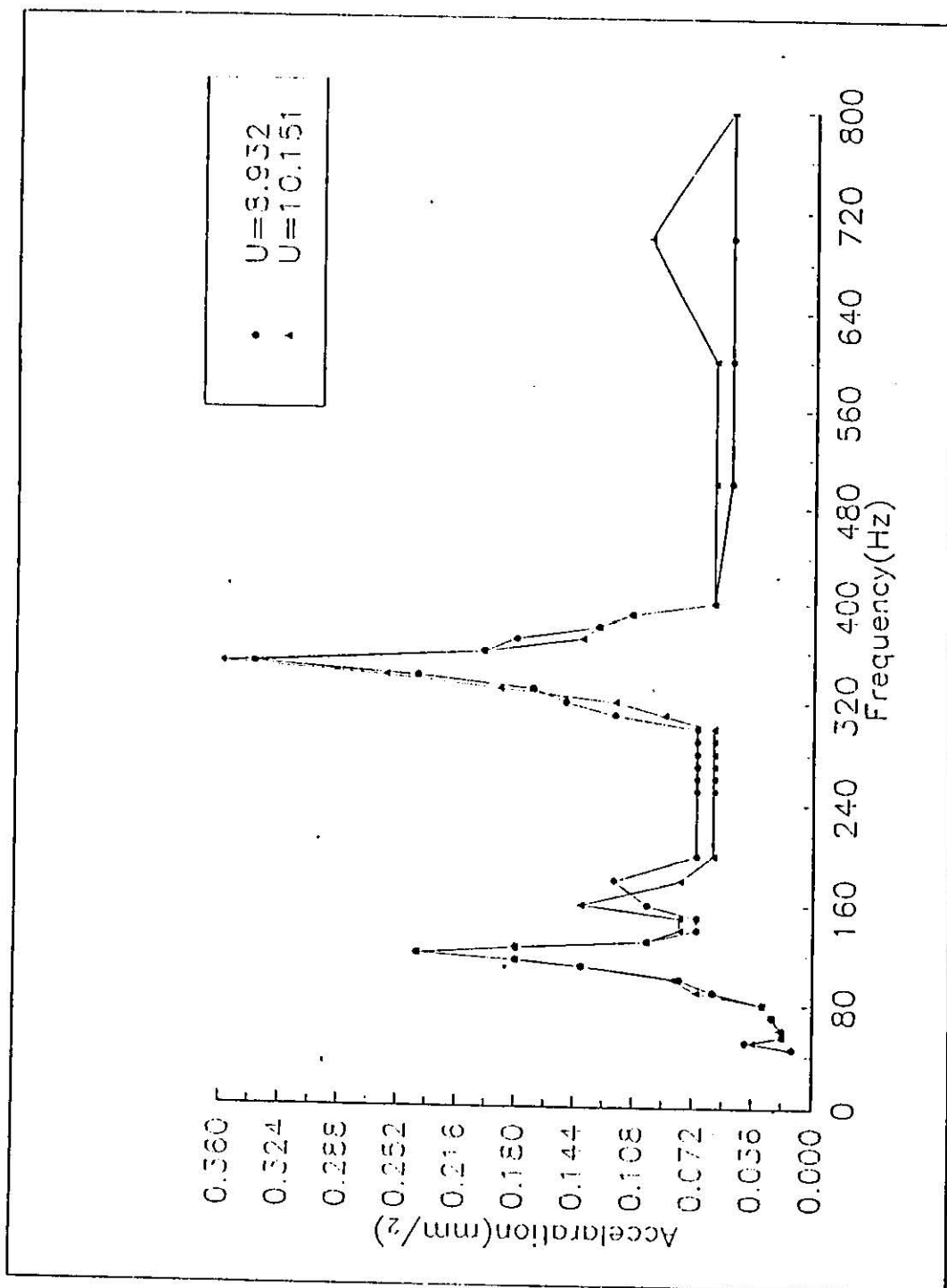


Figure 5.3 : Frequency distribution at U=8.93 m/s and U=10.15 m/s

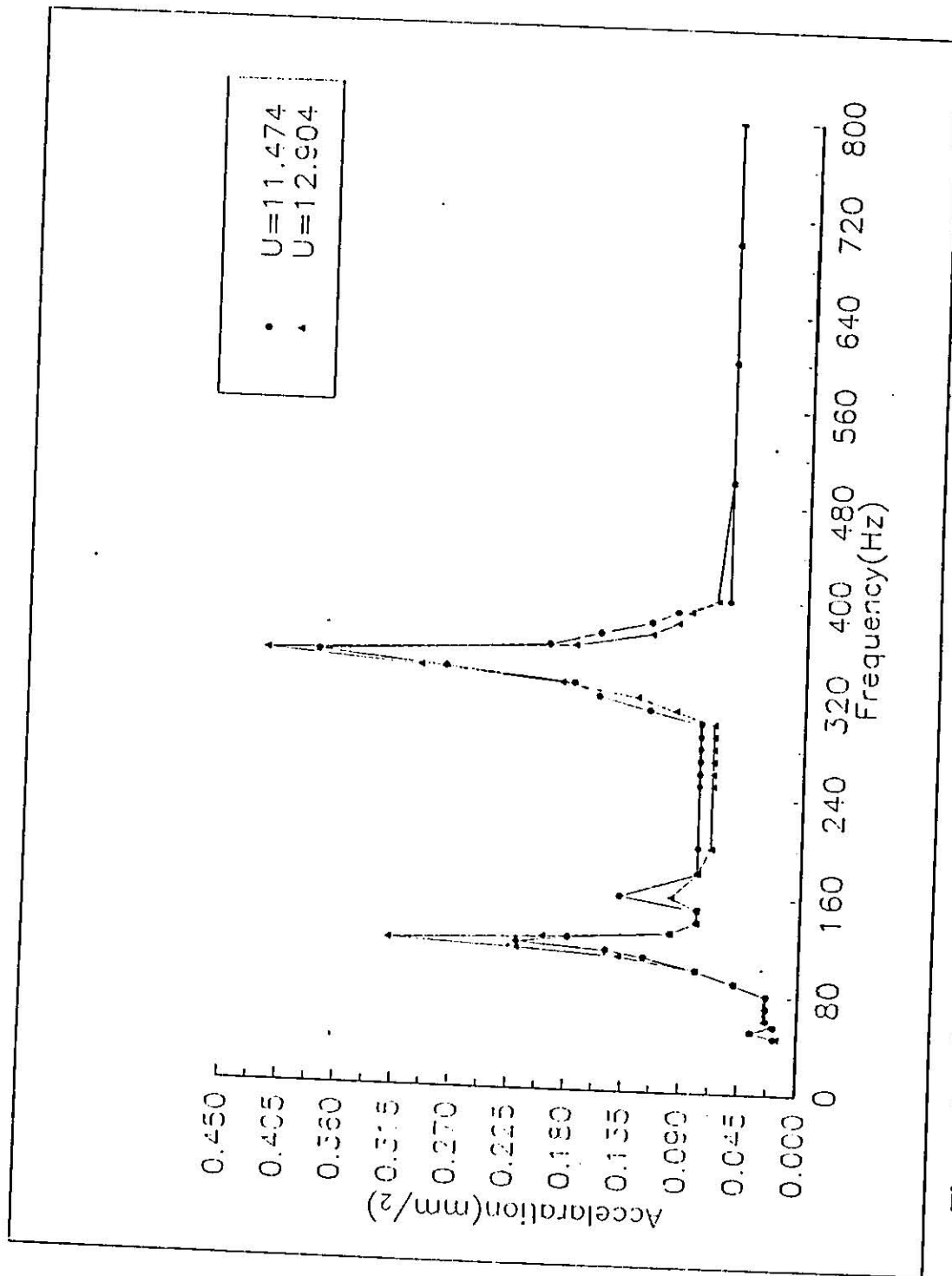


Figure 5.4 : Frequency distribution at $U=11.47$ m/s and $U=12.9$ m/s

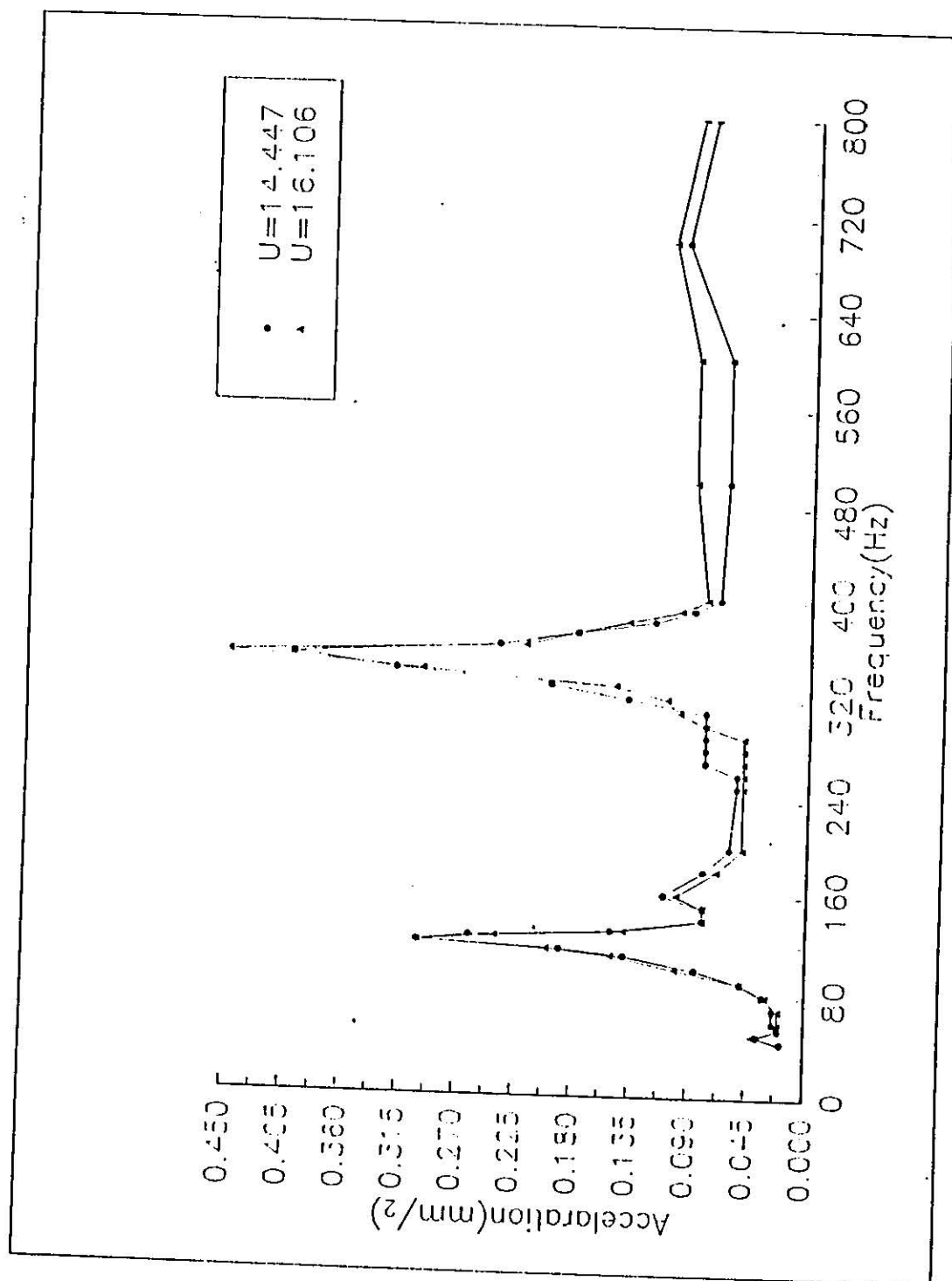


Figure 5.5 : Frequency distribution at $U=14.46$ m/s and $U=16.11$ m/s

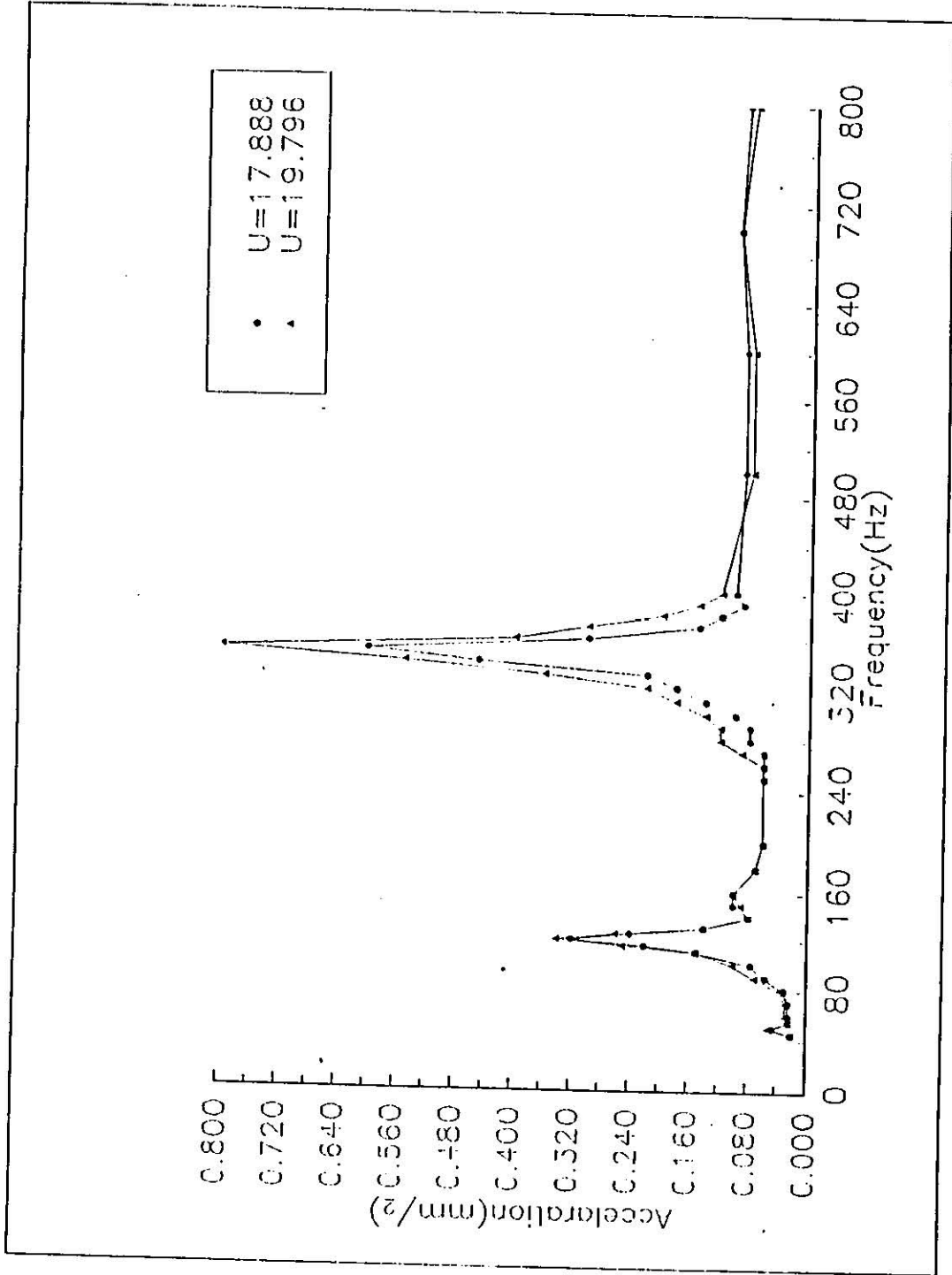


Figure 5.6 : Frequency distribution at U=17.89 m/s and U=19.87 m/s

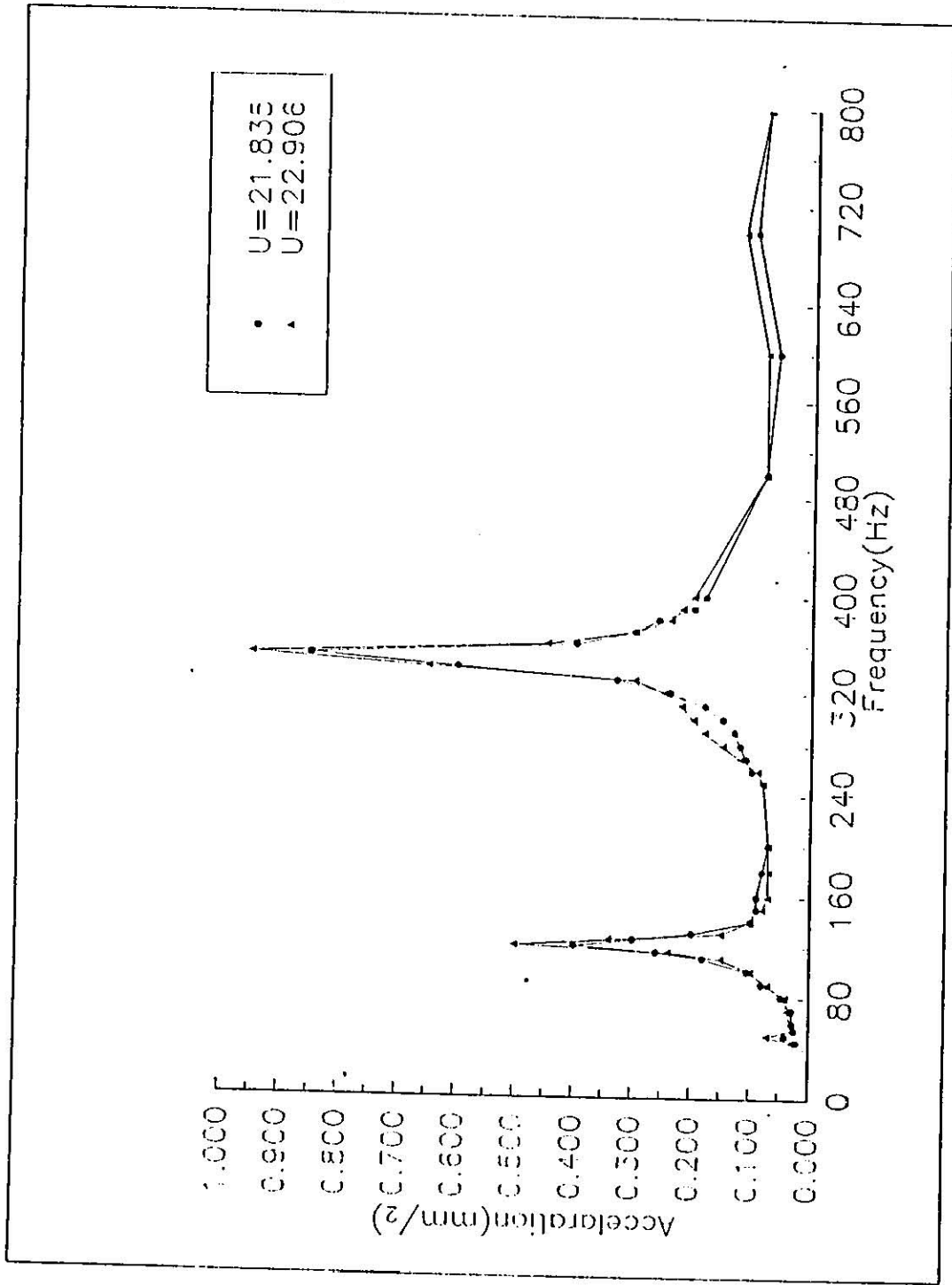


Figure 5.7 : Frequency distribution at U=21.835 m/s and U=22.906 m/s

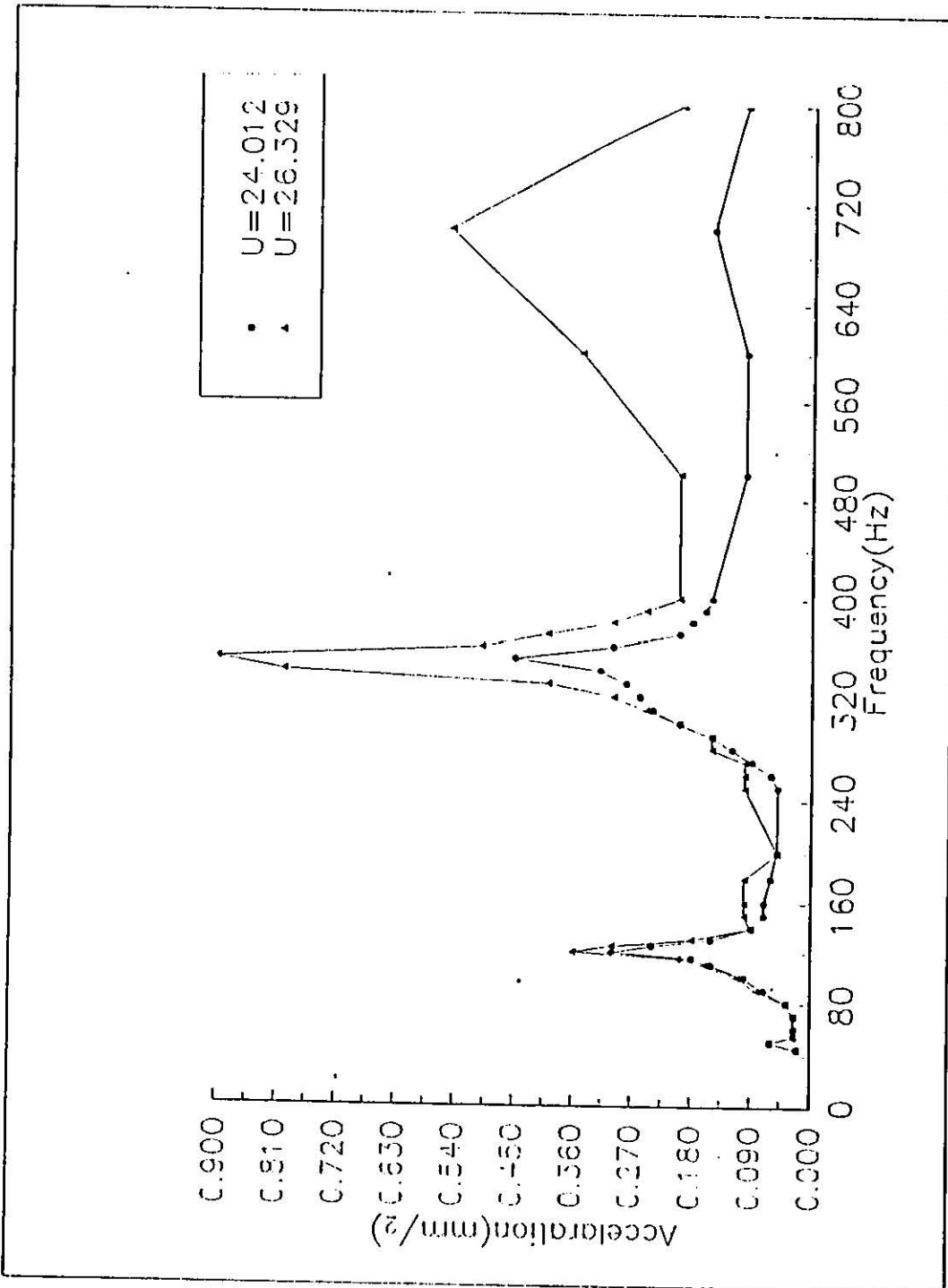


Figure 5.8 : Frequency distribution at U=24.01 m/s and U=26.33 m/s

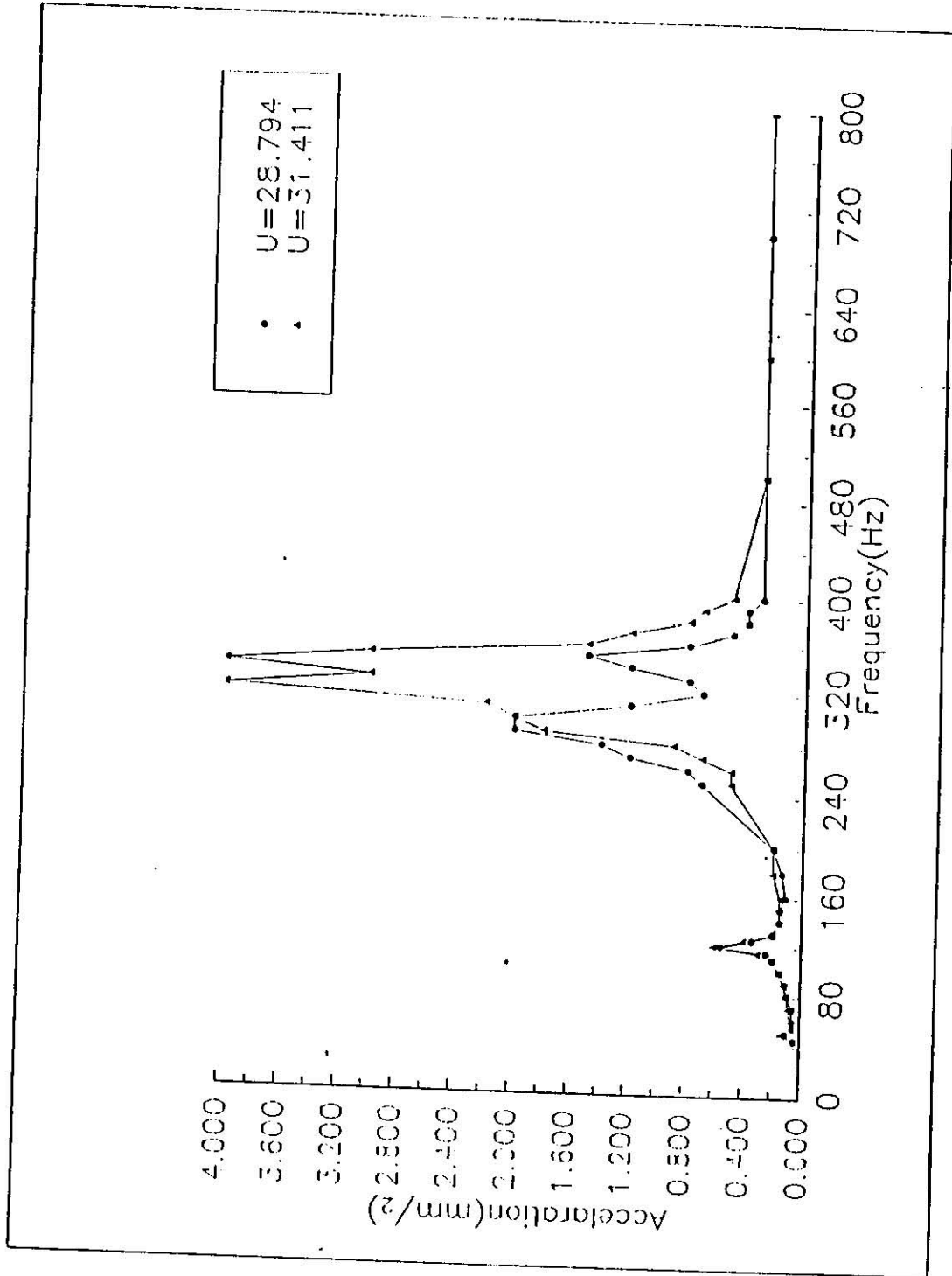


Figure 5.9 : Frequency distribution at $U=28.79$ m/s and $U=31.41$ m/s

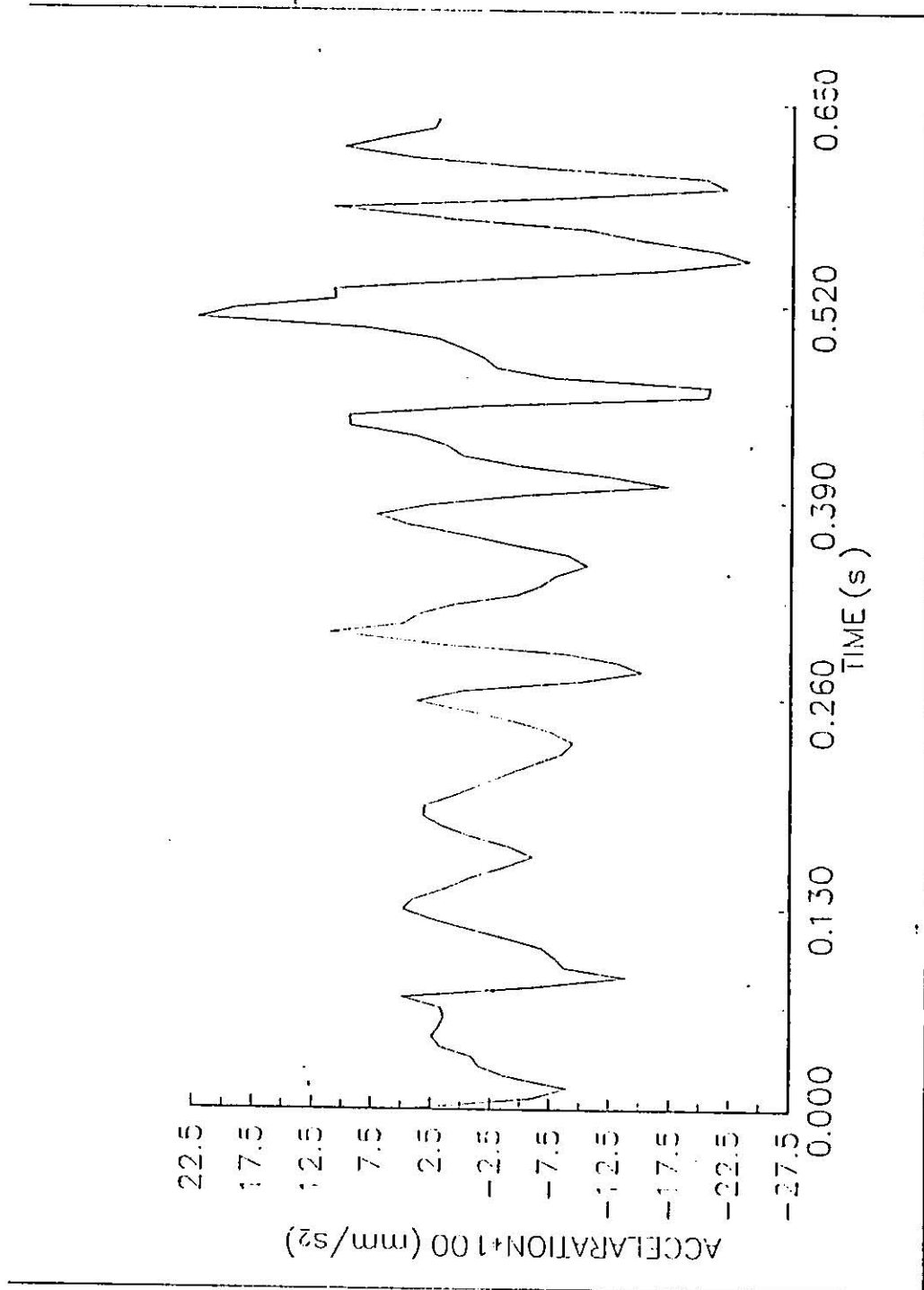


Figure 5.10 : The 1st time-series at $U=28.79$ m/s

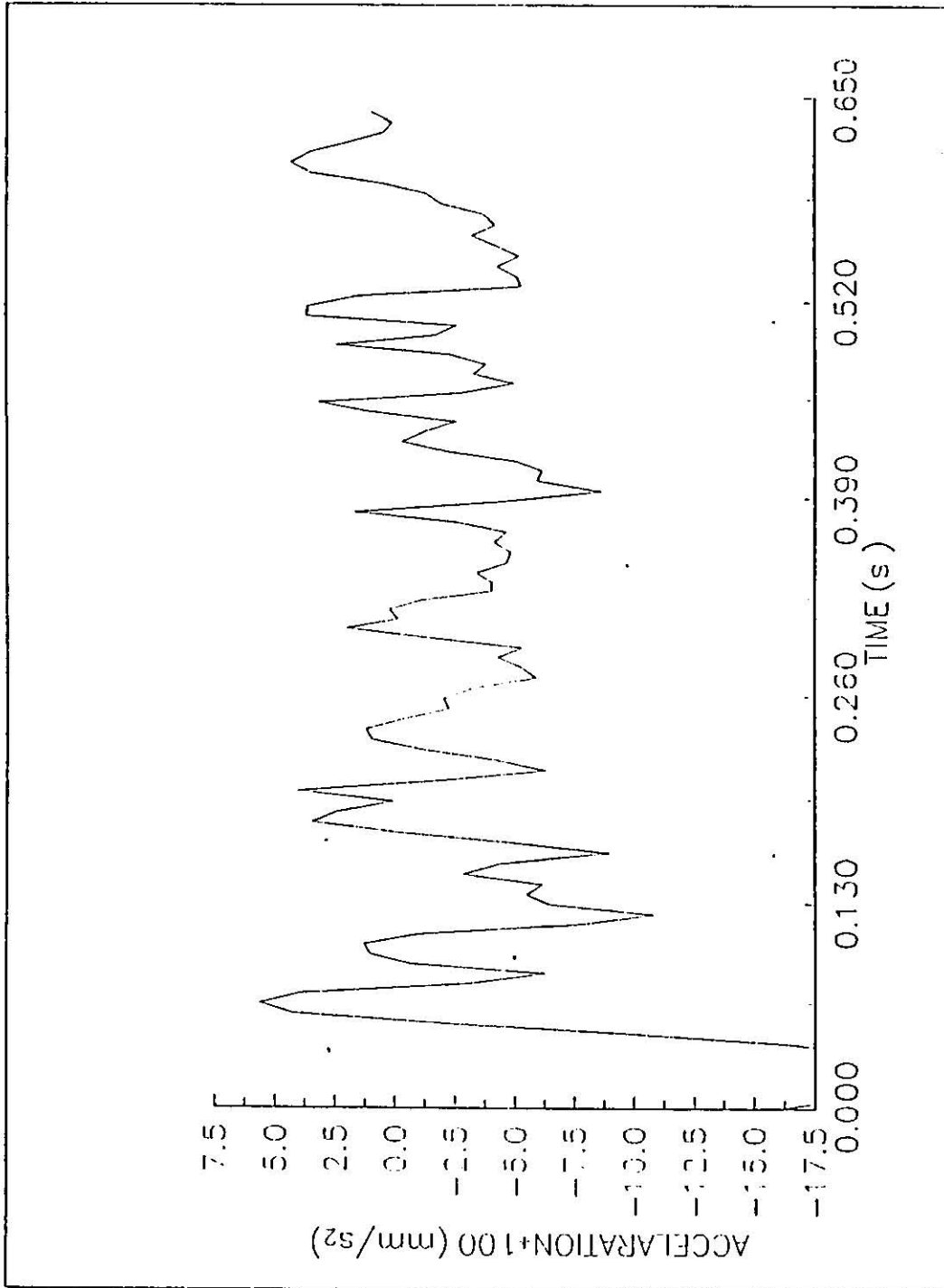


Figure 5.11 : The 2nd time-series at $U=28.79$ m/s

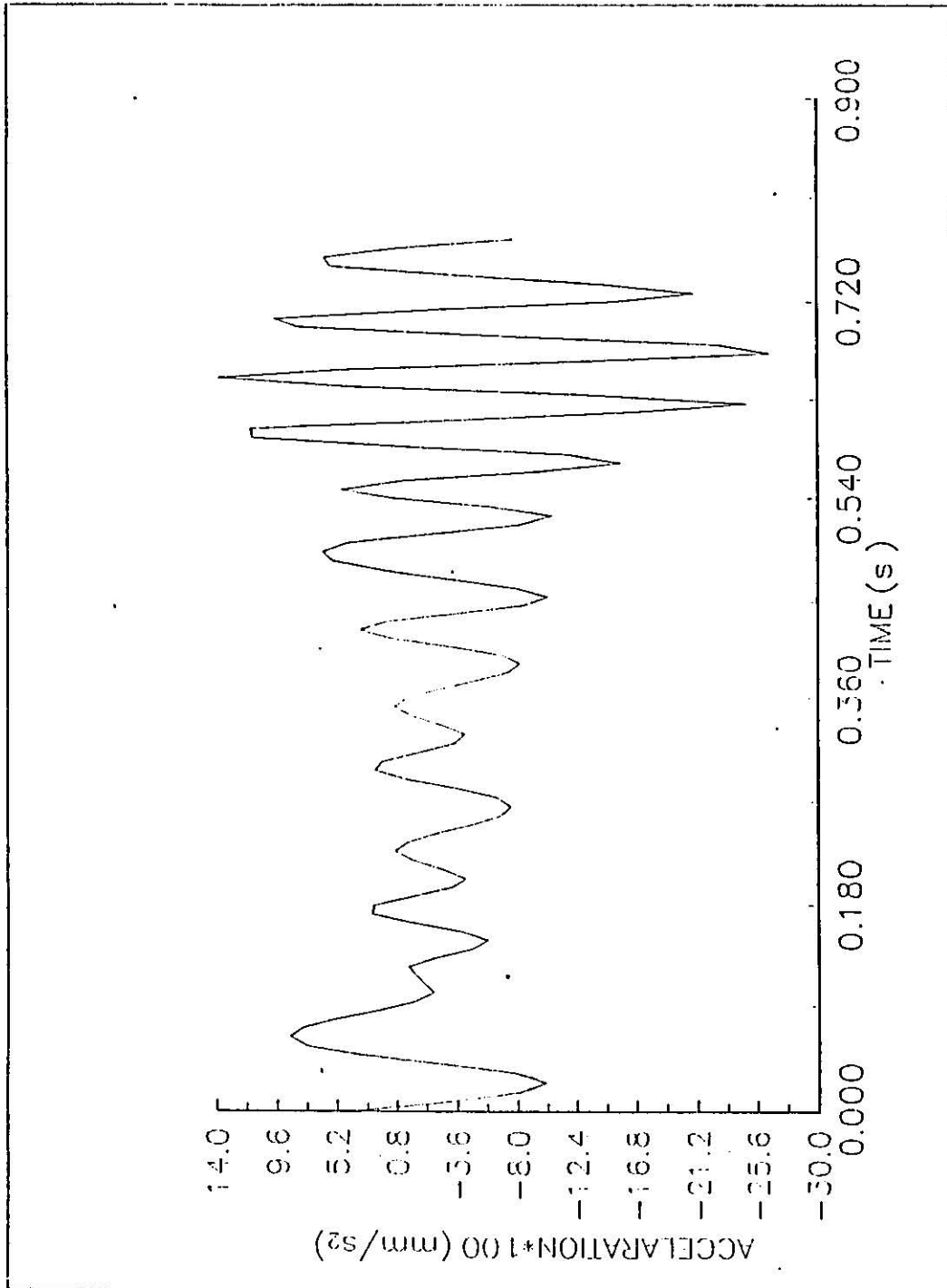


Figure 5.12 : The 3rd time-series at $U=22.0$ m/s

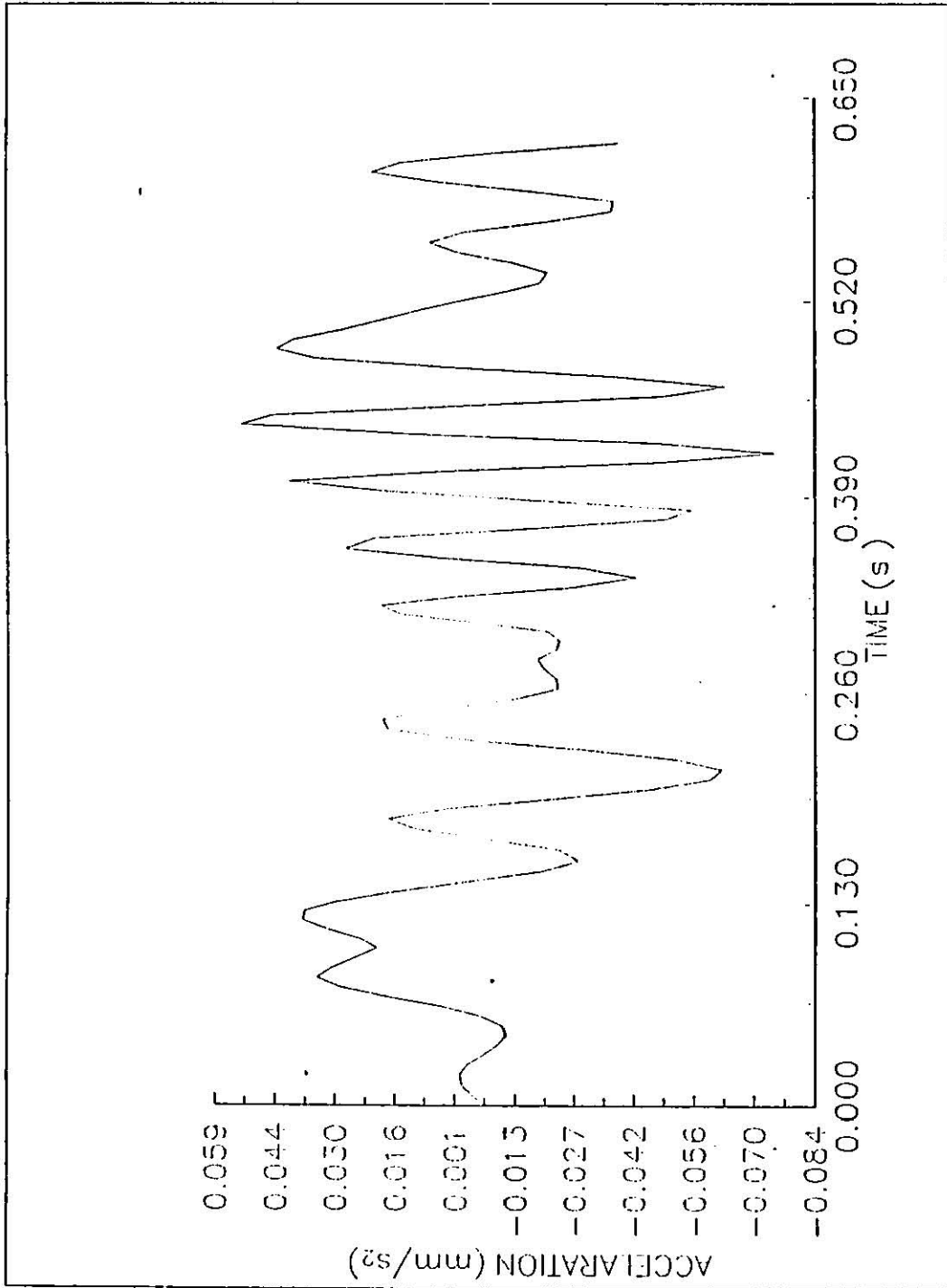


Figure 5.13 : The 4th time-series at $U=19.79$ m/s

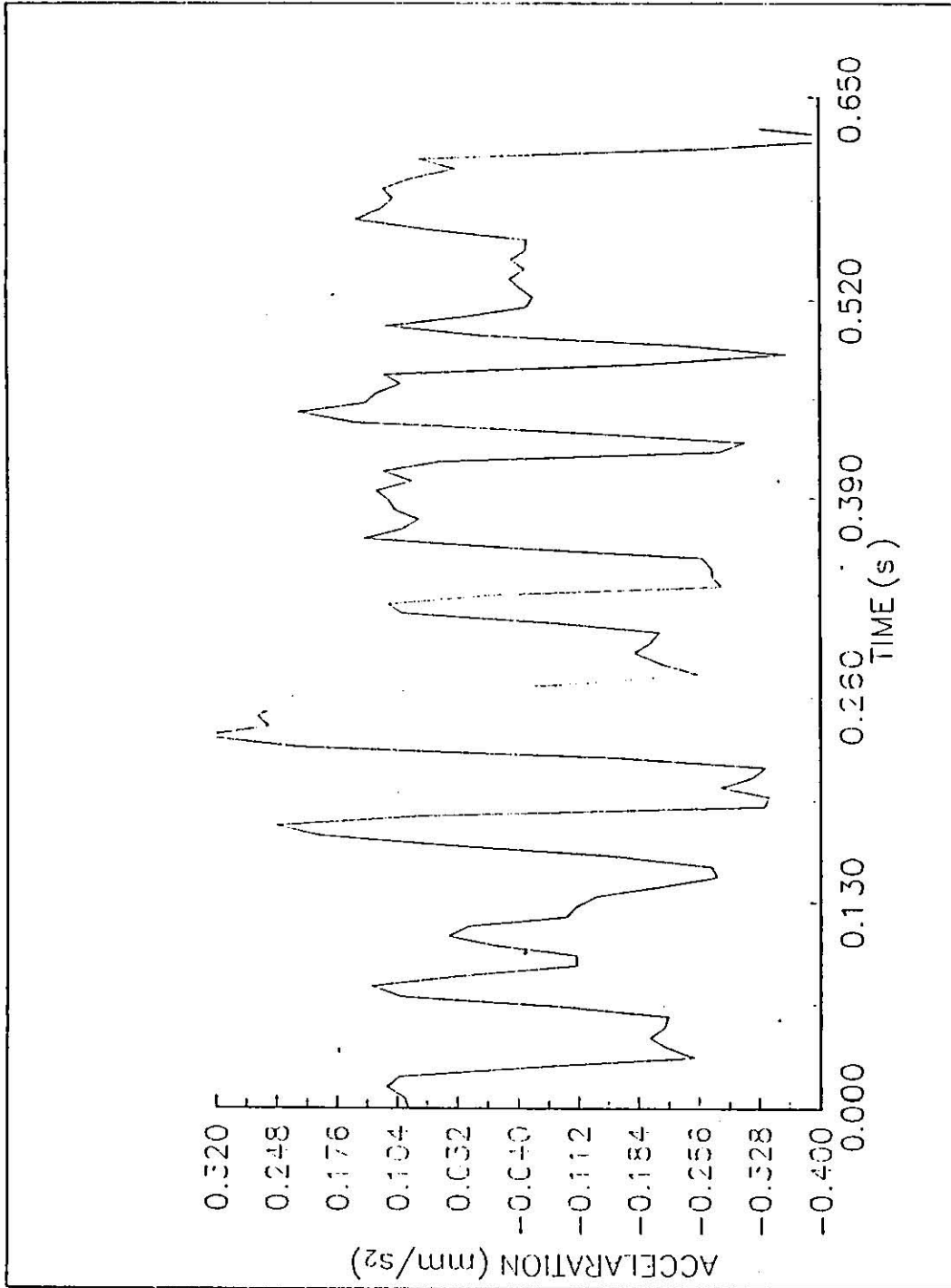


Figure 5.14 : The 5th time-series at $U=19.79$ m/s

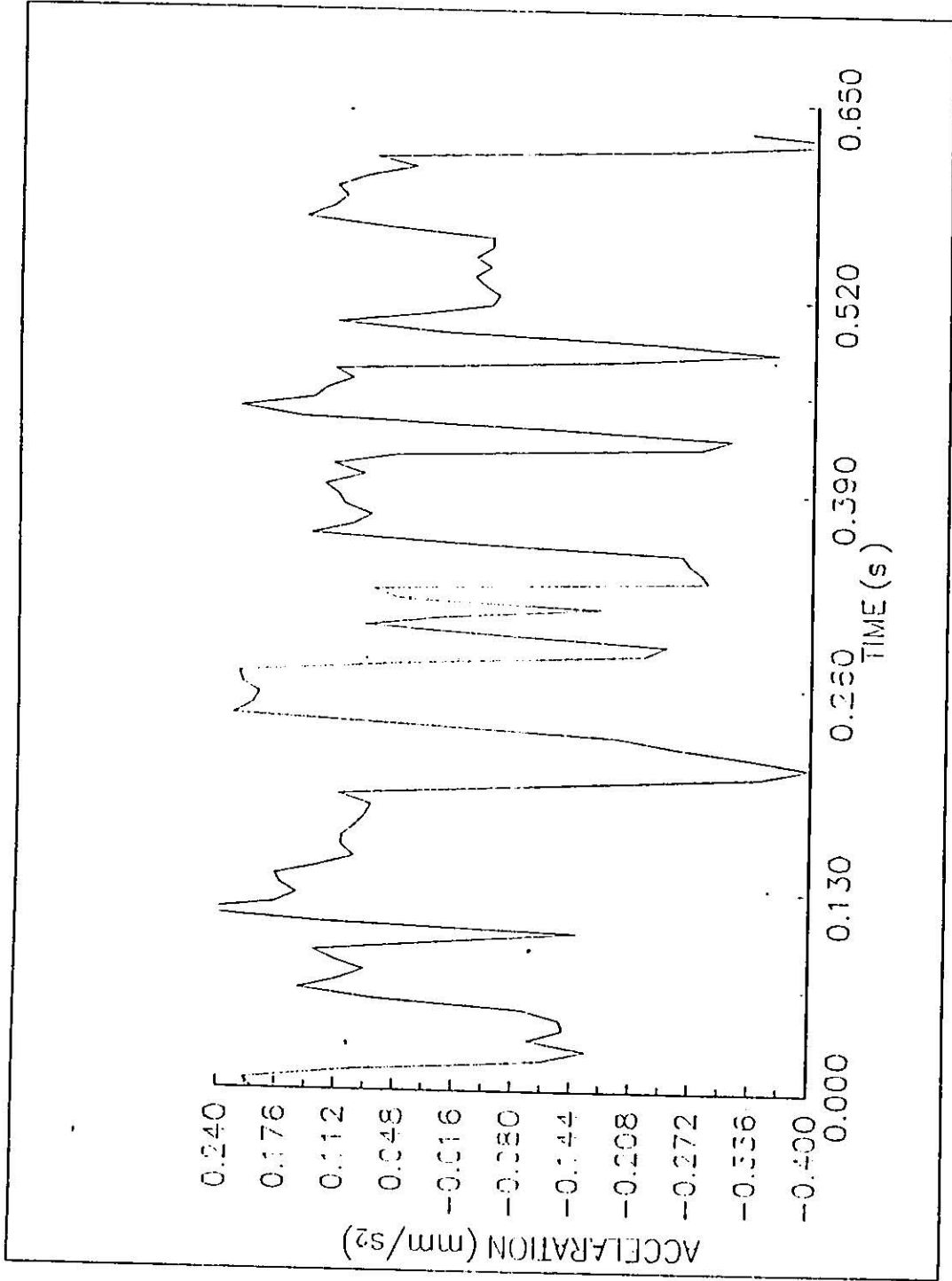


Figure 5.15 : The 6th time-series at U=17.9 m/s

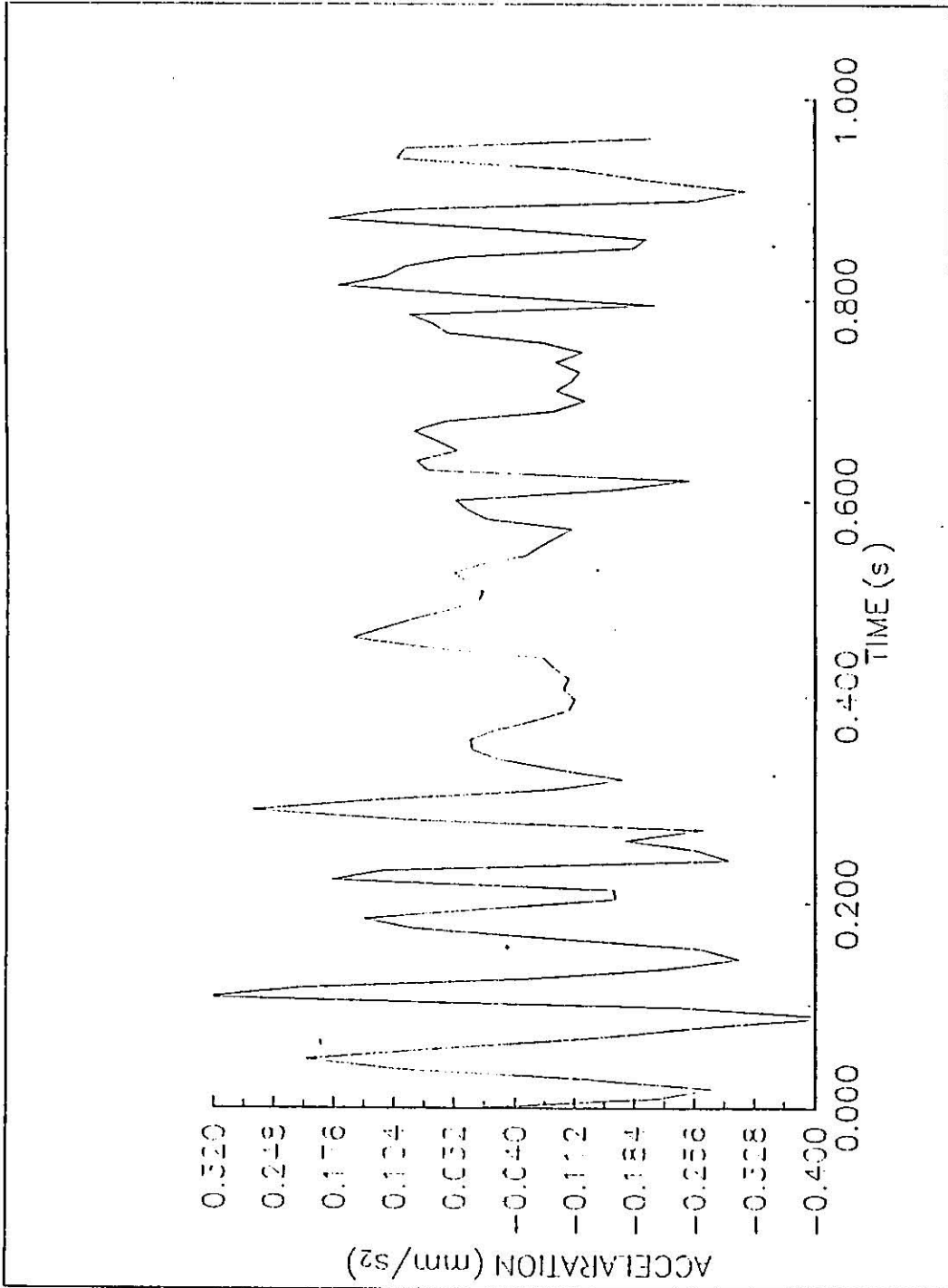


Figure 5.16 : The 7th time-series at U=24.01 m/s

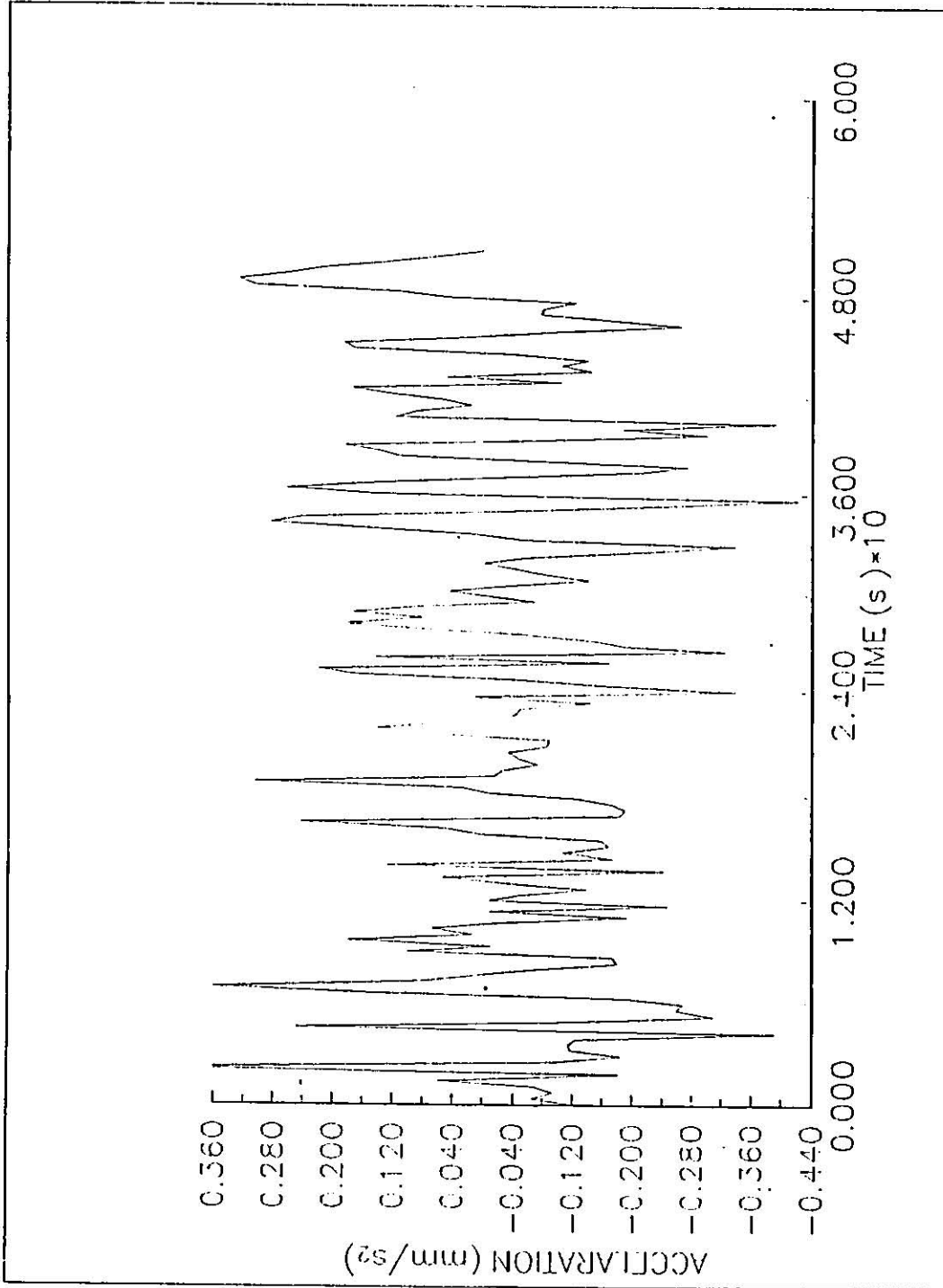


Figure 5.17 : The 8th time-series at $U=22.9$ m/s

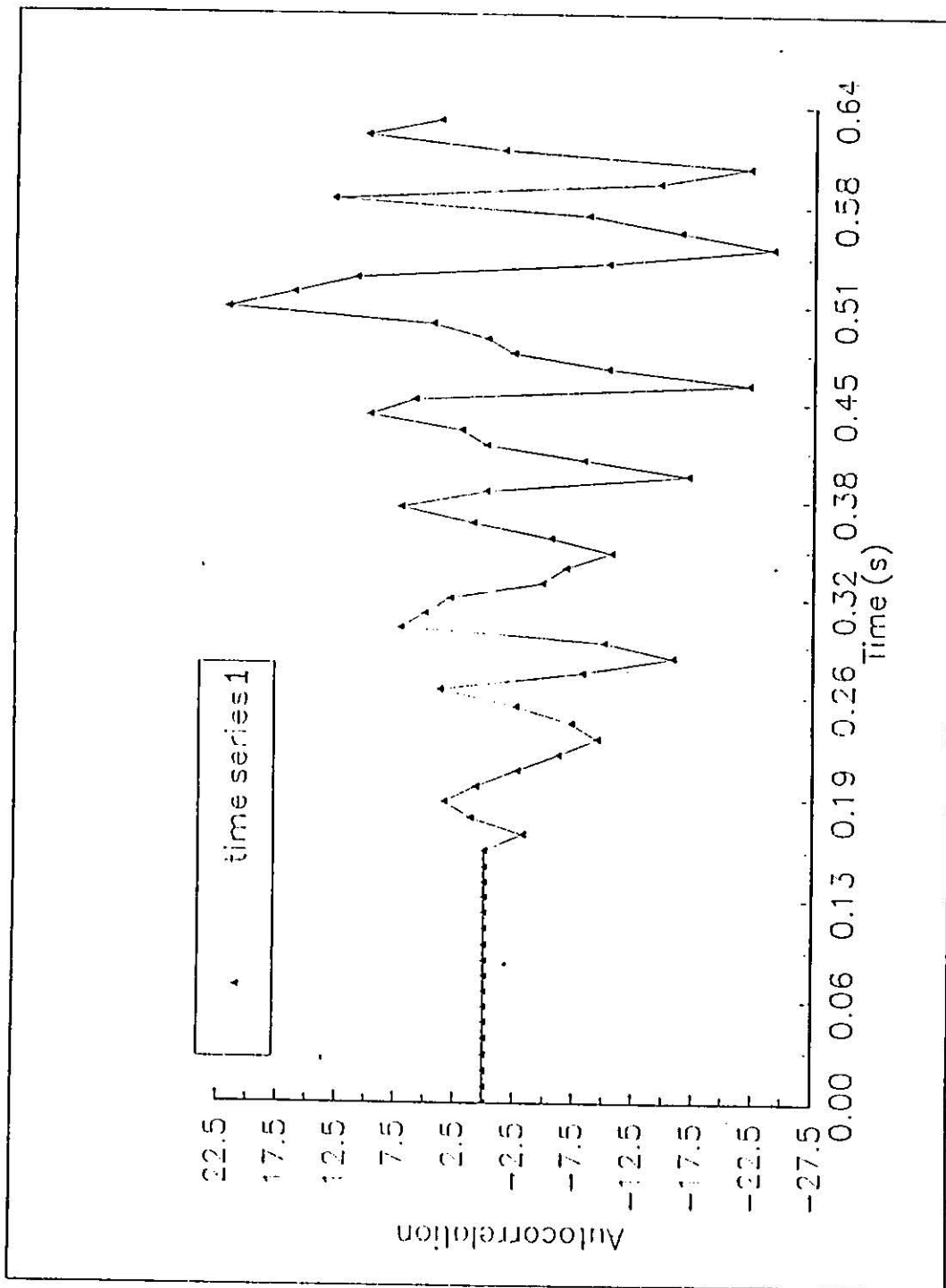


Figure 5.18 : The autocorrelation function of the 1st time-series

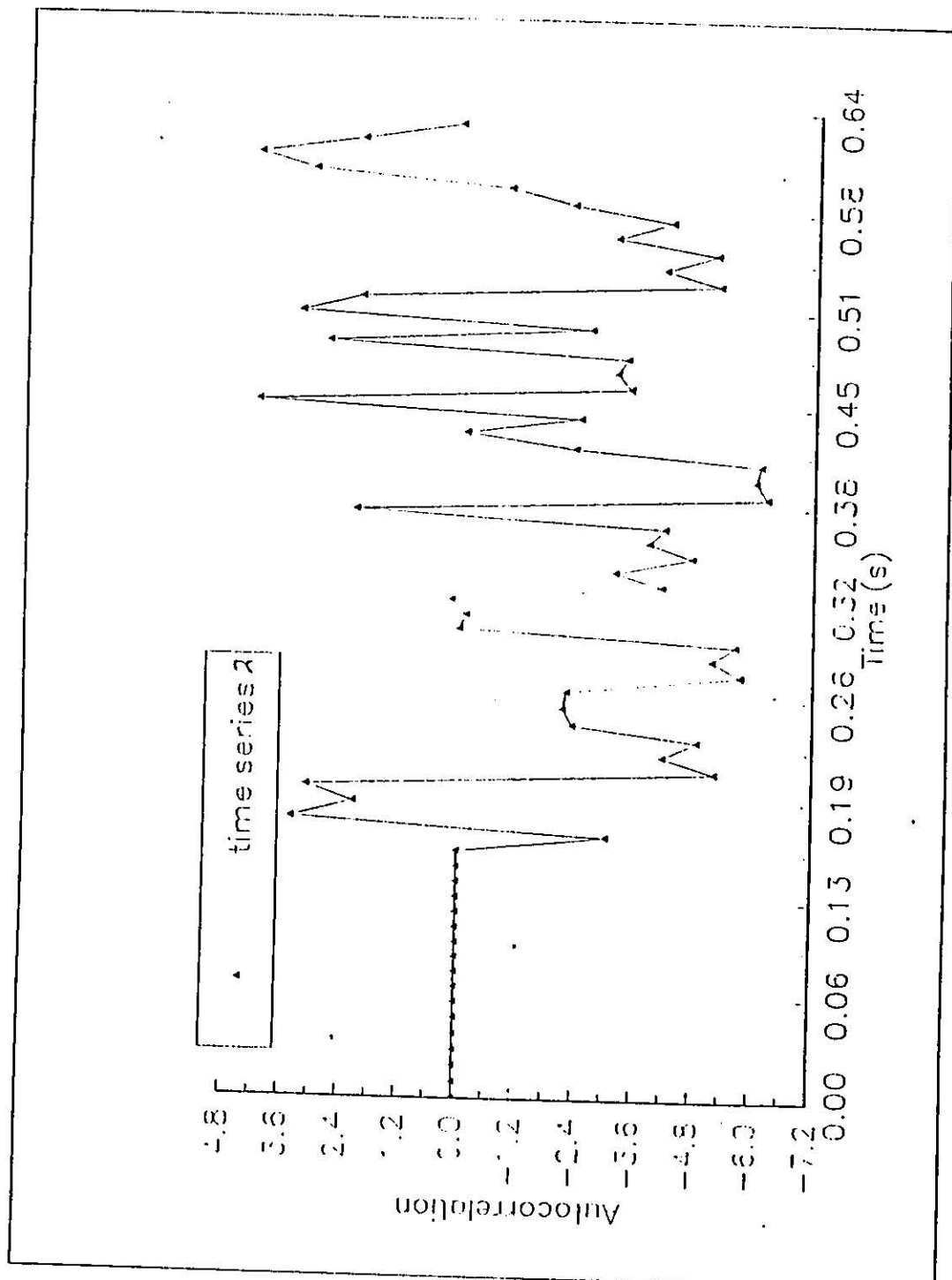


Figure 5.19 : The autocorrelation function of the 2nd time-series

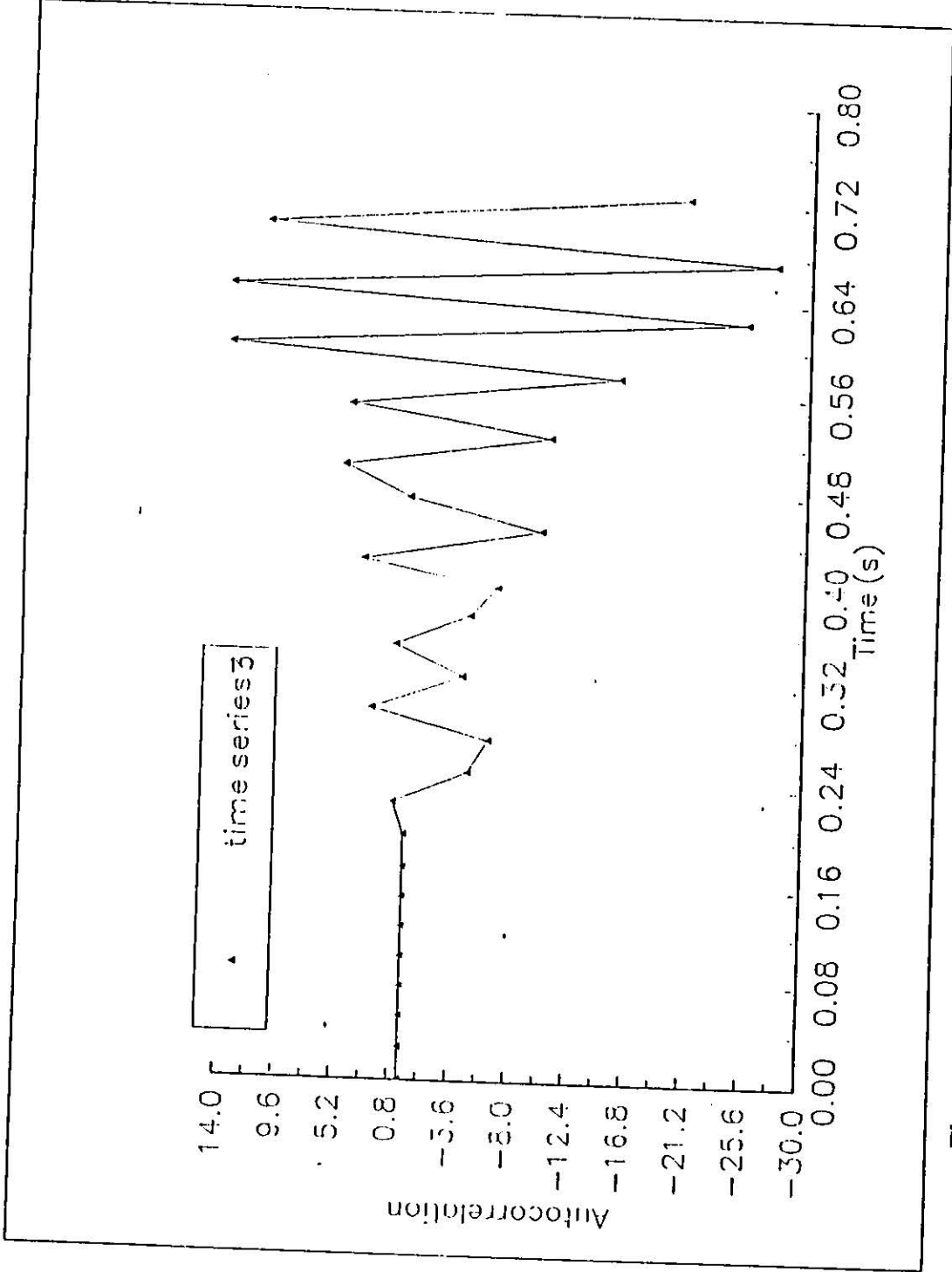


Figure 5.20 : The autocorrelation function of the 3rd time-series

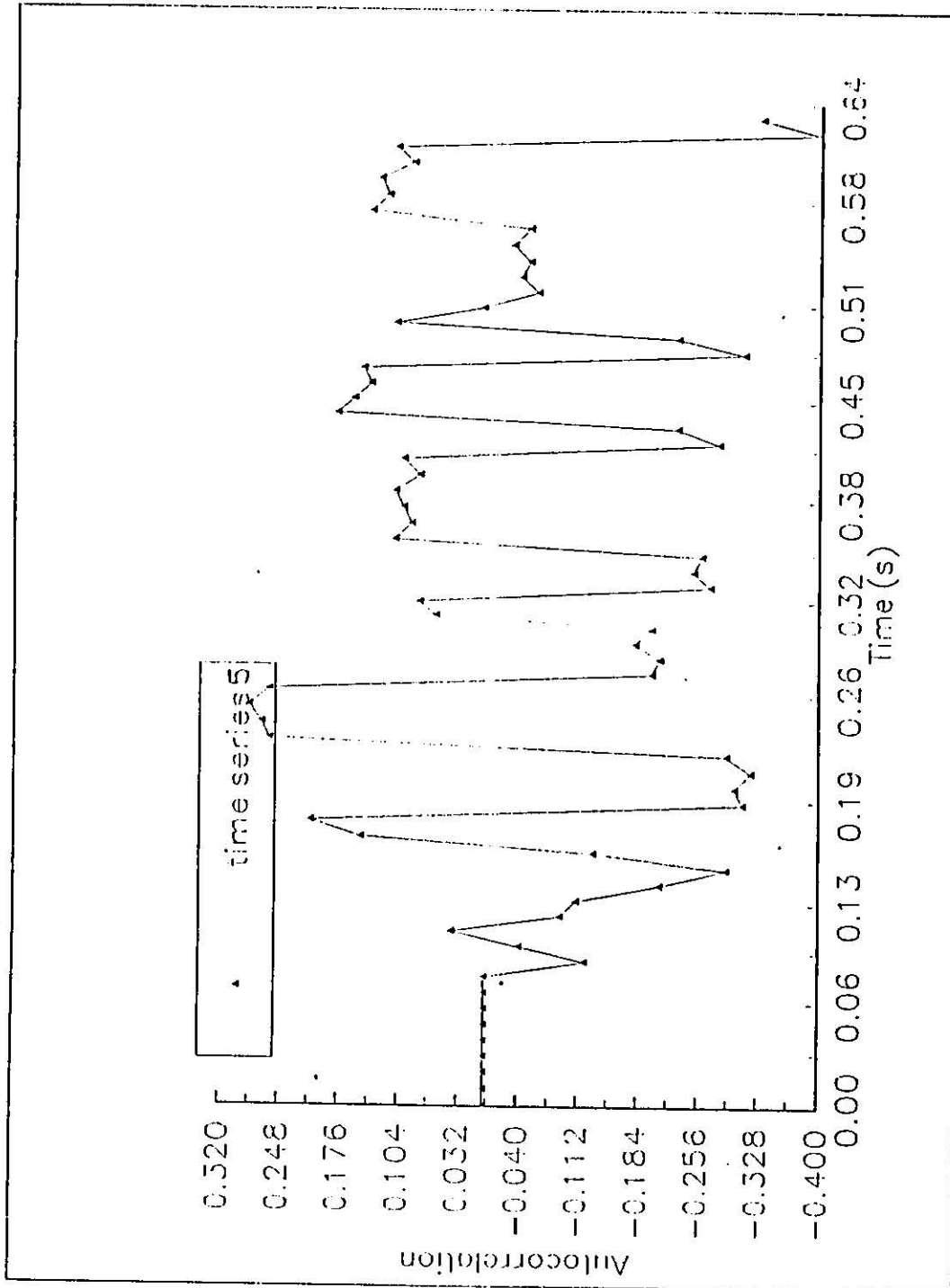


Figure 5.22 : The autocorrelation function of the 5th time-series

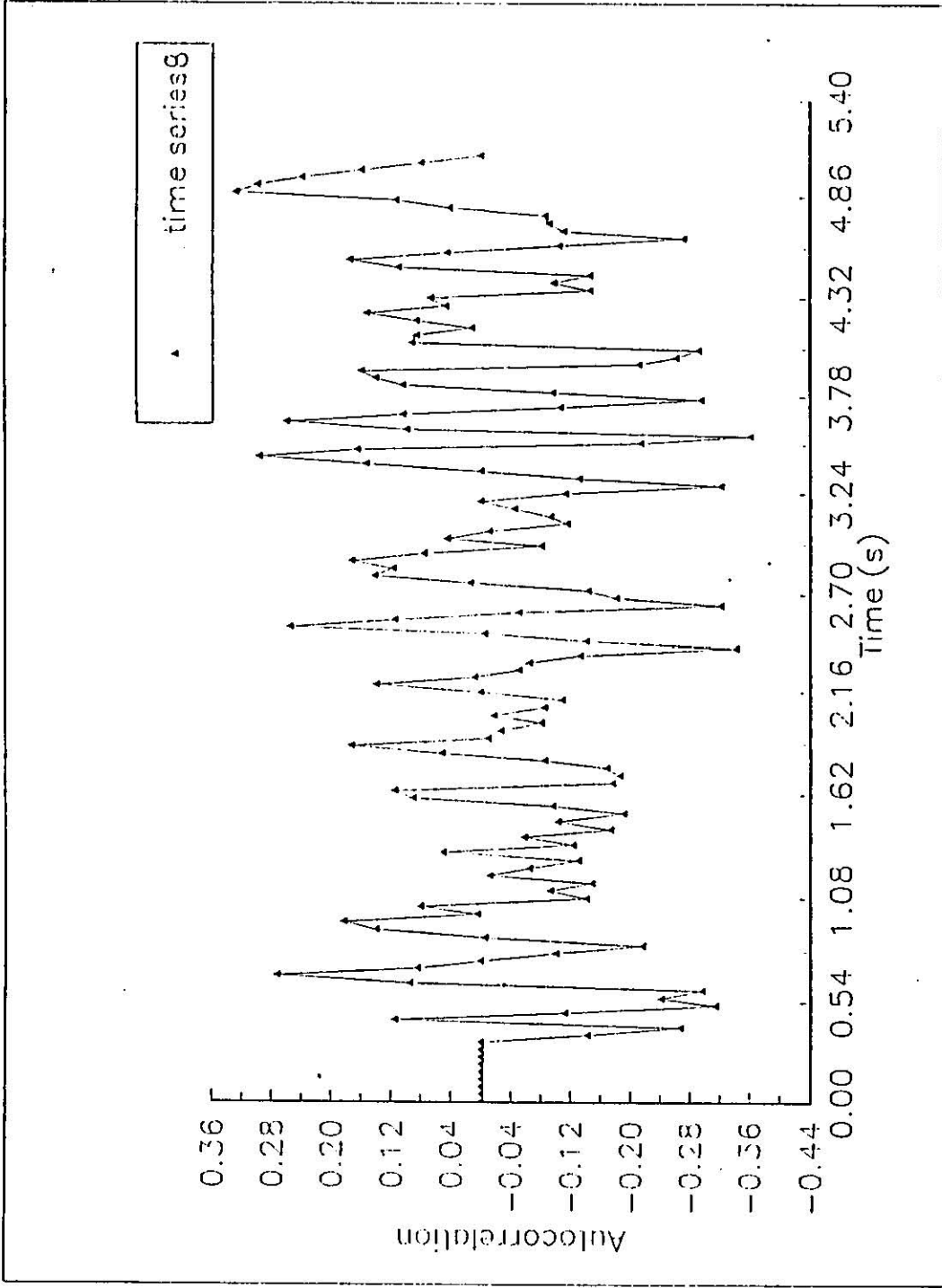


Figure 5.23 : The autocorrelation function of the 8th time-series

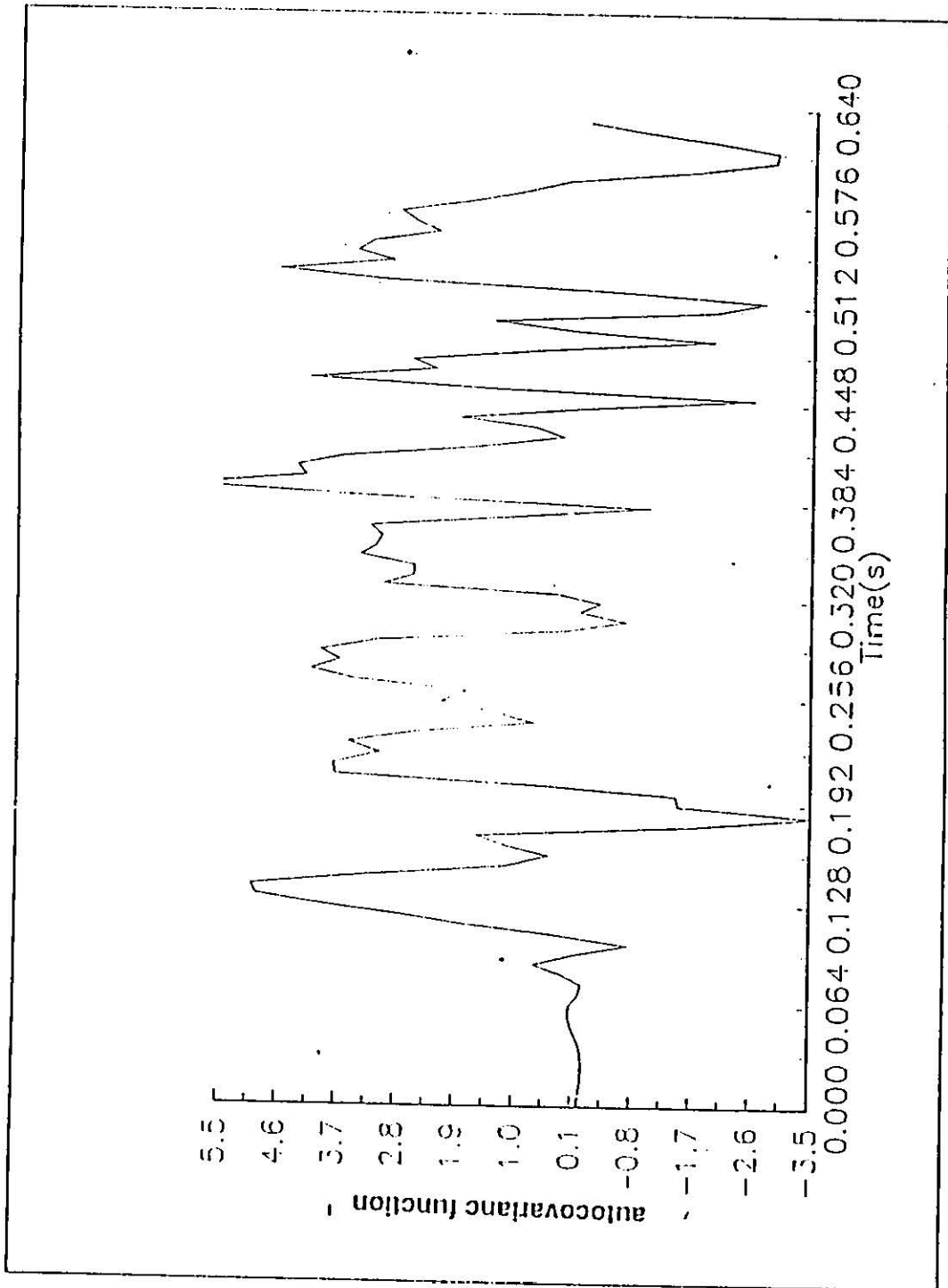


Figure 5.24 : The autocovariance function of the 1st time-series

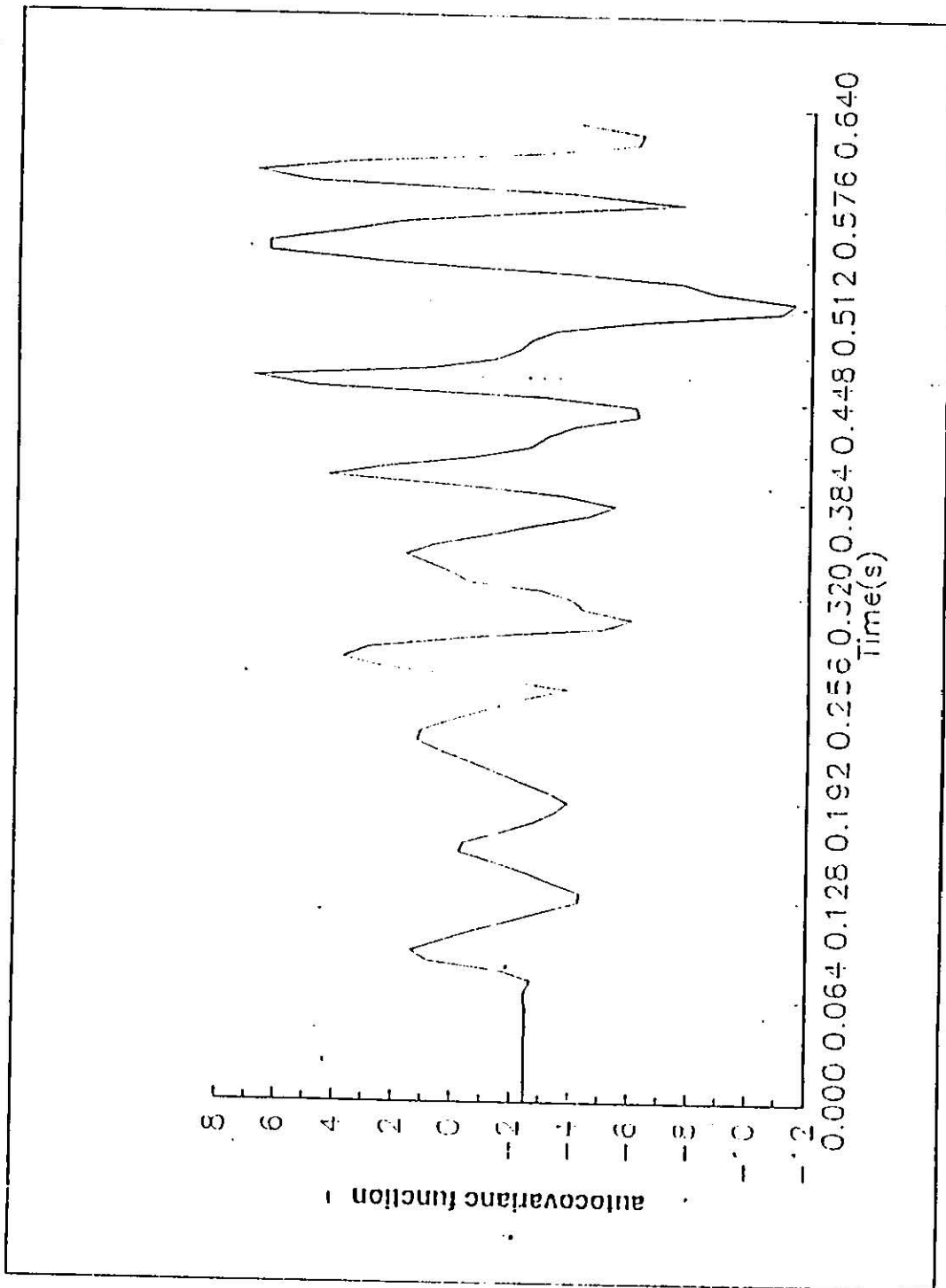


Figure 5.25 : The autocovariance function of the 2nd time-series

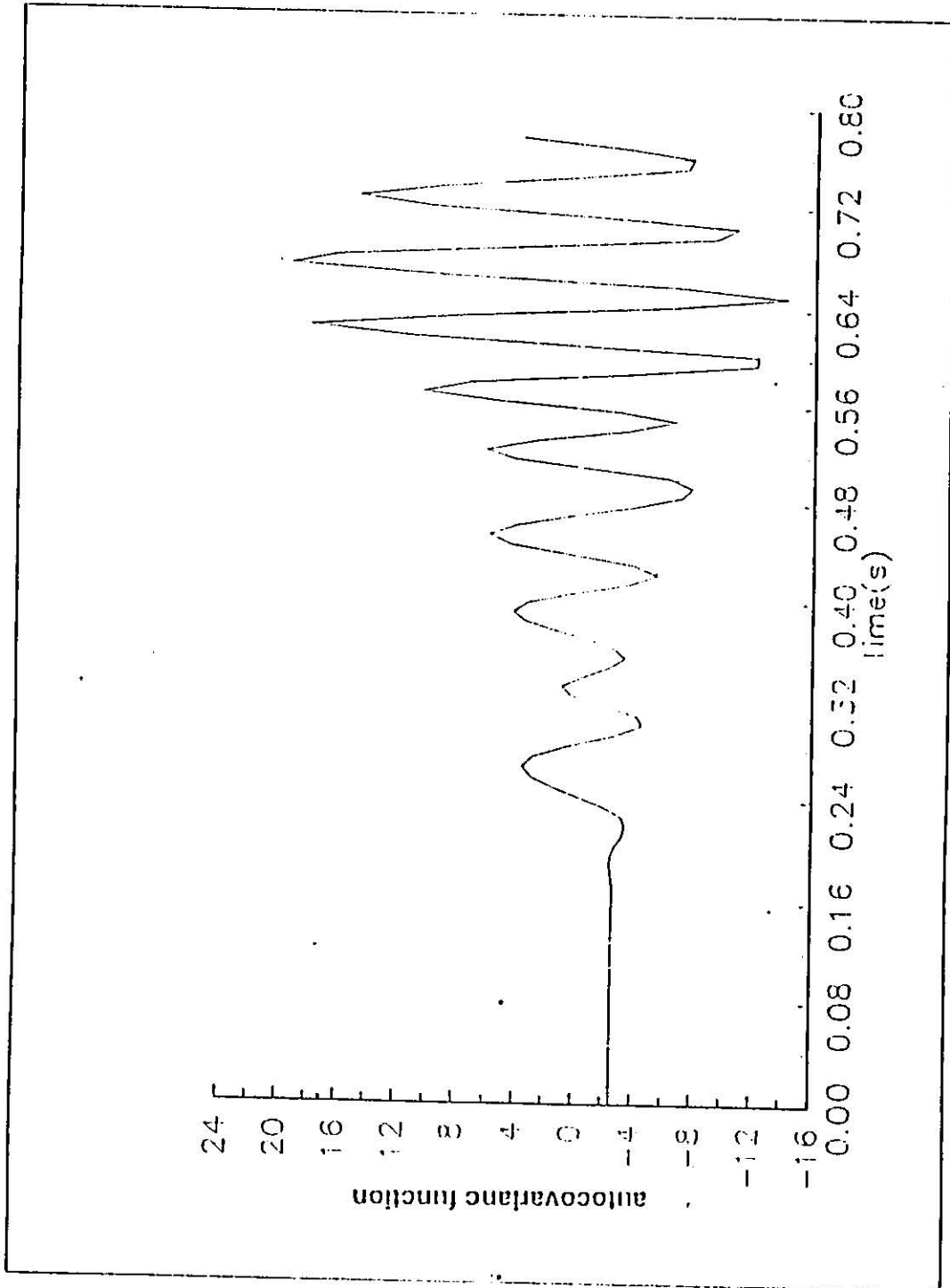


Figure 5.26 : The autocovariance function of the 3rd time-series

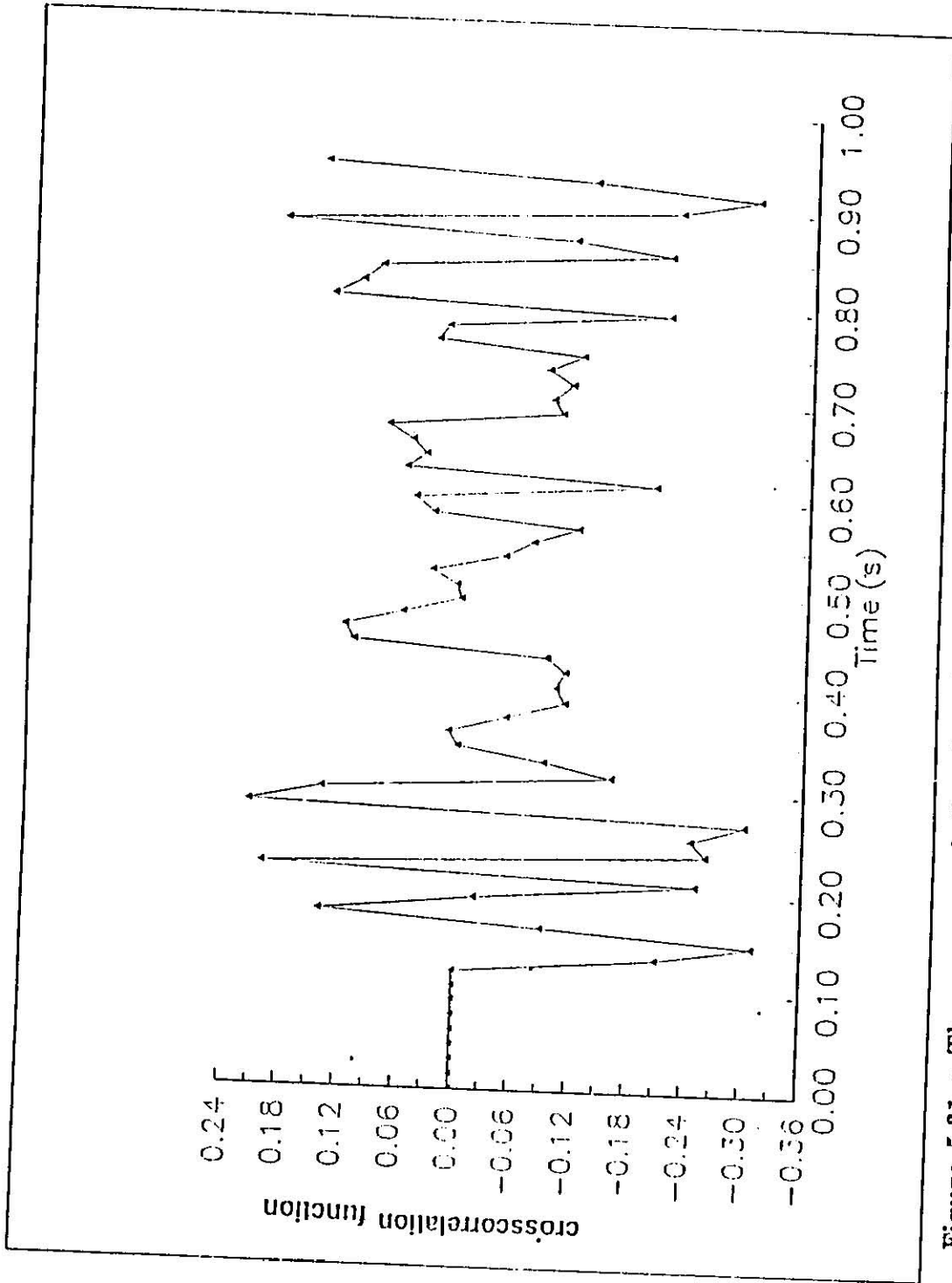


Figure 5.31 : The crosscorrelation function of the 4th and 5th time-series

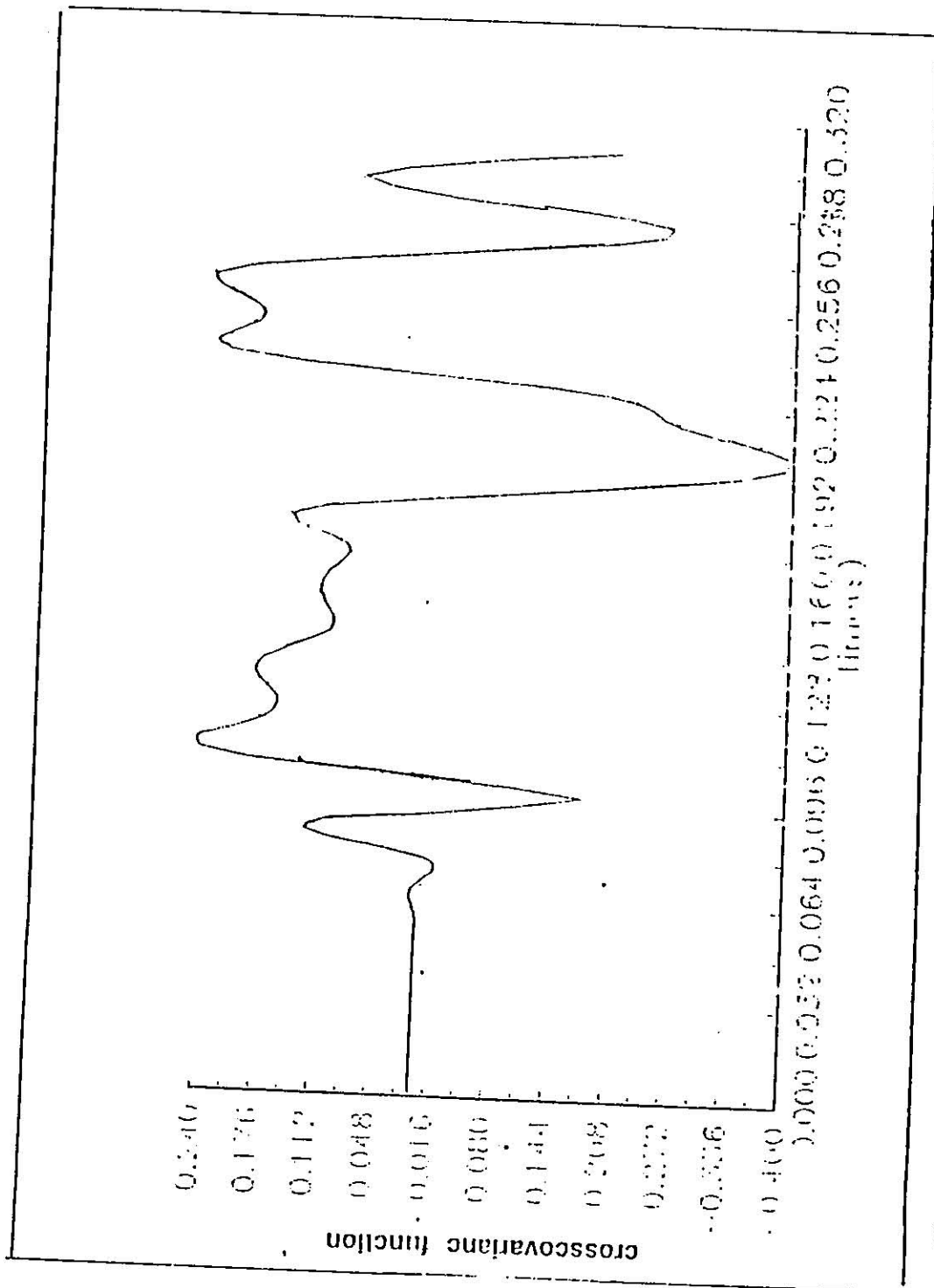


Figure 5.32 : The crosscovariance function of the 1st and 2nd time-series

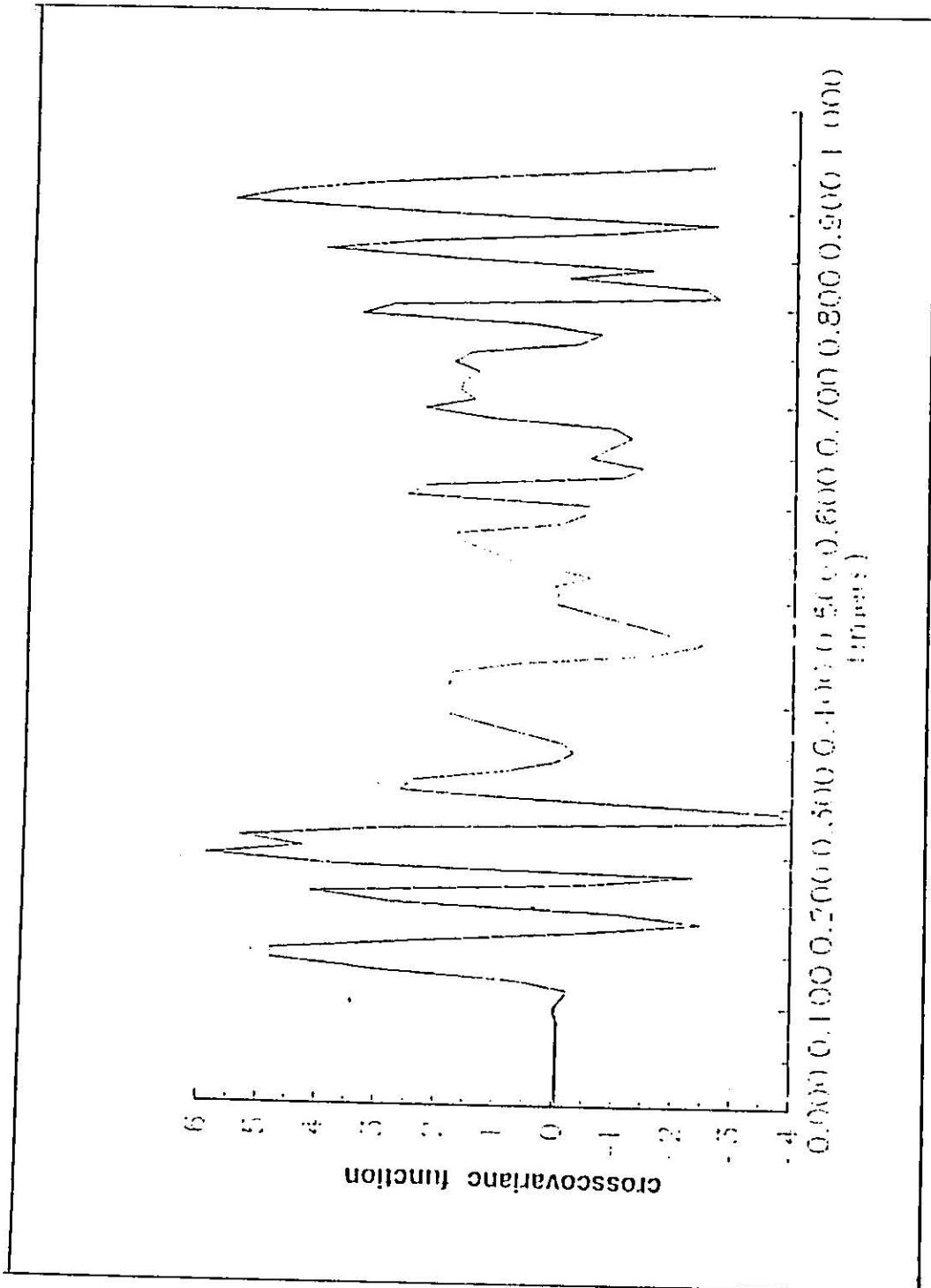


Figure 5.33 : The crosscovariance function of the 4th and 5th time-series

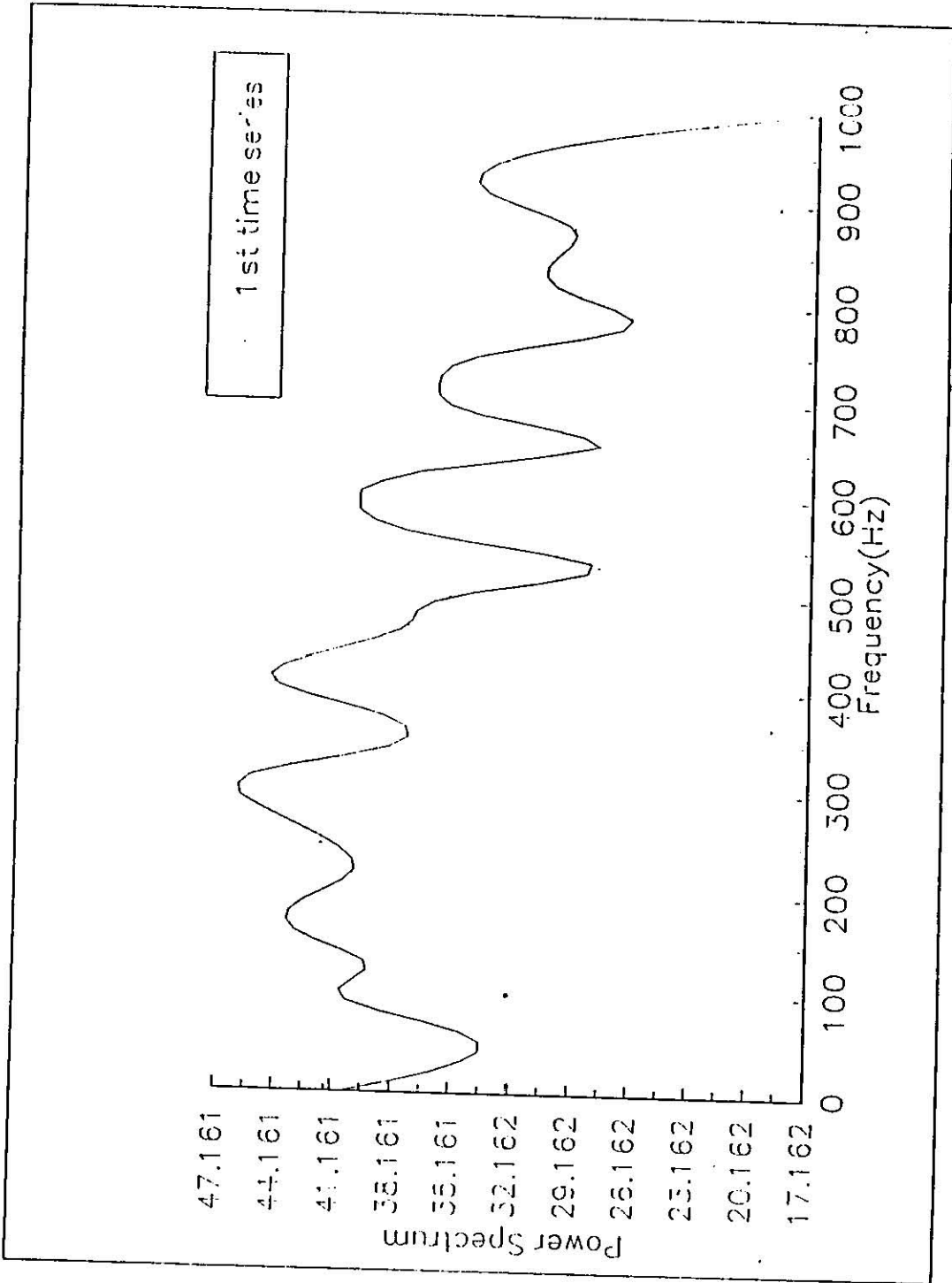


Figure 5.34 : The power spectrum of the autocorrelation function of the 1st time-series

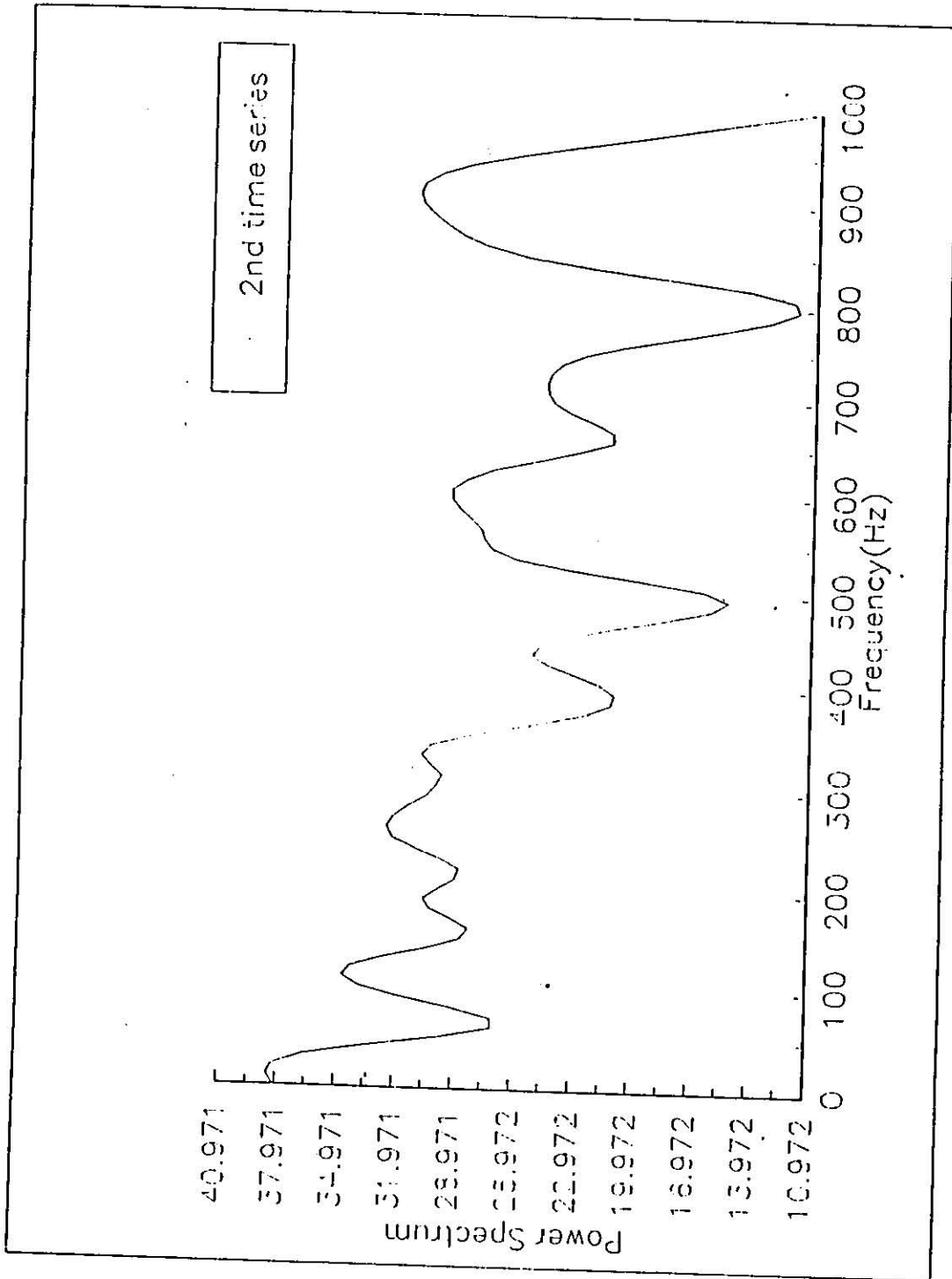


Figure 5.35 : The power spectrum of the autocorrelation function of the 2nd time-series

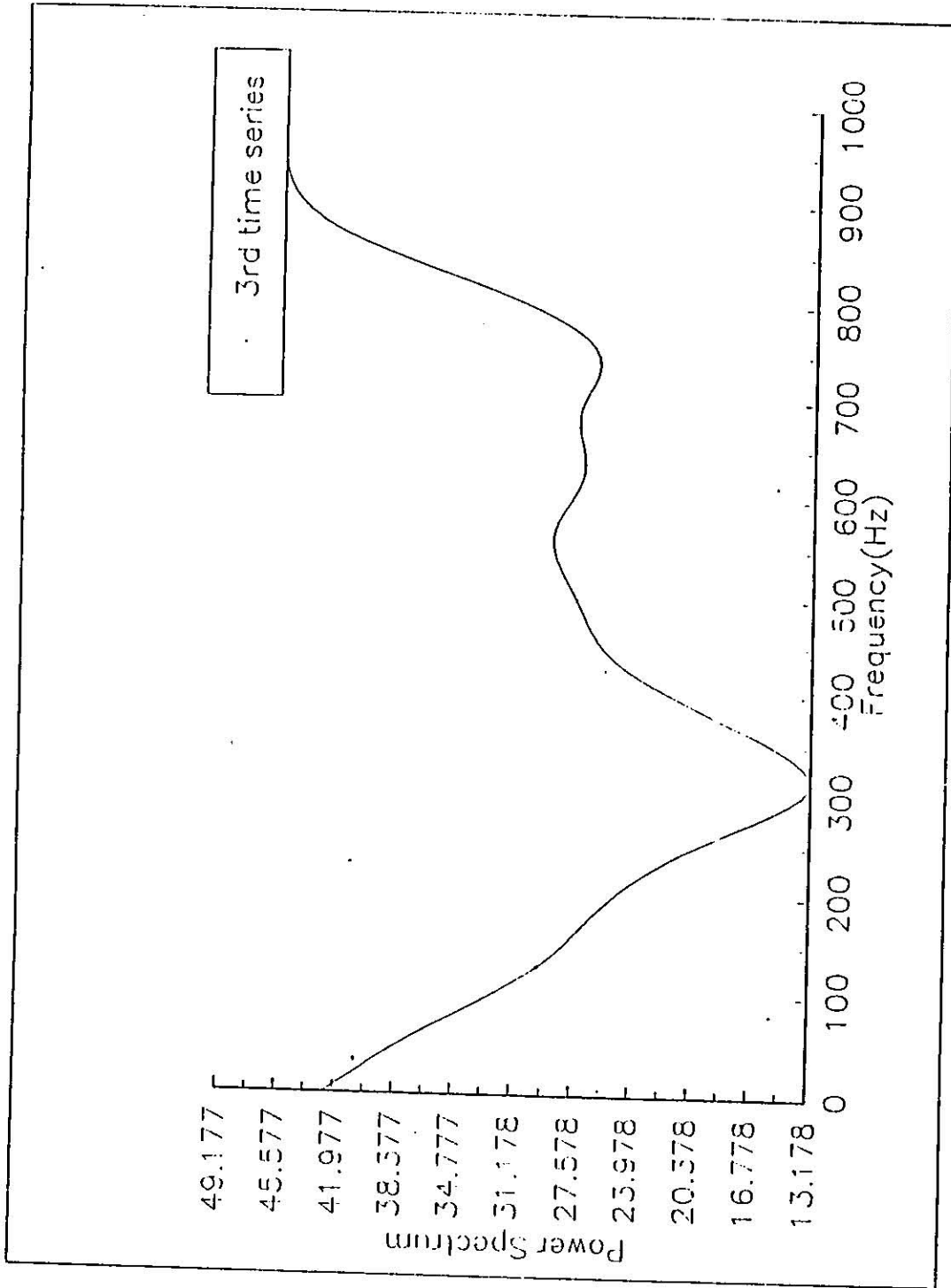


Figure 5.36 : The power spectrum of the autocorrelation function of the 3rd time-series

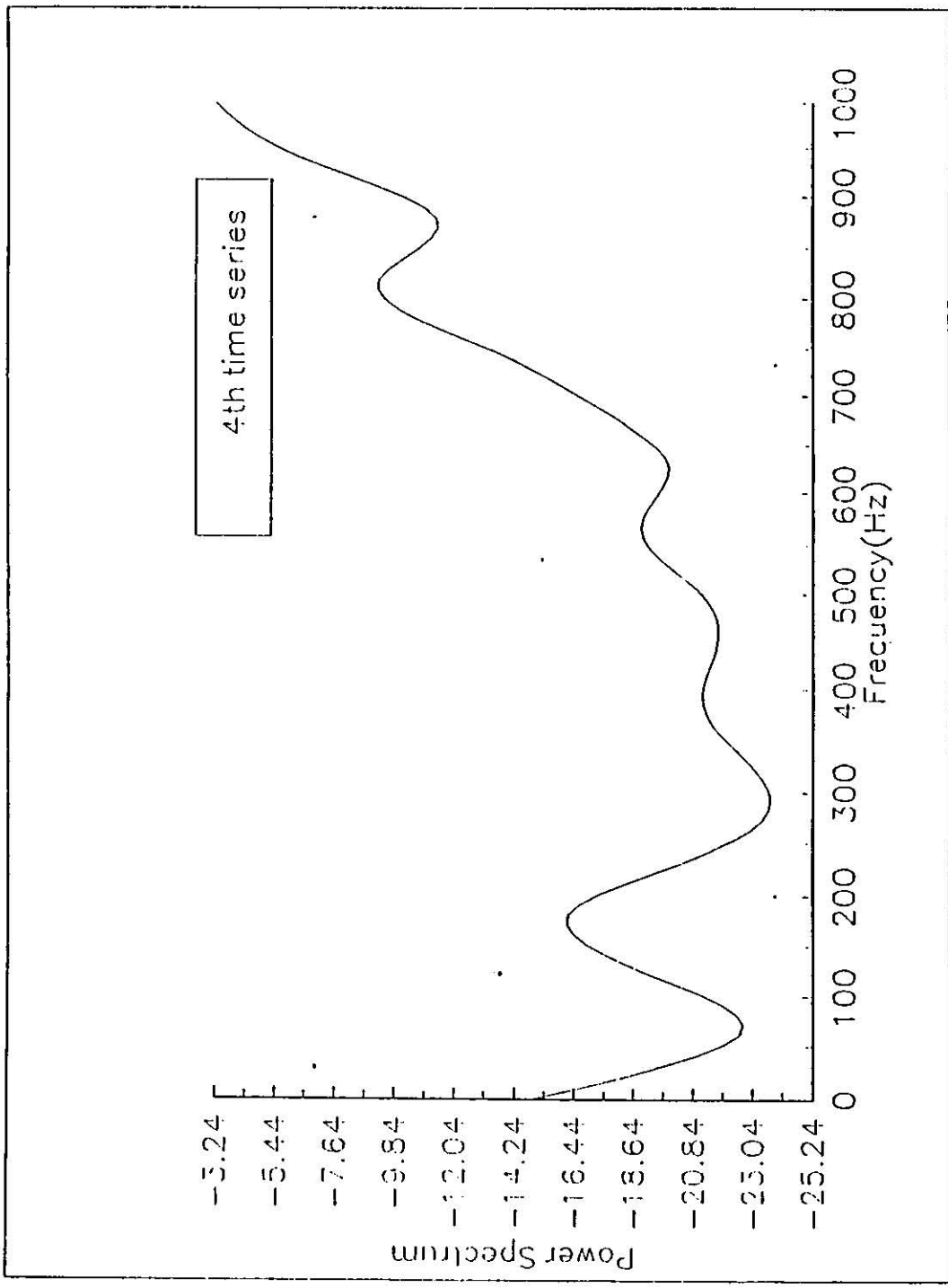


Figure 5.37 : The power spectrum of the autocorrelation function of the 4th time-series

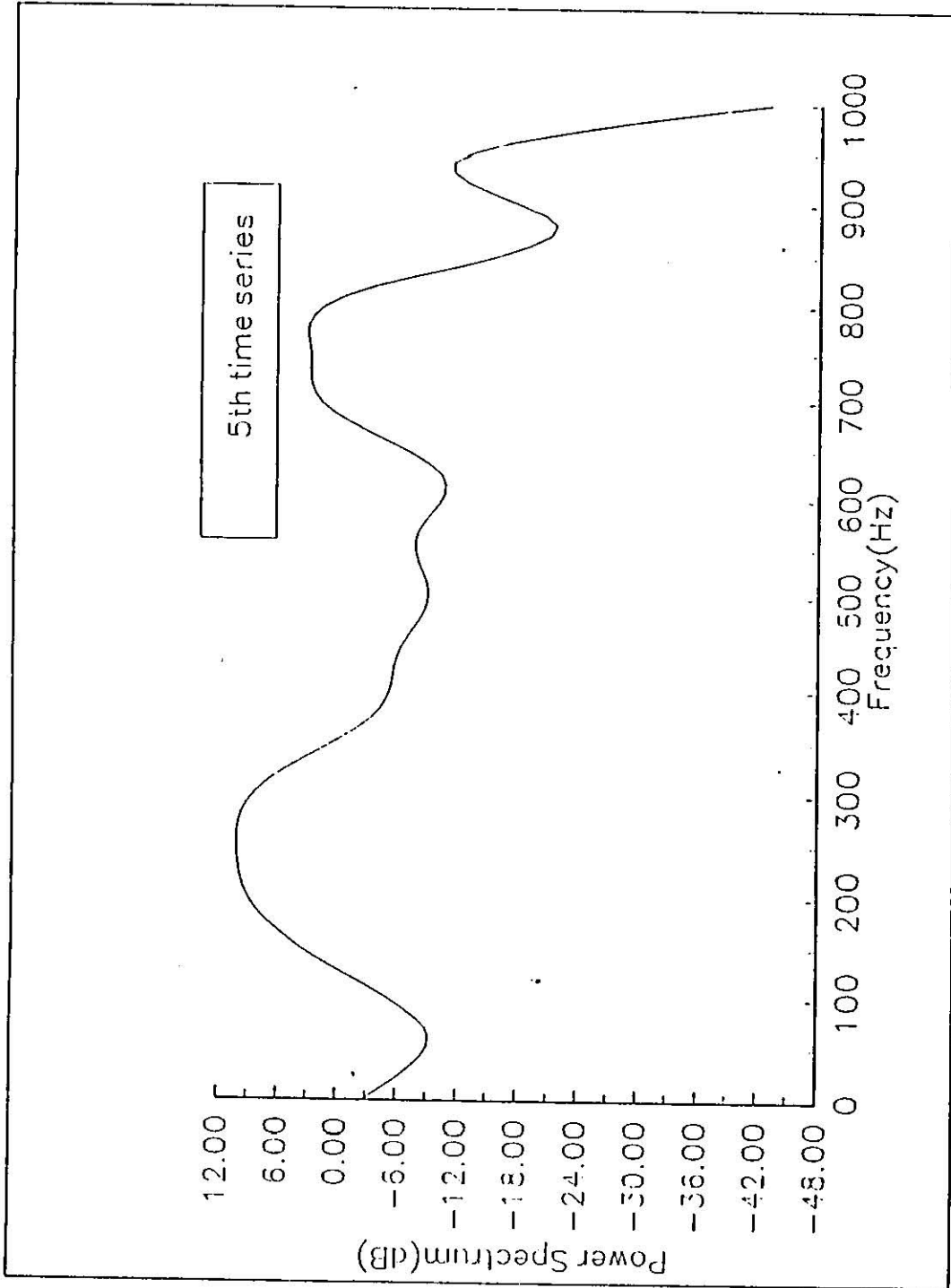


Figure 5.38 : The power spectrum of the autocorrelation function of the 5th time-series

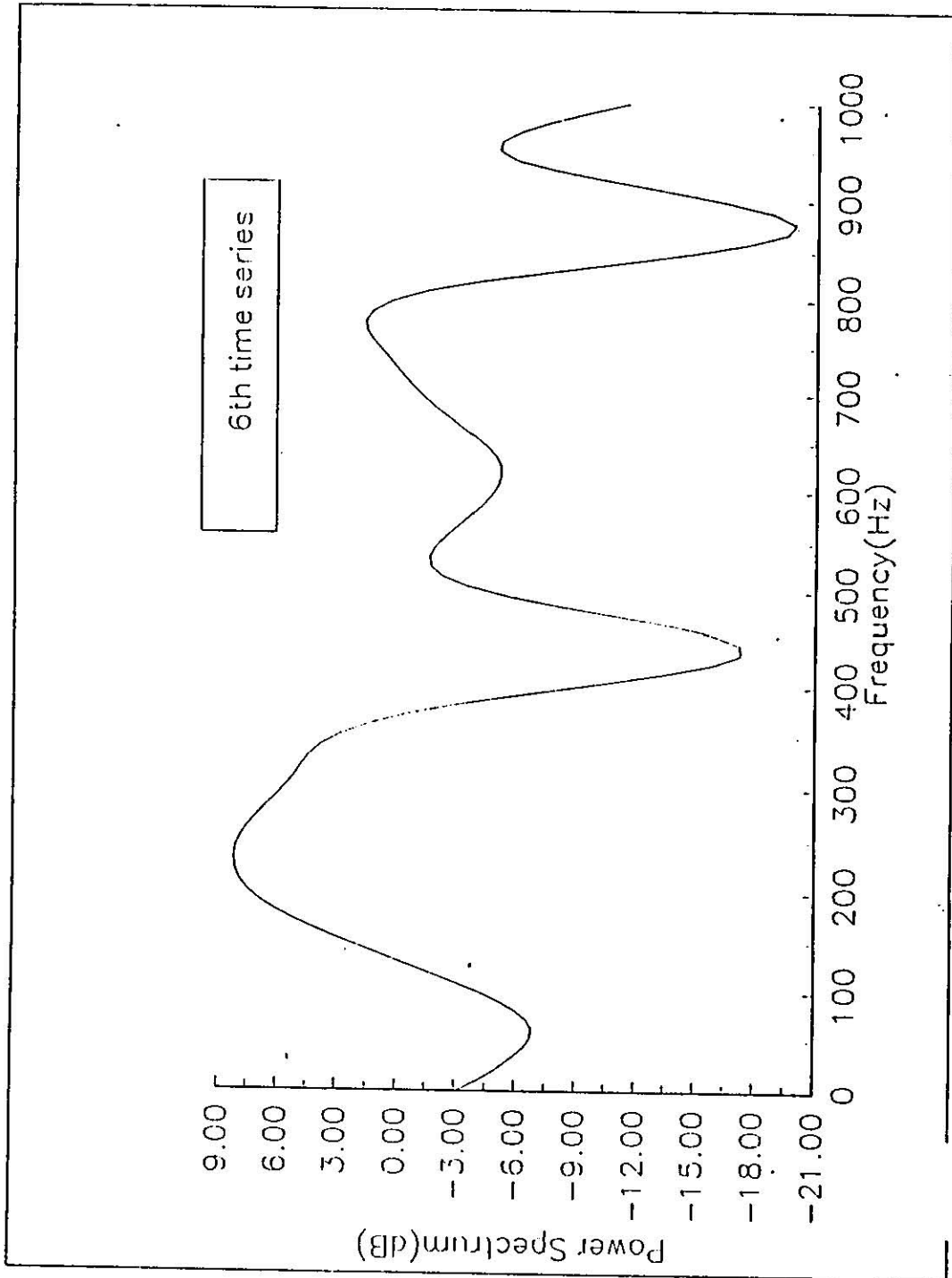


Figure 5.39 : The power spectrum of the autocorrelation function of the 6th time-series

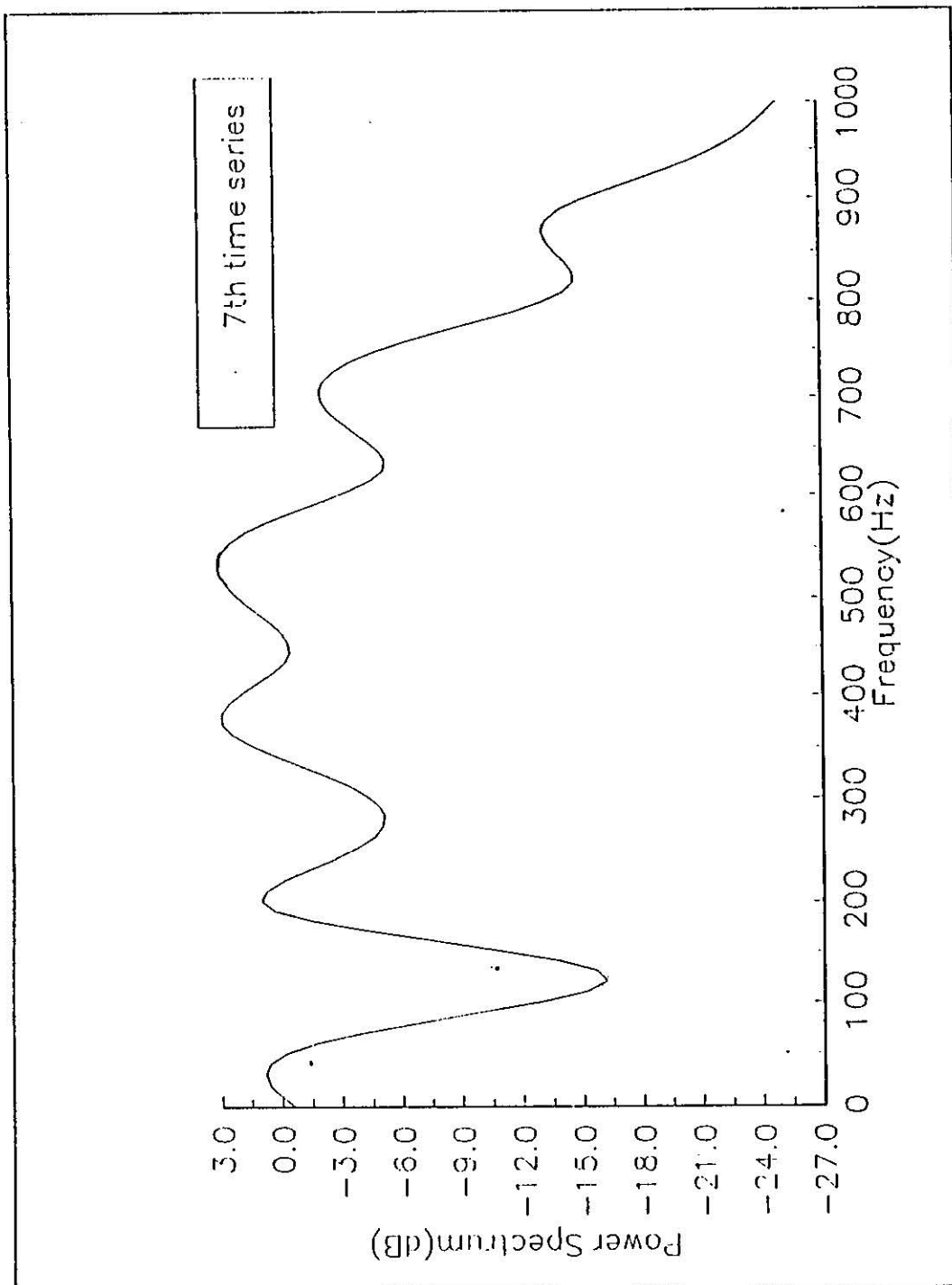


Figure 5.40 : The power spectrum of the autocorrelation function of the 7th time-series

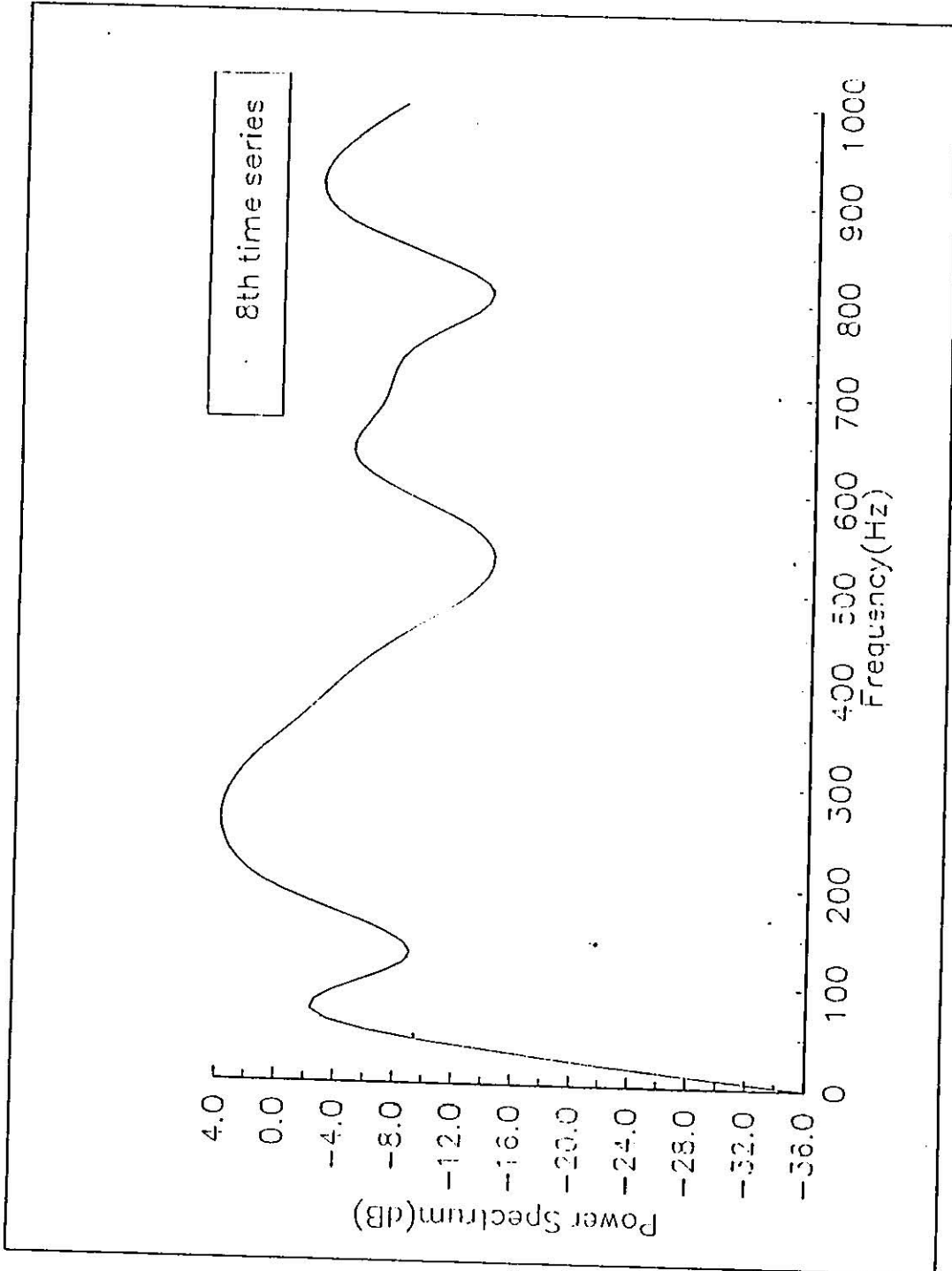


Figure 5.41 : The power spectrum of the autocorrelation function of the 8th time-series

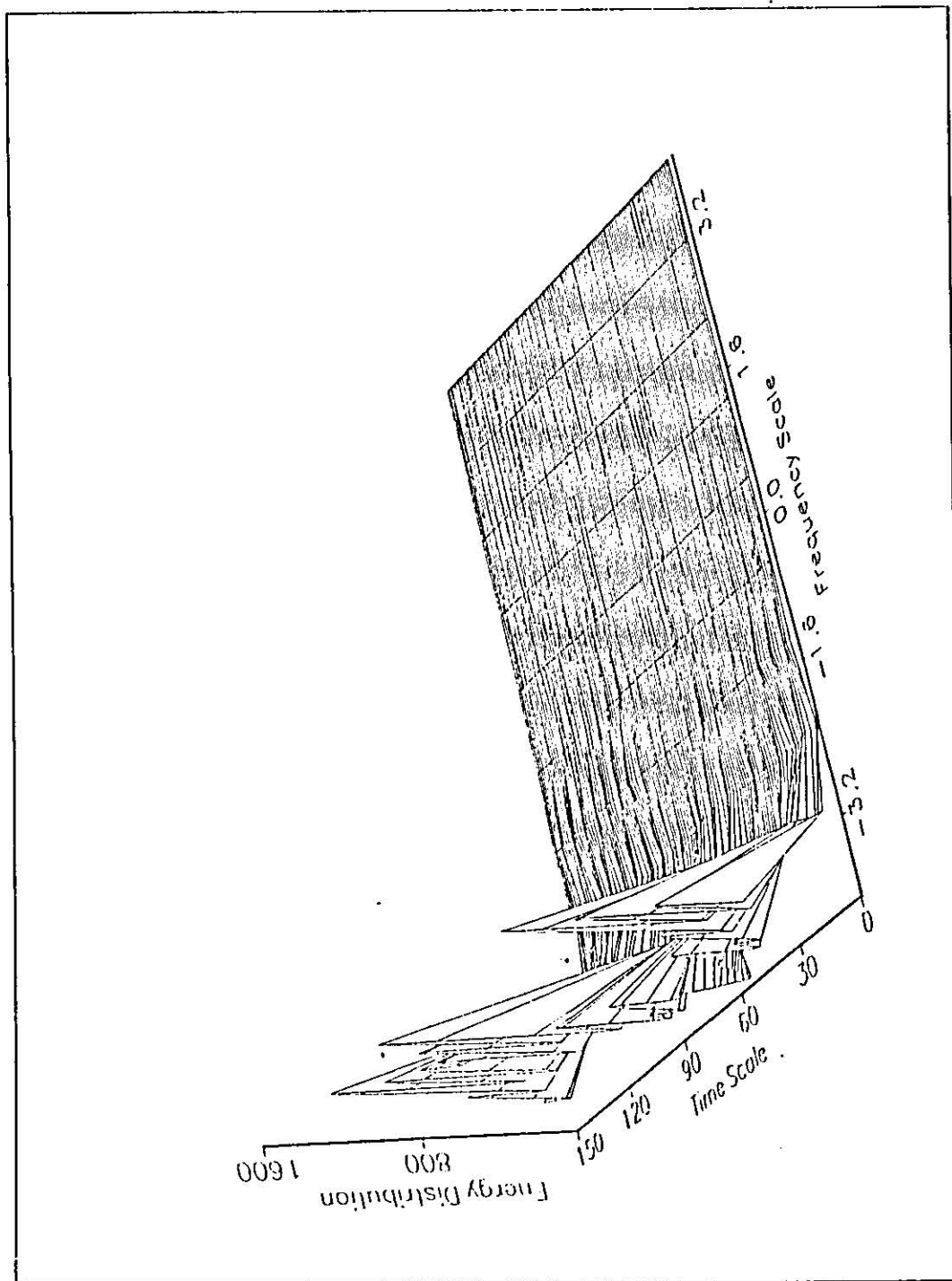


Figure 5.42 :The wavelet transform of the frequency distribution at $U=5.0$ m/s using Mallat wavelet

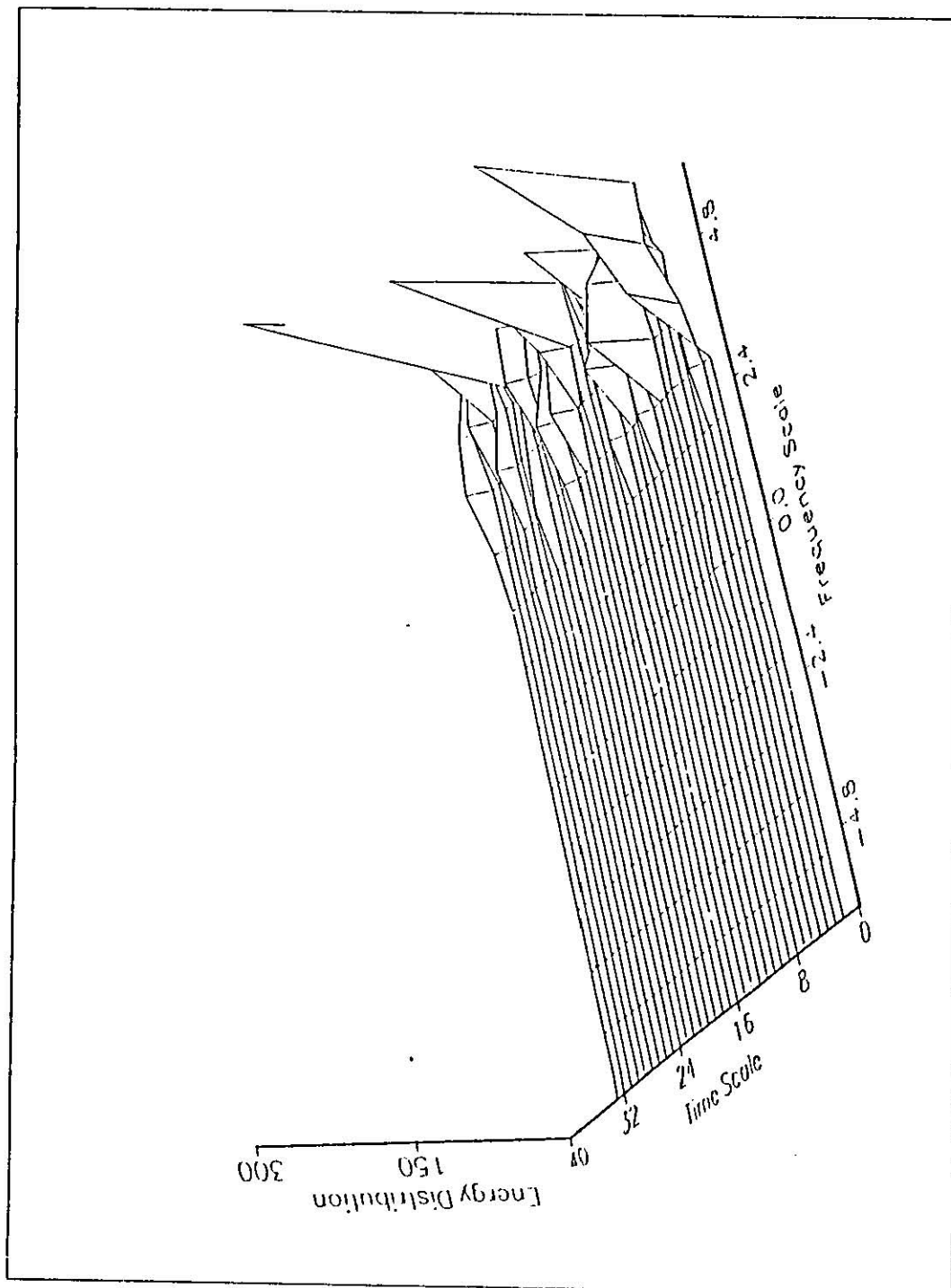


Figure 5.43 :The wavelet transform of the frequency distribution at $U=5.0$ m/s using Daubichies' wavelet

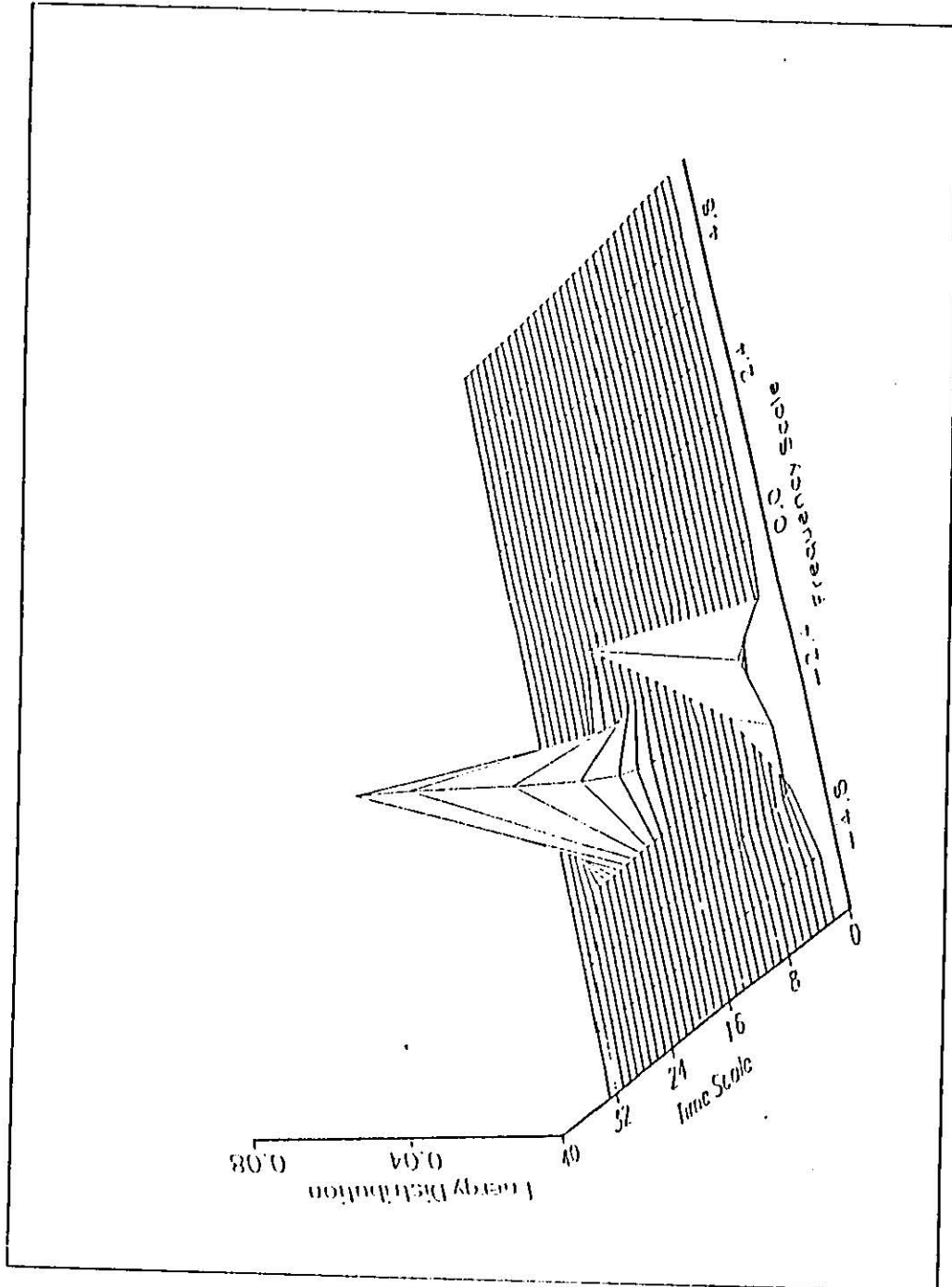


Figure 5.44 :The wavelet transform of the frequency distribution at $U=5.0$ m/s using Modulated Gaussian wavelet

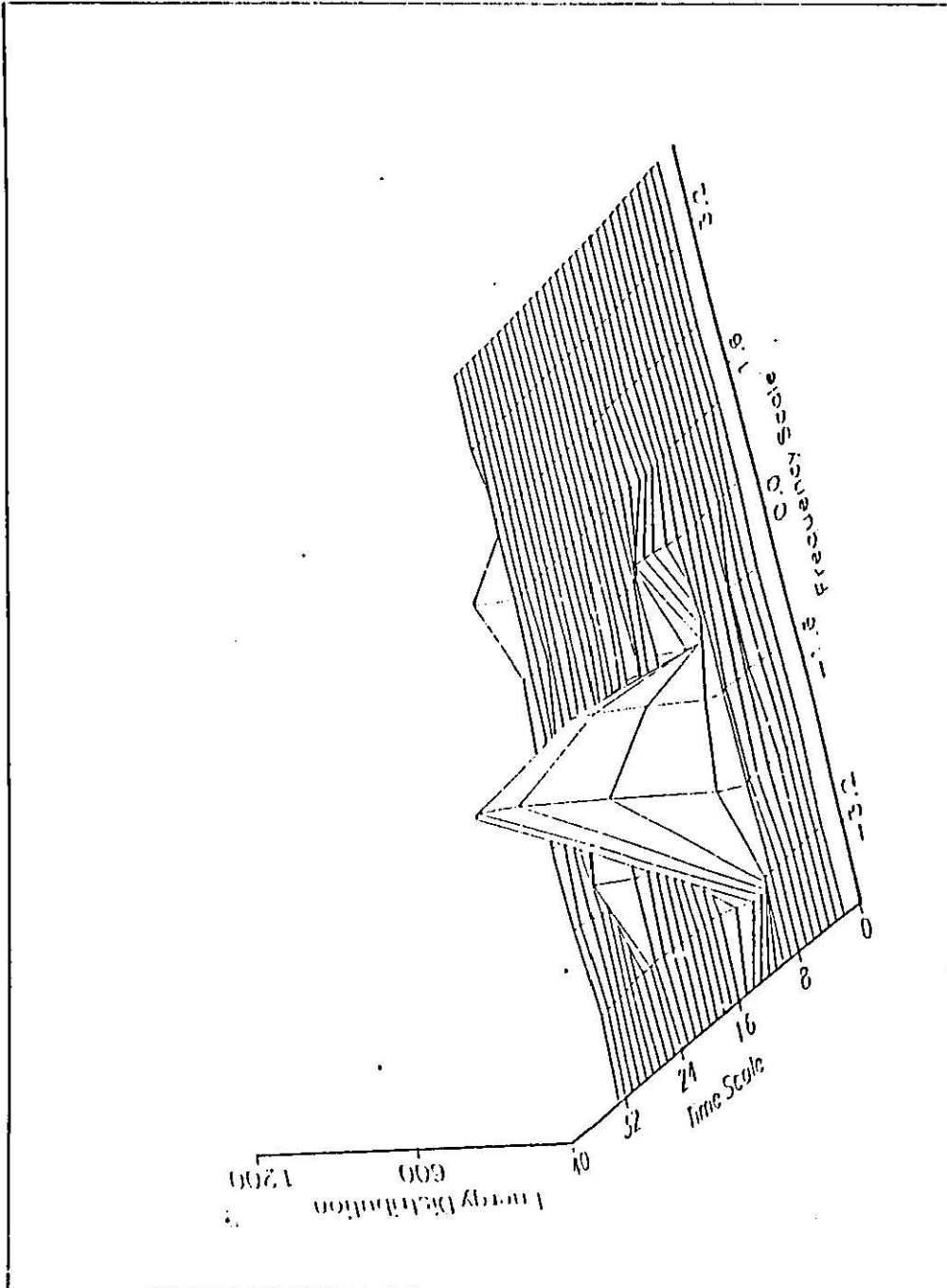


Figure 5.45 :The wavelet transform of the frequency distribution at $U=5.0$ m/s using 8th derivative of Gaussian wavelet

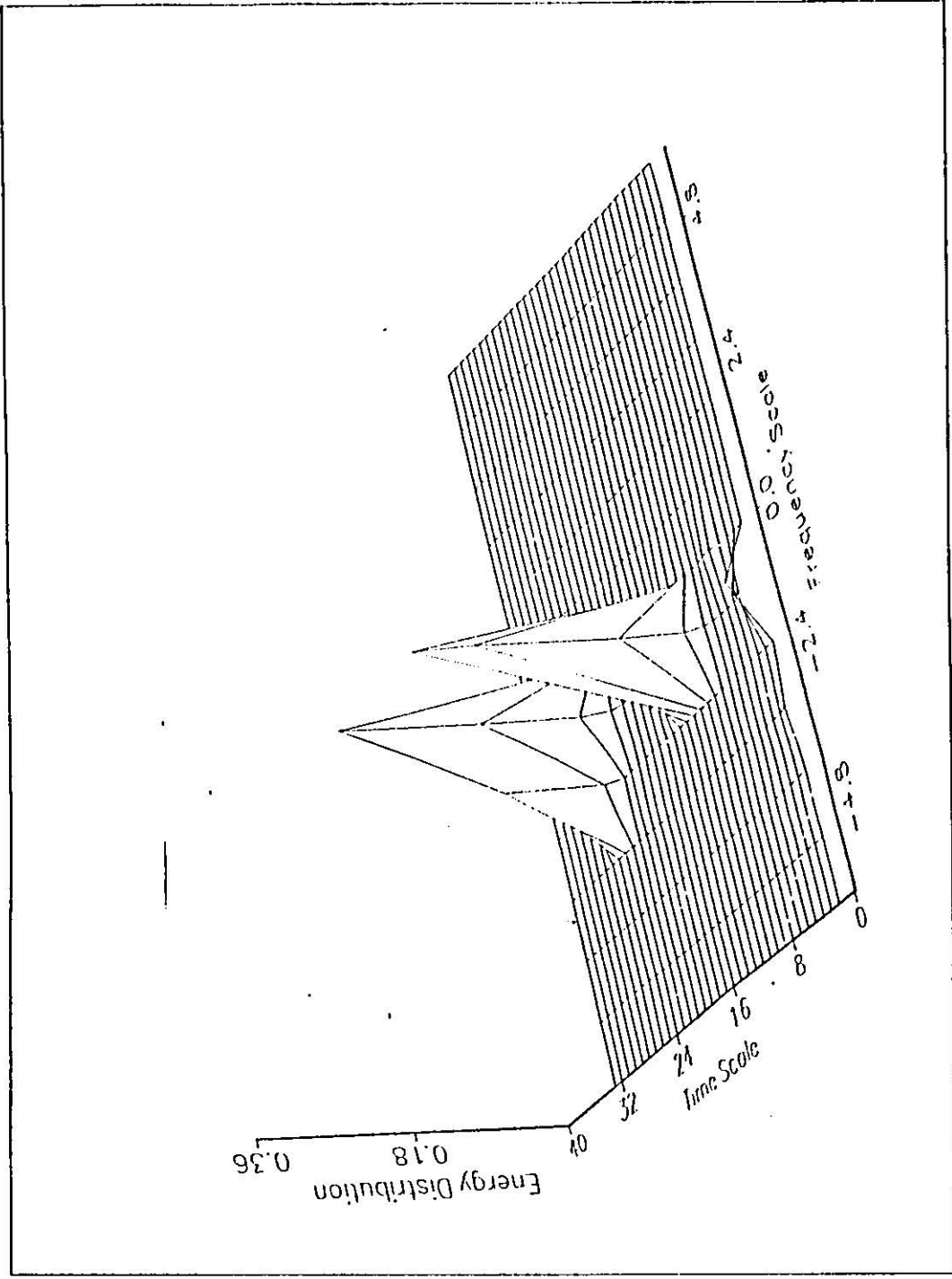


Figure 5.46 :The wavelet transform of the frequency distribution at $U=5.0$ m/s using (One cycle of sine) wavelet

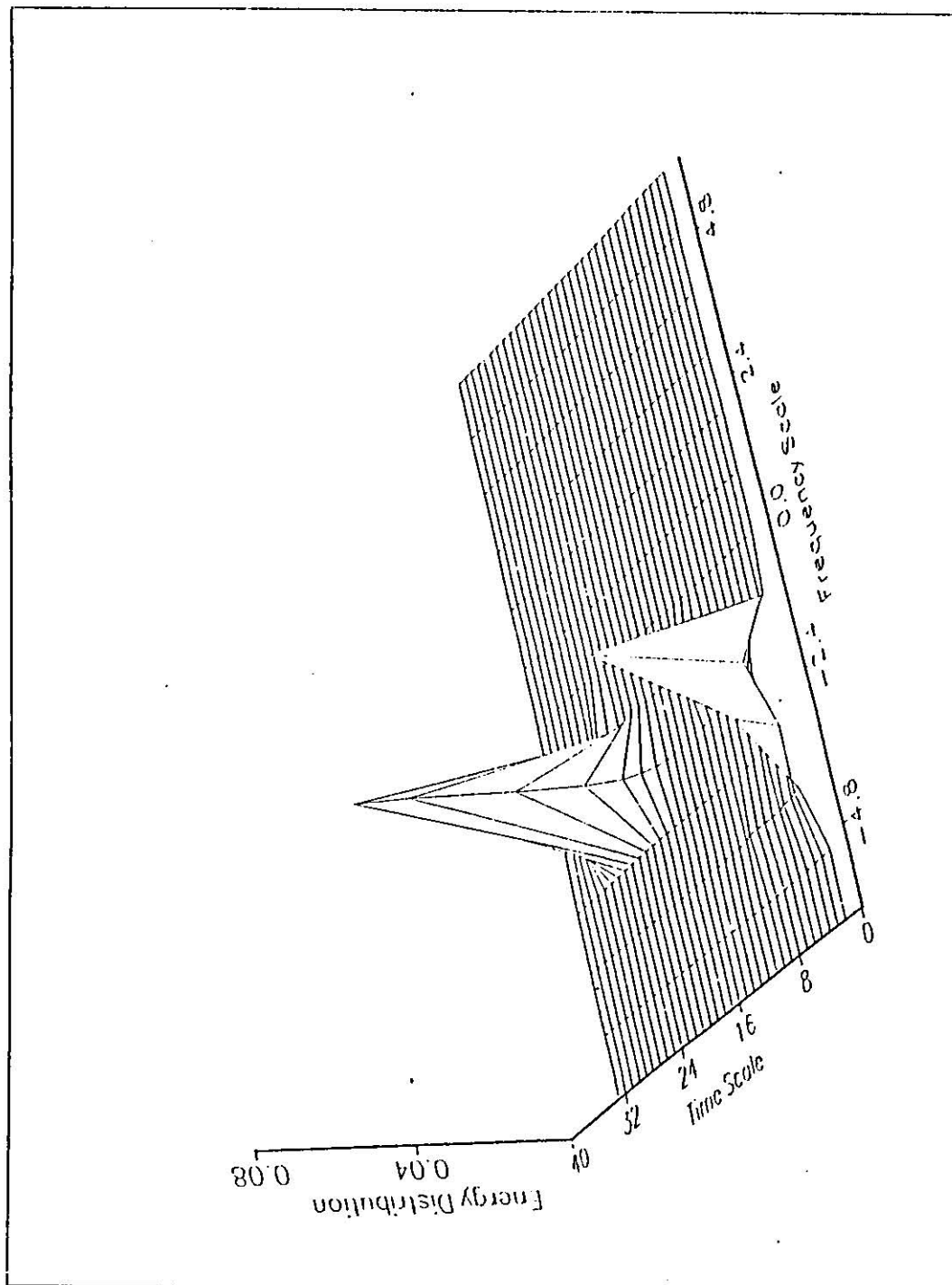


Figure 5.48 :The wavelet transform of the frequency distribution at $U=5.85$ m/s using Modulated Gaussian wavelet

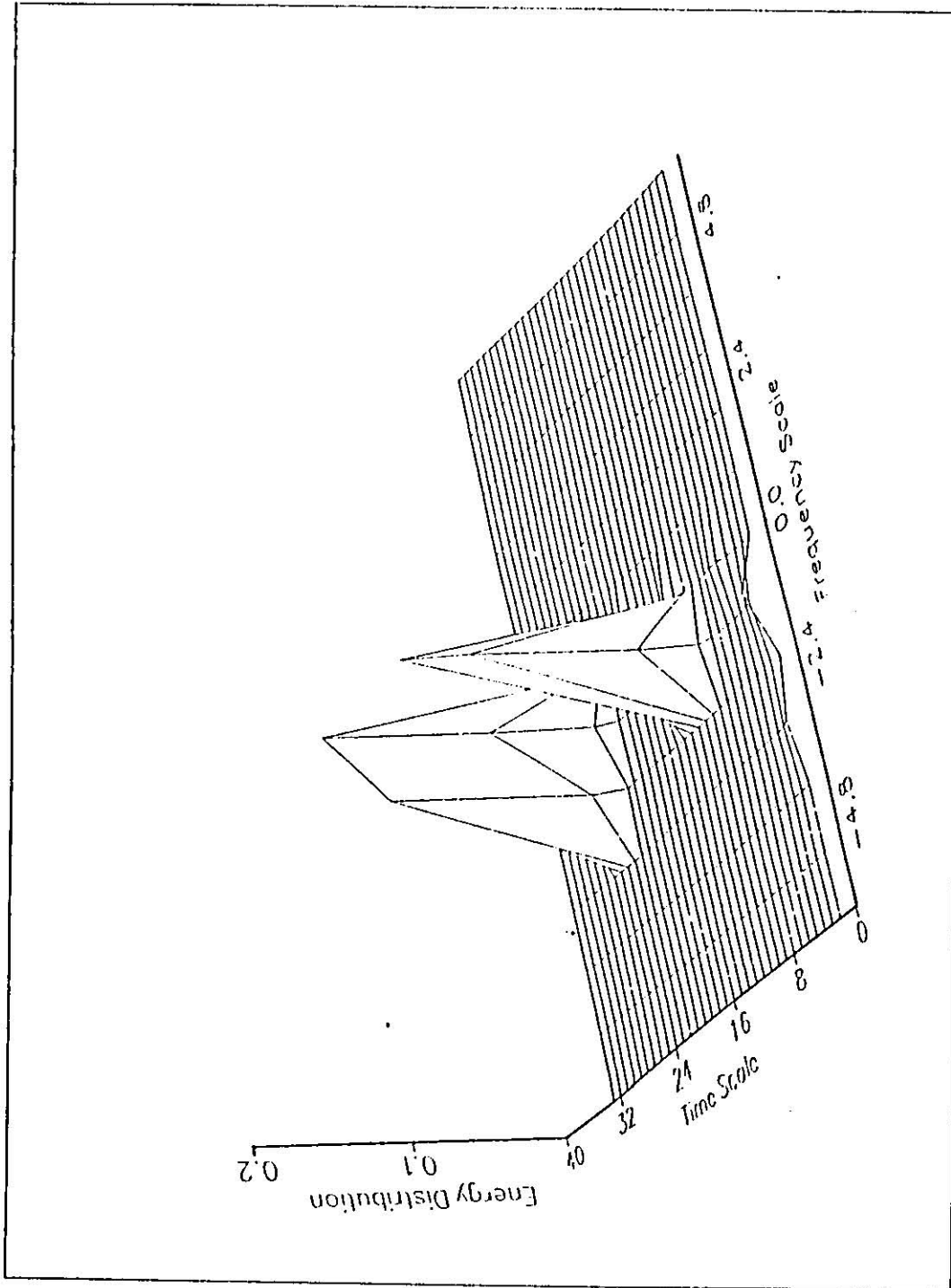


Figure 5.49 :The wavelet transform of the frequency distribution at $U=6.79$ m/s using Modulated Gaussian wavelet

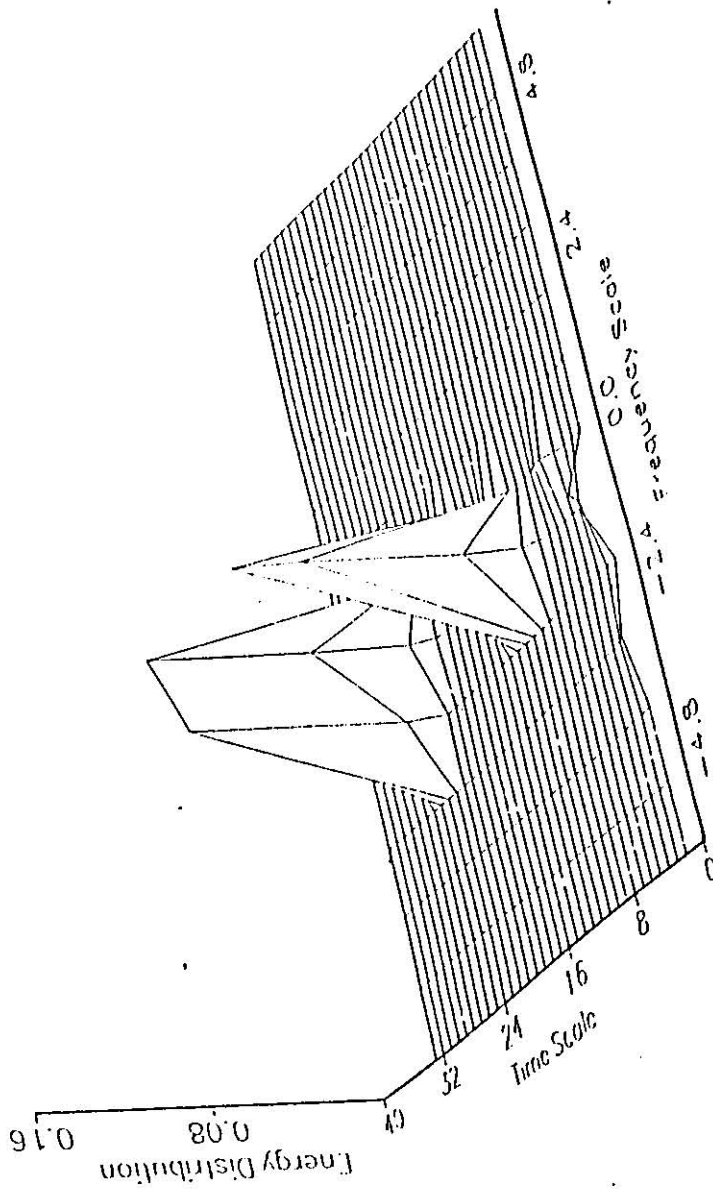


Figure 5.50 :The wavelet transform of the frequency distribution at $U=19.79$ m/s using Modulated Gaussian wavelet

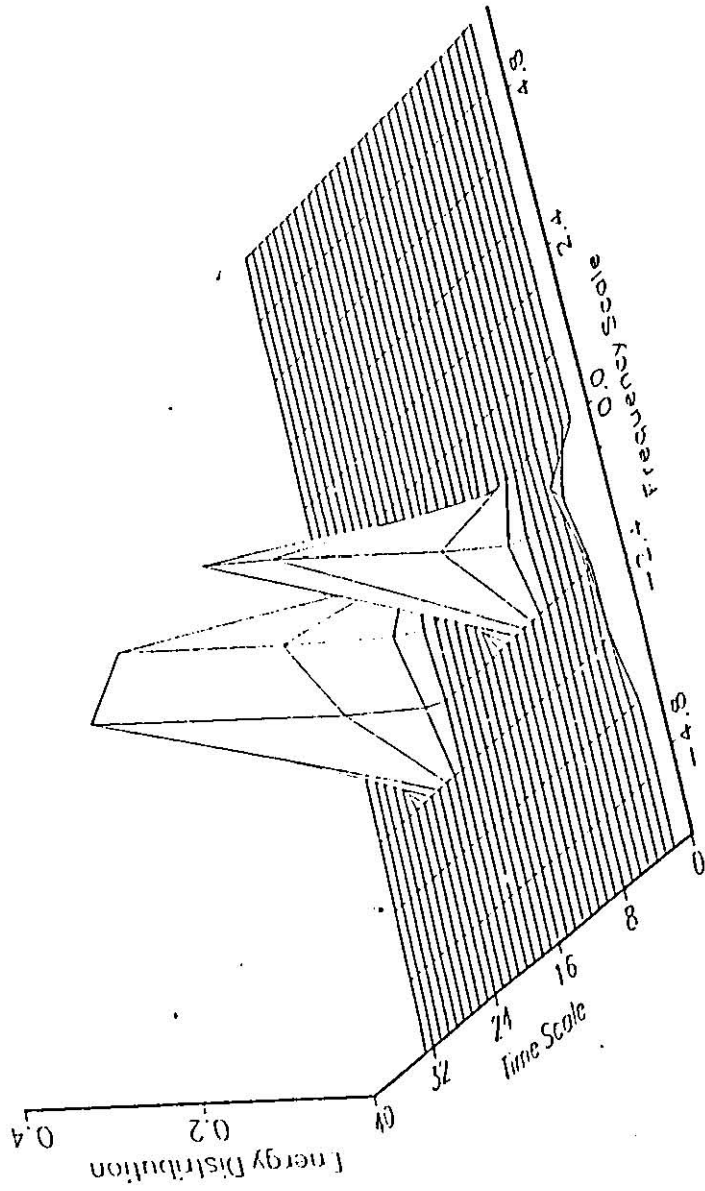


Figure 5.51 :The wavelet transform of the frequency distribution at $U=7.81$ m/s using Modulated Gaussian wavelet

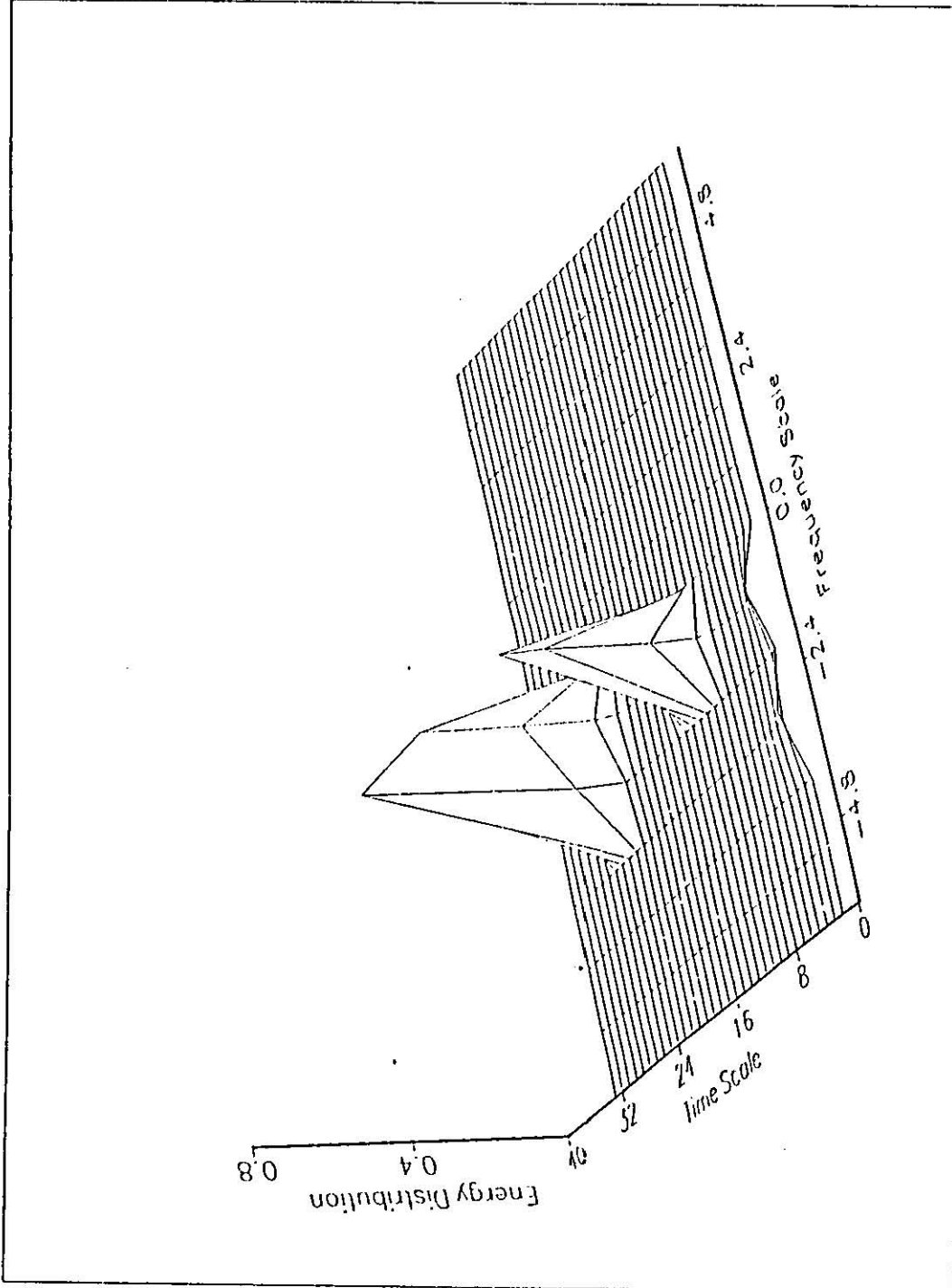


Figure 5.52 :The wavelet transform of the frequency distribution at $U=26.33$ m/s using Modulated Gaussian wavelet

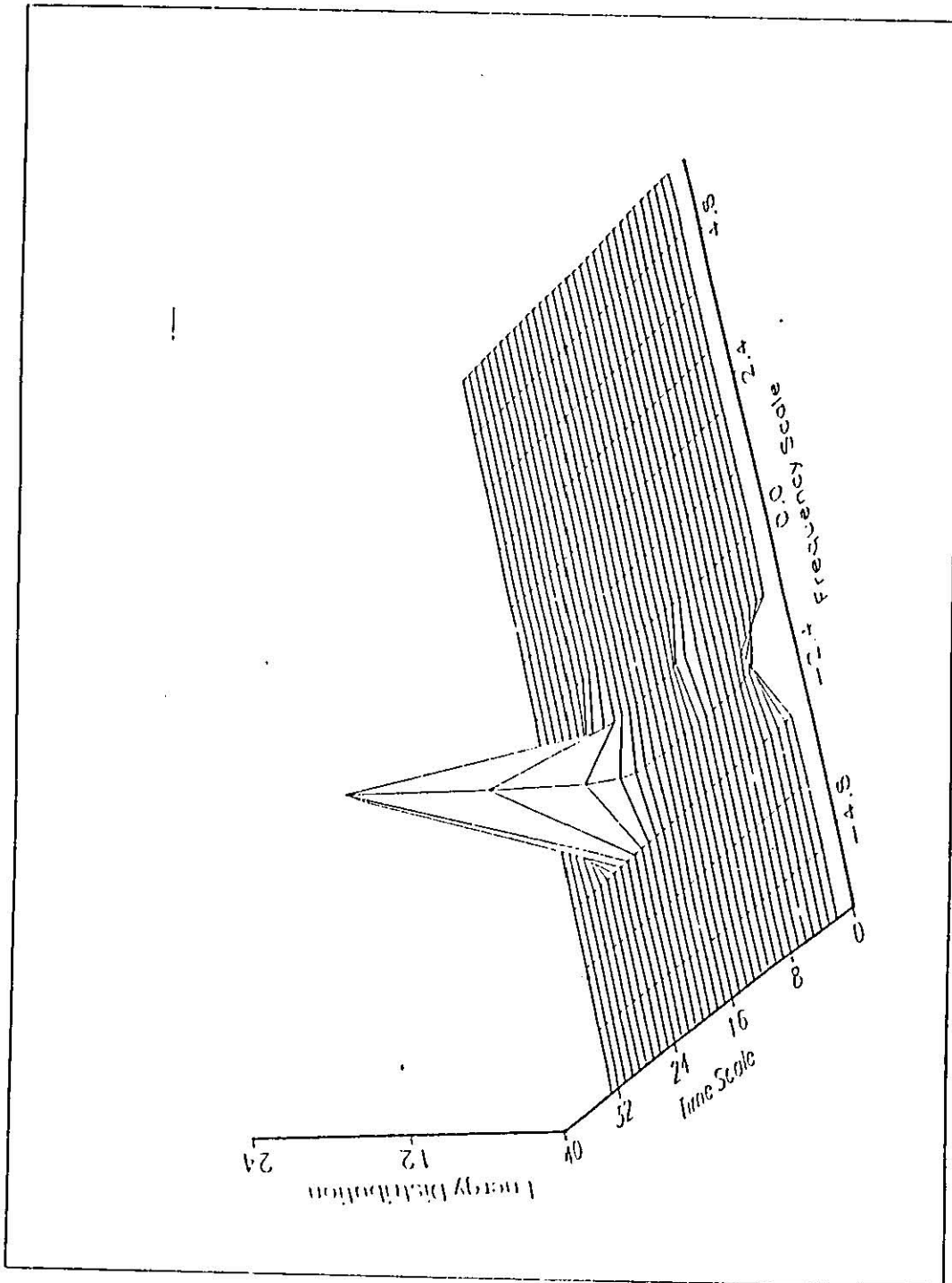


Figure 5.53 :The wavelet transform of the frequency distribution at $U=28.79$ m/s using Modulated Gaussian wavelet

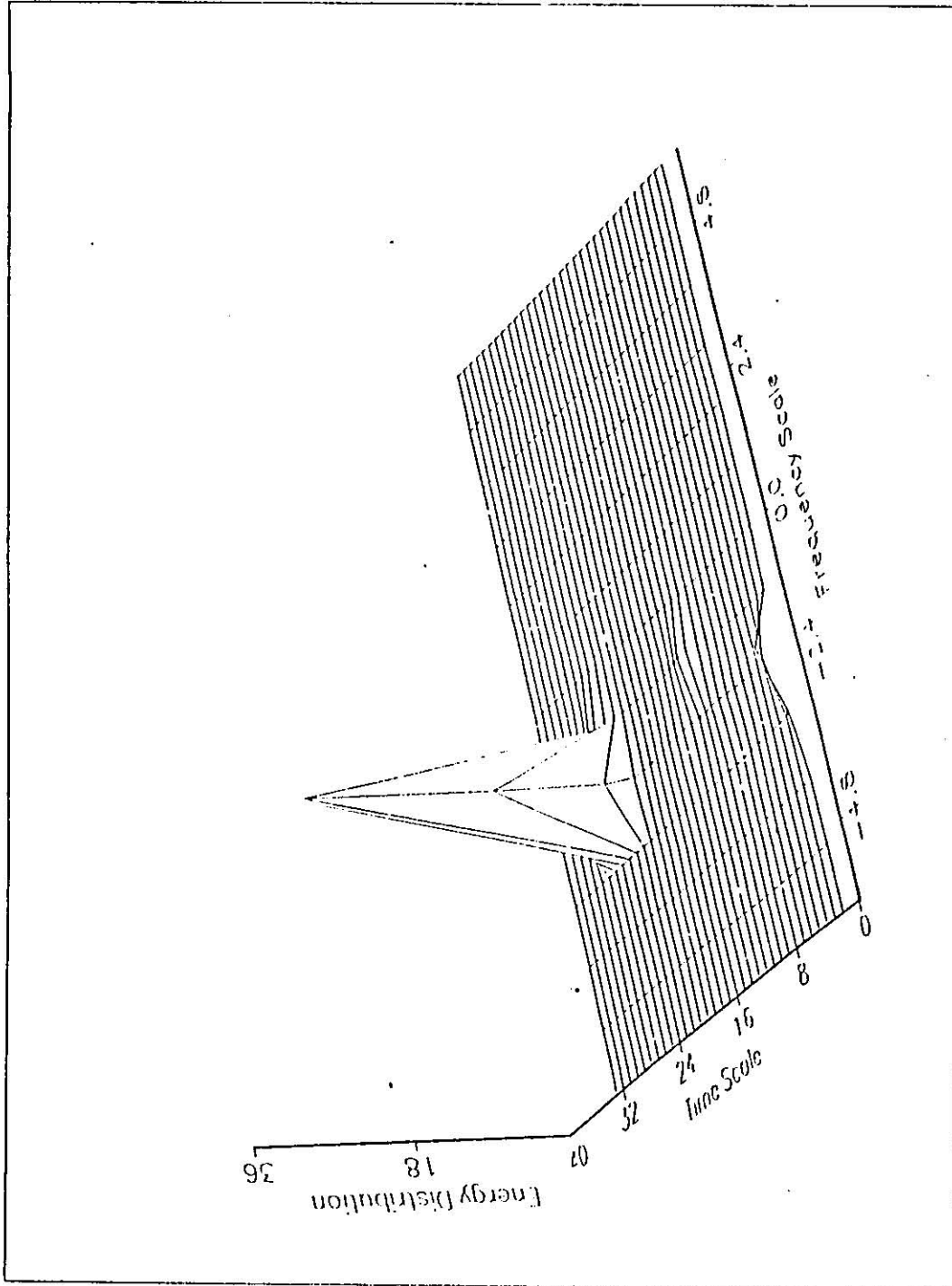
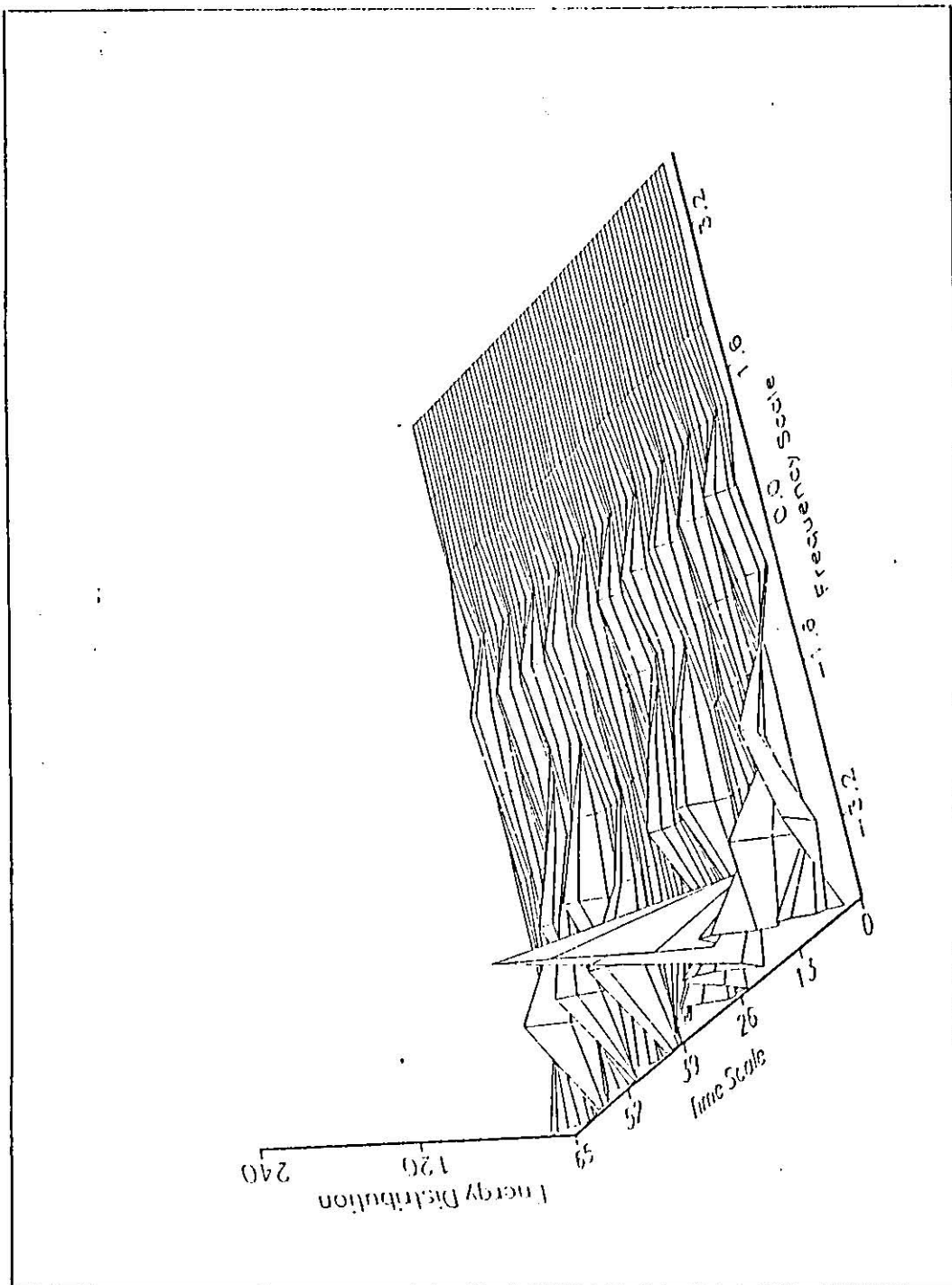


Figure 5.54 :The wavelet transform of the frequency distribution at $U=31.41$ m/s using Modulated Gaussian wavelet



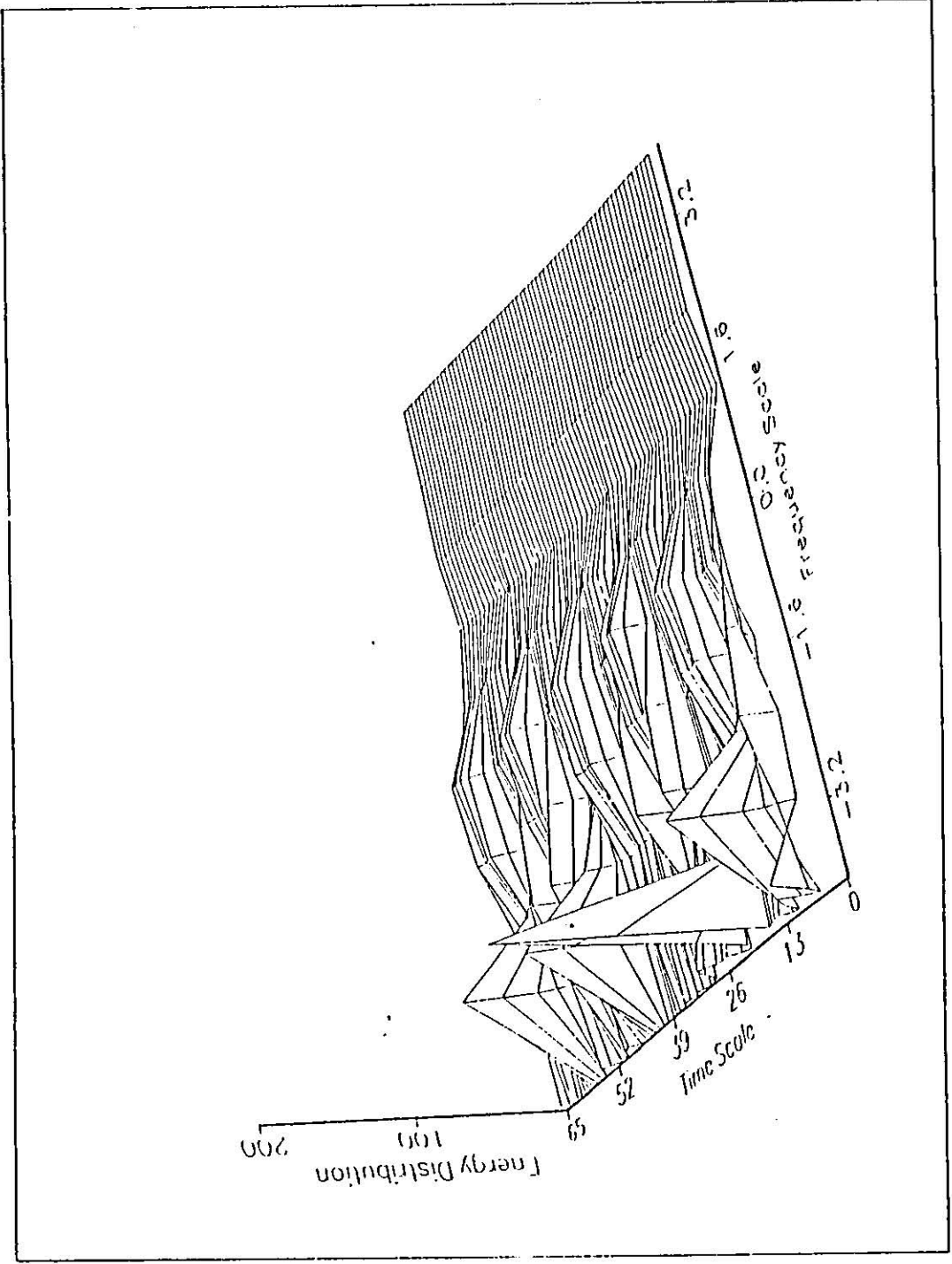


Figure 5.56 :The wavelet transform of the 1st time-series using Modified Gaussian wavelet

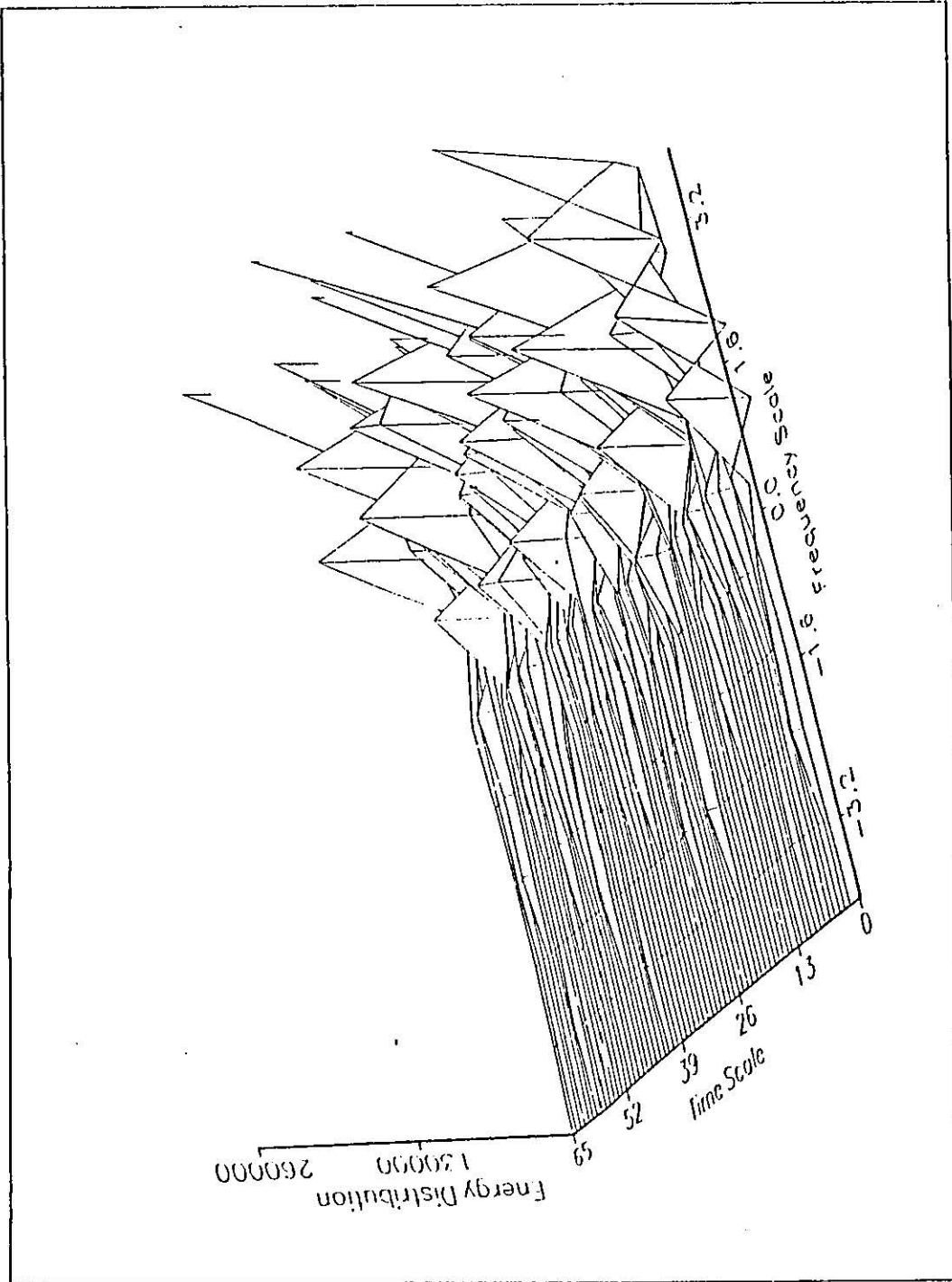


Figure 5.57 :The wavelet transform of the 1st time-series using Mexican Hat wavelet

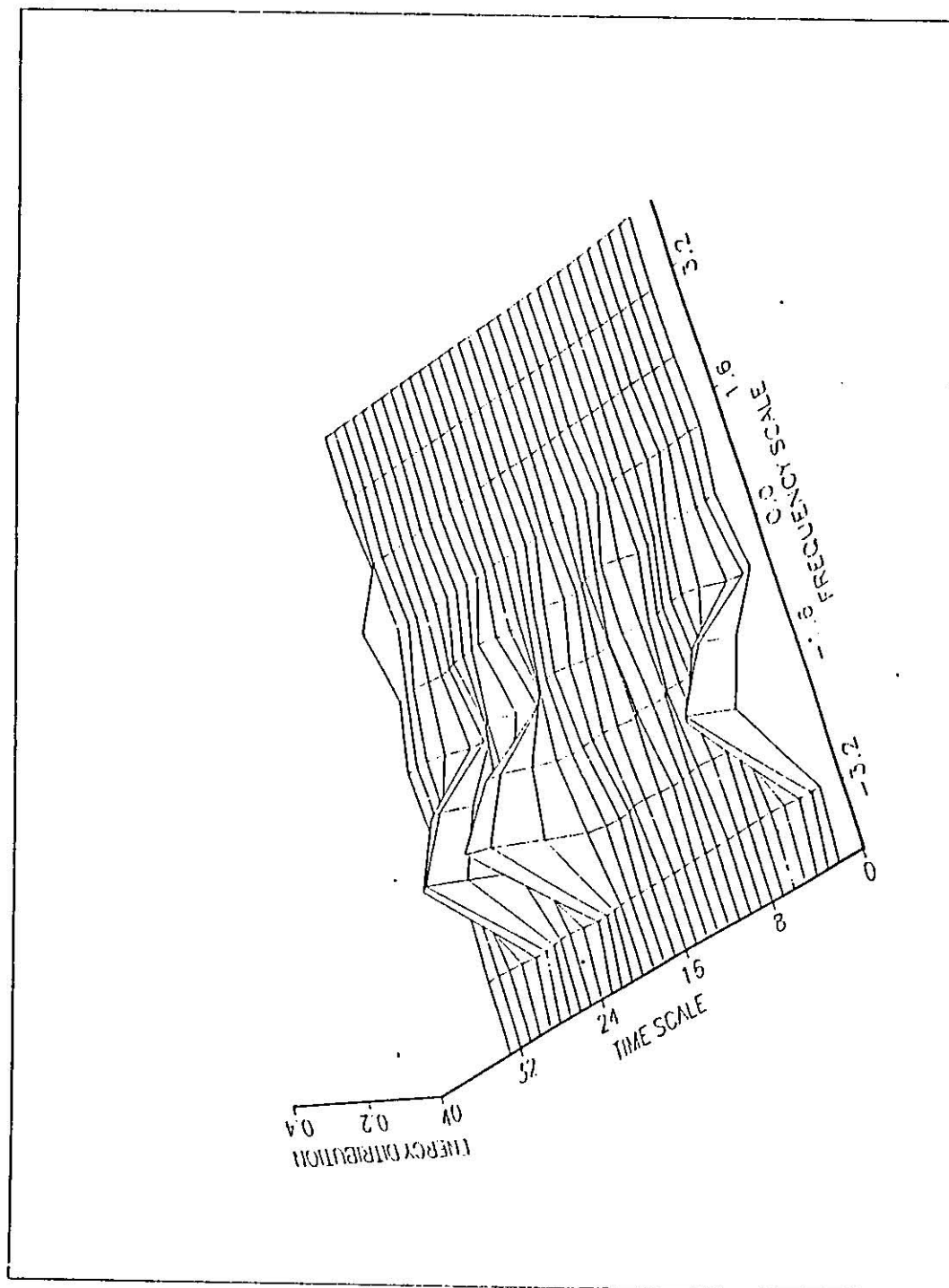


Figure 5.58 :The wavelet transform of the 2nd time-series using Modified Gaussian wavelet

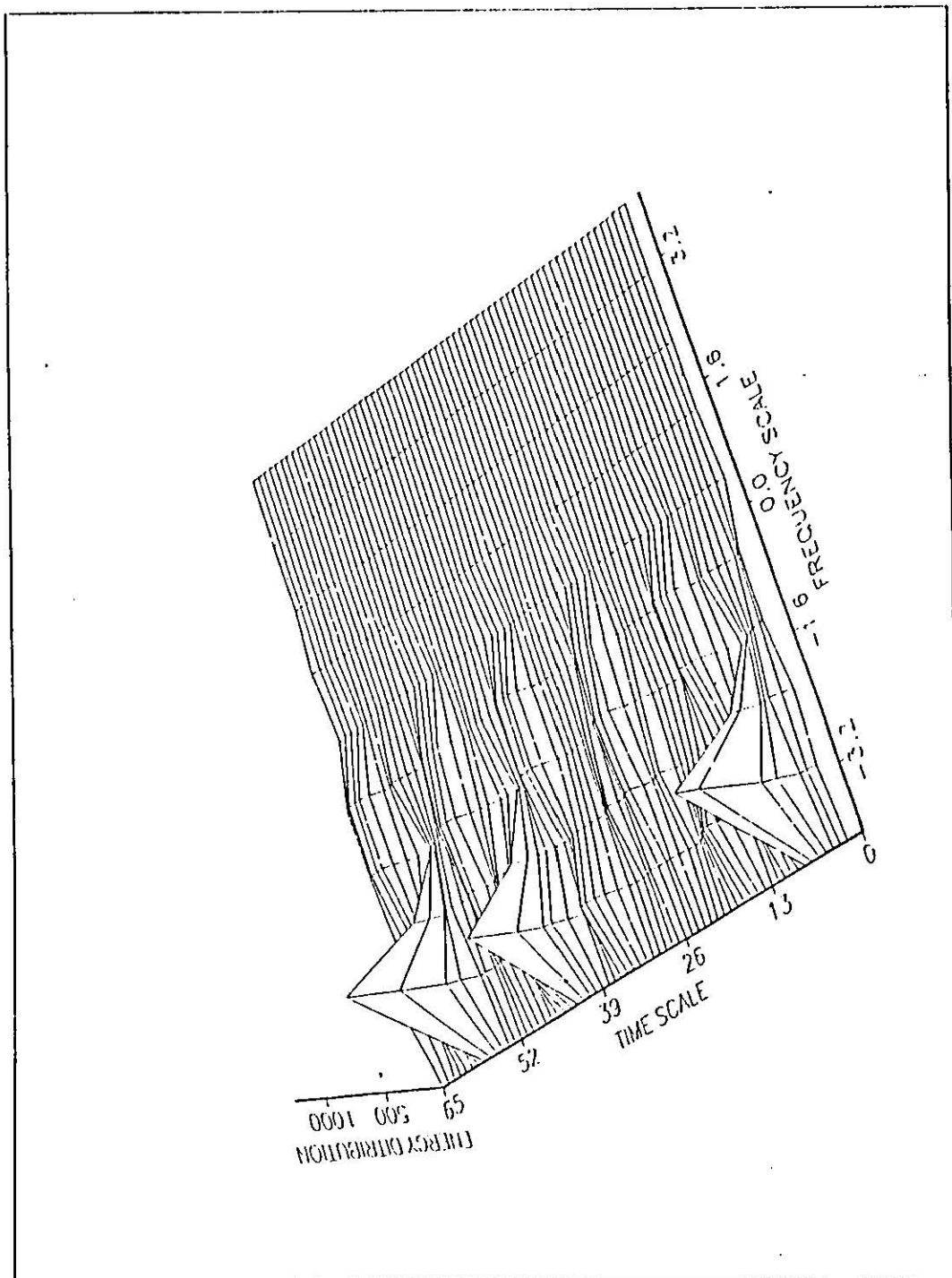


Figure 5.59 :The wavelet transform of the 3rd time-series using Modified Gaussian wavelet

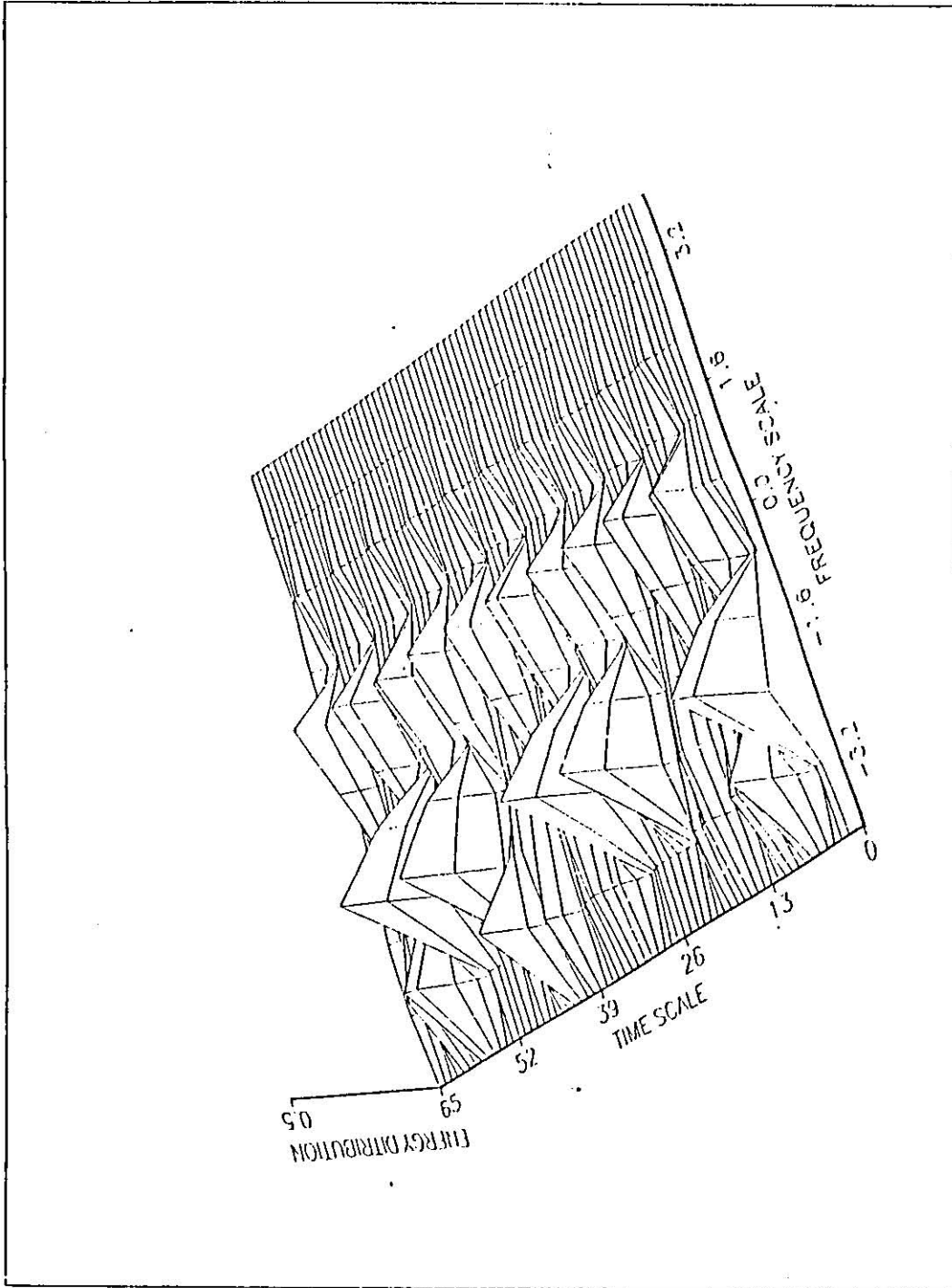


Figure 5.61 :The wavelet transform of the 6th time-series using Modified Gaussian wavelet

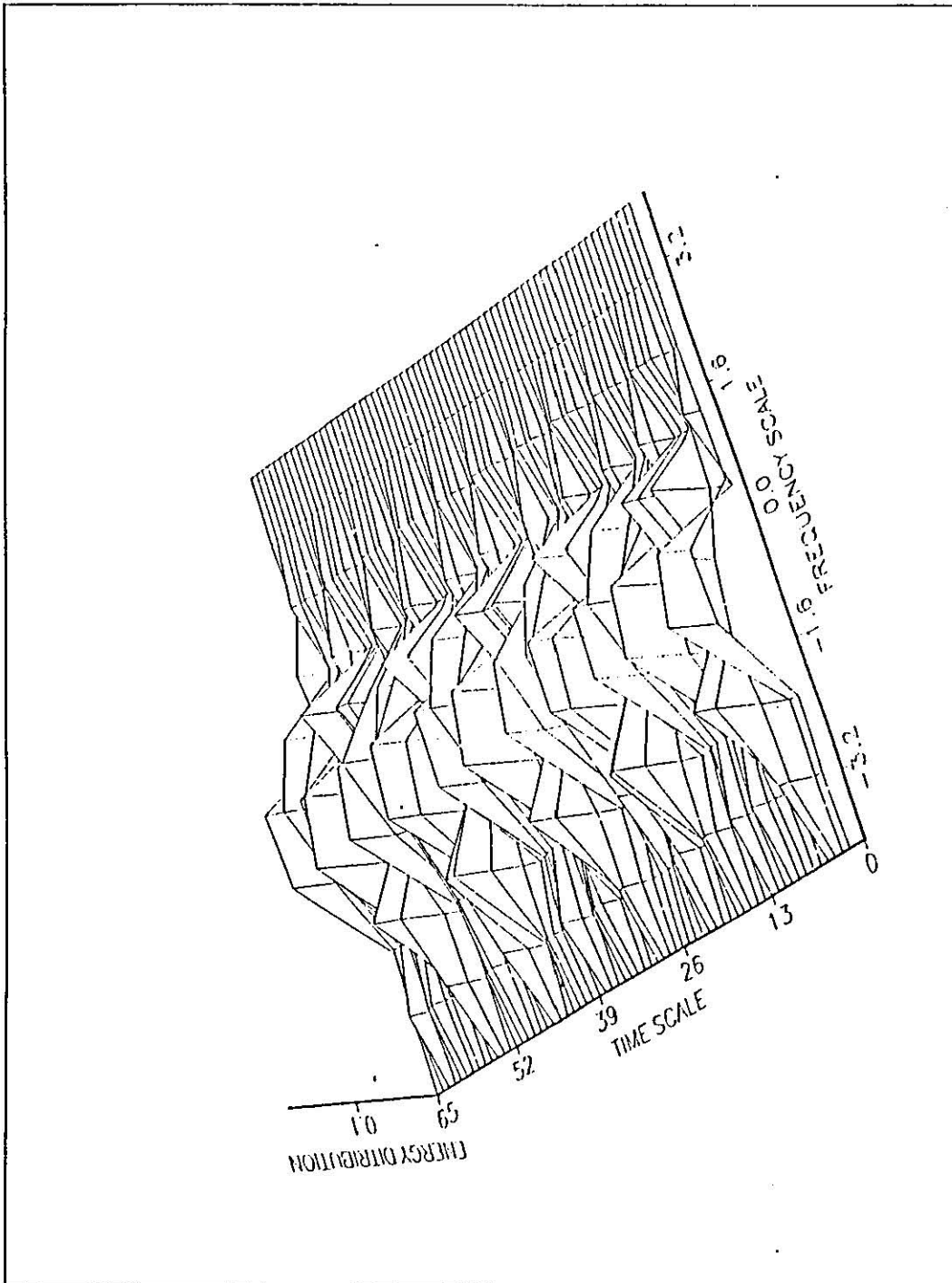


Figure 5.62 :The wavelet transform of the 7th time-series using Modified Gaussian wavelet

REFERENCES:-

- 1- OPPENHEIM, A. V. and SCHAVER, R. W. "Discrete Time Signal Processing" Prantice-Hall, Inc. (1989).
- 2- ALLEN, J.B. "Short-Term Spectral Analysis, Synthesis and Modification by Discrete Fourier Transform." IEEE Trans. Acoust. Speech, Sig. Proc., Vol. ASSP-25, pp. 235-238, June., (1977).
- 3- BROCKWELL, P. J. and DAVIS, R. A. "Time - Series Theory and Methods" Springer-Verlage. 2nd edition, (1991).
- 4- VAN DEN ENDEN, A. W. and VERNOECKS, N. A. M "Discrete-Time Signal Processing" Prantice-Hall (UK), (1989).
- 5- DAUEBECHIES, I. "Time-Frequency Localization Operators: A Geometric Phase Space Approach." IEEE Trans. on Inf. Th., Vol. 34, PP. 605-612, July (1988).
- 6- GABOR, D. "Theory of Communication." J. IEEE (London), Vol. 93 (III), pp. 429-457, (1946).
- 7- FILLER, J. R., MARSTON, P. L., and MIH, W. C., "Response of the Shear Layers Separating From a Circular Cylinder to Small Amplitude Rotational Oscillation, " J. Fluid Mech., Vol. 231, pp. 481-499., (1991).
- 8- TOKUMARU, P. T., and Dimotakis, P. E., " Rotary Oscillation Control of a Cylinder Wake," J. Fluid Mech. Vol. 224. pp. 77-90. (1991).
- 9- BLEVINS, R. D. "Flow-induced vibration", Van Nostrand Reynolds, New York, 1977.

- 29- ROCKWELL, D., "Active Control of Globally-Unstable Separated Flows," ASME International Symposium on Nonsteady Fluid Dynamics (Proceedings), FED- Vol. 92, pp. 379-394. (1990).
- 30- NAKAGAWA T. "A Formation Mechanism of Alternating Vortices Behind a Circular Cylinder at High Reynolds Number" J. of Wind Eng. and Ind. Aerodynamics, vol. 25, pp. 113-129, (1986).
- 31- BARBI C., FAVIER D. P., MAREVA C. and TELLIONIS D. P. "Vortex-Shedding and Lock-in of Stationary Cylinder in Oscillatory Flow" J. Fluid Mechanics, vol. 170, pp. 527-544, (1986).
- 32- SHIRAKASHI M., ISHIDA Y, and WAKIYA, S. "Higher Velocity Resonance of Circular Cylinders in Cross-Flow" Trans. of the ASME, J. of Fluid Eng., vol. 107, pp. 392-396, September (1985).
- 33- SHIRAKASHI M., MIZUGUCHI K. and BAE H. M. "Flow-Induced Excitation of an Elastically-Supported Cylinder Caused by Another Located Downstream in Cruciform Arrangement" J. of Fluid and Structures, vol. 3, pp. 595-607, (1989).
- 34- FUJITA, K., ITO T. and KOHNO, N. "Experimental Study of the Vibration of Circular Cylinders Subjected to Cross Flow: Case of Cross Flow Jetted from a Narrow Gap", J of Fluid & Struct. Vol. 4, pp. 99-124, (1990).
- 35- ECKERLE, W. A., and AWAD, J. K. "Effect of Freestream Velocity on the Three Dimensional Separated Flow Regions in Front of a Cylinder" J. of Fluid Engineering, vol. 113, pp. 37-44, March, (1991).
- 36- OTA, T., NISHIYAMA, H., AND TOAKA Y. "Flow Around an Elliptic Cylinder in the Critical Reynold Number Regime" Trans. of ASME, J. of fluid Eng. Vol. 109, pp. 149-155, June (1987).

- 37- MARN, J. and CATTON, I. "Analysis of Flow Induced Vibration Using the Vorticity Transport Equation", J. Fluid. Eng. Vo.. 115. pp. 485-492, Sep. (1993).
- 38- OBASAJU, E. D., NAUDASCTER, E. and ERMSHAUS, R. "Further Results On the Flow-Induced Streamwise Vibration of cylinders" J. Fluid and Struct., Vol. 6, pp. 51-66, (1992).
- 39- NUZZI, F., MAGNESS C. and ROCKWELL, D. "Three Dimensional Vortex Formation from an Oscillating, Non-Uniform Cylinder" J. Fluid. Mech. Vol. 238, pp. 31-54, (1992).
- 40- BAKER C. J. " The Oscillation of Horseshoe Vortex System, " Trans. of ASME, J. of Fluid Eng. Vol. 113. pp. 489-494, Sep., (1991).
- 41- MEYER, Y., "Orthonormal Waveletes." in (Com 89). pp. 21-37, 1989.
- 42- RADAR, C.M, "An improved Algorithm for High Speed Auto Correlation, "IEEE Trns. on Audio and Electroa coustics, pp. 33-9-342, Dec., (1972).
- 43- RABINER, L. R. and SCHATER , R. W., "Correlation Method For Power Spectrum Estimation," IEEE Trans. on Audio and Electroacoustice, pp. 2.2.1 - 2.2.14, Dec. (1972)
- 44- COOLEY, J. W. and TUKEY, J. W., "An Algorithm For Machine Computation of Complex Fourier Series", Math. of comput., Vol. 19, pp. 297-301, April (1965).
- 45- GROSSMANN, A. and MORLET, J. "Decomposition of Hardy Functions into Square Integrable Wavelets of Constant Shape". Siam J. Math. analysis Vol. 15, No. 4, pp. 723-736. (1984)

- 55- VETTERLI, M., and HERLEY C. "Wavelets and Filter Banks: Theory and Design", IEEE Trans on Signal Processing, Vol. 40, No. 9, pp. 2207-2232. (1992).
- 56- SHENSA, M. "The Discrete Wavelet Transform: Wedding the A Troun and Mallat Algorithms", IEEE Trans. on Sig. Processing, Vol. 40, No. 10, pp. 2464-2484. (1992).
- 57- MALLAT, S., "A Theory for Mutiresolution Signal Decomposition: The Wavelet Representation. , IEEE Trans. Pat Anal., Machine Intell., Vol 11, No. 7, pp. 674-693, (1989)
- 58- MALLAT, S., "Multifrequency Channel Decompositions of Images and Wavelet Models," IEEE Trans. Acoust, Speech., Sig. proc. Vol. 37, No. 12, PP 2091-2110 (1989).
- 59- DAUBECHIES, I., "The Wavelet Transform : A Method for time-Frequency Localization"., Chapter 8 of Advances in spectrum analysis and array processing. Vol. I. S. Haykin, ed., pp. 366-417, prentice Hall. Englewood Cliffis NJ, (1991).
- 60- TEWFIK, A. H. and KIM, M., "Correlation Structure of the Discrete Wavelet Coefficients of Fractional Browian Motions," IEEE Trans. on Info. Th., Vol. 38, No. 2, pp.910-917, (1992).
- 61- RIOUL, O., "A Discrete Time Multiresolution Theory ." IEEE Trans. Sig. Proc., Vol. 41, No. 8, pp. 2591-2606, (1993).
- 62- (COM 89) COBES, J.M., GROSSMANN, A. and TECHAMITCHIAN, P. EDS. Wavelets. Time - Frequency Methods and Phase - Space," Proc. of int. Conf. on Waveletes, Time - Frequency Methods and Phase Space: Inverse Problems and Theortical Imaging Maresille, France, Dec. 14-18, 1987. Springer - verlag. Berlin, (1989).

- 63- TEWFIK, A. H. SINHA, D. and JORGENSEN, P., "On the Optimal Choice of a Wavelet for Signal Representation," IEEE Trans. Info. Th., vol. 38, No. 2, pp. 747-765, (1992).
- 64- DAUBECHIES, I., "The wavelet Transform, Time - Frequency Localization and Signal Analysis", IEEE Trans. Info. Theory Vol. 36. No. 5, pp. 961-1005, Sept. (1990).
- 65- DAUBECHIES, I., and LAGARRIAS J. "Two-Scale Difference Equations I", Siam J. Math. Analysis, Vol. 22, pp. 1388-1410. (1991).
- 66- KADAMBE, S. and BOUDREAUX - BARTELS, G. F., "A Comparison of the Existence of Cross Terms in the Wigner Distribution and the Squared Magnitude of the Wavelet Transform and the Short Time Fourier Transform," IEEE Trans. Sig. Proc. Vol. 40, No. 10, pp. 2483-2499, (1992).
- 67- KADAMBE, S. and BOUDREAUX-BARTELS, G.F., "Application of the Wavelet Transform for Pitch Detection of Speech Signals." IEEE Trans. Info. Th. Vol. 38, No. 2, pp. 469-472, (1992).
- 68- GOUPILLAUD, P., GROSSMANH, A., and MORIET, J., "Cycle-Octave and Related Transforms in Seismic Signal Analysis," Geoexploartion, Vol. 23. pp. 85-102, (1992).
- 69- FLANDRIN, P., "Some Aspects of Non-Stationary signal Processing with Emphasis on Time-Frequency and Time -Scale Methods in Wavelets," Time Frequency Methods and Phase Space, M. Combs, A. Grossmann, and P. Tchamitchian Eds. Berlin: springer (IPTI), pp. 168-198. (1989).
- 70- FLANDRIN, P., MAGAND, F., and ZAKHARIA, M., "Generalized Target Description and Wavelet Decomposition."

- IEEE Trans. Acoust., Speech, Sig. Proc., vol. 38, no. 2, pp. 350-352. (1990).
- 71- HOLSCHNIEDER, N., KRONALAND-MARTIENT R. MORLET J. and Tchamitchian, P. " A real-time Algorithm for Signal Analysis with the Help of the Wavelet Transform", In (com 89), pp. 286-297, (1989).
- 72- DUTILLEUX, P., GROSSMANN, A., and KRONLAND-MARTIENT, R., "Application of the Wavelete Transform to the Analysis, Transformation and Synthesis of Musical Sounds." Proc. 25th AES Convention, nr. 2727. section A-2. (1988).
- 73- RIOUL, O. and DUHMEL, P. "Fast Algorithm for Discrete and Continuous Wavelet Transforms"., IEEE Trans. on Inf. Theory, Vol. 38, No. 2, pp 569-586. (1992).
- 74- RIOUL, O. and VETTERLI, M., "Wavelets and Signal Processing." IEEE Sig. Proc. Magazine, pp. 14-38. Oct. (1991).
- 75- KOVACEVIC, J., and VETTERLI, M. " Non Separable Multidimensional Perfect Reconstruction Filter Banks and Wavelete Bases for R^n " IEEE Trans. on Inf. th., Vol. 38, No. 2, pp. 533-555, (1992).
- 76- DELPRAT, N., GUILLEMAIN P. and TECHAMITCHIAN P. "Asympotic Wavelet and Gabor Analysis : Extraction of Instantaneous Frequencies" IEEE on inf. Theory, Vol. 38, No. 2, pp. 644-684. (1992).
- 77- MALLAT S., "Multiresolution Approximation and Wavelets." Trans. Am. Math. Soc., Vol. 135, pp. 69-88, (1989).

- 78- MALLAT, S. and HWANG, L. "Singularity Detection and Processing with Wavelets." IEEE trans on Inf. Theory, Vol. 38 , No.2, pp 617-643. (1992)
- 79- UNSER, M., ALDROUBI, A., and EDEN M. "On the asymptotic Convergence of B-Spline Wavelets to Gabor Functions", IEEE Trans, Info. Th., vol. 38, no. 2. (1992).
- 80- FLANDRIN, P., "Wavelet Analysis and Synthesis of Fractional Brownian Motion." IEEE Trans. Info. Th., Vol. 38, No. 2. (1992).
- 81- PARIS, G. and FRISCH, U. "Turbulence and Predictability in Geophysical Fluid Dynamics and Climate Dynamics," M. Ghil, R. Benzi, and G. Parisi, eds., North-Holland, Amsterdam, 1985, pp. 71-88.
- 82- MUZY, J. F. BACRY, E. and ARNEODO, A. "Wavelets and Multifractal Formalism for singular Signals: Application to Turbulence Data,"preprint, Centre de Recherche Paul Pascal, Pessac, France.
- 83- ARGOUL, F., ARBEODO, A. GRASSEAU, G. GAGNEY, Y. HOPFINGER, E. F. and FRISCH, U. "Wavelet Analysis of Turbulence Reveals the Multifractal Nature of the Richardson cascade," Nature 338, pp. 51-53. (1989).
- 84- ZABUSKY, N. "Computational Synergetics," Physics Today, July, pp. 2-11. (1984).
- 85- EVERSON, SIROVICH, L. and SREENIVASAN, K. R. "Wavelet Analysis on the Turbulent Jet." Phys. Lett. A, 145, pp. 314-324. (1990).
- 86- KOLMOGOROV, M. "A Refinement of Previous Hypotheses Concerning the Local Structure of Turbulence in Viscous

- Incompressible Fluid at a High Reynolds Number," J. Fluid Mech., 13, pp. 1, 82-85. (1961).
- 87- AL-BEDOOR, B. "Effect of flow History on The Flow Induced Vibrations of Rough Interfering Bodies., M.Sc Thesis, U. J., (1989).
- 88- HIJAWI, M. S. "Influence of Interference, Tubelence Intensity and Surface Roughness on the Flow- Induced Vibration of a circular cylinder" M.Sc Thesis, U. J., (1991).
- 89- FOX, T. A., " End Plats Interference Effects on the Aerodynamics of a Circular Cylinder in Uniform Flow" , Aeronautical Journal, pp. 10-14, (1992).
- 90- GRAHAM, J. M. R. "The Effect of End-plates on the Two-Dimensionality of a Vortex Wake" The Aeronautical Quarterly, pp. 237-247, August (1969).
- 91- GERICH, D. and ECKELMANN, H. " Influence of end plates and free ends on the shedding frequency of circular cylinders" J. of Fluid Mech. vol. 122, pp. 100-121, 1982.
- 92- ROUX, J. C., ROSSI, A., BACHELART, S. and VIDAL, C. "Experimental Observations of Complex Behaviour During a Chemical Reaction", Physica. 2D, 395, (1981).
- 93- SCHUSTER, H. G. "Deterministic Chaos" Dhsyik- Verlag, Weinheim, (1984).
- 94- Tsatsanis, K. and Giannakis, B. "Time-Varying System Identification and Model Validation Using Wavelets." IEEE Trans. on Sig. Proc., Vol. 41, No. 12, Dec. (1993).

Appendix A

PROPERTIES OF THE FOURIER TRANSFORM

Appendix A

PROPERTIES OF THE FOURIER TRANSFORM

A.1 Representation of Sequences by Fourier Transform

Many sequences can be represented by a Fourier integral of the form

$$x[n] = \frac{1}{2\pi} \int_{-\pi}^{\pi} X(\exp^{i\omega}) \exp^{i\omega n} d\omega \quad (\text{A.1})$$

where $X(\exp^{i\omega})$ is given by

$$x(\exp^{i\omega}) = \sum_{n=-\infty}^{\infty} x[n] \exp^{i\omega n} \quad (\text{A.2})$$

Equations (A.1) and (A.2) together form a Fourier representation for the sequence. Equation (A.1), the inverse Fourier transform, is a synthesis formula. That is, it represents $x[n]$ as a superposition of infinitesimally small complex sinusoids of the form $\frac{1}{2\pi} X(\exp^{i\omega})(\exp^{i\omega n})d\omega$ with ω ranging over an interval of length 2π and with $X(\exp^{i\omega})$ determining the relative amount of each complex sinusoidal component. Although in writing Equation (A.1) we have chosen the range of values for ω between $-\pi$ and $+\pi$, any interval of length 2π can be used. Equation (A.2), the Fourier transform, is an expression for computing $X(\exp^{i\omega})$ from the sequence $x[n]$, i.e., for analyzing the sequence $x[n]$ to determine how much

of each frequency component is required to synthesize $x[n]$ using Equation (A.1).

Sometimes we will refer to Equation (A.2) more explicitly as the discrete-time Fourier transform, particularly when it is important to distinguish it from the continuous-time Fourier transform.

In general, the Fourier transform is a complex-valued function of ω . As with the frequency response, we sometimes express $X(\exp^{i\omega})$ in rectangular form as

$$x(\exp^{i\omega}) = X_R(\exp^{i\omega}) + iX_I(\exp^{i\omega}) \quad (\text{A.3})$$

or in polar form as

$$x(\exp^{i\omega}) = |X(\exp^{i\omega})| \exp^{i\angle X(\exp^{i\omega})} \quad (\text{A.4})$$

The quantities $|X(\exp^{i\omega})|$ and $\angle X(\exp^{i\omega})$ are called the magnitude and phase, respectively, of the Fourier transform. The Fourier transform is also sometimes referred to as the the Fourier spectrum or simply the spectrum. Also, the terminology magnitude spectrum or amplitude spectrum is sometimes used to refer to $|X(\exp^{i\omega})|$ and the angle or phase $\angle X(\exp^{i\omega})$ is sometimes called the phase spectrum.

A.2 Symmetry Properties of the Fourier Transform

In using Fourier transforms, it is useful to have a detailed knowledge of the way that properties of the sequence manifest themselves in the Fourier transform and vice versa. Symmetry properties of the Fourier transform are often very useful. The following discussion presents these

properties. A conjugate-symmetric sequence $x_e[n]$ is defined as a sequence for which $x[n] = x^*[-n]$, where $*$ denotes complex conjugate. A conjugate-antisymmetric sequence $x_o[n]$ is defined as a sequence for which $x[n] = -x^*[-n]$. Any sequence $x[n]$ can be expressed as a sum of a conjugate-symmetric sequence and a conjugate-antisymmetric sequence. Specifically,

$$X[n] = X_e[n] + X_o[n] \quad (\text{A.5})$$

where

$$X_e[n] = \frac{1}{2}(X[n] + X^*[-n]) \quad (\text{A.6})$$

and

$$X_o[n] = \frac{1}{2}(X[n] - X^*[-n]) \quad (\text{A.7})$$

A real sequence that is conjugate-symmetric such that $X_e[n] = X_e[-n]$ is called even sequence, and a real sequence that is conjugate-antisymmetric such that $X_o[n] = -X_o[-n]$ is called an odd sequence.

A Fourier transform $X(\exp^{i\omega})$ can be decomposed into a sum of conjugate-symmetric and conjugate-antisymmetric functions as

$$X(\exp^{i\omega}) = X_e(\exp^{i\omega}) + X_o(\exp^{i\omega}) \quad (\text{A.8})$$

where

$$X_e(\exp^{i\omega}) = \frac{1}{2}(X(\exp^{i\omega}) + X^*(\exp^{-i\omega})) \quad (\text{A.9})$$

and

$$X_o(\exp^{i\omega}) = \frac{1}{2}(X(\exp^{i\omega}) - X^*(\exp^{-i\omega})) \quad (\text{A.10})$$

Clearly, $X_e(\exp^{i\omega})$ is a conjugate-symmetric and $X_o(\exp^{i\omega})$ is conjugate-antisymmetric; i.e.,

$$X_e(\exp^{i\omega}) = X_e^*(\exp^{-i\omega}) \quad (\text{A.11})$$

properties. A conjugate-symmetric sequence $x_e[n]$ is defined as a sequence for which $x[n] = x^*[-n]$, where $*$ denotes complex conjugate. A conjugate-antisymmetric sequence $x_o[n]$ is defined as a sequence for which $x[n] = -x^*[-n]$. Any sequence $x[n]$ can be expressed as a sum of a conjugate-symmetric sequence and a conjugate-antisymmetric sequence. Specifically,

$$X[n] = X_e[n] + X_o[n] \quad (\text{A.5})$$

where

$$X_e[n] = \frac{1}{2}(X[n] + X^*[-n]) \quad (\text{A.6})$$

and

$$X_o[n] = \frac{1}{2}(X[n] - X^*[-n]) \quad (\text{A.7})$$

A real sequence that is conjugate-symmetric such that $X_e[n] = X_e[-n]$ is called even sequence, and a real sequence that is conjugate-antisymmetric such that $X_o[n] = -X_o[-n]$ is called an odd sequence.

A Fourier transform $X(\exp^{i\omega})$ can be decomposed into a sum of conjugate-symmetric and conjugate-antisymmetric functions as

$$X(\exp^{i\omega}) = X_e(\exp^{i\omega}) + X_o(\exp^{i\omega}) \quad (\text{A.8})$$

where

$$X_e(\exp^{i\omega}) = \frac{1}{2}X(\exp^{i\omega}) + X^*(\exp^{-i\omega}) \quad (\text{A.9})$$

and

$$X_o(\exp^{i\omega}) = \frac{1}{2}X(\exp^{i\omega}) - X^*(\exp^{-i\omega}) \quad (\text{A.10})$$

Clearly, $X_e(\exp^{i\omega})$ is a conjugate-symmetric and $X_o(\exp^{i\omega})$ is conjugate-antisymmetric; i.e.,

$$X_e(\exp^{i\omega}) = X_e^*(\exp^{-i\omega}) \quad (\text{A.11})$$

and

$$X_o(\exp^{i\omega}) = X_o^*(\exp^{-i\omega}) \quad (\text{A.12})$$

As with sequence, if a real function of a continuous variable is conjugate-symmetric, it is referred to as an even function, and a real conjugate-antisymmetric function of a continuous variable is referred to as an odd function. The symmetry properties of the Fourier transform are summarized in table A.1 . The first six properties apply for a general complex sequence $x[n]$ with Fourier transform $X(\exp^{i\omega})$

A.3 Fourier Transform Theorems

In addition to the symmetry properties, a variety of theorems relate operations on the sequence to operations on the Fourier transform. These theorems are quite similar in most cases to corresponding theorems for continuous-time signals and their Fourier transforms. To facilitate the statement of these theorems, we introduce the following operator notation:

$$X(\exp^{i\omega}) = f\{x[n]\} \quad (\text{A.13})$$

$$x[n] = f^{-1}\{X(\exp^{i\omega})\} \quad (\text{A.14})$$

$$X[n] \stackrel{f}{\longleftrightarrow} X(\exp^{i\omega}) \quad (\text{A.15})$$

That is, f denotes the operation of "taken the fourier transform of $x[u]$ ", and f^{-1} is the inverse of that operation. Most of the theorems will be stated without proof. The theorems in this section are summarized in table A.2.

A.3.1 Linearity of the Fourier Transform

If

$$X_1[n] \stackrel{f}{\iff} X_1(\exp^{i\omega}) \quad (\text{A.16})$$

and

$$X_2[n] \stackrel{f}{\iff} X_2(\exp^{i\omega}) \quad (\text{A.17})$$

then

$$aX_1[n] + bX_2 \stackrel{f}{\iff} aX_1(\exp^{i\omega}) + bX_2(\exp^{i\omega}) \quad (\text{A.18})$$

A.3.2 Time Shifting and Frequency Shifting

If

$$X[n] \stackrel{f}{\iff} X(\exp^{i\omega}) \quad (\text{A.19})$$

then for the time-shifted sequence,

$$X[n - n_d] \stackrel{f}{\iff} \exp^{-i\omega n_d} X(\exp^{i\omega}) \quad (\text{A.20})$$

and for the frequency-shifted Fourier transform,

$$\exp^{i\omega_0 n} x[n] \stackrel{f}{\iff} X(\exp^{i(\omega - \omega_0)}) \quad (\text{A.21})$$

A.3.3 Time Reversal

If

$$X[n] \stackrel{f}{\iff} X(\exp^{i\omega}) \quad (\text{A.22})$$

then if the sequence is time reversed,

$$X[-n] \stackrel{f}{\iff} X(\exp^{-i\omega}) \quad (\text{A.23})$$

and if $x[n]$ is real, this theorem reduces to

$$X[-n] \stackrel{f}{\iff} X^*(\exp^{i\omega}) \quad (\text{A.24})$$

A.3.4 Differentiation in Frequency

If

$$X[n] \stackrel{f}{\longleftrightarrow} X(\exp^{i\omega}) \quad (\text{A.25})$$

then

$$nX[n] \stackrel{f}{\longleftrightarrow} i \frac{dX(\exp^{i\omega})}{d\omega} \quad (\text{A.26})$$

A.3.5 Parseval's Theorem

If

$$X[n] \stackrel{f}{\longleftrightarrow} X(\exp^{i\omega}) \quad (\text{A.27})$$

then

$$E = \sum_{n=-\infty}^{+\infty} |X[n]|^2 \quad (\text{A.28})$$

or,

$$E = \frac{1}{2} \int_{-\pi}^{\pi} |X(\exp^{i\omega})|^2 d\omega \quad (\text{A.29})$$

The function $|X(\exp^{i\omega})|^2$ is called the energy density spectrum since it determines how the energy is distributed in frequency. Necessarily, the energy density spectrum is defined only for finite-energy signals. Parseval's

A.3.6 The Convolution Theorem

If

$$X[n] \stackrel{f}{\longleftrightarrow} X(\exp^{i\omega}) \quad (\text{A.30})$$

and

$$h[n] \stackrel{f}{\longleftrightarrow} H(\exp^{i\omega}) \quad (\text{A.31})$$

and if

$$y[n] = \sum_{k=-\infty}^{\infty} x[k]h[n-k] = x[n] * h[n] \quad (\text{A.32})$$

then

$$Y(\exp^{i\omega}) = X(\exp^{i\omega}) \cdot H(\exp^{i\omega}) \quad (\text{A.33})$$

A.3.7 The Modulation or Windowing Theorem

If

$$X[n] \xleftrightarrow{f} X(\exp^{i\omega}) \quad (\text{A.34})$$

and

$$w[n] \xleftrightarrow{f} W(\exp^{i\theta}) \quad (\text{A.35})$$

and if

$$y[n] = x[n]w[n] \quad (\text{A.36})$$

then

$$Y(\exp^{i\omega}) = \frac{1}{2\pi} \int_{-\pi}^{\pi} X(\exp^{i\theta})W(\exp^{i(\omega-\theta)}) \quad (\text{A.37})$$

Table A.1 SYMMETRY PROPERTIES OF THE FOURIER TRANSFORM

Sequence $x[n]$	Fourier Transform $X(e^{j\omega})$
1. $x^*[n]$	$X^*(e^{-j\omega})$
2. $x^*[-n]$	$X^*(e^{j\omega})$
3. $\Re\{x[n]\}$	$X_e(e^{j\omega})$ (conjugate-symmetric part of $X(e^{j\omega})$)
4. $j\Im\{x[n]\}$	$X_o(e^{j\omega})$ (conjugate-antisymmetric part of $X(e^{j\omega})$)
5. $x_e[n]$ (conjugate-symmetric part of $x[n]$)	$X_R(e^{j\omega})$
6. $x_o[n]$ (conjugate-antisymmetric part of $x[n]$)	$jX_I(e^{j\omega})$

The following properties apply only when $x[n]$ is real.

7. Any real $x[n]$	$X(e^{j\omega}) = X^*(e^{-j\omega})$ (Fourier transform is conjugate-symmetric)
8. Any real $x[n]$	$X_R(e^{j\omega}) = X_R(e^{-j\omega})$ (real part is even)
9. Any real $x[n]$	$X_I(e^{j\omega}) = -X_I(e^{-j\omega})$ (imaginary part is odd)
10. Any real $x[n]$	$ X(e^{j\omega}) = X(e^{-j\omega}) $ (magnitude is even)
11. Any real $x[n]$	$\angle X(e^{j\omega}) = -\angle X(e^{-j\omega})$ (phase is odd)
12. $x_e[n]$ (even part of $x[n]$)	$X_R(e^{j\omega})$
13. $x_o[n]$ (odd part of $x[n]$)	$jX_I(e^{j\omega})$

Table (A.2) FOURIER TRANSFORM THEOREMS

Sequence $x[n]$ $y[n]$	Fourier Transform $X(e^{j\omega})$ $Y(e^{j\omega})$
1. $ax[n] + by[n]$	$aX(e^{j\omega}) + bY(e^{j\omega})$
2. $x[n - n_d]$ (n_d an integer)	$e^{-j\omega n_d} X(e^{j\omega})$
3. $e^{j\omega_0 n} x[n]$	$X(e^{j(\omega - \omega_0)})$
4. $x[-n]$	$X(e^{-j\omega})$ $X^*(e^{j\omega})$ if $x[n]$ real.
5. $nx[n]$	$j \frac{dX(e^{j\omega})}{d\omega}$
6. $x[n] * y[n]$	$X(e^{j\omega}) Y(e^{j\omega})$
7. $x[n]y[n]$	$\frac{1}{2\pi} \int_{-\pi}^{\pi} X(e^{j\theta}) Y(e^{j(\omega - \theta)}) d\theta$

Parseval's Theorem

$$8. \sum_{n=-\infty}^{\infty} |x[n]|^2 = \frac{1}{2\pi} \int_{-\pi}^{\pi} |X(e^{j\omega})|^2 d\omega$$

$$9. \sum_{n=-\infty}^{\infty} x[n]y^*[n] = \frac{1}{2\pi} \int_{-\pi}^{\pi} X(e^{j\omega}) Y^*(e^{j\omega}) d\omega$$

APPENDIX B

SOME TFRS IN ALPHABETICAL ORDER

"Passive" Unterberger distribution (PUD):

$$\text{PUD}_x(t, f) = \int_0^{\infty} X(fu) X^*(\frac{f}{u}) \frac{1}{u} e^{j2\pi t(u-1/u)} du$$

Pseudo Wigner distribution (PWVD):

$$\text{PWVD}_x^{(n)}(t, f) = \int_{-\frac{t}{2}}^{t+\frac{t}{2}} x(t+\frac{\tau}{2}) x^*(t-\frac{\tau}{2}) \eta(\frac{\tau}{2}) \eta^*(-\frac{\tau}{2}) e^{-j2\pi f\tau} d\tau = \int_{-\infty}^{\infty} H(f-f') W_x(t, f') df'$$

$$\text{with } H(f) = \int_{-\frac{t}{2}}^{t+\frac{t}{2}} \eta(\frac{\tau}{2}) \eta^*(-\frac{\tau}{2}) e^{-j2\pi f\tau} d\tau$$

Real-valued generalized Wigner distribution (RGWD):

$$\text{RGWD}_x^{(n)}(t, f) = \text{Re} \left\{ \text{GWD}_x^{(n)}(t, f) \right\}$$

Reduced interference distribution (RID)¹:

$$\text{RID}_x(t, f) = \int_{-\infty}^{\infty} \int_{-\infty}^{\infty} S(\tau\nu) A_x(\tau, \nu) e^{j2\pi(\nu-f\tau)} d\tau d\nu,$$

$$\text{with } s(\alpha) = 0 \text{ for } |\alpha| > 1/2, S(\beta) \in \mathbb{R}, S(0) = 1, \left. \frac{d}{d\beta} S(\beta) \right|_{\beta=0} = 0$$

Rihaczek distribution (RD):

$$\text{RD}_x(t, f) = \int_{-\infty}^{\infty} x(t+\tau) x^*(t) e^{-j2\pi f\tau} d\tau = x^*(t) X(f) e^{j2\pi ft}$$

Scalogram (SCAL):

$$\text{SCAL}_x^{(n)}(t, f) = |W_x^{(n)}(t, f)|^2 = \left| \int_{-\infty}^{\infty} x(t') \sqrt{\left| \frac{f}{f_0} \right|} \gamma \left(\frac{f}{f_0} (t' - t) \right) dt' \right|^2$$

Smoothed pseudo Wigner distribution (SPWVD):

$$\text{SPWVD}_x^{(g, n)}(t, f) = \int_{-\infty}^{\infty} \left[\int_{-\infty}^{\infty} g(t-t') x(t'+\frac{\tau}{2}) x^*(t'-\frac{\tau}{2}) d\tau' \right] \eta(\frac{\tau}{2}) \eta^*(-\frac{\tau}{2}) e^{-j2\pi f\tau} d\tau = \int_{-\infty}^{\infty} \int_{-\infty}^{\infty} g(t-t') H(f-f') W_x(t, f') dt' df' \text{ with } H(f) = \int_{-\infty}^{\infty} \eta(\frac{\tau}{2}) \eta^*(-\frac{\tau}{2}) e^{-j2\pi f\tau} d\tau$$

Spectrogram (SPEC):

$$\text{SPEC}_x^{(n)}(t, f) = |\text{STF}_x^{(n)}(t, f)|^2 = \left| \int_{-\infty}^{\infty} x(t') \gamma(t' - t) e^{-j2\pi ft'} dt' \right|^2$$

Wigner distribution (WD):

$$W_x(t, f) = \int_{-\infty}^{\infty} x(t+\frac{\tau}{2}) x^*(t-\frac{\tau}{2}) e^{-j2\pi f\tau} d\tau = \int_{-\infty}^{\infty} X(f+\frac{\nu}{2}) X^*(f-\frac{\nu}{2}) e^{j2\pi\nu t} d\nu$$

Nonlinear, nonquadratic TFRs

Signal-adaptive radially-Gaussian kernel distribution (RGD)²:

$$\text{RGD}_x(t, f) = \int_{-\infty}^{\infty} \int_{-\infty}^{\infty} \Psi_x(\tau, \nu) A_x(\tau, \nu) e^{j2\pi(\nu-f\tau)} d\tau d\nu,$$

$$\text{with } \Psi_x(\tau, \nu) = \exp \left[-\frac{(\tau/\tau_0)^2 + (\nu/\nu_0)^2}{2\sigma_x^2(\Theta)} \right], \quad \Theta = \arctan \frac{\nu/\nu_0}{\tau/\tau_0}$$

Cohen's nonnegative distribution (CND):

$$\text{CND}_x^{(c, \rho)}(t, f) = \frac{|x(t)|^2 |X(f)|^2}{E_x} \left[1 + c \rho \left(\xi_x(t), \eta_x(f) \right) \right]$$

$$\text{with } \xi_x(t) = \frac{1}{E_x} \int_{-\infty}^{\infty} |x(t)|^2 dt, \quad \eta_x(f) = \frac{1}{E_x} \int_{-\infty}^{\infty} |X(f)|^2 df, \quad E_x = \int_{-\infty}^{\infty} |x(t)|^2 dt$$

Appendix C

SOME DESIRABLE MATHEMATICAL PROPERTIES OF ENERGETIC QUADRATIC TFR_s

Appendix D

MULTIRESOLUTION THEORY

D.1 Introduction to Multiresolution Theory

The analysis of a nonstationary signal often involves a compromise between how well discontinuities can be located, and how finely long-term behavior can be identified. These two factors impose the restrictions in using a suitable window and in determining its length when dealing with Short Time Fourier Transform (STFT). When using wavelet transform (WT) one looks at a signal at different scales or "resolutions". At these different resolutions the details of a signal generally represents different views of the scene, i.e, at a coarse resolution, these details correspond to the overall view which may be a stationary view but a finer resolution reveals the discontinuities.

Now, let A_{2^j} be the operator which approximates a signal at a resolution 2^j . The signal $f(x)$ is measurable and has a finite energy, that is, $f(x) \in L^2(\mathbb{R})$, where $L^2(\mathbb{R})$ denotes the vector space of measurable, square integrable one-dimensional functions $f(x)$.

Some of the properties of A_{2^j} are summarized below [47]

1. A_{2^j} is a linear operator and it is a projection operator on a partic-

ular vector space $V_{2^j} \in L^2(R)$, where V_{2^j} is the set of all possible approximations at the resolution 2^j of a function in $L^2(R)$. A_{2^j} is not modified if it is approximated again, i.e. $A_{2^j} \odot A_{2^j} = A_{2^j}$

2. $A_{2^j} f(x)$ is the most similar approximated function to the $f(x)$, that is $\forall g(x) \in V_{2^j}$

$$\|g(x) - f(x)\| \geq \|A_{2^j} f(x) - f(x)\| \quad (D.1)$$

Hence, the operator A_{2^j} is an orthogonal projection on the vector space V_{2^j}

3. The approximation at a resolution 2^{j+1} contains the same signal at 2^j , i.e, $\forall j \in z$

$$V_{2^j} \subset V_{2^{j+1}} \quad (D.2)$$

4. An approximation operation is similar at all resolutions. The spaces of approximated functions should thus be derived from one another by scaling each one by the ratio of their resolution values, i.e, $\forall j \in z$

$$f(x) \in V_{2^j} \iff f(2x) \in V_{2^{j+1}} \quad (D.3)$$

5. When $f(x)$ is translated by a length proportional to 2^{-j} , $A_{2^j} f(x)$ is translated by the same amount and is characterized by the same samples which have been translated when $f_k(x) = f(x - k)$, at a resolution $j=0$,

$$A_1 f_k(x) = A_1 f(x - k) \in V_{2^{j+1}} \quad (D.4)$$

6. As the resolution j increases to $+\infty$ the approximated signal should converge to the original signal, conversely as the resolution go to zero

the approximated signal contains less information and converge to zero.

$$\lim_{j \rightarrow \infty} V_{2^j} = \bigcup_{-\infty}^{\infty} V_{2^j} \text{ is dense in } L^2(\mathbb{R}) \quad (\text{D.5})$$

and

$$\lim_{j \rightarrow \infty} V_{2^j} = \bigcap_{-\infty}^{\infty} V_{2^j} = \{0\} \quad (\text{D.6})$$

If a set of vector spaces V_{2^j} satisfy the properties (D-1 to D-6) it will be a multiresolution approximation of $L^2(\mathbb{R})$

The operator A_{2^j} is an orthogonal projection of V_{2^j} . In order to numerically characterize this operator, one must find an orthogonal basis of V_{2^j} and this is achieved by the following theorem [47]

Theorem 1: let V_{2^j} be a multiresolution approximation of $L^2(\mathbb{R})$. There exist a unique function $\phi(x) \in L^2(\mathbb{R})$ called a "scaling function", such that if we set $\phi_{2^j}(x) = 2^j \phi(2^j x)$ for $j \in \mathbb{Z}$, the dilation of $\phi(x)$ by 2^j , then $\sqrt{2^{-j}} \phi_{2^j}(x - 2^{-j}n)$ where $n \in \mathbb{Z}$ is an orthogonal basis of V_{2^j}

For example one can build an orthogonal basis at any V_{2^j} by dilating a function $\phi(x)$ with a coefficient 2^j and translating the resulting function on a grid whose interval is proportional to 2^{-j} . The functions $\phi_{2^j}(x)$ are normalized with respect to $L^1(\mathbb{R})$ norm. The coefficient $2^{-(j/2)}$ appears in the basis set in order to normalize the functions in the $L^2(\mathbb{R})$ norm. For a given multiresolution approximation V_{2^j} where $j \in \mathbb{Z}$, there exists a unique scaling function $\phi(x)$ which satisfies theorem 1. But for different resolutions approximations, the scaling functions are different.

Lemarie [46] has shown that the scaling function associated with such

a multiresolution approximation can be written

$$\hat{\phi}(\omega) = \frac{1}{\omega^n \sqrt{\Sigma_{2n}(\omega)}} \quad (\text{D.7})$$

where $(n=2+2p)$ and $(2p+1)$ is the order of the polynomial and splines

$$\Sigma_n(\omega) = \sum_{-\infty}^{\infty} \frac{1}{(\omega + 2k\pi)^n} \quad (\text{D.8})$$

Mallat [47] computed a closed form of $\Sigma_n(\omega)$ by calculating the derivative of order $(n-2)$ of the equation

$$\Sigma_2(\omega) = \frac{1}{4 \sin(\omega/2)} \quad (\text{D.9})$$

The orthogonal projection on V_2^j can now be computed by decomposing the signal $f(x)$ on an orthonormal basis given by theorem 1, $\forall f(x) \in L^2(\tilde{R})$

$$A_{2^j} f(x) = 2^{-j} \sum_{-\infty}^{\infty} \langle f(u), \phi(u - 2^{-j}n) \rangle \phi_{2^j}(x - 2^{-j}n) \quad (\text{D.10})$$

where in general

$$\langle f(u), g(u) \rangle = \int_{-\infty}^{\infty} f(u)g(u)du \quad (\text{D.11})$$

The approximation of this signal at 2^j is given by

$$A_{2^j}^d f(x) = \langle f(u), \phi_{2^j}(u - 2^{-j}n) \rangle \quad (\text{D.12})$$

where $A_{2^j}^d f(x)$ is the discrete approximation of $f(x)$ at the resolution 2^j .

The above equation, however, can be interpreted as a convolution product evaluated at a point $2^{-j}n$, or

$$A_{2^j}^d f(x) = (f(u) * \phi_{2^j}(-u))(2^{-j}n) \quad (\text{D.13})$$

where $*$ stands for convolution product.

Moreover, as $\phi(x)$ is a low-pass filter, this discrete signal can be interpreted as a low-pass filtering of $f(x)$ followed by a uniform sampling at the rate 2^j .

In an approximation operation when removing the details of $f(x)$ smaller than 2^{-j} , we suppress the highest frequencies of this function. Also the family of functions $\sqrt{2^{-j}}\phi_{2^j}(x - 2^{-j}n)$ $n \in z$ is an orthonormal family [47].

To calculate these discrete approximations, let $\phi(x)$ be the scale function and the family $\sqrt{2^{-(j+1)}}\phi_{2^{j+1}}(x - 2^{-(j+1)}k)$ where $k \in z$ is an orthonormal basis at $V_{2^{j+1}}$. One knows that for any $n \in z$, the function $\phi_{2^j}(x - 2^{-j}n)$ is a member of V_{2^j} which is included in $V_{2^{j+1}}$, and thus $\phi(x)$ can be expanded in this orthonormal basis of $V_{2^{j+1}}$ as equation (D.11)

$$\phi_{2^j}(x - 2^{-j}n) = 2^{-(j+1)} \sum_{k=-\infty}^{\infty} \langle \phi_{2^j}(u - 2^{-j}n), \phi_{2^{j+1}}(u - 2^{-(j+1)}k) \rangle \phi_{2^{j+1}}(x - 2^{-(j+1)}k) \quad (D.14)$$

The above equation can be written as

$$2^{-(j+1)} \langle \phi_{2^j}(u - 2^{-j}n), \phi_{2^{j+1}}(u - 2^{-(j+1)}k) \rangle = \langle \phi_{2^{-1}}(u), \phi(u - (k - 2n)) \rangle \quad (D.15)$$

And by the same way

$$\langle f(u), \phi_{2^j}(u - 2^{-j}n) \rangle = \sum_{k=-\infty}^{\infty} \langle \phi_{2^{-1}}(u), \phi(u - (k - 2n)) \rangle \langle f(u), \phi_{2^{j+1}}(u - 2^{-(j+1)}k) \rangle \quad (D.16)$$

Let H be a discrete filter whose impulse response is given by

$$h(n) = \langle \phi_{2^{-1}}(u), \phi(u - n) \rangle \quad (D.17)$$

and

$$H(\omega) = \sum_{k=-\infty}^{\infty} h(n) \exp^{-in\omega} \quad (D.18)$$

and let \tilde{H} be the mirror filter with impulse response $\tilde{h}(n) = h(-n)$. Then

$$\langle f(u), \phi_{2^j}(u - 2^{-j}n) \rangle = \sum_{k=-\infty}^{\infty} \tilde{h}(2n - k) \langle f(u), \phi_{2^{j+1}}(u - 2^{-(j+1)}k) \rangle \quad (\text{D.19})$$

Equation (D-19) says

1. $A_{2^j}^d =$ The convolution of $A_{2^{j+1}}^d f(u)$ with \tilde{H} and keeping every other sample of the output.
2. All $A_{2^j}^d f(u)$, when $j \geq 0$, can be computed from $A_1^d f(u)$ by this process.
3. This discrete filter H with the above mentioned impulse response has a certain relation with the scale function and is determined in another theorem by Mallat [47], that is,

$$\hat{\phi}(\omega) = \prod_{p=1}^{\infty} H(2^{-p}\omega) \quad (\text{D.20})$$

and

$$\hat{\phi}(2\omega) = H(\omega)\hat{\phi}(\omega) \quad (\text{D.21})$$

And from equation (D-8)

$$H(\omega) = \sqrt{\frac{\Sigma_{2n}(\omega)}{2^{2n}\Sigma_{2n}(2\omega)}} \quad (\text{D.22})$$

D.2 The Wavelet Representation

The WT is simply the difference of the information available at two successive resolutions 2^j and 2^{j+1} and can be called the detailed signal. The role which the scale function play in the case of the resolution signal is the same to the role of the wavelet function in the case of the detail signal. The procedure used in the previous section

to illustrate the construction of the scale function will be closely followed in explaining the development of the wavelet function;

Theorem 2 : Let $(V_{2^j})_{j \in \mathbb{Z}}$ be a multiresolution vector space sequence, $\phi(x)$ the scaling function, and H the corresponding conjugate filter, let $\psi(x)$ be a function whose Fourier transform (FT) is given by,

$$\Lambda \hat{\psi}(\omega) = G(\omega/2) \hat{\phi}(\omega/2) \quad (\text{D.23})$$

with

$$G(\omega) = \exp^{-i\omega} H(\omega + \pi) \quad (\text{D.24})$$

Let $\psi_{2^j}(x) = 2^j \psi(2^j(x))$ denote the dilation of $\psi(x)$ by 2^j . Then $(\sqrt{2^{-j}} \psi(x - 2^{-j}n))_{n \in \mathbb{Z}}$ is an orthonormal basis of O_{2^j} and $(\sqrt{2^{-j}} \psi_{2^j}(x - 2^{-j}n))_{n, j \in \mathbb{Z}}$ is an orthonormal basis of $L^2(\mathbb{R})$, where O_{2^j} is an orthogonal complement of V_{2^j} in $V_{2^{j+1}}$, OR; $O_{2^j} \oplus V_{2^j} = V_{2^{j+1}}$

It follow from (D-23) and (D-24),

$$\hat{\psi}(\omega) = \exp^{-i\omega/2} H(\omega/2 + \pi) \hat{\phi}(\omega/2) \quad (\text{D.25})$$

, or,

$$\hat{\psi}(\omega) = \frac{\exp^{-i\omega/2}}{\omega^n} \sqrt{\frac{\Sigma_{2n}(\omega/2 + \pi)}{\Sigma_{2n}(\omega)\Sigma_{2n}(\omega/2)}} \quad (\text{D.26})$$

Now, one can select the appropriate scaling function, for example, taking $p=1$ and thus $n=4$, a multiresolution approximation built from cubic splines can be obtained, that is,

$$N_1(\omega) = 5 + 30(\cos(\frac{\omega}{2})^2) + 30(\cos(\frac{\omega}{2})^2)(\sin(\frac{\omega}{2})^2)) \quad (\text{D.27})$$

and

$$N_2(\omega) = 2(\cos(\frac{\omega}{2})^2)(\sin(\frac{\omega}{2})^4)) + 70(\cos(\frac{\omega}{2})^4) + \frac{2}{3}(\sin(\frac{\omega}{2})^6) \quad (\text{D.28})$$

then

$$\Sigma_8(\omega) = \frac{N1(\omega) + N2(\omega)}{105(\sin(\omega/2))^8} \quad (\text{D.29})$$

From this function the wavelet function has been completely determined. However depending upon choice of $H(\omega)$, the scaling function $\phi(x)$ can have good localization both in time (spatial) and Fourier domains.

The decomposition of a signal in an orthonormal wavelet basis gives an intermediate representation between time and Fourier representations, and this can characterize the local regularity of a function $f(x)$ based on the coefficients in a wavelet orthonormal basis expansion, for example, from the asymptotic rate of decrease of the wavelet coefficients, one can determine whether the function $f(x)$ is n times differentiable at a point, say, x_0 .

Now, let $P_{O_{2^j}}$ be the orthogonal projection on the vector space O_{2^j} , according to theorem 2, this operator can be written as

$$P_{O_{2^j}} = 2^{-j} \sum_{n=-\infty}^{\infty} \langle f(u), \psi_{2^j}(u - 2^{-j}n) \rangle \psi_{2^j}(x - 2^{-j}n) \quad (\text{D.30})$$

and this is the detail signal at 2^j , also similar to (D-11) and (D-12) the discrete detail signal can be implemented as,

$$D_{2^j} f(x) = \langle f(u), \psi_{2^j}(u - 2^{-j}n) \rangle \quad (\text{D.31})$$

or,

$$D_{2^j} f(x) = (f(u) * \psi_{2^j}(-u))(2^{-j}n)_{n \in \mathbb{Z}} \quad (\text{D.32})$$

i.e, the discrete detail signal is the convolution of $f(u)$ with $\psi(-u)$ evaluated at a point $2^{-j}n$. Also, the wavelet $\psi(x)$ can be interpreted

as a band-pass filter whose frequency bands are approximately equal to $[-2\pi, -\pi] \cup [\pi, 2\pi]$. Hence the D_{2^j} describes $f(x)$ in the frequency bands $[-2^{-(j+1)}\pi, -2^{-j}\pi] \cup [2^{-j}\pi, 2^{-(j+1)}\pi]$

It is useful to say that this model is difficult to be interpreted in terms of a frequency decomposition because the overlap of the frequency channels, despite that this overlapping can be controlled thanks to the orthogonality of the decomposition function, the interpretation in the frequency domain provides an intuitive approach to the model [47]. Following the same steps from (D-13 to D-20) one can compute the wavelet representation.

For any $n \in \mathbb{Z}$, the function $\psi_{2^j}(x - 2^{-j}n)$ is a member of $O_{2^j} \subset V_{2^{j+1}}$, and can be expanded as

$$\psi_{2^{j+1}}(x - 2^{-j}n) = 2^{-(j+1)} \sum_{k=-\infty}^{\infty} \langle \psi_{2^j}(u - 2^{-j}n), \phi_{2^{j+1}}(u - 2^{-(j+1)}k) \rangle \phi_{2^{j+1}}(x - 2^{-(j+1)}k) \quad (D.33)$$

The above equation can be written as

$$2^{-(j+1)} \langle \psi_{2^j}(u - 2^{-j}n), \phi_{2^{j+1}}(u - 2^{-(j+1)}k) \rangle = \langle \psi_{2^{-1}}(u), \phi(u - (k - 2n)) \rangle \quad (D.34)$$

And then

$$\langle f(u), \psi_{2^j}(u - 2^{-j}n) \rangle = \sum_{k=-\infty}^{\infty} \langle \psi_{2^{-1}}(u), \phi(u - (k - 2n)) \rangle \langle f(u), \phi_{2^{j+1}}(u - 2^{-(j+1)}k) \rangle \quad (D.35)$$

let G be a discrete filter whose impulse response is given by

$$g(n) = \langle \psi_{2^{-1}}(u), \phi(u - n) \rangle \quad (D.36)$$

and let \tilde{H} be the mirror filter with impulse response $\tilde{h}(n) = h(-n)$.

Then

$$\langle f(u), \psi_{2^j}(u - 2^{-j}n) \rangle = \sum_{k=-\infty}^{\infty} \tilde{g}(2n - k) \langle f(u), \psi_{2^{j+1}}(u - 2^{-(j+1)}k) \rangle \quad (D.38)$$

Equation (D.38) says

- (a) D_{2^j} = The convolution of $A_{2^{j+1}}^d f(u)$ with \tilde{H} and retaining every other sample of the output.
- (b) $A_1^d f(u)$ can be computed by successive decomposing $A_{2^{j+1}}^d f(u)$ into $A_{2^j}^d f(u)$ and $D_{2^j}^d f(u)$ for $-J \leq j \leq -1$
- (c) The impulse response of filter G is related to the impulse response of the filter H by

$$g(n) = (-1)^{|1-n|} h(1-n) \quad (D.39)$$

and G is a high pass filter and thus equation (D-38) can be considered as a high-pass filtering of the discrete signal $A_{2^{j+1}}^d f(u)$

Appendix E

Computer Programs

```

CCCCCCCCCCCCCCCCCCCCCCCCCCCCCCCCCCCCCCCCCCCCCCCCCCCCCCCCCCCC
C  MAIN PROGRAM : CORRELATION METHOD FOR POWER SRECTRUM ESTIMATION  C
C    BY USING THE FAST FOURIER TRANSFORM                          C
C  INPUT      : M    THE SECTION SIZE                            C
C              N    THE NO. OF SAMPLES TO BE USED IN THE ANALYSIS C
C              MODE THE DATA FORMAT TYPE                       C
C              MODE = 0 AUTO CORRELATION                        C
C              MODE = 1 CROSS CORRELATION                      C
C              MODE = 2 AUTO COVARIANCE                       C
C              MODE = 3 CROSS COVARIANCE                      C
C              IWIN = 1 RECTANGULAR WINDOW                    C
C              IWIN = 2 HAMMING WINDOW                        C
C              L    THE NO. OF CORR. USED IN THE SPECTRAL     C
C              ESTIMATE . 2<=L>=M                             C
C              NFFT  THE SIZE OF FFT USED TO GIVE THE SPECTRAL C
C              ESTIMATE . L<=NFFT>=MAXM                       C
CCCCCCCCCCCCCCCCCCCCCCCCCCCCCCCCCCCCCCCCCCCCCCCCCCCCCCCCCCCC

```

```

DIMENSION XA(512),XFR(257),XAS(512),TT(512),Y(512)
DIMENSION JWIN(2,4)
DIMENSION ILAG(257)
COMPLEX X(512),Z(257),XMN,XI,YI
C REAL NSECT
INTEGER TTI,TTO
DATA JWIN(1,1), JWIN(1,2),JWIN(1,3), JWIN(1,4) /1HR,1HE,1HC,1HT/
DATA JWIN(1,1), JWIN(1,2),JWIN(1,3), JWIN(1,4) /1HH,1HA,1HM,1HG/
OPEN(UNIT=1,FILE='TTI.DAT',STATUS='OLD')
OPEN(UNIT=4,FILE='TTT.DAT',STATUS='OLD')
OPEN(UNIT=5,FILE='TTT9.DAT',STATUS='OLD')
OPEN(UNIT=2,FILE='TTO.OUT',STATUS='NEW')
OPEN(UNIT=3,FILE='LP1.OUT',STATUS='NEW')
OPEN(UNIT=8,FILE='pl1.out',STATUS='NEW')
OPEN(UNIT=9,FILE='pl2.out',STATUS='NEW')
MAXM=512
MAXH=MAXM/2+1
DO 10 I=1,MAXH
  ILAG(I)=I-1
10 CONTINUE
20 READ (1,2) M
2  FORMAT(I4)
  WRITE (2,1)M
1  FORMAT (18H SECTION SIZE = ,I4)

  IF(M.GT.0.AND.M.LE.MAXM) GO TO 30
  WRITE(2,3)
3  FORMAT(30H ILLEGAL INPUT--REENTER VALE )
  GO TO 20
30 READ(1,5)N
5  FORMAT(I5)
  WRITE (2,4) N
4  FORMAT(38HTOTAL NUMBER OF ANALYSIS SAMPLES =, I5)
  LSHFT=M/2
  MHLF1=LSHFT+1
  NSECT=(DBLE(N)+DBLE(LSHFT)-1.)/DBLE(LSHFT)
  READ (1,7)MODE
7  FORMAT(I1)
  WRITE(2,6) MODE
6  FORMAT(10H MODE = ,I1)
  READ (1,9)FS

```



```

9      FORMAT(F10.4)
      WRITE(2,8)FS
8      FORMAT(30H SAMPLING FREQUENCY IN HZ   =, F10.4)

      WRITE(2,11)M,N,MODE,FS
11     FORMAT(3H M=,I4,4H N=,I5,7H MODE=,I1, 20H SAMPLING FREQUENCY= ,
      *   F10.4)
      IF(MODE.LT.2)GO TO 80
      SS=1.
      NRD=LSHFT
      XSUM=0.
      YSUM=0.
      DO 70 K=1,N
      READ (4,333) TT(K),XA(K)
      XAS(K)=XA(K)
C      PRINT*,TT(K),XA(K)
      XSUM=XSUM+XA(k)
      IF(MODE.EQ.2)GO TO 70
      READ(5,333) TT(K),Y(K)
      YSUM=YSUM+XA(k)
70     CONTINUE
      XMEAN= XSUM/DBLE(N)
      YMEAN = YSUM/DBLE(N)
      IF(MODE.EQ.2) YMEAN=XMEAN
      WRITE(3,21)
21     FORMAT(//)
      WRITE (3,12)XMEAN,YMEAN
12     FORMAT(7HXMEAN= ,F15.4,   8H YMEAN=, F15.4)
      XMN= DCMLPX(XMEAN,YMEAN)
80     SS=1.
      NRDY=M
      NRDX=LSHFT
      DO 90 I=1,N
      Z(I)=(0.,0.)
90     CONTINUE
      DO 444 I=1,N
C      READ(4,333) TT(I),XA(I)
C      READ(5,333) TT(I),Y(I)
444     CONTINUE
      DO 190 K=1,NSECT
      NSECT1=NSECT-1
      IF (K.LT.NSECT1)GO TO 110
      NRDY =N-(K-1)*LSHFT
      IF (K.EQ.NSECT) NRDX=NRDY
      IF (NRDY.EQ.M) GO TO 110
      NRDY1=NRDY+1
      DO 100 I=NRDY1,M
      X(I)=(0.,0.)
100    CONTINUE
110    DO 120 I=1,N

      X(I)=DCMLPX(XA(I),XA(I))
C      PRINT*,X(I)
120    CONTINUE
      IF(MODE.EQ.0.OR.MODE.EQ.2)GO TO 140
C      CALL GETY(XA,NRDY,SS)
      DO 130 I=1,NRDY
C      READ(5,333) TT(I),XA(I)
      X(I)=DCMLPX(REAL(Y(I)),Y(I))
130    CONTINUE

```

```

333  FORMAT(F8.5,6X,F9.6)
140  IF(MODE.LT.2)GO TO 160
      DO 150 I=1,M
      X(I)=X(I)-XMN
150  CONTINUE
160  NRDX1=NRDX+1
      DO 170 I=1,M
      X(I)=DCMPLX(0.,AIMAG(X(I)))
C    PRINT*,X(I)
170  CONTINUE
      CALL FFT1(X,M,0)

C    print*,x(I)
      DO 180 I=2,M
      J=M+2-I
      XI=(X(I)+CONJG(X(J)))*.5
      YI=(X(J)-CONJG(X(I)))*.5
      YI =DCMPLX(AIMAG(YI),REAL(YI))
      Z(I)=Z(I)+CONJG(XI)*YI
C    print*,z(I)
180  CONTINUE

      XI=X(1)
      Z(1)=Z(1)+DCMPLX(REAL(XI)*AIMAG(XI),0.)
      XI=X(MHLF1)
      Z(MHLF1)=Z(MHLF1)+DCMPLX(REAL(XI)*AIMAG(XI),0.)
      SS=SS+DBLE(LSHFT)
190  CONTINUE
C    IDFT /CORR
      DO 200 I=1,M
      J=M+2-I
      X(I)=Z(I)
      X(J)=CONJG(Z(I))
C    print*,x(I),x(J)

200  CONTINUE
      X(1)=Z(1)
      X(MHLF1)=Z(MHLF1)
      CALL FFT1(X,M,1)
      FN=DBLE(N)
      DO 210 I=1,MHLF1
      XA(I)=DBLE(X(I))/N

210  CONTINUE
C    PRINT
      WRITE (3,21)
      WRITE (3,22)
22  FORMAT (21H CORRELATION FUNCTION)
      WRITE (3,21)
      WRITE (3,23)
23  FORMAT (6X,3HLAG,12X,4HCORR)
      WRITE(3,24)(TT(I),XA(I),I=1,N)
      do 59 i=1,n
      write(9,91)TT(I),XA(I)
91  format(f7.4,5x,f8.4)
59  continue
24  FORMAT (F6.4,9X,E10.3)
      WRITE (3,21)
C    WINDOW CORR
      READ (1,26) IWIN

```

```

26   FORMAT (I1)
    WRITE (2,25)IWIN
25   FORMAT (43H WINDOW TYPE      ( 1=RECTANGULAR, 2=HAMMING)      ,I1)
    READ (1,32)L
32   FORMAT (I4)
    WRITE (ITO,31)L
31   FORMAT (35H NO OF CORRELATION VALUES USED      = ,I4)
    READ (1,32) NFFT
    WRITE (2,33) NFFT
33   FORMAT (14H FFT SIZE      =,I4)
    NHLF1=NFFT/2+1
    WRITE(3,35) JWIN(IWIN,1), JWIN(IWIN,2), JWIN(IWIN,3),
*       JWIN(IWIN,4), L,NFFT
35   FORMAT(13H WINDOW TYPE=, 4A1,3X,22H NO OF WINDOW VALUES=,
*       I4,3X, 11HFFT SIZE=, I4)
C   BE WARE IF X NOT EQUAL TO Y -----WIN CORR FUN
    PI=4.*ATAN(1.0)
    DO 230 I=2,L
    IF (IWIN.EQ.1) GO TO 220
220  XA(I)=XA(I)*(0.54+.46*COS(PI*DBLE(I-1)/DBLE(L-1)))
    IF (MODE.EQ.1 .OR. MODE.EQ.3) GO TO 230
    J=NFFT+2-I
    XA(J)=XA(I)
230  CONTINUE
    NLAST = NFFT +1 -L
    IF (MODE.EQ.1 .OR. MODE.EQ.3) NLAST=NFFT
    L1=L+1
    DO 240 I=L1,NLAST
240  XA(I)=0.
    CONTINUE
    DO 250 I=1,NFFT
250  XA(I)=DCMPLX(XA(I),0.)
    CONTINUE
    CALL FFT1(X,NFFT,0)
C   LOG POWER IN DB
    XFS=FS/DBLE(NFFT)
    NHF=NFFT/2
    NHF1=NHF+1
    DO 260 I=1,NHF1
260  XFR(I)=DBLE(I-1)*XFS
C   PRINT*,X(I),ABS(X(I))
    IF(X(I).EQ.0.0) GO TO 260
    T=LOG10(ABS(X(I)))
    XA(I)=20.*T
260  CONTINUE
C   LOG POWER (DB)      PLOT
    WRITE (3,21)
    WRITE (3,38)
38   FORMAT (19H LOG POWER SPECTRUM)
    WRITE (3,21)
    WRITE (3,39)
39   FORMAT (5X,4HFREQ,7X,2HDB,5X,4HFREQ,7X,2HDB,5X,
*       4HFREQ,7X,2HDB,5X,4HFREQ,7X,2HDB)
    WRITE(3,88)
88   FORMAT(//)
    WRITE(3,9976)(XFR(I),XA(I),I=1,NHLF1)
    do 69 i=1,NHLF1
    write(8,92)xfr(i),xa(i)
92   FORMAT(F9.4,5X,F11.4)
69   CONTINUE

```

```
K=K/2
GO TO 20
30 J=J+K
40 CONTINUE
PI=4.0*ATAN(1.0)
DO 70 L=1,M
LE=2**L
LE1=LE/2
U=(1.0,0.0)
W=DCMPLX(COS(PI/DBLE(LE1)),-SIN(PI/DBLE(LE1)))
IF (INV.NE.0) W=CONJG(W)
DO 60 J=1,LE1
DO 50 I=J,N,LE
IP=I+LE1
T=X(IP)*U
X(IP)=X(I)-T
X(I)=X(I)+T
50 CONTINUE
U=U*W
60 CONTINUE
70 CONTINUE
IF(INV.EQ.0)RETURN
DO 80 I=1,N
80 X(I)=X(I)/DCMPLX(REAL(N),0.)
CONTINUE
RETURN
END
```

```

CCCCCCCCCCCCCCCCCCCCCCCCCCCCCCCCCCCCCCCCCCCCCCCCCCCCCCCCCCCC
C   THIS TRANSFORM REPRESENT THE FOURIER TRANSFORM OF THE      C
C   CONVOLUTION OF A CHOSEN WAVELET g(t). AND A GIVEN SIGNAL  C
C   g(t) CAN BE OBTAINED BY USING THE INVERSE FOURIER        C
C   TRANSFORM.                                               C
C   CHOOSE YOUR WAVELET                                       C
C   1 POLYNOMIAL SPLINES OF ORDER 3                            C
C   2 DAUBECHIES TIGHT FRAME                                  C
C   3 Y MEYERS CONSTRUCTION                                   C
C   4 THE MEXICAN HAT                                         C
C   5 THE 8TH DERITIVES OF THE GAUSIAN                       C
C   6 ONE CYCLE OF THE SINE FUNCTION                         C
C   7 THE MODULATED GAUSSIAN                                  C
CCCCCCCCCCCCCCCCCCCCCCCCCCCCCCCCCCCCCCCCCCCCCCCCCCCCCCCCCCCC

```

```

C
DIMENSION TT(1000), XA(-500:500,1000)
COMPLEX*16 XX(-500:500,1000),X(-500:500,1000),W(-500:500,1000)
COMPLEX*16 H(-500:500,1000),W1(-500:500,1000),W2(-500:500,1000)
COMPLEX*16 WW(-500:500,1000)
DOUBLE PRECISION A1(-500:500,1000),A2(-500:500,1000),A(-500:500,1000)
DOUBLE PRECISION A3(-500:500,1000),A4(-500:500,1000),AA(-500:500,1000)
COMMON/A/IIP,DI,BII
OPEN(UNIT=1,FILE='WAV.DAT',STATUS='OLD')
OPEN(UNIT=2,FILE='GT.OUT',STATUS='NEW')
OPEN(UNIT=3,FILE='GW.OUT',STATUS='NEW')
OPEN(UNIT=4,FILE='TSWT4.OUT',STATUS='NEW')
OPEN(UNIT=5,FILE='SGW.OUT',STATUS='NEW')
OPEN(UNIT=6,FILE='SGT.OUT',STATUS='NEW')
OPEN(UNIT=7,FILE='TFWT.OUT',STATUS='NEW')
OPEN(UNIT=8,FILE='TF.OUT',STATUS='NEW')
OPEN(UNIT=9,FILE='FR18.DAT',STATUS='OLD')
OPEN(UNIT=11,FILE='TFA.OUT',STATUS='NEW')
DATA DI/2./,BII/1./
READ (1,1) IIP
C 1  FORMAT('CHOSE YOUR WAVELET'/'1 POLYNOMIAL SPLINES OF ORDER 3 '/
C   $ '2 DAUBECHIES TIGHT FRAME'/'3 Y MEYERS CONSTRUCTION'/'4 THE
C   $ MEXICAN HAT'/'5 THE 8TH DERITIVES OF THE GAUSIAN'/'ONE CYCLE
C   $ OF THE SINE FUNCTION',I2)
READ (1,6)NOR,NOS,LI
READ(1,1)KOO
1  FORMAT(I2)
HH=1.
C 2  FORMAT('WHAT IS THE NO. OF SAMPLES',I4/'WHAT IS THE RESOLUTION
C   $ LEVEL',I2)
DO 3 K=1,NOS
READ(1,4) TT(K),XA(LI,K)
4  FORMAT(F8.5,6X,F9.6)
X(LI,K) = CMPLX(XA(LI,K),0.)
3  CONTINUE
CALL FFTC(X,NOS,0)
PI=4.*ATAN(1.)
INFT=4.
6  FORMAT(I3,2X,I4,1X,I2,2X,F12.6)
C   WRITE(*,5)KOO
C 5  FORMAT('1 TIME-SCALE REPRESENTATION
C   $ /2 TIME-FREQUENCY REPRESENTATION',I1)
C   IF(KOO.EQ.3) CALL WT(IIP,PI,M,N,DI,BII,NOS,NOR,H)
C   IF(KOO.EQ.2) GO TO 77

```

All Rights Reserved - Library of University of Jordan - Center of Thesis Deposit

```

DO 99 N=2,NOS+1
  DO 88 M=-INFT,INFT
    CALL WT(IIP,M,N,PI,DI,BII,NOS,NOR,H)
    DO 77 J=1,NOS
      W1(M,J)=H(M,J)*XA(LI,J)
      CONTINUE
77    CALL FINT(W1,NOS,M,HH)
      W(M,N)=(SQRT(2.**M))*W1(M,NOS+1)
      CALL FFTC(W,NOS,1)
      A1(M,N)=REAL(W(M,N))
      A2(M,N)=DIMAG(W(M,N))
      A(M,N)=(A1(M,N))**2+(A2(M,N))**2
      WRITE(4,134) M,N,A(M,N)
      FORMAT(I3,3X,I3,2X,F58.7)
134    CONTINUE
88    CONTINUE
99    CONTINUE
STOP
END

SUBROUTINE WT(IIP,M,N,PI,DI,BII,NOS,NOR,H)
COMPLEX*16 XS(1000),XX(-500:500,1000),H(-500:500,1000)
COMPLEX*16 TTT
DOUBLE PRECISION A1(-500:500,1000),A(-500:500,1000),AI(-500:500,1000)
DOUBLE PRECISION AII(-500:500,1000)
DO 2 J=2,NOS
  W=REAL(J)
  XS(J)=PSI(IIP,DI,BII,W)
C PRINT*,IIP,DI,W,XX1
  A1(M,J)=REAL(XS(J))
  AI(M,J)=DIMAG(XS(J))
WRITE(3,*)M,N,J,W,A1(M,J),AI(M,J)
  AA=DBLE((DI**M)*W)
C BB=DBLE(FO*W/N)
C XX(M,J)=PSI(IIP,DI,BII,AA)
XXX(M,J)=PSI(IIP,DI,BII,BB)
A(M,J)=REAL(XX(M,J))
AII(M,J)=DIMAG(XX(M,J))
WRITE(5,*)M,N,J,AA,A(M,J),AII(M,J)
56 FORMAT(I2,2X,I2,2X,I2,2X,F21.2,4X,G21.5,G16.5)
  TTT=CMPLX(0.,DI**M*BII*N*J)
  H(M,J)=EXP(TTT)*XX(M,J)
C WRITE(8,88) M,J,TTT,H(M,J)
C 88 FORMAT(I3,3X,I3,F25.4,4X,F28.20)
2 CONTINUE
RETURN
END

COMPLEX FUNCTION PSI(IIP,DI,BII,W,K1)
COMPLEX G,TT1
PI=4.*ATAN(1.)
IF(IIP.LT.1.OR.IIP.GT.7) RETURN
GO TO (1,2,3,4,5,6,7), IIP
1 X1=5.+30.*(COS(PI*W/2.))**2+30.*(SIN(PI*W/2.))**2*(COS(PI*W/2.))**2
X2=2.*(COS(PI*W/2.))**2*(SIN(PI*W/2.))**4+70.*(COS(PI*W/2.))**4+
$ 2./3.*(SIN(PI*W/2.))**6
SIGMA8=(X1+X2)/(105.*(SIN(PI*W/2.)))
X3=5.+30.*(COS(PI*W/4.))**2+30.*(SIN(PI*W/4.))**2*(COS(PI*W/4.))**2
X4=2.*(COS(PI*W/4.))**2*(SIN(PI*W/4.))**4+70.*(COS(PI*W/4.))**4+
$ 2./3.*(SIN(PI*W/4.))**6
SIGMA7=(X3+X4)/(105.*(SIN(PI*W/4.)))

```

المخلص

تحليل الإهتزازات الذاتية الناتجة عن السريان باستخدام التحويلات المويجية

الطالب : محمد سليمان أبو سمك

إشراف : الدكتور محمد نادر حمدان

تحظى ظاهرة الإهتزازات الذاتية الناتجة عن السريان بإهتمام الباحثين الكبير نظراً لأهميتها العملية في تصميم المنشآت الهندسية التي قد تتعرض للإنهيار نتيجة الإهتزازات الذاتية المحثوثة الناتجة عن سريان الموائع فوق هذه المنشآت. وبالرغم من الجهود المبذولة للتوصل الى تفسير دقيق يمكن من خلاله التنبؤ بالسلوك الفيزيائي لهذه الظاهرة ومن ثم إمكانية وصفها رياضياً إلا أن هذا الهدف ما زال بعيد المنال. ومن هنا جاءت أهمية هذه الدراسة حيث تم استخدام أساليب رياضية حديثة، التحويلات قصيرة الموجه أو المويجية (Wavelet Transforms)، لم يجر استخدامها سابقاً لدراسة هذه الظاهرة الى جانب الأساليب التقليدية مثل اقترانات العلاقات الذاتية (Autocorrelation Functions) والتقاطعية (Crosscorrelation Functions) واقترانات الاختلافات الذاتية (Autocovariance Functions) والتقاطعية (Crosscovariance Functions) والتحليل الطيفي (Power Spectral Analysis). كذلك تم استخدام عدد من المويجيات (Wavelets) في تحليل الإشارات العشوائية غير الثابتة (Nonstationari Signals) للإهتزازات الذاتية الناتجة عن السريان بواسطة التحويلات قصيرة الموجه.

وعند المقارنة بين هذه المويجيات في دراسة الإهتزازات الذاتية الناتجة عن السريان مثلت المويجه (Modulated Gaussian Wavelet) الاختيار الأفضل من حيث قدرتها على تمثيل الإشارات الإهتزازية الناتجة عن السريان بشكل ملائم ودقيق علمياً أو من حيث سهولة التمثيل الرياضي، كذلك فقد أظهرت التحويلات قصيرة الموجه عدداً من الخصائص المهمة المتعلقة بهذه الإهتزازات تحديداً فيما يتعلق بالحدود الإنتقالية (Transient Boundaries) والسلوك المشوش (Chaotic Behaviour) لم يمكن التوصل لها باستخدام الأساليب التقليدية، وبالاستفادة من الوسائل التلافيفية السريعة (Fast Convolution Techniques) مثل (Fast Fourier Transform) فقد تم تقليل الوقت اللازم لإجراء الحسابات الرياضية المتعلقة باستخدام التحليلات قصيرة الموجه.

وأستناداً الى هذه النتائج فقد تم تقديم عدد من التوصيات التي قد تحدد إتجاهات للعمل المستقبلي في استخدام التحليلات قصيرة الموجه في دراسة عددٍ من المواضيع المرتبطة بالإهتزازات الذاتية الناتجة عن السريان مثل الدفق الإضطرابي (Turbelent Flow) وظاهرة الظلال الدوامية (Vortex - Shedding Phenomenon) حيث يمكن استخدام نتائج تلك الأبحاث للوصول الى فهم أدق للإهتزازات الذاتية الناتجة عن السريان.